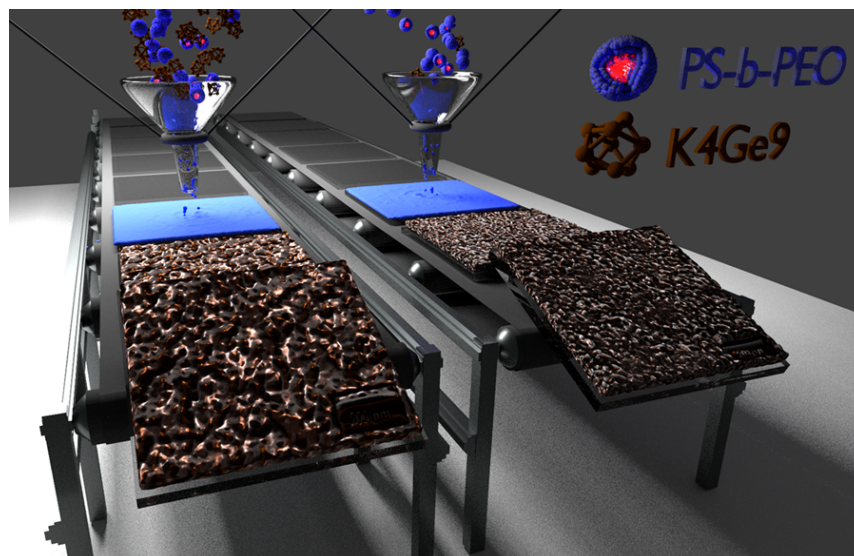




Annual Report 2017



Physik-Department  
Lehrstuhl für Funktionelle Materialien  
mit dem  
Fachgebiet Physik Weicher Materie  
Technische Universität München



Prof. Dr. Winfried Petry  
Chair of Functional Materials  
Physik-Department

Deputy chairman for Prof. Dr. Petry:  
Prof. Dr. Peter Müller-Buschbaum

Prof. Dr. Christine M. Papadakis  
Soft Matter Physics Group

Physik-Department  
Technische Universität München  
James-Franck-Straße 1  
85748 Garching

Secretaries: Marion Waletzki  
Carola Kappauf

Tel.: +49(0)89 289 12452  
Fax: +49(0)89 289 12473

Email: [muellerb@ph.tum.de](mailto:muellerb@ph.tum.de)  
[papadakis@tum.de](mailto:papadakis@tum.de)  
[marion.waletzki@ph.tum.de](mailto:marion.waletzki@ph.tum.de)  
[carola.kappauf@ph.tum.de](mailto:carola.kappauf@ph.tum.de)  
<http://www.functmat.ph.tum.de>  
<http://www.softmatter.ph.tum.de>

Editor: Dr. Lin Song

**Cover-page picture:**

Tunable structure of mesoporous Germanium thin films based on wet-chemical processing routines for application in next generation hybrid solar cells.

**Copyright:**

Inquiries about copyright and reproduction, etc. should be addressed to the authors.

## Preface

It is a great pleasure to present the annual report for the year 2017 in the name of the staff of the Chair of Functional Materials and the Soft Matter Physics Group. It provides an overview of our teaching, research, and development activities. Our research activities are focused on functional materials and cover a broad range from soft matter physics to developments of methods and instrumentation. We examine the fundamental physics of material properties using mainly scattering methods (neutron, x-ray and light scattering). The general goal of our research is to explain the functional characteristics of soft condensed matter from the knowledge of the molecular dynamics and nanostructure.

In 2017, the chair activities covered the specific areas of responsive polymers, thin polymer films, polymer films for application in photovoltaics and polymer-hybrid systems as well as real-time characterization, instrumentation and new materials. The activities in the fields of polymer films for application in photovoltaics and polymer-hybrid systems are successfully increasing. With *"TUM.solar"*, the keylab in the network of the Bavarian Collaborative Research Project *"Solar Technologies go Hybrid"* (SolTec) headed by Prof. Müller-Buschbaum was successfully renewed and is running in the sixth year of funding. Research activities on *"Structure of organometal halide perovskite films as determined with grazing-incidence x-ray scattering methods"* on *"Hybrid photovoltaics - from fundamentals towards application"* and on *"Capturing the sun: A review of the challenges and perspectives of perovskite solar cells"* were featured on covers of the high impact journal *Advanced Energy Materials*. Moreover, polymers with complex architecture, responsive polymers under high pressure, doubly switchable polymers, multiresponsive polymers as well as polymers for medical applications were in the focus of the research. A major review on solvent vapor annealing of nanostructured block copolymer thin films was published.

The in-house experiments available in the laboratories of the chair were supplemented by the lively activities at numerous large scale facilities, comprising synchrotron radiation and neutron scattering experiments, also at the FRM II. In particular, the in-house x-ray scattering experiments were operated with full time schedule. The imaging ellisometer was significantly upgraded to spectroscopic mode to allow for more elaborate measurements. With the addition of set-ups to measure solar cell efficiencies and the development of a novel in-operando IV-measurement chamber for characterization of solar cells, new experimental options were added to our facilities. In collaboration with our guest, Prof. Alfons Schulte, the sample environment for high-pressure research was substantially improved, now allowing for investigations of both, the dynamics and the kinetics.

In 2017, the Chair of Functional Materials comprised 9 fellows, 48 PhD students, 32 master students, 2 bachelor students, 8 student assistants and 7 administrative and technical staff members. 5 PhD theses were accomplished; moreover, 23 master theses as well as 20 bachelor theses were finished. As all the years before, we had the pleasure to host numerous guests from abroad, which stimulated a lively and inspiring scientific atmosphere.

In general, all members of the chair were very active at conferences and workshops, participating with both talks and posters. Moreover, important conferences were organized by members of the chair: At the Physics Department, Prof. Christine M. Papadakis and Prof. Peter Müller-Buschbaum hosted the Kolloid-Tagung *"Multiresponsive Systems"* (48th General meeting of the German Colloid Society) with ca. 150 participants, and Prof. Christine M. Papadakis hosted the 3rd Workshop *"Fluorescence Correlation Spectroscopy in Soft Matter Science"* with more

than 40 participants. Prof. Peter Müller-Buschbaum co-organized the 7th MSE Colloquium *"Highlights in Energy Research"*. Prof. Winfried Petry organized the *"Neutrons for Health"* conference in Bad Reichenhall and the *"3rd Biennial Science Meeting of the MLZ"* in Grainau. Again, two Edgar-Lüscher seminars were organized by Prof. Peter Müller-Buschbaum, this year on the subjects *"Astrophysik und Kosmologie"* and *"Moderne Materialien"*.

Regarding teaching activities of the chair, we offered general physics lectures for the TUM elite engineers in the Munich School of Engineering (MSE) (Müller-Buschbaum). Specialized lectures comprised *"Polymer physics"* (Papadakis) and *"Nanostructured soft materials"* (Müller-Buschbaum). Prof. Papadakis had a sabbatical and spent some time at the University of Central Florida, Orlando, U.S.A. She acted again as a deputy women's representative of the Physics Department. Moreover, Prof. Müller-Buschbaum is heading the activities in the *"Network Renewable Energies (NRG)"* in the MSE.

As a service to the community, Prof. Papadakis acted as one of the Editors-in-Chief of *"Colloid and Polymer Science"* and Prof. Müller-Buschbaum served as Associate Editor at *"ACS Applied Materials & Interfaces"*.

This annual report comprises a selection of the different research topics and projects carried out in the individual groups of the chair. It highlights the dedicated and successful research activities and collaborations with other groups and large scale facilities. We wish all chair members a fruitful continuation and a very successful year 2018.

Peter Müller-Buschbaum and Christine M. Papadakis

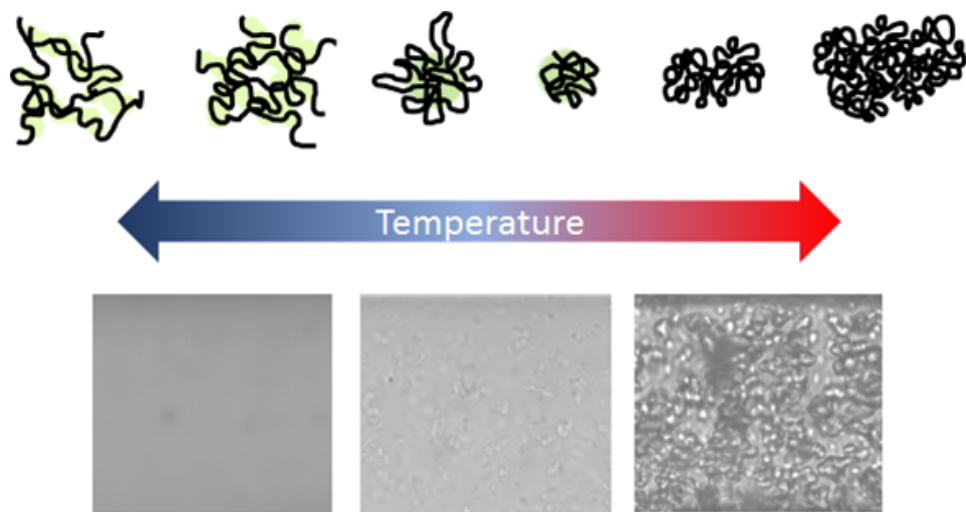
March 2018

## Contents

<b>1</b>	<b>Responsive polymers</b>	<b>7</b>
1.1	Pressure-dependence of poly( <i>N</i> -isopropylacrylamide) mesoglobule formation in aqueous solution . . . . .	8
1.2	Multi-responsive hydrogels from telechelic polyelectrolytes . . . . .	10
1.3	Structural investigations on multi-responsive physical hydrogels . . . . .	12
1.4	The structural, thermal and dynamic behavior of the thermoresponsive polymer poly(Nisopropylmethacrylamide) . . . . .	14
1.5	Polymeric bottle brushes with diblock side arms . . . . .	16
1.6	Morphological study of a drug delivery system based on poly(2-oxazoline) bottle brushes . . . . .	18
1.7	Macromolecular pHPMA-based drug delivery system - behavior in protein environment . . . . .	20
<b>2</b>	<b>Thin films</b>	<b>23</b>
2.1	Structural investigation of carbon onion thin films . . . . .	24
2.2	Investigation on the electronic/magnetic structure of magnetic nanoparticles embedded in polymer matrix . . . . .	26
2.3	Impact of precursor concentration on crystallinity and nanostructure of titanium dioxide in diblock copolymer templated sol-gel processes . . . . .	28
2.4	Swelling and exchange kinetics in PNIPAM microgel thin films investigated in-situ with time-of-flight neutron reflectometry . . . . .	30
2.5	Low-temperature fabrication of mesoporous titania thin films . . . . .	32
2.6	Thin films of ultrahigh molecular weight diblock copolymers . . . . .	34
2.7	Sputter deposition of gold electrodes on photoactive polymer thin films for organic electronics . . . . .	36
2.8	Self-assembly of quantum confined perovskite nanoplatelets in perovskite thin film . . . . .	38
2.9	Doping of the n-Type Polymer P(NDI2OD-T2) for improvement of its thermoelectric properties . . . . .	40
<b>3</b>	<b>Photovoltaics</b>	<b>43</b>
3.1	High efficiency organic solar cells based on low band-gap polymers . . . . .	44
3.2	Printed organic thin films for photovoltaic applications . . . . .	46
3.3	Active layers for hybrid solar cells based on laser-ablated metal oxide nanoparticles and water-soluble polythiophenes . . . . .	48
3.4	PBDB-T-SF for high efficiency solar cells . . . . .	50
3.5	Low temperature fabricated ZnO films for solid-state dye-sensitized solar cells . . . . .	52
3.6	Sputter deposition of gold contacts for hybrid solar cells . . . . .	54
3.7	Printing ITO-free electrode for low bandgap polymer solar cells . . . . .	56
3.8	Spray deposition of polymer thin films for photovoltaic application . . . . .	58
<b>4</b>	<b>Polymer-hybrid system</b>	<b>61</b>
4.1	Mathematical modeling of distribution of droplet size in thermal spray coating process . . . . .	62
4.2	Morphology phase diagram of printed titania films derived from block copolymer assisted sol-gel templating . . . . .	64
4.3	Morphology-function relationship in thermoelectric nanocomposites from PEDOT:PSS with inorganic silicon nanoparticles . . . . .	66
4.4	Conductive dry adhesives for detecting biosignals . . . . .	68

4.5	Influence of inorganic nanoparticles on the morphology of polymer blends for photovoltaic applications . . . . .	70
4.6	Printed diblock copolymer films embedded with magnetic nanoparticles . . . . .	72
4.7	Nanostructured TiO <sub>2</sub> lithium-Ion battery anode templated by electron conductive amphiphilic block copolymer . . . . .	74
4.8	Inner structure analysis on annealing treated colloidal quantum dots solids . . . . .	76
4.9	An insight into atmospheric degradation processes by mapping local nanoheterogeneities within hybrid polycrystalline perovskite films . . . . .	78
<b>5</b>	<b>Real-time characterization</b>	<b>81</b>
5.1	Investigating the degradation of PffBT4T-2OD: PC <sub>70</sub> BM solar cells by in-operando GIWAXS measurements . . . . .	82
5.2	In-situ tracking of composition and morphology of a diblock copolymer film with GISAXS during exchange of solvent vapors at elevated temperatures . . . . .	84
5.3	Degradation of plain 3D and 3D\2D heterojunction hybrid perovskite films in high humidity probed with in-situ GISANS . . . . .	86
5.4	Following the thickness evolution and water uptake of PEDOT:PSS thin films under high humidity conditions by in-situ time-of-flight neutron reflectometry . . . . .	88
5.5	Water swelling and exchange kinetics in multi-stimuli responsive polymer thin films followed with in-situ time of flight neutron reflectometry . . . . .	90
5.6	In-situ GISAXS during sputter deposition of metal nanolayers on functional polymer thin films . . . . .	92
5.7	Spray deposition of conducting composite films of PEDOT:PSS and cellulose studied with in-situ GISAXS . . . . .	94
5.8	In-situ study of spray deposited titania nanostructures . . . . .	96
5.9	In-situ GISAXS investigation of gold sputter deposition on colloidal polystyrene thin films . . . . .	98
<b>6</b>	<b>Instrumentation and new materials</b>	<b>101</b>
6.1	Monolithic U-Mo plates for the EMPIRE experiment . . . . .	102
6.2	A quasi-elastic and inelastic neutron scattering study of the alkaline and alkaline-earth borohydrides LiBH <sub>4</sub> , Mg(BH <sub>4</sub> ) <sub>2</sub> and the mixture LiBH <sub>4</sub> + Mg(BH <sub>4</sub> ) <sub>2</sub> . . . . .	104
6.3	Ordering in quaternary Heusler derivatives . . . . .	106
<b>7</b>	<b>Teaching and outreach</b>	<b>109</b>
7.1	Lectures, seminars and lab courses . . . . .	109
7.2	Conferences and public outreach . . . . .	111
7.3	Service to the community . . . . .	119
<b>8</b>	<b>Publications, talks and funding</b>	<b>121</b>
8.1	Publications . . . . .	121
8.2	Talks . . . . .	126
8.3	Posters . . . . .	134
8.4	Invited talks at LS Funktionelle Materialien . . . . .	139
8.5	Funding . . . . .	140
<b>9</b>	<b>The chair</b>	<b>142</b>
9.1	Staff . . . . .	142
9.2	Graduations . . . . .	145
9.3	Guests . . . . .	148

## 1 Responsive polymers



## 1.1 Pressure-dependence of poly(*N*-isopropylacrylamide) mesoglobule formation in aqueous solution

B.-J. Niebuur, K.-L. Claude, S. Pinzek, C. Cariker<sup>1</sup>, K.N. Raftopoulos, V. Pipich<sup>2</sup>, M.-S. Appavou<sup>2</sup>, A. Schulte<sup>1</sup>, C.M. Papadakis

<sup>1</sup> University of Central Florida, Orlando, USA

<sup>2</sup> JCNS at MLZ, Garching, Germany

Aqueous solutions of the thermoresponsive polymer poly(*N*-isopropylacrylamide) (PNIPAM) may serve as a simple model system to investigate the effect of pressure on the aggregation behavior of complex biological systems. Of special importance in this respect is the hydrophobic interaction, as it displays interesting behavior when pressure is applied: At high pressure, the hydrophobic groups are hydrated, thus weakening the hydrophobic interaction [1].

Previous research showed, that PNIPAM does not phase-separate macroscopically, but forms mesoglobules in the size range of 50 nm to 1  $\mu\text{m}$ , depending on the conditions [2,3]. In the present study, we aim to elucidate the relation between the hydration state of PNIPAM and the mesoglobule size. At this, we study a 3 wt% solution of PNIPAM (36 000 g mol<sup>-1</sup>) using Raman spectroscopy as well as very small angle neutron scattering (VSANS). Raman spectroscopy was performed with a LabRam HR 800 system (JY Horiba) at a spectral resolution of 2 cm<sup>-1</sup>. The excitation source was a frequency-doubled Nd:YAG laser with a wavelength of 532 nm. Spectra were acquired with an integration time of 5 min and corrected for dark current. VSANS experiments were performed at the instrument KWS-3 at the JCNS at MLZ. A  $q$  range of  $2 \times 10^{-4}$  -  $2 \times 10^{-3}$   $\text{\AA}^{-1}$  was covered. Measurements of 5 min were repeated multiple times at each temperature and pressure. The 2D scattering patterns were corrected for background scattering and azimuthally averaged.

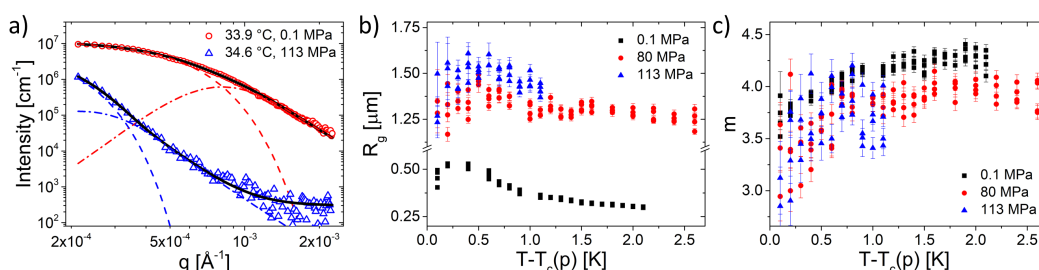


Figure 1.1:

(a) Representative VSANS curves from a 3 wt% PNIPAM solution in D<sub>2</sub>O including fits of the Beaucage model (black lines) and their individual components: Guinier term (dashed-dotted lines) and Porod term (dashed lines). (b)  $R_g$  and (c)  $m$  of the mesoglobules.

Fig. 1.1a shows representative VSANS curves obtained above the cloud point (CP) at 0.1 MPa and 113 MPa. The curves feature a shoulder in the measured  $q$  range, which marks the presence of large domains in the system. At 113 MPa, the shoulder is shifted to lower  $q$  values; thus the domains are much larger at high pressure than at atmospheric pressure. To extract quantitative information, the scattering curves were fitted with the Beaucage model, which contains the radius of gyration of the particles,  $R_g$ , as well as the Porod exponent,  $m$ , indicative of the surface structure. Large differences in morphology between atmospheric and high pressure are observed. At atmospheric pressure,  $R_g$  increases slightly from  $\sim 0.4$   $\mu\text{m}$  directly after phase separation to  $\sim 0.55$   $\mu\text{m}$  at  $T_{cp} + 0.3$  K whereas at 113 MPa, it stays constant at  $\sim 1.5$   $\mu\text{m}$  (Fig. 1.1b). At all pressures,  $R_g$  decreases with a further increase of temperature. This may be due to

a nonequilibrium state directly after phase separation, which is followed by rearrangements.

The Porod exponent,  $m$  (Fig. 1.1c), depends only weakly on pressure. At atmospheric pressure, it changes from  $\sim 3.7$  directly after phase separation to  $\sim 4.2$ . This shows that water in the outer layer of the initially smooth aggregates diffuses out, resulting in a concentration gradient at the surface. At high pressures,  $m$  increases from  $\sim 3.5$  to  $\sim 4$ , which shows that the initially rough aggregates smooth with increasing temperature without forming a concentration gradient at the surface.

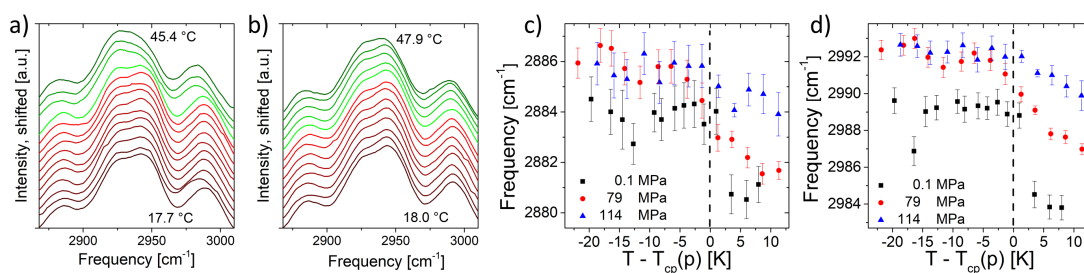


Figure 1.2:

Raman spectra at the CH stretching region at atmospheric pressure (a) and at 114 MPa (b), red curves represent measurements in the one-phase region and green curves in the two-phase region. (c)  $\nu_s(\text{CH}_3)$  and (d)  $\nu_{as}(\text{CH}_3)$  in dependence on temperature.

Raman spectroscopy measurements in dependence on temperature around the CP give insight into the hydrophobic hydration. The spectra at atmospheric pressure, Fig. 1.2a, shows a shift in position of the peaks at  $\sim 2885 \text{ cm}^{-1}$  and  $\sim 2990 \text{ cm}^{-1}$ , which are assigned to symmetric ( $\nu_s(\text{CH}_3)$ ) and antisymmetric stretching of the CH<sub>3</sub> groups ( $\nu_{as}(\text{CH}_3)$ ), respectively. At 114 MPa, in contrast (Fig. 1.2b), hardly any changes are discernible. The peak positions are extracted by fitting Lorentzian distributions to the spectra, and are shown in Fig. 1.2c and Fig. 1.2d for  $\nu_s(\text{CH}_3)$  and  $\nu_{as}(\text{CH}_3)$ , respectively. Below  $T_{CP}$ , both peak frequencies are constant at all pressures whereas decrease above. As CH<sub>3</sub> groups and water form improper hydrogen bonds, this points to dehydration of the hydrophobic side groups of PNIPAM after phase separation. At atmospheric pressure, the decrease in frequency is abrupt whereas at high pressure, it is smooth. Thus, the change of the hydration state is much less pronounced at high pressure than at atmospheric pressure, meaning the CH<sub>3</sub> groups stay hydrated to a certain degree even in the two-phase state at high pressure.

The observations from VSANS and Raman spectroscopy point to a difference in growth process of the mesoglobules. At atmospheric pressure, the chains are dehydrated and therefore collapsed and form aggregates that cannot grow easily due to low chain mobility. At high pressure, the chains remain hydrated which allows steady growth of the mesoglobules because rearrangements during merging are not hindered. In conclusion, the use of pressure as a variable enables changes in the hydration state of PNIPAM above the CP, which is reflected in the chain hydration and therefore the size and surface structure of the mesoglobules. [4]

- [1] F. Meersman, J. Wang, Y. Wu, K. Heremans, *Macromolecules* **38**, 8923-8928 (2005)
- [2] A.V. Gorelov, A. Du Chesne, K.A. Dawson, *Phys. A* **240**, 443-452 (1997)
- [3] C. Balu, M. Delsanti, P. Guenoun, F. Monti, M. Cloitre, *Langmuir* **23**, 2404-2407 (2007)
- [4] B.-J. Niebuur, K.-L. Claude, S. Pinzek, C. Cariker, K.N. Raftopoulos, V. Pipich, M.-S. Appavou, A. Schulte, C.M. Papadakis, *ACS Macro Lett.* **6**, 1180-1185 (2017)

## 1.2 Multi-responsive hydrogels from telechelic polyelectrolytes

C. Ko, M. A. Dyakonova, S. Gkempoura<sup>1</sup>, M. M. S. Lencina<sup>1</sup>, M. Rikkou-Kalourkoti<sup>2</sup>, C. Patrickios<sup>2</sup>, C. Tsitsilianis<sup>1</sup>, C. M. Papadakis

<sup>1</sup> University of Patras, Patras, Greece

<sup>2</sup> University of Cyprus, Nicosia, Cyprus

Multiresponsive polymeric hydrogels offer a rich switching behavior. This characteristic enables them to be an ideal candidate for injectable hydrogels, especially for drug delivery [1][2]. We investigate the structural properties of self-assembled pH- and thermo-responsive hydrogels from triblock terpolymers, bearing a pH-responsive central block and thermo-responsive hydrophobic end blocks, namely P(*n*BuMA-*co*-TEGMA)-*b*-PDMAEMA-*b*-P(*n*BuMA-*co*-TEGMA) (*n*BuMA, TEGMA and DMAEMA are *n*-butyl methacrylate, tri-(ethylene glycol)methyl ether methacrylate and 2-(dimethylamino)ethyl methacrylate). By varying temperature, it is possible to alter the water-solubility of the P(*n*BuMA-*co*-TEGMA) blocks and, thus, to influence the exchange dynamics of the stickers. As a consequence, the rheological properties of the hydrogels depend strongly on pH and temperature. A transition from a dynamic hydrogel network to a kinetically frozen network upon an increase in temperature was found. pH variation significantly affects the dynamic behavior of the hydrogels. We carried out small-angle X-ray scattering (SAXS) measurements on 4 and 1 wt% hydrogels or solutions from P(*n*BuMA<sub>10</sub>-*co*-TEGMA<sub>10</sub>)-*b*-PDMAEMA<sub>100</sub>-*b*-P(*n*BuMA<sub>10</sub>-*co*-TEGMA<sub>10</sub>) at pH 2.3, 6.6 and 7.9, respectively, in dependence on temperature.

Small-angle X-ray scattering (SAXS) measurements were carried out using a GANESHA 300XL SAXS instrument (SAXSLAB Aps, Copenhagen/Denmark) with a GENIX 3D microfocus X-ray source and point collimation. The X-ray wavelength was 1.54 Å. The sample-detector distances (SDDs) were chosen at ca. 400 and 1000 mm to cover a *q* range from 0.005 to 0.7 Å<sup>-1</sup>. The 4 wt% samples at pH 2.3 and pH 6.6 were gel-like, whereas the one at were mounted into a sandwich sample holder with mica windows. The 4 wt% sample at pH 7.9 and all 1 wt% samples were liquid and mounted in a quartz capillary. In both cases, the sample thickness was ca. 2 mm. All measurements were carried out in a temperature range from 10 to 50 °C. The scattering curves feature a maximum as well as weak shoulders. They were fitted by a model (Fig. 0.1a.) comprising a simplified sphere form factor  $P_{cl}(q)$  describing the micelles, the hard-sphere structure factor  $S_{HS}(q)$  describing their correlations, and the Ornstein-Zernike structure factor  $S_{OZ}(q)$  representing thermal fluctuations, Porod's law  $P_{Porod}(q)$  describing large aggregates or large-scale inhomogeneities, and the incoherent background  $I_{bkg}(q)$ .

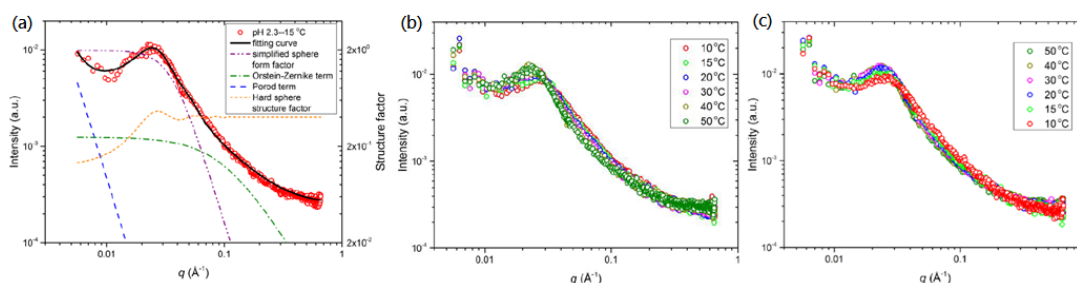


Figure 1.3:

SAXS curves from a 4 wt% hydrogel at pH 2.3 at 15 °C along with the fitting models and their contributions (a), (b,c) SAXS curves at pH 6.6 during a heating (b) and a cooling run (c).

We find that the radius of the micelles  $R_{mic}$  is 38-48 Å at 4 wt% at pH 6.6 and 38-54 Å at 1 wt% at pH 6.6 respectively. These flower-like micelles are connected to each other by the PDMAEMA blocks. The hard-sphere radius  $R_{HS}$ , indicating the correlation distance between micelles, is 95-110 Å at 4 wt% pH 6.6 and 135-155 Å at 1 wt% pH 6.6. The volume fraction of micelles is about 0.14-0.2 and depends only weakly on polymer concentration. The correlation length, related to the mesh size of a transient polymer network formed by the PDMAEMA bridges, is 5-30 Å.

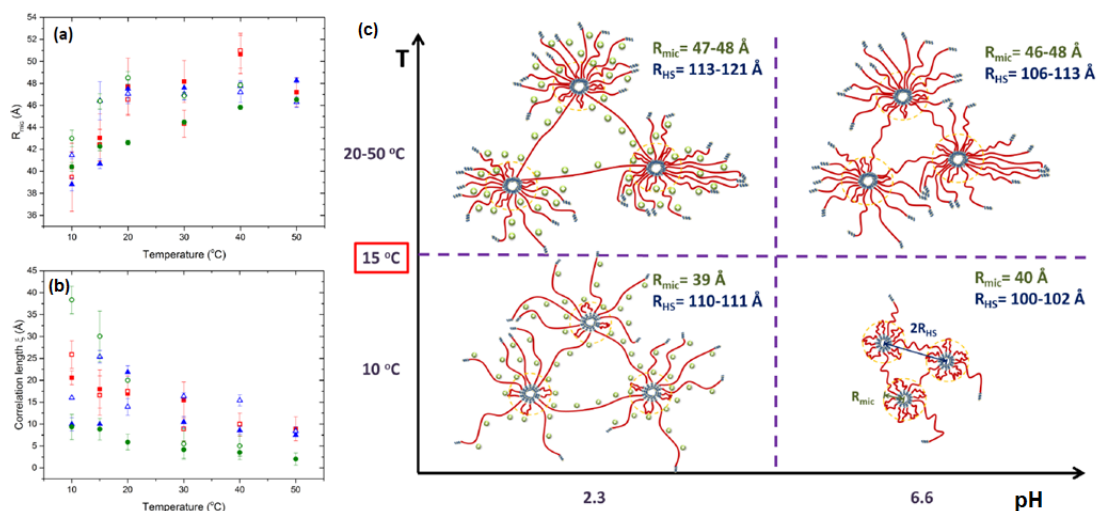


Figure 1.4:

Schematic representation of the structures of the 4 wt% hydrogels in dependence on temperature and pH.

At high temperatures, the micellar radius as well as the hard-sphere radius are larger than at low temperatures. This is attributed to the enhancement of hydrophobicity of thermo-responsive TEGMA blocks upon increasing temperature, resulting in an increased aggregation number. This gives rise to more stretched PDMAEMA chains in the shell of the micelles due to steric hindrance. In addition, the network of PDMAEMA chains becomes denser at higher temperature. This is reflected in the decrease of the correlation length with temperature. We found that the hard-sphere radius increases with decreasing pH, which we attribute to the fact that, at low pH, the pH-responsive PDMAEMA blocks are protonated and positively charged. Thus, the fraction of bridging PDMAEMA blocks increases. Meanwhile, less micelles are observed at low concentration. In addition, it is found that the distance between micelles is large at low concentrations.

To sum up, the structural properties of self-assembly hydrogels in dependence of temperature and pH were successfully determined by SAXS and quantitatively analyzed by fitting the SAXS curves by a model. The morphology of hydrogels from the present telechelic polyelectrolyte can be tuned by pD and temperature simultaneously. This characteristic enables it to be an ideal candidate for injectable hydrogels.

[1] C. Tsitsilianis, *Soft Matter* **6**, 2372-2388 (2010).

[2] D. Schmaljohann, *Adv. Drug Deliv. Rev.* **58**, 1655-1670 (2006).

### 1.3 Structural investigations on multi-responsive physical hydrogels

F. Jung, C. Ko, S. Gkempoura<sup>1</sup>, M. Rikkou-Kalourkoti<sup>2</sup>, R. Schweins<sup>3</sup>,  
C. S. Patrickios<sup>2</sup>, C. Tsitsilianis<sup>1</sup>, C. M. Papadakis

<sup>1</sup> University of Patras, Patras, Greece

<sup>2</sup> University of Cyprus, Nicosia, Cyprus

<sup>3</sup> Institut Laue-Langevin, Grenoble, France

Stimuli-responsive physical hydrogels strongly change their properties upon a small change of the environment and may be used for tissue engineering or for drug delivery [1]. In thin films, they find use as fast sensors or switchable membranes [2]. By employing multi-responsive systems, which respond to more than one stimuli, a high degree of versatility can be achieved.

In the present work, we investigate the structure of the multi-responsive, telechelic triblock copolymer (*n*-BuMA<sub>10-co</sub>-TEGMA<sub>10</sub>)-*b*-PDMAEMA<sub>100</sub>-*b*-(*n*-BuMA<sub>10-co</sub>-TEGMA<sub>10</sub>). The endblocks are statistical copolymers of the hydrophobic *n*-BuMA and the thermoresponsive TEGMA with a symmetric block composition. Tuning the copolymer composition enables control over the lower critical solution temperature (LCST) of the endblocks. The PDMAEMA midblock is a weak cationic polyelectrolyte with a dissociation constant  $pK_a \sim 7$ . At lower pH values, it is protonated, whereas at higher pH, it is uncharged. Furthermore, PDMAEMA exhibits an LCST at high pH values. In aqueous solution, this type of block copolymer is expected to form either flower-like micelles, where the endblocks make up the core and PDMAEMA the shell, or a physical network, with the hydrophobic end blocks acting as crosslinks which are bridged by the PDMAEMA midblock. The dynamics of the network may be tuned by varying the temperature around the cloudpoint. Ionization through pH variation allows stretching of the intermediate block and thus tunes the gelation behavior.

Fig. 1.5a shows small-angle neutron scattering (SANS) curves measured on 4 wt% polymer solutions in D<sub>2</sub>O at different pH and temperature values. At this concentration, gel formation was observed. The experiments were performed at beamline D11 at ILL, with detector distances varying between 1.5 and 28 m to cover a larger *q*-range. All curves were fitted using a combination of a core-shell form factor with polydisperse core correlated by a hard-sphere structure factor, the Ornstein-Zernike structure factor and a Porod power law. Since the scattering length densities (SLDs) of the core, the shell and the solvent are highly correlated in the fits, only the SLD of the shell was varied during a single fit while the other two were kept constant. This way, a large range of core SLDs were probed, which ranged from 0.64 to  $6.38 \times 10^{-6} \text{ \AA}^{-2}$ , where the limits represent the SLD of the pure endblocks and pure D<sub>2</sub>O, respectively, and the fit with the lowest  $\chi^2$  was chosen as the most reliable one. The process was then repeated a few times while narrowing down the range of probed SLDs, which finally resulted in information about the D<sub>2</sub>O content in the micelle core.

Fig. 1.5b-c show the obtained core radius and shell thickness of the micelles, respectively. At pH 7.9, where PDMAEMA is uncharged, both core radius and shell thickness increase sharply from 1.9 nm to 4.5 nm and from 4.0 nm to 4.9 nm, respectively, at  $\sim 30 \text{ }^\circ\text{C}$ . This can be explained by an increase of the aggregation number of the micelles, which is caused by the increased hydrophobicity of the endblocks above the LCST. Additionally, the shell thickness was found to decrease at  $\sim 50 \text{ }^\circ\text{C}$  to 4.1 nm, which is due to a collapse of the PDMAEMA shell when approaching its LCST. At lower pH, where PDMAEMA is ionized, an increase of both core radius and shell thickness with temperature is observed, but no transition temperature is found. The increase may be explained by better integration of the TEGMA units into the core due to an increase in hydrophobicity, while a strong increase in aggregation number, as observed for pH 7.9, is prevented by the electrostatic repulsion of the positively charged PDMAEMA. The shell thickness is overall larger for low pH, which is due to stretching of the charged PDMAEMA block.

The hard sphere radius, which is related to the distance between micelles, is shown in dependence on temperature in Fig. 1.5d. It increases steadily from 10.4 nm to 12.6 nm for pH 7.9, while for lower pH, it increases from 10.1 nm to 11.5 nm and from 10.3 nm to 11.6 nm for pH 6.6 and pH 2.3, respectively. For the lower pH values, it follows the behavior of the shell thickness, indicating that the distance between micelles is primarily related to the stretching of the PDMAEMA block. For pH 7.9, it is decoupled from the shell thickness, and overall larger compared to the lower pH. This indicates that the increase of the distance between micelles is due to the increased aggregation number, and that the micelles, while still correlated, are not connected by bridging PDMAEMA midblocks, but form mostly flower-like micelles.

Fig. 1.5e shows the SLD of the core, where a larger value indicates a high D<sub>2</sub>O content and vice versa. At pH 7.9, the D<sub>2</sub>O content is low, and decreases initially with increasing temperature. This is due to the increased hydrophobicity of the endblocks and is consistent with the core radius decreasing, thus becoming denser. At higher temperatures, the amount of D<sub>2</sub>O increases significantly due to increased aggregation number. At lower pH values, the water content in the core increases as the LCST is approached, and then steadily decreases with further increase of temperature, which may be due to a progressive dehydration of the endgroups.

In conclusion, the dependence of the micelle structure on pH and temperature is schematically shown in Fig. 1.5f. While it was found that the midblock is stretched at low pH values due to ionization, which was expected, a sharp change of structural properties at the LCST could only be found at high pH values.

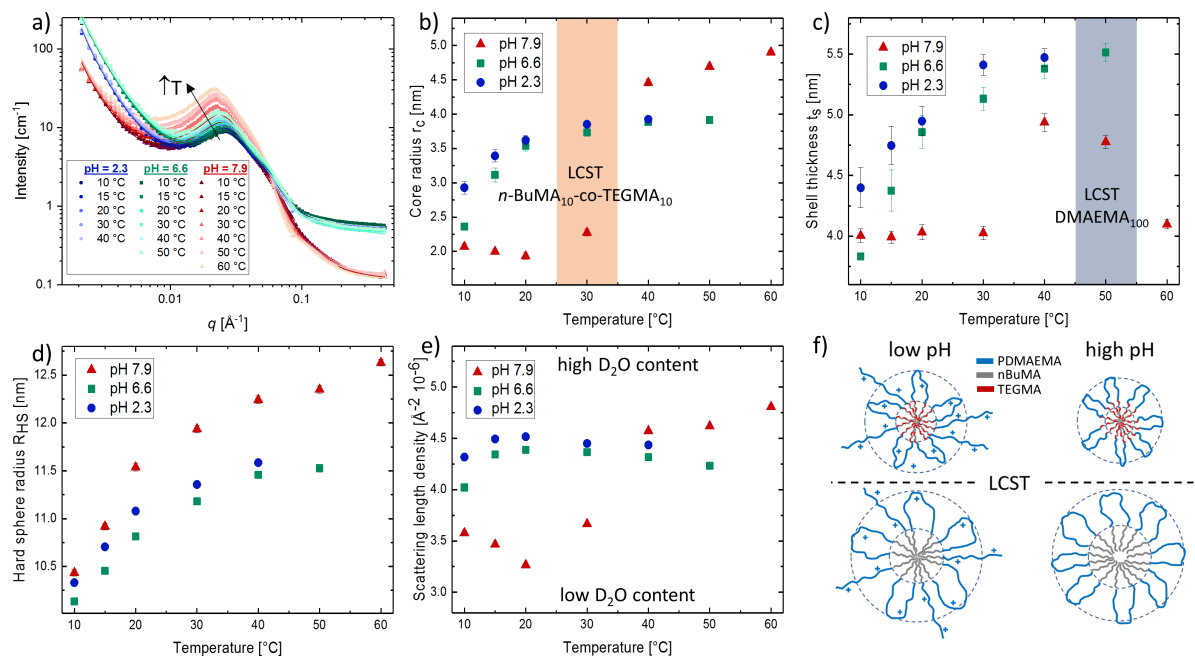


Figure 1.5:

(a) SANS curves measured on 4 wt% D<sub>2</sub>O solutions at the pH and temperature values given in the inset. (b)-(e) Temperature dependence of core radius, shell thickness, hard-sphere radius and scattering length density of the core, respectively. Observed transition temperatures are indicated with shaded areas. (f) Schematics of the structure of the micelles in various pH and temperature regimes.

[1] C. Tsitsilianis, *Soft Matter* **6**, 2372-2388 (2010)

[2] I. Tokarev, S. Minko, *Soft Matter* **5**, 511-524 (2009)

#### 1.4 The structural, thermal and dynamic behavior of the thermoresponsive polymer poly(Nisopropylmethacrylamide)

C. Ko, K.-L. Claude, D. Schanzenbach<sup>1</sup>, B. Niebuur, X. Zhang, D. Aravopoulou<sup>2</sup>, A. Kyritsis<sup>2</sup>, H. Frielinghaus<sup>3</sup>, P. Müller-Buschbaum, A. Laschewsky<sup>1,4</sup>, C. M. Papadakis

<sup>1</sup> Universität Potsdam, Potsdam-Golm, Germany

<sup>2</sup> National Technical University of Athens, Athens, Greece

<sup>3</sup> Maier-Leibnitz-Zentrum, Garching, Germany

<sup>4</sup> Fraunhofer Institute for Applied Polymer Research, Potsdam-Golm, Germany

Poly(N-isopropylmethacrylamide) (PNIPMAM) is a thermoresponsive polymer, exhibiting lower critical solution temperature (LCST) behavior in aqueous solution with a cloud point at 43 °C [1]. The coil-to-globule transition of PNIPMAM chains makes it a potential candidate in applications like tissue engineering and fluidic microvalves. Understanding the fundamental mechanism of structural changes is crucial to further design materials for applications. We investigate the structural, thermal and dynamic properties of aqueous PNIPMAM solution in dependence on concentration.

The PNIPMAM samples (12 and 20 kg/ml) were synthesized by free radical polymerization method. They were investigated in D<sub>2</sub>O. Turbidimetry, differential scanning calorimetry (DSC), small-angle neutron scattering (SANS) were carried out in a concentration range from 5 mg/ml to 150 mg/ml in a large temperature range around the cloud point.

DSC gives insight into the thermal properties of PNIPMAM at the phase transition. At a heating rate of 1 K/min, a peak was observed at 43-46 °C, reflecting the dehydration. Two characteristic temperatures,  $T_{onset}$  and  $T_{peak}$ , were determined from the specific heat capacity. The turbidimetry measurements at a heating rate of 0.2 K/min revealed the cloud points  $T_{CP}$  in the range 38.5-40 °C, i.e. at much lower temperatures.  $T_{onset}$ ,  $T_{peak}$  and  $T_{CP}$  are compiled in Fig. 1.6 in dependence on the polymer concentration. Thus, the phase diagram comprises three regimes, named I-III.

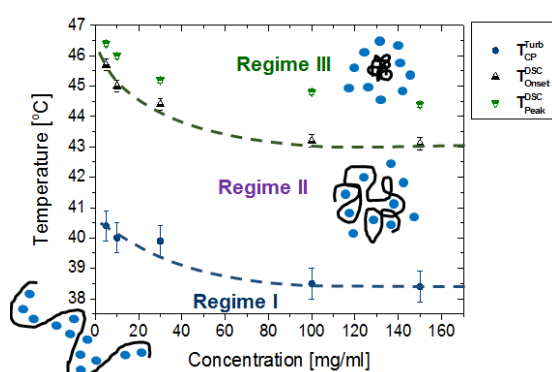


Figure 1.6: Phase diagram of PNIPMAM in D<sub>2</sub>O determined by different methods.

DLS reveals a single mode for a 30 mg/ml PNIPMAM solution (12 kg/ml) which is diffusive. This mode may thus be attributed to the cooperative motion of polymer chains in the solvent. Two transition temperatures are evident in the heating and cooling process, respectively. They correspond to the temperatures obtained in DSC and turbidimetry (Fig. 1.6). In the cooling process, the phase transition of the system proceeds only gradually. The dynamic correlation length is 6-8 nm.

SANS measurements provide information about the structural changes of PNIPMAM solutions at the transition temperatures. Representative SANS data from 150 and 100 mg/ml are shown in Fig. 1.7 a. Most of them feature two decays, one at high  $q$  values, being due to local concentration fluctuations, and one at low  $q$  values, being due to large inhomogeneities or aggregates. Interestingly, the scattering at high  $q$  values changes only at high temperatures, i.e. at the transition temperature between regimes II and III. Moreover, it is surprising that already in regime I, large-scale inhomogeneities are present. The data were analyzed by fitting models for scattering from a polymer solution, namely Ornstein-Zernike (OZ) model, which reveals information about the length scales of the concentration fluctuations. The correlation length slightly increases with temperature from in regime I and decreases at the transition between regimes I and II. In regimes II and III, the correlation length increases with temperature from 1 nm to 1.6 nm. Besides, the OZ exponent is about 3.9 for both concentrations in regime I, which points to compact particles, and decreases dramatically to values around 2.8 in regimes II and III. In some cases, the aggregate size can be determined using the Beaucage model, and reveals radii of gyration of ca. 50-100 nm. The aggregates are loose from 30-43 °C, and become compact above 47 °C. From the structural parameters from SANS, two different transition temperatures can be distinguished; however, the behavior is different for the two concentrations.

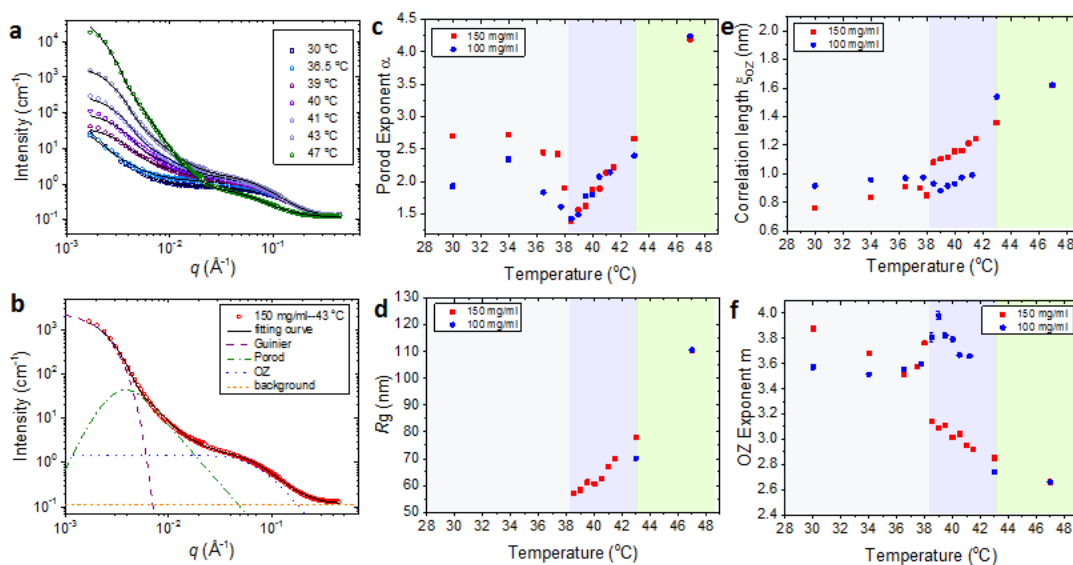


Figure 1.7:

(a) The SANS scattering curves of 150mg/ml in D<sub>2</sub>O solutions., (b) Fitting model for curves with bending at low  $q$  values. (c) Porod exponent (d) Radius of gyration (e) OZ correlation length (f) OZ exponent of the 150 mg/ml and 100 mg/ml polymer solutions.

The following picture emerges for the phase transition mechanism of PNIPMAM: In regime I, the solutions are in the one-phase state. However, forward scattering in this regime reveals loosely packed large aggregates. In regime II, aggregates become more prominent, possibly due to association of the hydrophobic groups. In regime III, the chains collapse, as expected for thermoresponsive polymers, and the aggregates continue to grow.

The project is funded by Deutsche Forschungsgemeinschaft (DFG).

[1] K. Kunota, K. Hamano, and N. Kuwahara., *Polymer Journal*, **22**,1051–1057, (1990).

## 1.5 Polymeric bottle brushes with diblock side arms

J.J. Kang, J. Zhao<sup>1</sup>, S. Pispas<sup>1</sup>, C.M. Papadakis

<sup>1</sup> National Hellenic Research Foundation, Athens, Greece

Bottle brush polymers, composed of a backbone polymer grafted by polymeric side chains - ideally on each backbone monomer - feature characteristic self-assembly behavior in bulk, solutions and on surfaces due to their special architecture. With the benefits of nanoscale periodic domains resulting from the self-assembly, which are tunable by adjusting the molar masses of the backbone and the side chains, bottle brush polymers can be potential materials for various applications, such as photonic crystals, nano-encapsulation and drug delivery. If the side chain is composed of both thermoresponsive and hydrophilic monomers, the bottle brushes are amphiphilic and have lower critical solution behavior in aqueous solution. The thermoresponsive moieties are responsible for a conformational change of the bottle brush with temperature.

In the present study, we investigate a thermoresponsive bottle brush block copolymer with a poly(*p*-hydroxystyrene) (PHOS) backbone and poly(propylene oxide)-*block*-poly(ethylene oxide) (PPO-*b*-PEO) side chains [1]. The thermoresponsive PPO block is directly attached to the backbone and is thus in aqueous solution protected to some extent by the hydrophilic PEO endblock. The weight fraction of PPO in the side chain is 59.2 %. While PEO homopolymers are water soluble up to 100 °C, PPO homopolymers can be dissolved in water only partially (solubility of 40 % at 20 °C). Therefore, it is expected that, in aqueous solution, the bottle brush copolymer undergoes a conformational change upon heating. In order to detect the transition temperature and to characterize the structural variations, dynamic light scattering (DLS) and small-angle X-ray scattering (SAXS) were used in a wide temperature range.

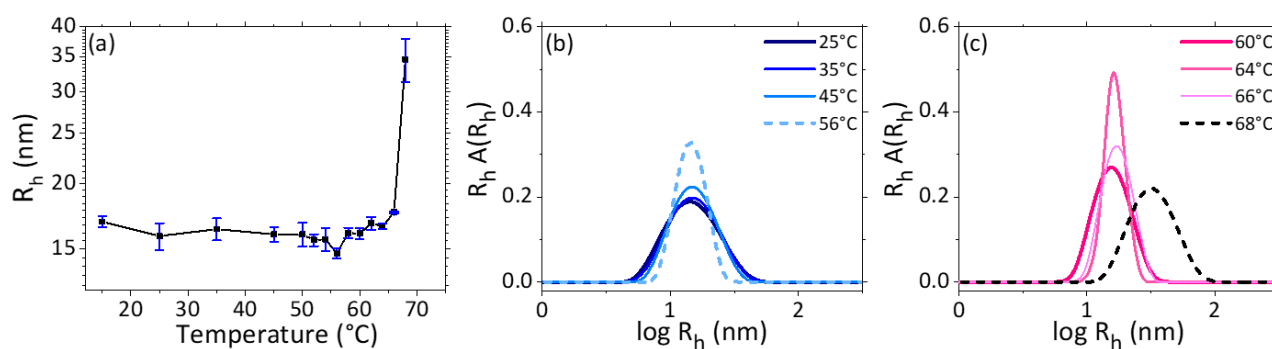


Figure 1.8: Results from DLS. (a) Dependence of  $R_h$  on temperature (b, c) at selected low (b) and high temperatures (c).

DLS measurements were carried out on a 10 mg/ml solution from room temperature to 70 °C. The autocorrelation functions were analyzed by numerical inverse Laplace transformation, giving the distribution of relaxation times or, equivalently, of hydrodynamic radii,  $R_h$ . From each peak in the distribution function, the average  $R_h$  value is extracted. The solution becomes turbid at temperatures higher than 70 °C, which results in multiple scattering, hampering DLS measurements. In Fig. 3.15, the average hydrodynamic radius and the corresponding distribution functions are shown in dependence on temperature. At room temperature,  $R_h$  is

15.9 nm, and this value is maintained as the temperature is elevated to 64 °C. While the average value is unchanged, the width of the size distribution decreases with increasing temperature. Above 64 °C,  $R_h$  sharply increases to 34.6 nm at 68 °C with a broad distribution.

SAXS measurements were carried out at a concentration of 40 mg/ml to ensure a higher scattering signal. (Fig. 3.16) At room temperature, the curves feature a maximum at  $0.12 \text{ nm}^{-1}$  which implies a certain degree of ordering of the bottle brush copolymer. Estimating the radius of the bottle brush copolymers from the position of the first minimum of the form factor results in ca. 15 nm. Upon heating, the maximum gradually decreases and completely disappears, as the temperature reaches 59 °C. Thus, the spatial correlation between the bottle brush copolymer gets lost. Moreover, the second maximum of the form factor becomes more pronounced (at  $0.38 \text{ nm}^{-1}$ ) as the temperature increases, indicating that the shape of the bottle brush copolymer becomes more well-defined. From 59 °C to 64 °C, the scattering intensity drops and vanishes completely, which might be due to the formation of large aggregates, therefore a decrease in the number of scattering particles. To summarize, SAXS results show the bottle brush copolymers are swollen and thus well correlated at low temperatures. As they are heated, the PPO blocks presumably collapse, the brush size shrinks and the correlation between them is lost. Finally, very large aggregates form at 64 °C, possibly due to the strong hydrophobicity of the PPO blocks.

Comparing the results from DLS and SAXS, the particle size of the bottle brush copolymers is found to be consistent. The well-defined particle shape at 55 °C, observed in SAXS, is confirmed by the narrow  $R_h$  distribution in DLS. The disagreement of the temperature where large aggregates form (64 °C in SAXS, 70 °C in DLS) may be due to the difference in polymer concentration. The study thus shows intricate changes which are more complex than the ones witnessed in simple diblock copolymers.

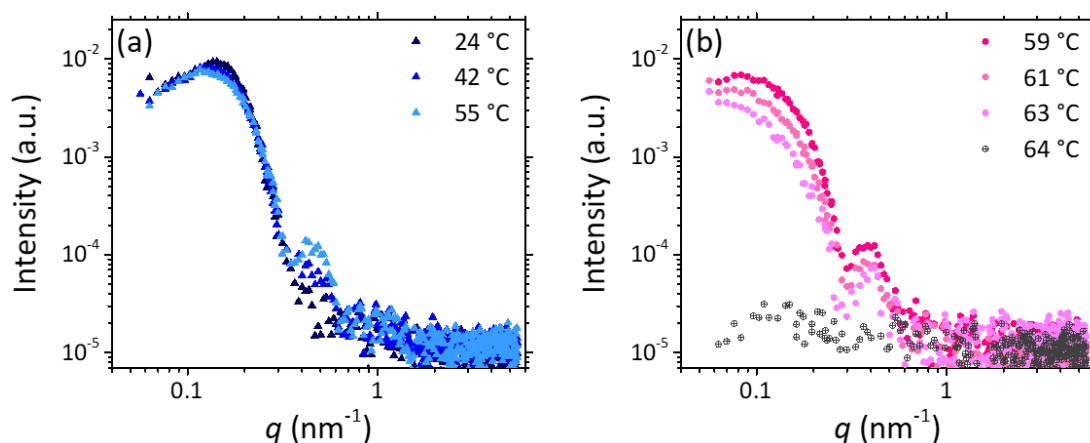


Figure 1.9: SAXS curves at selected low (a) and high temperatures (b).

[1] J. Zhao, G. Mountrichas, G. Zhang, S. Pispas, *Macromolecules* **43**, 1771 (2010)

## 1.6 Morphological study of a drug delivery system based on poly(2-oxazoline) bottle brushes

K. Shehu, J-J. Kang, C. Sachse<sup>1</sup>, R. Jordan<sup>1</sup>, C. M. Papadakis

<sup>1</sup> Technische Universität Dresden, Dresden, Germany

Bottlebrush polymers consist of a polymer backbone with densely grafted side chains. They can be used as nano carriers in drug delivery systems. For instance, paclitaxel (PTX), a hydrophobic drug known for its potential to treat several types of cancers, suffers from limitations like low water solubility ( $\sim 1\mu\text{g}/\text{mL}$ ). A high drug loading capacity is required to facilitate the cancer treatment, however, this may lead to significant changes in the morphology and stability of the carrier system [1]. Bottle brush copolymers have been suggested to serve as stable carriers for PTX. Bottle brushes from poly(2-oxazoline)s are well-suited with this purpose due to their biocompatibility. Moreover, they can be tuned to be hydrophobic or hydrophilic by choice of the side group [2].

In the present study, a bottle brush copolymer with a hydrophobic poly(2-isopropenyl-2-oxazoline) backbone and hydrophilic side chains of poly(2-ethyl-2-oxazoline); P(iPOx)-g-P(EtOx), Fig.1.10a, is investigated with respect to its size and inner structure in aqueous solution in dependence on temperature. At this, dynamic light scattering (DLS) is used. A dilute solution of P(iPOx)<sub>100</sub>-g-P(EtOx)<sub>17</sub> was prepared at 1 wt %. The DLS instrument features a HeNe laser having a wavelength of 632.8 nm. The scattered light goes through a polarizer into the detector and the scattering intensity is recorded in terms of time. DLS analysis gives the hydrodynamic radius ( $R_h$ ) of the bottle brush polymer, derived from the autocorrelation function of the intensity trace.

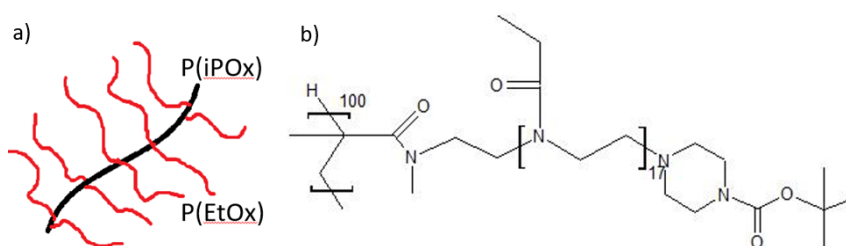


Figure 1.10:

(a) Bottle brush copolymer with P(iPOx) backbone and P(EtOx) sidechain. (b) Chemical structure of the bottle brush copolymer under study

In the present experiment, five measurements, having each a duration of 30 seconds, were carried out. After each temperature change, a waiting time of 600 s was applied to reach thermal equilibrium. The sample was heated from room temperature to 50 °C. At 50 °C and above, the obtained data cannot be analyzed due to the solution becoming turbid. Representative autocorrelation curves are shown in Fig. 1.11. Two decays are observed, implying that two types of particles are present in this solution.

The distribution of hydrodynamic radii is shown in Fig. 1.12a. It features two peaks, namely  $R_h$  at 5 nm and 270 nm. The position of the peak at 5 nm is assumed to belong to the single bottle brushes. This peak is stable between 25 °C and 44 °C. Only at 48 °C the peak becomes broader, which may be due to proximity of the transition to the turbid phase. In contrast, the position of the peak at 270 nm fluctuates between between 25 °C to 44 °C, and becomes broad at 48 °C. Fig. 1.12b shows the average hydrodynamic radii in dependence on temperature, which confirms these observations. Thus, it has been observed that the size of the small particles

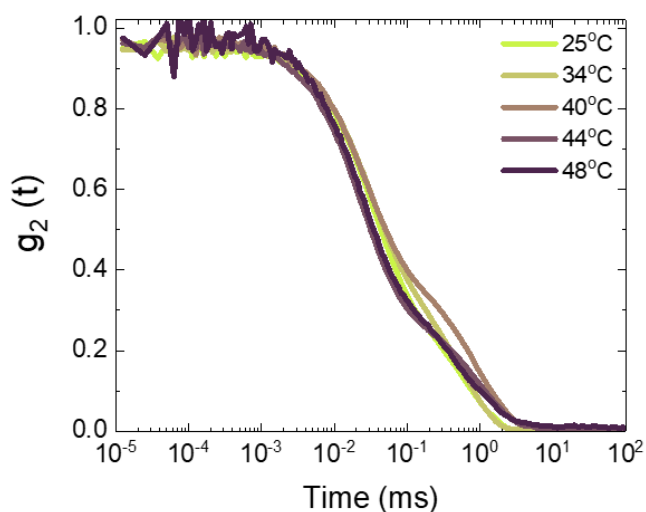


Figure 1.11:  
Representative autocorrelation functions given in the legend at a scattering angle of 90 degrees

remains rather constant. On the contrary, for the large particles there is a considerable change in size. These large particles may be biproducts from the synthesis. It has been observed that there are both small particles, of several nanometer, and large particles, of up to hundred nanometers, coexisting in the dilute bottle brush solution. Further scattering experiments will be conducted on the system to disclose the structural information of these particles.

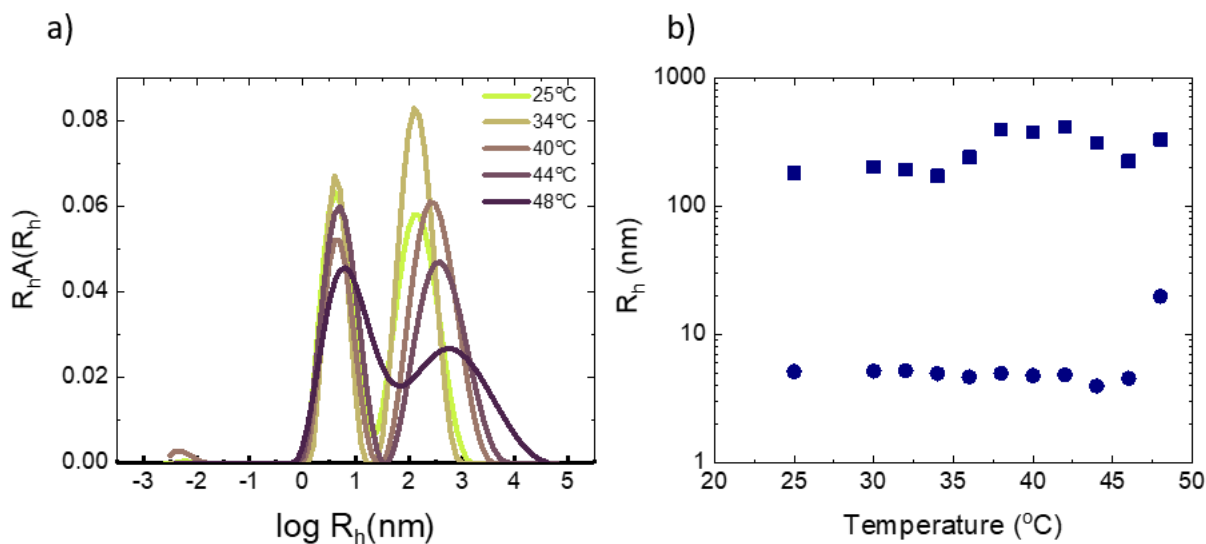


Figure 1.12:  
(a) Distribution functions of the hydrodynamic radii corresponding to the data in figure 0.2.  
(b) Average hydrodynamic radii in dependence on temperature. Circles: small particles, Squares: large particles.

- [1] S. Jaksch, A. Schulz, Z. Di, R. Luxenhofer, R. Jordan, C. M. Papadakis, *Macromol. Phys. Chem.* **217**, 1448-1456 (2016)
- [2] A. Schulz, S. Jaksch, R. Schubel, E. Wegener, Z. Di, Y. Han, A. Meister, J. Kressler, A. V. Kabanov, R. Luxenhofer, C. M. Papadakis, R. Jordan, *ASC Nano* **8** (3), 2686-2696 (2014)

## 1.7 Macromolecular pHPMA-based drug delivery system - behavior in protein environment

X. Zhang, B.-J. Niebuur, P. Chytil<sup>1</sup>, T. Etrych<sup>1</sup>, S. K. Filippov<sup>1</sup>, A. Kikhney<sup>2</sup>, D. C. F. Wieland<sup>2</sup>, D. I. Svergun<sup>2</sup>, C. M. Papadakis

<sup>1</sup> Institute of Macromolecular Chemistry, Prague, Czech Republic

<sup>2</sup> The European Molecular Biology Laboratory, Outstation Hamburg, Germany

In dilute aqueous solution, polymeric drug carriers based on poly(*N*-(2-hydroxypropyl)methacrylamide) (pHPMA) copolymers (Fig. 1.13 a) with hydrophobic cholesterol side groups and the anti-cancer drug doxorubicin (Dox) have been found to form elongated core-shell nanoparticles (NPs) by self-assembly (Fig. 1.13 b) [1]. However, little is known about how these drug carriers behave in real human blood environment. Human blood contains hundreds of proteins, which are expected to interact with the NPs and make the investigation extremely complicated. Therefore, experiments where the effect of a single protein type is investigated are more appropriate. At this, we study the copolymers in an aqueous solution of human serum albumin (HSA), the most abundant protein in human blood.

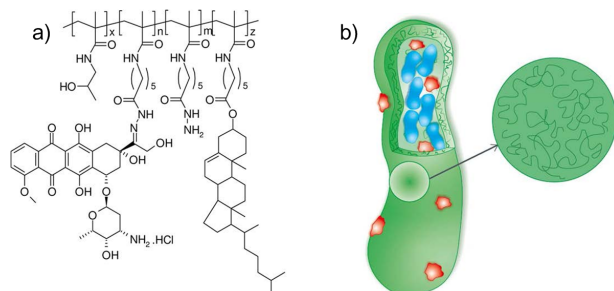


Figure 1.13: a) Schematic drawing of the HPMA copolymer-drug conjugate bearing cholesterol moieties. b) Structure of the self-assembled NPs. Green: pHPMA, blue: cholesterol, red: Dox. Reprinted with permission from [1]. Copyright 2012 American Chemical Society.

In the present study, we investigate interactions between HSA and the NPs formed by the copolymer pHPMA-Chol ( $M_w = 33290$  g/mol, 2.1 mol % cholesterol) and pHPMA-Chol-Dox ( $M_w = 50000$  g/mol, 2.1 mol % cholesterol, 6.0 wt % Dox) using synchrotron small-angle X-ray scattering (SAXS) and isothermal titration calorimetry (ITC).

All samples were dissolved in phosphate buffered saline (PBS), then mixed with an aqueous solution of HSA, resulting in HSA concentrations in the range of 0.35 - 35.0 mg/ml. Polymer solutions without HSA were measured as control. All samples were measured at 37 °C at beamline P12, DESY, Hamburg. The scattering patterns were azimuthally integrated. In the ITC experiments, HSA solutions (52.0 mg/ml) were titrated into the solutions of pHPMA-Chol or pHPMA-Chol-Dox, both at 2.0 mg/ml. The measured power peaks were integrated over time, resulting in titration heat values describing the enthalpy change due to binding events.

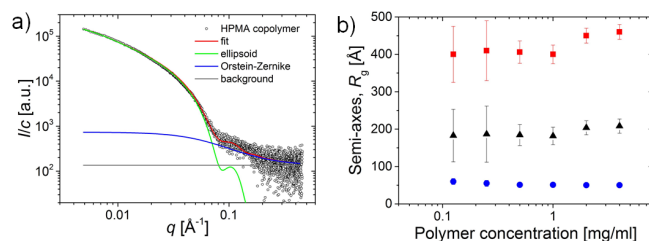


Figure 1.14: (a) SAXS curve of pHPMA at 2.0 mg/ml in PBS together with the fit and its contributions. (b) Resulting values of the semi-major axis, semi-minor axis and radius of gyration of the ellipsoidal NPs in dependence on its concentration.

The SAXS curves of pHPMA-Chol were modeled by a form factor of ellipsoids, together with an Ornstein-Zernike structure factor describing correlations between the pHPMA chains surrounding the NPs (Fig. 1.14 a). In the absence of HSA, the radius of gyration was calculated based on the semi-major and -minor axes and was found to be independent of the polymer concentration (Fig. 1.14 b). Upon addition of HSA, the scattering from the mixed solutions was successfully modeled by a sum of the individual scatterings from the NP and HSA (Fig. 1.15 a and b), meaning that there is no significant interaction between the NP and HSA. Nevertheless, slight mismatch is observed at low  $q$  values, pointing to a scenario where only a few HSA molecules bind to the NPs (Fig. 1.15 a). When Dox is present, the fits are perfect over the full  $q$  range and thus no interaction is observed (Fig. 1.15 b). This weak binding is further confirmed using ITC where strong exothermic binding heat is observed in the absence of Dox. When Dox is present, the titration heat is initially 5 times less, and saturated at the 20th titration, meaning that less HSA molecules bind to the NPs than the case where Dox is absent. We speculate that, Dox, which is distributed along the whole NP, hinders HSA from binding to the NPs (Fig. 1.16 b).

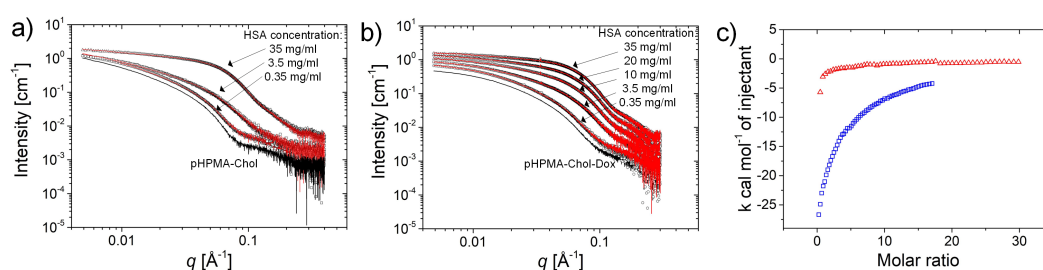


Figure 1.15:

(a, b) Fits of the SAXS curves of the mixed solutions of pHPMA-Chol/HSA (a) and of pHPMA-Chol-Dox/HSA (b) using a sum of the scattering curves of the respective components. The polymer concentration is constant at 4 mg/ml and the HSA concentrations are given in the figure. The lowermost curves in (a) and (b) are the ones from the pure polymer solutions. (c) ITC results of HSA titrated into the solution of pHPMA-Chol (blue) and into the solution of pHPMA-Chol-Dox (red)

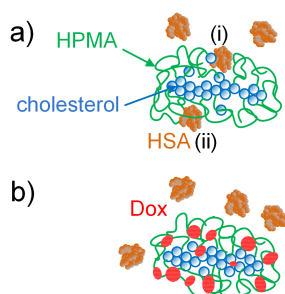


Figure 1.16:

Schematic drawing of the NP/HSA interaction: (a) When Dox is absent, HSA binds to cholesterol (i) or gets caught in the meshes of pHPMA (ii). (b) When Dox is present, it is distributed uniformly along the whole NP and hinders both (i) and (ii).

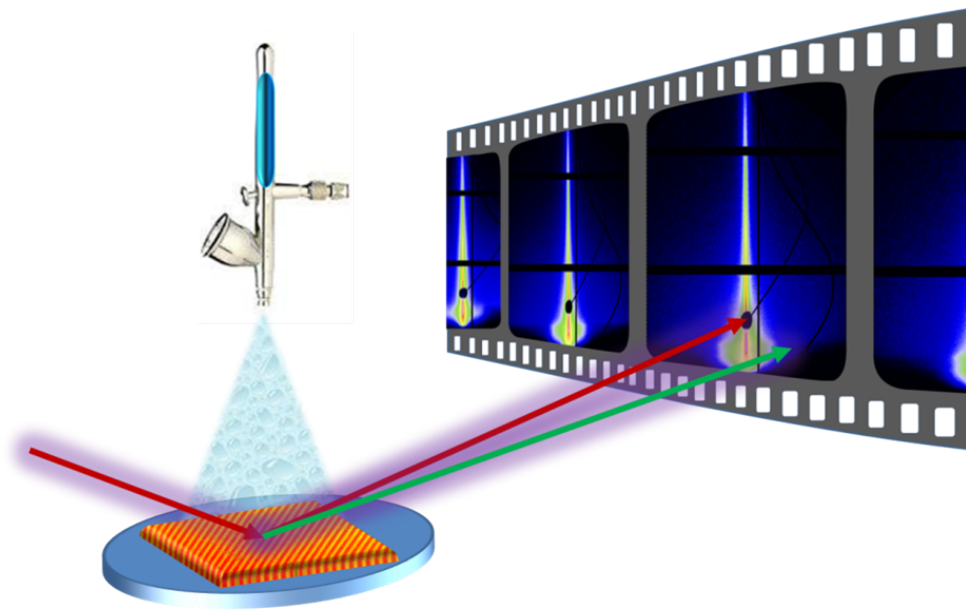
To summarize, we have investigated pHPMA-based copolymers for drug delivery in the presence of the blood protein HSA by synchrotron SAXS and ITC. In the absence of Dox, only few HSA molecules bind to the NPs. This binding is, however, strongly hindered when Dox is present, meaning that the delivery of drugs should not be affected by HSA.

The project is funded by DFG (PA771/17-1) and the Grant Agency of the Czech Republic (grant no. 15-10527J) in the framework of the Memorandum of Understanding of Scientific Cooperation.

[1] S. K. Filippov, P. Chytil, P. V. Konarev, M. Dyakonova, C. M. Papadakis, A. Zhigunov, J. Plestil, P. Stepanek, T. Etrych, K. Ulbrich, and D. I. Svergun, *Biomacromolecules* **13**, 2594 (2012)



## 2 Thin films



## 2.1 Structural investigation of carbon onion thin films

C. L. Weindl, F. C. Löhner, P. Müller-Buschbaum

For decades, carbon nanostructures have played a prominent role in electrochemical energy storage. Especially carbon nanonion films as a conductive additive for supercapacitors can be implemented to improve electrical characteristics. These onions with an almost spherical shape consist of several enclosed fullerene-like carbon shells. Amongst various ways to synthesize these onions, the most commonly used technique is the graphitization of nanodiamonds at temperatures above 1700 °C. [1] These high temperatures lead to a high degree of  $sp^2$ -hybridization and thereby, result in comparatively high electrical conductivity values ( $2-4 \text{ S cm}^{-1}$ ), a large surface area and nanoscopic size of 10 nm diameter (100 nm technically possible). [2] However, not much is yet known about the synthesis and morphology of thin films with implemented carbon onions. Therefore, we aim to investigate the influence of different processing pathways on the structural and optoelectronic properties of these films.

In first studies, we optimized processing parameters such as the type of solvent, concentration and spin coating velocity in order to avoid generating discontinuous or inhomogeneous films. For these samples, cleaned glass substrates were covered with a thin PEDOT:PSS layer to enhance the coverage of the nano onion films. Figure 2.1 shows exemplary optical microscopy images for samples synthesized using high (a,c) vs. low (b,d) concentration of nano onions in 1,2-dichlorobenzene with different magnification ( $\times 10$  vs.  $\times 50$ ).

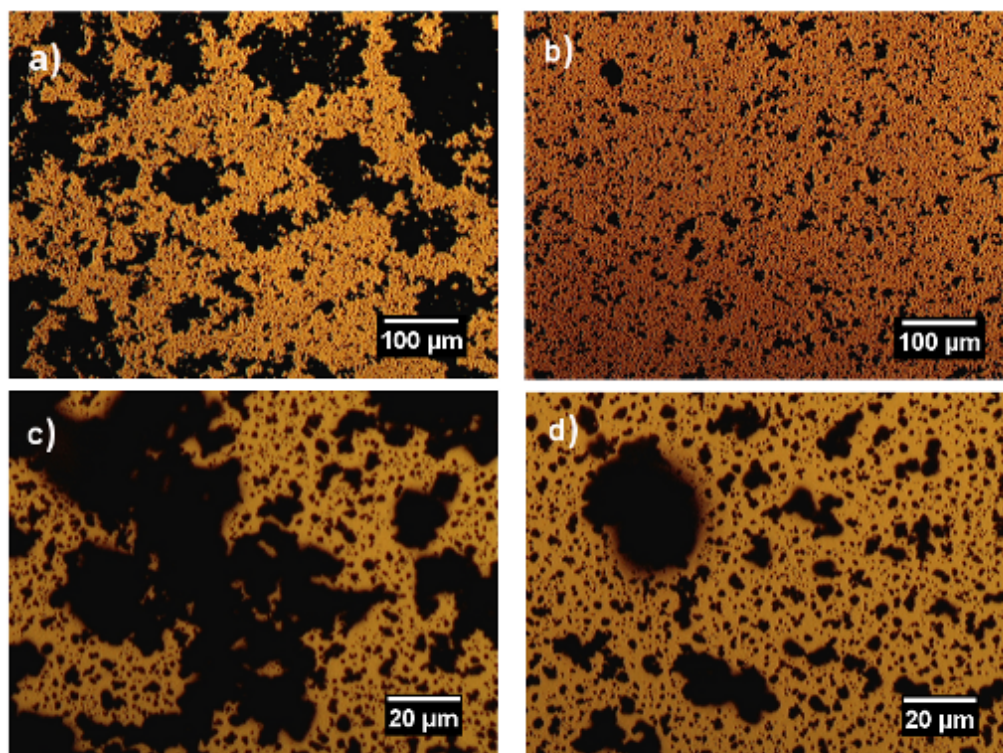


Figure 2.1:  
Microscopy images of PEDOT:PSS-carbononion films with different magnification (upper  $\times 10$ , lower  $\times 50$ ) and concentration (a,c high)(b,d low)

Comparing samples of a high concentration (a) with a low concentration (b) of nano onions, we can mainly see the difference in the size of the larger domains. The dimensions of the small

clusters are nearly equal for both samples. For higher concentrations, these clusters tend to agglomerate into superclusters, building domains but not a homogeneous film. In c) and d) the higher resolution shows blurred pixels at the edge of larger domains, which result from the pronounced height difference. To achieve better results, there are different ways to tackle the problem. For example optimization of the spin-coating speed and the usage of a filter to exclude large carbon nano onion clusters from the solution may enhance the film homogeneity and coverage. The aim is to have a continuous layer with fewer domains. To get information about the electronic structure, photoluminescence measurements have been carried out. The results are shown in Figure 2.2.

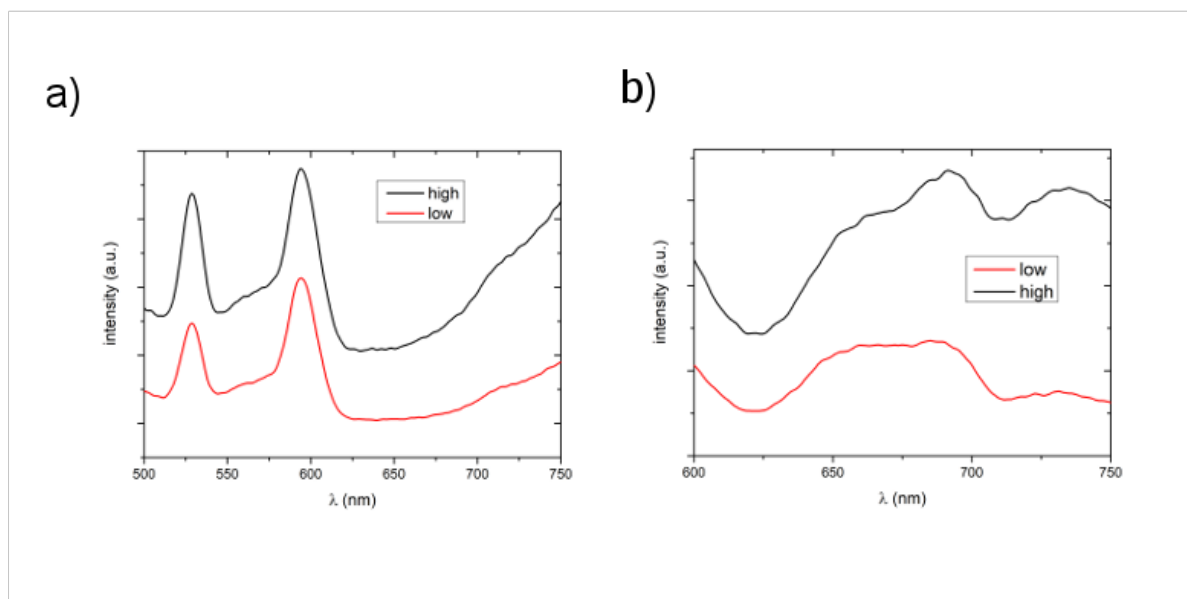


Figure 2.2:

Photoluminescence measurements with different excitation wavelengths for samples with a high vs. a low concentration of nano onions [a) 400 nm, b) 500 nm]

For an excitation wavelength of 400 nm, as shown in Figure 2.2 a), similar features can be determined with a shift to higher intensities for the more concentrated sample. Starting at around 650 nm, a deviation in the gradient is visible. To have a closer look at this, the excitation wavelength has been moved to 500 nm as shown in Figure 2.2 b). This increase of the wavelength may be the reason for various intensity characteristics that may result from different behavior at the absorption edges. One reason for this behavior could be the additional excitation of a plasmon. This work gives a brief insight into the behavior of carbon onion thin films and shows that further investigations are needed to fully understand the structural and optoelectronic properties of these nanostructures.

[1] M. Zeiger, N. Jäckel, V. N. Mochalin, V. Presser, *J. Mater. Chem. A*, 2016, **4**, 3172-3196

[2] M. Zeiger, N. Jäckel, D. Weingarh, V. Presser, *Carbon*, 2015, **Volume 94**, 507-517

## 2.2 Investigation on the electronic/magnetic structure of magnetic nanoparticles embedded in polymer matrix

K. Biswas, S. Xia, P. Müller-Buschbaum

Nanostructured hybrid thin films built with diblock polymer (DBC) as a matrix and magnetic nanoparticles (NPs) as additive gain increasing scientific interest because of their wide application in areas such as magnetic sensor and storage device [1]. So far lots of investigations have been focused on the DBC film nanostructuring and dispersion of magnetic NPs. Literature shows that the arrangement of magnetic NPs, which plays an indispensable role in the applications, is greatly influenced by the DBC morphology. Various NPs arrangements can be obtained via tuning the structures of DBC [2]. However, the electronic and magnetic structure of magnetic NPs with different alignment, which is also essentially important, has been rarely studied. In the present work, hybrid films composed of the polystyrene-*b*-poly (ethylene oxide) (PS-*b*-PEO) and surface-functionalized magnetic NPs ( $\text{Fe}_3\text{O}_4$  coated with oleic acid chains) are prepared via spin coating. Owing to the hydrophobic grafting, the employed magnetic NPs can be preferentially dispersed inside PS blocks. To achieve various NPs arrangements in polymer matrix, magnetic films with different NP concentrations were experimented.

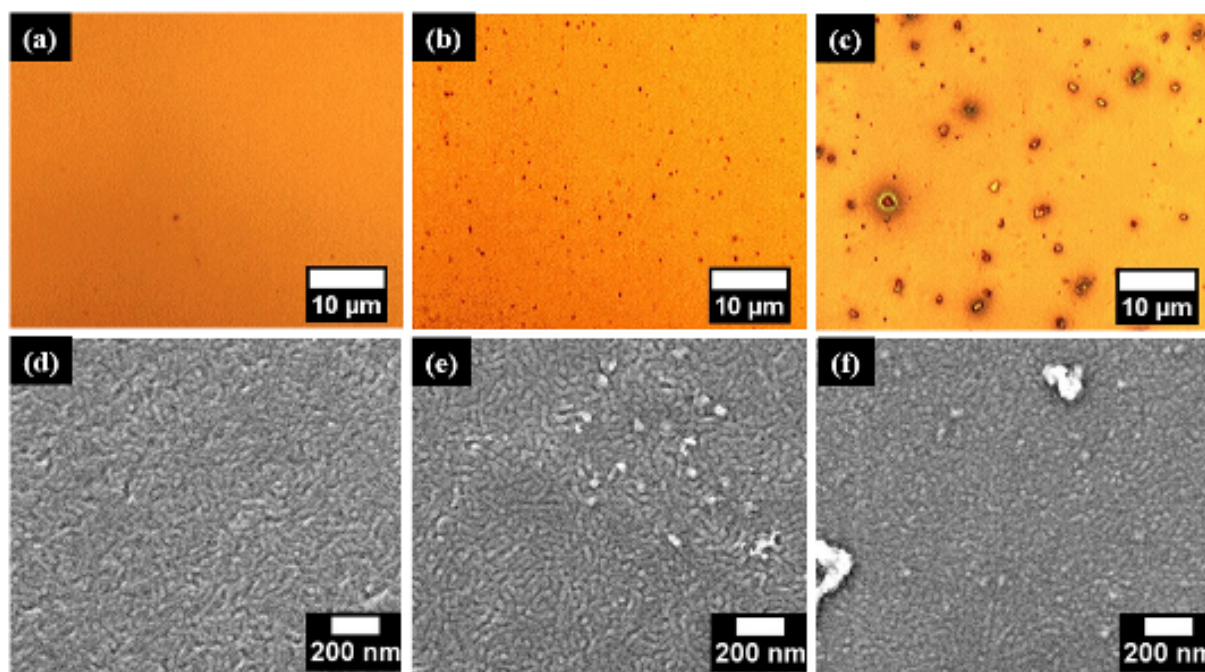


Figure 2.3:

OM (upper) and SEM (lower) images of magnetic films with different NP concentrations (a, d) 0 wt %, (b, e) 1 wt % and (c, f) 5 wt %.

The macro- and nanostructure of magnetic films were characterized via optical microscopy (OM) and scanning electron microscopy (SEM). OM images (Fig. 2.3 a-c) show that all films are homogeneous at macroscale. At low NP concentration (1 wt %), NP aggregates (shown as dark dots in Fig. 2.3 b) form on the film surface. At higher concentration (5 wt %), the size of the aggregates increases. SEM graphs display the film morphology evolution with NP concentration at nanoscale. For the NP-free film, a cylindrical morphology with parallel geometry as respect to the substrate can be obviously observed in Fig. 2.3d. With slight loading of magnetic NPs, the order of the nano-cylinders gets improved. Meanwhile, NP

aggregates with small size are also found on the surface. At high loading of NPs, the orientation of cylindrical nanostructure changes from parallel to perpendicular in partial surface area.

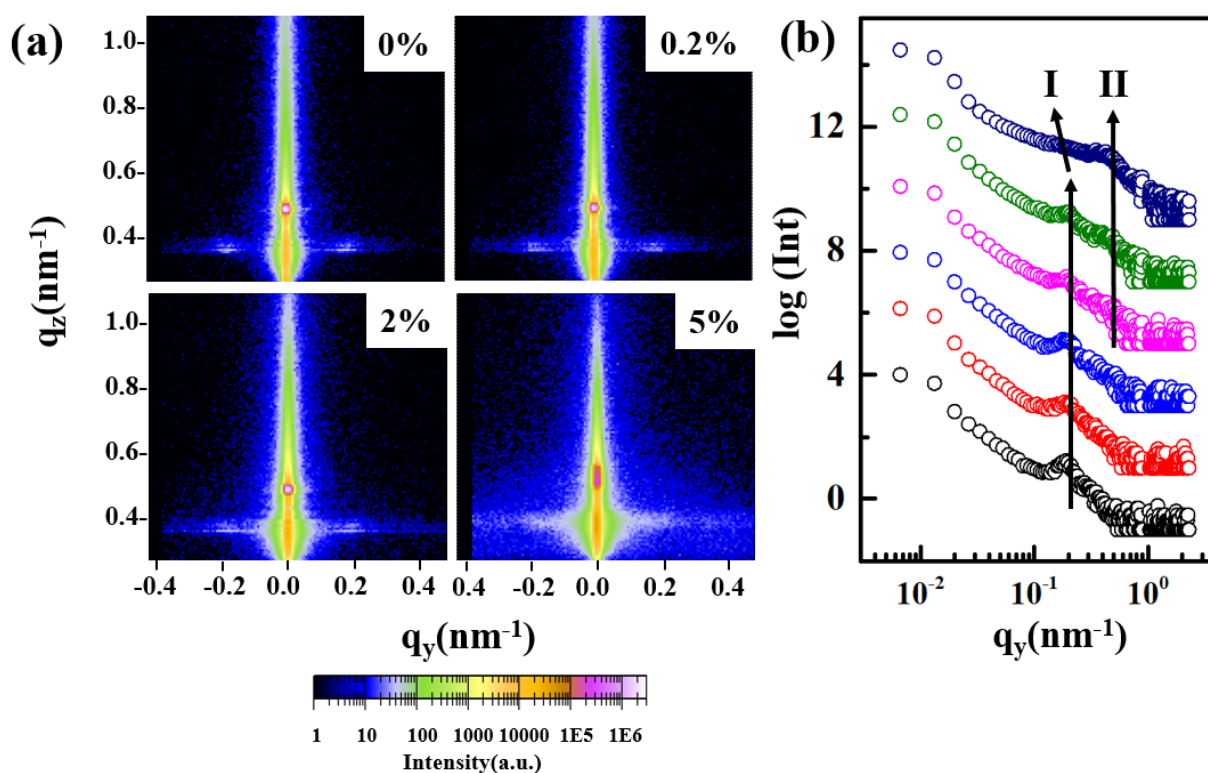


Figure 2.4:

(a) 2D GISAXS patterns of magnetic films with different NPs concentrations. (b) horizontal line cuts extracted from the corresponding 2D GISAXS Patterns. From bottom to top, NP concentrations are 0, 0.2, 0.5, 1, 2 and 5 wt %, respectively. The two black arrows marked with I and II show the two characteristic peaks.

To probe the inner structure of the magnetic films, grazing incidence small angle X-ray scattering (GISAXS) was utilized. The obtained 2D GISAXS patterns are shown in Fig. 2.4 a, and characteristic features can be observed. Scattering behaviors of films with NP concentration below 5 wt % are found to be similar, but distinct difference appears at the highest concentration. To get more detailed information on the inner structure, horizontal line cuts were made and plotted in Fig. 2.4 b. Two featured peaks marked as peak I and peak II are displayed in Fig. 2.4 b. Peak I arises from the microphase separation of DBC and resembles the inter-domain distance. With increasing NP concentration (< 5 wt %), peak I shifts slightly to lower  $q_y$  values, indicating the smooth increase of the inter-domain distance. At 5 wt %, it shifts to a much lower position, which suggests a sharp increment of inter-domain distance. Peak II appears from 1 wt %, and becomes more and more prominent with concentration increasing. This peak may originate from closely packed NPs. Modeling of the data is necessary for better interpretation. The electric and magnetic structure of the hybrid films will be studied via high resolution fluorescence detected X-ray absorption near edge structure spectra.

- [1] T. Pietsch, P. Müller-Buschbaum, B. Mahltig, A. Fahmi, *ACS Appl.Mater.Interfaces.* **7**, 12440-12449(2015)
- [2] Y. Yao, E. Metwalli, B. Su, V. Körstgens, D. Moseguí González, A. Miasnikova, A. Laschewsky, M. Opel, G. Santoro, S V. Roth, P. Müller-Buschbaum, *ACS Appl.Mater.Interfaces.* **7**, 13080-13091(2015)

### 2.3 Impact of precursor concentration on crystallinity and nanostructure of titanium dioxide in diblock copolymer templated sol-gel processes

N. Hohn, S. Schlosser and P. Müller-Buschbaum

Diblock copolymer templating combined with sol-gel chemistry is a well known and powerful tool to obtain unique titanium dioxide nanostructures. Possible applications are found in the field of photovoltaics, gas sensing, water purification, Li-ion batteries and many more.

To further investigate this field the amphiphilic diblock polymer polystyrene-*b*-polyethylene oxide (PS-*b*-PEO) with a weight distribution of 20.5-*b*-8 is used as a structure directing agent. For thin film preparation the template is dissolved in the good solvent toluene at a concentration of 100 mg/ml. After a stirring time of 3 h different amounts of the precursor titanium (IV) isopropoxide (TTIP) are added to the solution. To further facilitate a transition to large scale printing processes, blade coating is used as a deposition technique to obtain a composite thin film. Subsequently, the film is immersed into a 1-butanol bath after a fixed evaporation time of 50 s. This immersion into a bad solvent strongly drives the phase separation process of the polymer template. Finally, the polymer template is removed via a calcination step at 550 °C for 3 h. As a result nanoporous titanium dioxide thin films are obtained, which are especially useful for photovoltaic applications.

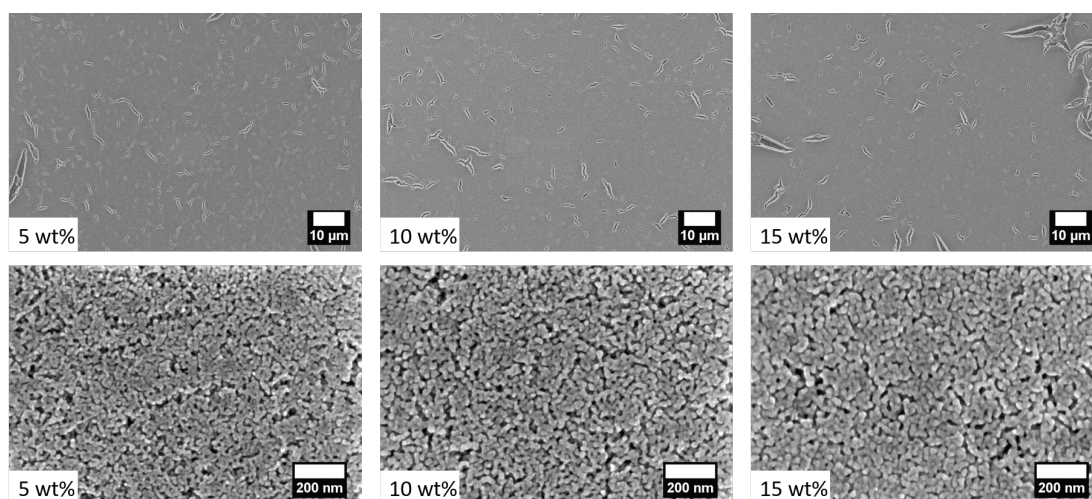


Figure 2.5: Scanning electron images of sol-gel synthesized nanoporous titanium dioxide thin films. The precursor to template ratio is increased from left to right as indicated in the inset.

Initial characterization is carried out via scanning electron microscopy (SEM) and captured images of the surface morphology can be seen in Figure 2.5b). At low magnification cracks due to the calcination step are present for all different precursor concentrations. However, at higher magnification (bottom row) a densification of surface structures becomes visible for an increasing precursor concentration.

To confirm if a similar behavior can be found in the bulk of the thin film, grazing incidence small angle X-ray scattering measurements have been performed using a Ganesha SAXSLAB instrument with a wavelength of 1.54 Å, a sample-detector distance of 1056.2 m and an incidence angle of 0.35°. Horizontal cuts have been performed at the material specific Yoneda peak position and the respective cuts are depicted in Figure 2.6. From bottom to top the precursor ratio is increased as indicated in the inset. Observed peaks indicate a lateral structure formation. Accordingly, the arrow marks a shift of the peak position towards smaller  $q_y$  values. This tran-

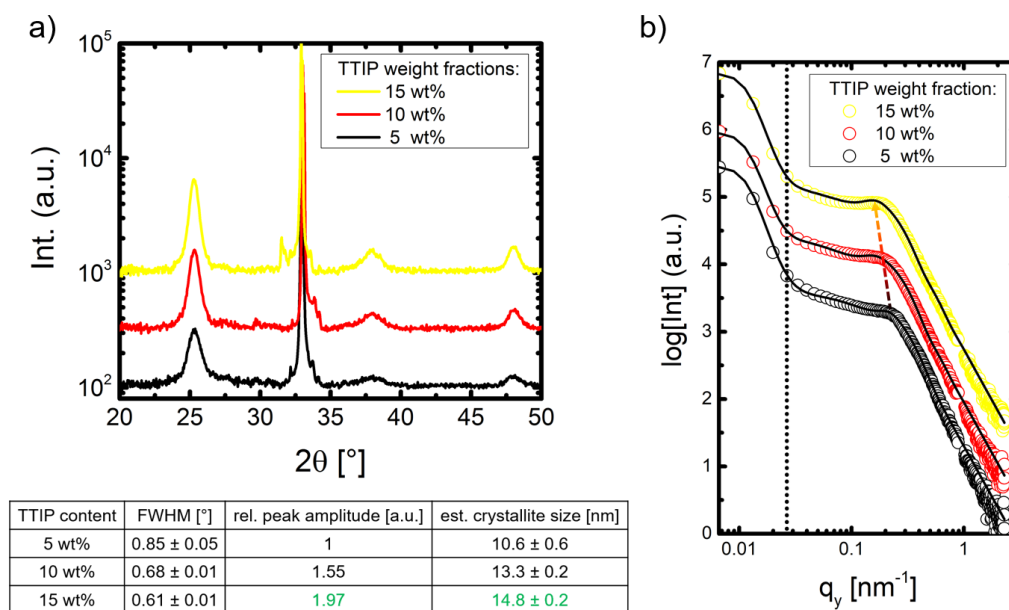


Figure 2.6:

Characterization of nanoporous titanium dioxide thin films via a) X-ray diffraction and b) grazing incidence small angle X-ray scattering (horizontal cuts at the Yoneda peak position, y-shifted for clarity). The table at the bottom is referring to the X-ray diffraction measurements and is showing an increase in crystallite size for higher precursor ratios as obtained from the Scherrer equation.

sition is representing a growth of present titanium dioxide structures in lateral direction, which is in good agreement with the observed surface behavior via SEM.

Finally, the nanoporous titanium dioxide thin films have been analyzed via X-ray diffraction (XRD) measurements to ensure suitability for photovoltaic applications. Within this frame an anatase phase has been found as depicted in Figure 2.6a). Relative comparison of crystallite sizes via the Scherrer equation yields a tendency towards larger crystallite sizes with increasing precursor ratio as indicated in the table below the XRD spectra.

In conclusion, increasing the precursor to polymer ratio is found to lead to a densification of surface and bulk structures inside a nanoporous titanium dioxide thin film. The material is found very promising for photovoltaic applications, as crystallinity is confirmed and a basis for large scale application is set via the blade coating approach.

- [1] Y. Cheng, J. S. Gutmann, *J. Am. Chem. Soc.*, **128**(14), 4658 (2006)
- [2] J. Szeifert, D. Fattakhova-Rohlfing, D. Georgiadou, V. Kalousek, J. Rathousky, D. Kuang, S. Wenger, S. Zakeeruddin, M. Grätzel and T. Bein, *Chem. Mater.*, **21**(7), 1260 (2009)
- [3] C. Stegelmeier, A. Exner, S. Hauschild, V. Filiz, J. Perlich, S. V. Roth, V. Abetz, S. Förster, *Macromolecules*, **48**(5), 1524 (2015)
- [4] Y. Yoneda, *Phys. Rev.*, **131**(5), 2010 (1963)
- [5] R. Lazzari, *J. Appl. Crystallogr.*, **35**(4), 406 (2002)
- [6] G. Kaune, M. Memesa, R. Meier, M. A. Ruderer, A. Diethert, S. V. Roth, M. D'Acunzi, J. S. Gutmann, P. Müller-Buschbaum, *ACS Appl. Mater. Interfaces*, **1**(12), 2862 (2009)

## 2.4 Swelling and exchange kinetics in PNIPAM microgel thin films investigated in-situ with time-of-flight neutron reflectometry

T. Widmann, J-F. Moulin<sup>1</sup>, Y. Hertle<sup>2</sup>, T. Hellweg<sup>2</sup>, P. Müller-Buschbaum

<sup>1</sup> HZG at MLZ, Garching, Germany

<sup>2</sup> University of Bielefeld, Bielefeld, Germany

Responsive polymers are the basis of a multitude of smart materials that react to an external stimulus such as light, temperature or humidity with a large change in one or more of their physical properties like conductivity or volume. In the field of medicinal research thermoresponsive polymers enjoy high interest as they can be designed biocompatible and biodegradable and can use small differences in temperature around their critical solution temperature to show large changes in volume [1]. Here, poly(N-isopropylacrylamide), PNIPAM is one of the most intensely investigated materials [2]. PNIPAM exhibits a LCST type behavior around a critical temperature of  $T_c = 32^\circ\text{C}$  in solution.

We investigated microgels composed of PNIPAM and N,N'-Methylenebisacrylamide (BIS) as cross-linker, illustrated in Fig. 2.7 a), in a thin film geometry. This leads to a compact layer of microgel colloids that exhibits a collective thermoresponsive behavior. At fixed temperatures below  $T_c$ , the microgel is hydrophilic and responsive to changes in the surrounding humidity. Upon an increase in the relative humidity, the water vapor will penetrate into the microgel film and bind to the polar groups of PNIPAM and BIS, resulting in a swelling of the film. Exchanging the water atmosphere with for example a heavy water atmosphere, leads to an exchange process of the low-molecular penetrants until the system equilibrates. Using time of flight neutron reflectometry (TOF-NR), the contrast in scattering length density between water and heavy water allows us to follow such solvent exchange and swelling processes in-situ.

We prepared a microgel solution of 5 %wt using a microgel with a 10:1 molar ratio of NIPAM to BIS. Spin-coating the solution at 500 rpm, we obtained a homogeneous monolayer of microgel colloids with a thickness of around 23 nm. A custom made humidity chamber with a reservoir for liquid injection was used as sample environment, which allowed us to control relative humidity and temperature. The temperature was kept at a constant  $26.5^\circ\text{C}$ , well below the LCST of PNIPAM.

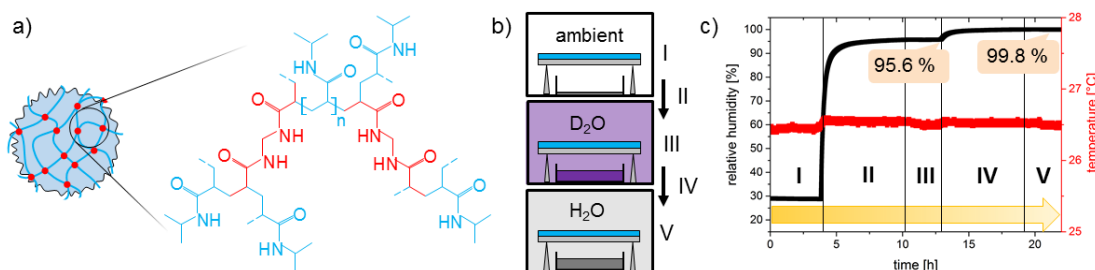


Figure 2.7:

a) Microgel network structure composed of NIPAM (blue) and N,N'-Methylenebisacrylamide (red) b) Experimental procedure consisting of 3 static TOF-NR measurements at ambient (I), D<sub>2</sub>O (III) and H<sub>2</sub>O atmosphere and two in-situ TOF-NR measurements of the swelling process with D<sub>2</sub>O (II) and the D<sub>2</sub>O → H<sub>2</sub>O exchange process (IV) c) Humidity and temperature data during the experiment

The measurement protocol is illustrated in Fig. 2.7 b) and is a five step procedure. Starting with a static measurement under ambient atmosphere (I), D<sub>2</sub>O is injected into the chamber reservoir

(II). An atmosphere of  $D_2O$  builds up as seen in Fig. 2.7 c) reaching a relative humidity of nearly 96 % after 6 hours. The diffusion of the vapor molecules and the induced swelling of the microgel film are followed in-situ using TOF-NR. Subsequently, a static measurement on the then  $D_2O$  swollen film is taken (III). Next, the  $D_2O$  is removed and replaced by  $H_2O$  and the exchange kinetic of the two vapor species is again followed in-situ (IV). Finally, another static is taken of the now  $H_2O$  saturated film (V).

The static measurements are taken over two hours each and the resulting reflectivity curves are plotted in Fig. 2.8 a).

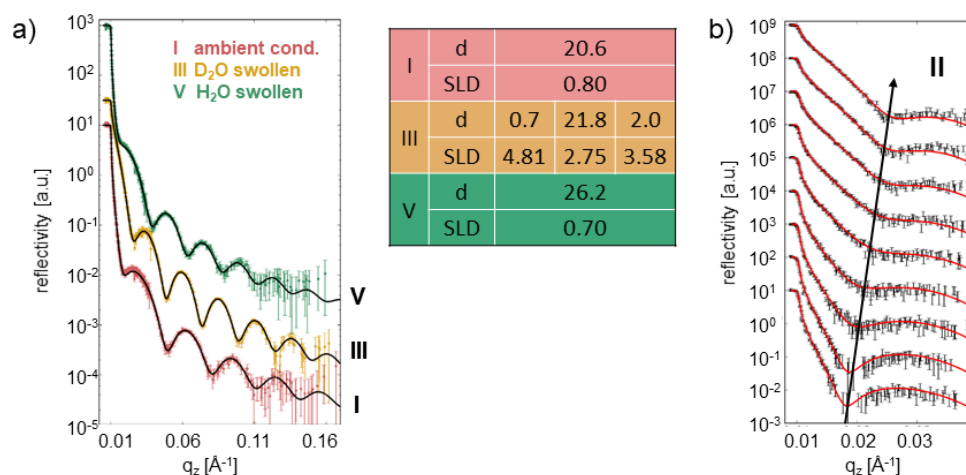


Figure 2.8:

a) Neutron reflectometry data of the equilibrated states at the beginning (red) after the swelling of the film with  $D_2O$  (yellow) and after the  $D_2O \rightarrow H_2O$  exchange process (green). The table lists the results from the fits (black lines) b) Evolution of the NR spectrum during the swelling step (II). The increasing intensity (arrow) is due to the sorption of  $D_2O$

The static NR data is fitted with MOTOFIT [3] and the values for the SLD and layer thickness are extracted and listed in the table besides Fig 2.8 a). In the first swelling process shown in Fig 2.8 b), the film swells from a thickness of 20.6 nm by 3.9 nm to a thickness of overall 24.5 nm. This is due to the diffusion of the heavy water molecules into the polymer bulk. However, from the fitting of the data it became evident that the  $D_2O$  is not uniformly distributed throughout the polymer film but accumulates near the polymer sheet interfaces. Hence, we obtain enrichment layers of  $D_2O$  at the polymer-silicon and the polymer-air interfaces, with the latter being the thicker one.

After the  $D_2O \rightarrow H_2O$  exchange process the measured reflectivity could be modeled as a single layer. However, considering the SLD of pure water of  $-0.56 \cdot 10^6 \text{Å}^{-2}$  the slightly lower SLD after the exchange process compared to the initial state of the film, we can conclude that there still is  $D_2O$  remaining in the polymer bulk.

Finally, the high increase in film thickness during the exchange kinetic compared to the small increase in relative humidity during step IV shown in Fig 2.7 c) may indicate a higher hydrophilicity of the material towards  $H_2O$  compared to  $D_2O$ .

[1] X. Cheng, Y. Jin, T. Sun, R. Qi, B. Fan, H. Li, *RSC Adv.* **5**, 4162-4170 (2015)

[2] A. Campanella, Z. Di, A. Luchini, L. Paduano, A. Klapper, O. Petracic, M.S. Appavou, P. Müller-Buschbaum, H. Frielinghaus, D. Richter, *Polymer* **60**, 176-185 (2015)

[3] A. Nelson, *J. Appl. Cryst.* **39**, 273-276 (2006)

## 2.5 Low-temperature fabrication of mesoporous titania thin films

L. Song, V. Körstgens, D. Magerl, B. Su, T. Fröschl<sup>1</sup>, N. Hüsing<sup>1</sup>, P. Müller-Buschbaum

<sup>1</sup> Materialchemie, Chemie und Physik der Materialien, Universität Salzburg, Salzburg, Austria

Because of the chemical and optical stability, excellent photoelectronic and photochemical properties, non-toxicity and low cost, nanostructured titania films have received great research interest in a wide variety of fields, such as photovoltaics, gas sensing, photocatalysis and Li-ion batteries. To meet different application requirements, various forms of titania nanostructures have been developed, such as nanotubes, nanowires, nanorods and so on. In particular, foam-like titania nanostructures are of high interest as they have a high surface-to-volume ratio and an interconnected network. Sol-gel synthesis in combination with polymer templates is a common way to achieve foam-like morphology of titania nanostructures. Typically, high-temperature calcination is used to burn away the polymer templates. Alternatively, removal of polymer templates at low temperatures has a high significance regarding energy-saving and cost-efficiency [1]. Moreover, the low-temperature route allows for fabrication of nanostructured titania films on polymer foils, which has a potential for flexible devices. In the present work, a diblock copolymer polystyrene-block-polyethyleneoxide (PS-b-PEO)

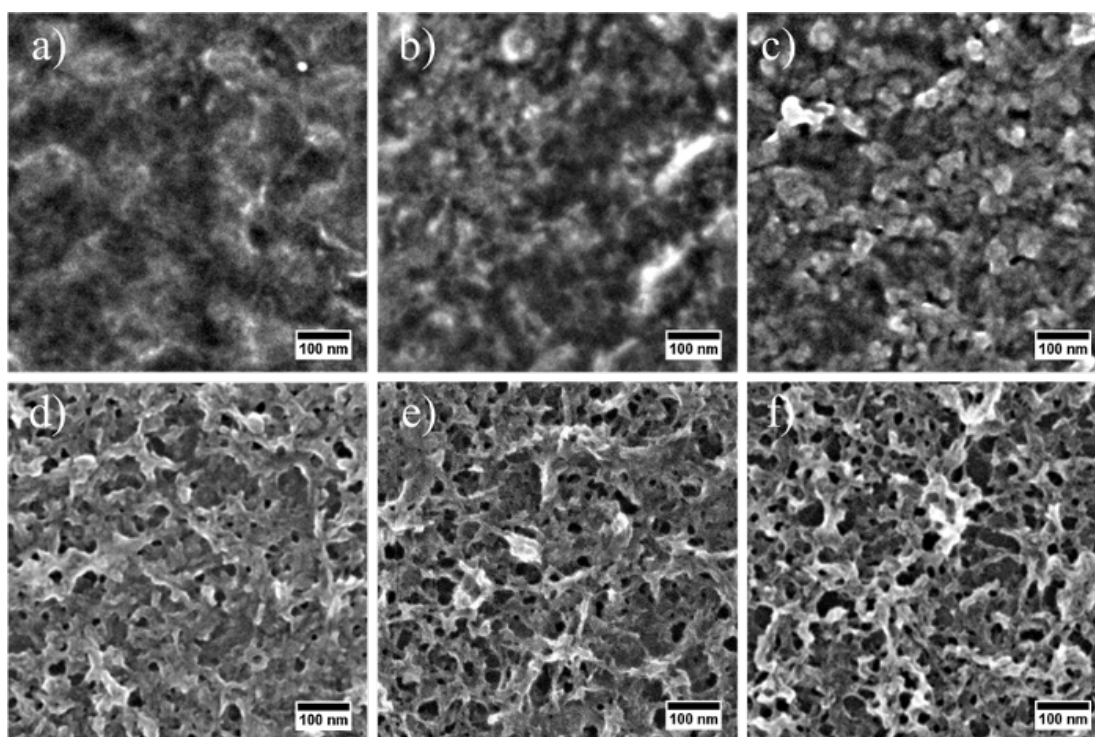


Figure 2.9:

Plan view SEM images of titania films after UV irradiation for different times: a) 0 h, b) 1 h, c) 3 h, d) 6 h, e) 12 h, f) 24 h.

is used as structure-directing agent and ethylene glycol-modified titanate (EGMT) is used as titania precursor in the sol-gel process. The so-called diblock copolymer assisted sol-gel synthesis allows for extended control of titania nanostructures and interconnected network. UV irradiation is selected as a low-temperature route to remove the PS-b-PEO template. This work mainly focuses on the efficiency of UV exposure and the influence of UV treatment on photoelectronic properties of nanostructured titania films [2]. The surface morphology of

titania films after UV irradiation for different times are measured with scanning electron microscopy (SEM) measurements. Fig. 2.9a displays the surface morphology of an as-prepared titania:PS-b-PEO composite film (before UV irradiation), which is used as the reference in this study. The reference film shows a homogeneous titania:PS-b-PEO composite film without obvious aggregates of titania or PS-b-PEO, indicating a well-mixed phase of titania and polymer template. Fig. 2.9b-d illustrate the evolution of surface morphology of titania films after UV treatment for 1 h, 3 h, 6 h, 12 h, 24 h. After 1 h UV exposure the mixed phase is still preserved, suggesting 1 h UV treatment is not enough for a complete removal of the PS-b-PEO template. However, a precursor of mesopores can be seen on the sample surface as compared to the as-prepared composite films, suggesting the polymer template on the film surface is extracted to a certain degree. Isolated nanostructured titania appears on the sample surface after 3 h UV irradiation (Fig. 2.9c), suggesting more PS-b-PEO is removed from the film surface. After 6 h UV exposure mesopores and interconnected titania network can be observed, although the mixed phase still remain in some areas. After UV treatment for 12 h and 24 h, interconnected titania network with mesopores are clearly observed and the PS-b-PEO template appears to be removed completely.

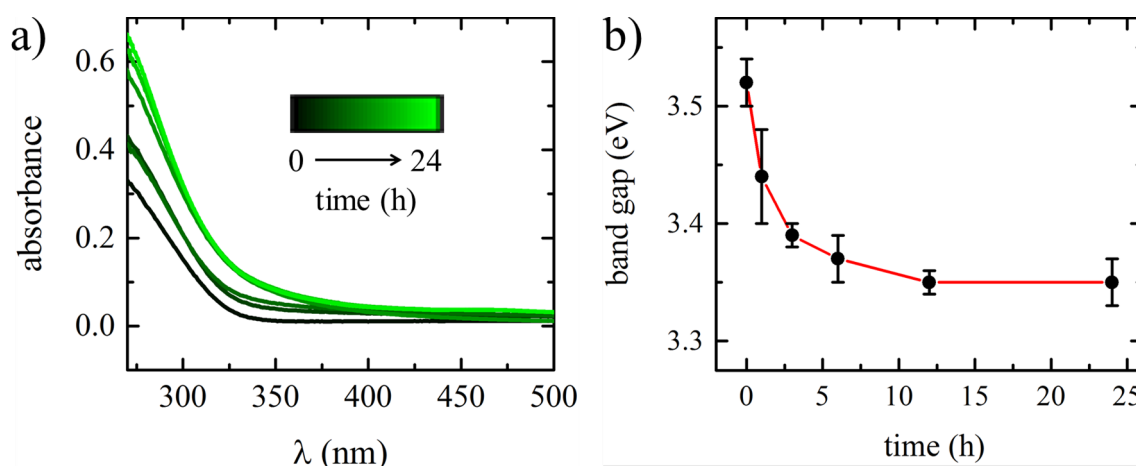


Figure 2.10:

a) UV/Vis absorption spectra of titania films after UV irradiation for different times as indicated by a color code (see inset). b) The extracted band gap energies from UV/Vis absorption spectra after UV irradiation for different times. The red line is a guide to the eyes.

The optical properties of the titania films with different UV exposure times are characterized with UV/Vis measurements. The UV/Vis absorption spectra are displayed in Fig. 2.10a. All samples only absorb light in the UV range (wavelength below 350 nm), which is due to the wide band gap energy of titania. Moreover, the indirect band gap energy of titania films can be calculated from the UV/Vis spectra using Tauc's equation and the results are displayed in Fig. 2.10b. The extracted band gap energies decrease with increasing UV treatment time and stay unchanged after 12 h UV irradiation. The same values of band gap energies for the samples UV-treated for 12 h and 24 h suggest a complete removal of the PS-b-PEO template.

- [1] L. Song, A. Abdelsamie, C. J. Schaffer, V. Körstgens, W. Wang, T. Wang, E. D. Indari, T. Fröschl, N. Hüsing, T. Haeberle, P. Lugli, S. Bernstorff, P. Müller-Buschbaum, *Adv. Funct. Mater.* **26**, 7084 (2016)
- [2] L. Song, V. Körstgens, D. Magerl, B. Su, T. Fröschl, N. Hüsing, S. Bernstorff, P. Müller-Buschbaum, *MRS Advances* **2**, 2315 (2017)

## 2.6 Thin films of ultrahigh molecular weight diblock copolymers

W. Cao, S. Xia, M. Appold<sup>1</sup>, M. Gallei<sup>1</sup>, P. Müller-Buschbaum

<sup>1</sup> TUD, Darmstadt, Germany

Block copolymer self-assembly has attracted considerable attention for many decades because it can yield ordered structures in a wide range of morphologies, including spheres, cylinders, bicontinuous structures, lamellae, vesicles, and many other complex or hierarchical assemblies. So far, most studies have used block copolymers with low or medium scale molecular weight [1-3]. Due to scaling of the micro-phase separation structure with the molecular weight of the block copolymers, large periods (higher than 80 nm) can be achieved with ultrahigh molecular weight (UHMW) block copolymers ( $M_n$ , number average molecular weight, higher than 800 kg/mol) [4]. In thin film geometry this implies a confinement of the polymers.

However, the application of UHMW block copolymers is challenging. UHMW block copolymers have problems in getting into thermodynamic equilibrium and in forming well-ordered micro-phase separation structures due to its very low chain mobility caused by the highly entangled chain conformations even at temperatures higher than the glass transition temperature ( $T_g$ ). To address this issue, solvent annealing process need to be selected as post-treatment [2]. This annealing processes can increase the mobility of the long polymer chains effectively, so that the rearrangement of micro-phase separation structures can be realized.

For solvent annealing process, tetrahydrofuran (THF) was used, which is a nonselective good solvent for the two blocks of polystyrene-block-polymethylmethacrylate (PS-*b*-PMMA). In this work, different polymer concentrations and solvent annealing times are studied to achieve highly ordered micro-phase separation structures. The film morphology is probed with optical microscopy (OM), atomic force microscopy (AFM), scanning electron microscopy (SEM) and grazing incidence small angle x-ray scattering (GISAXS).

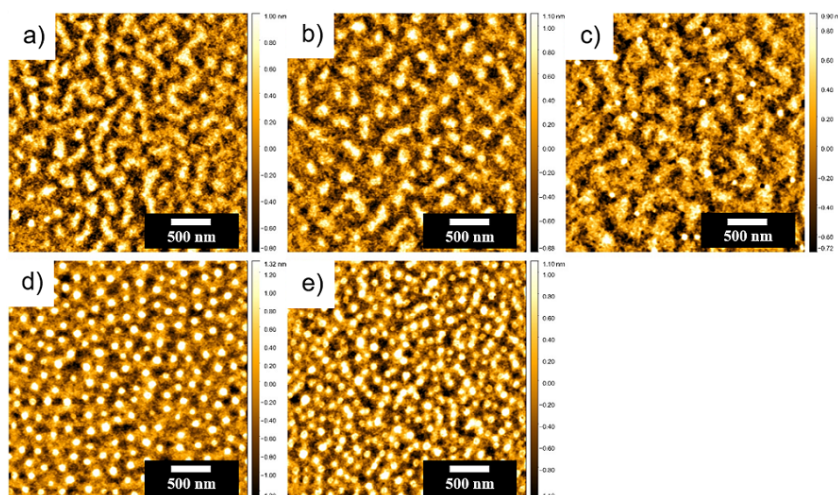


Figure 2.11:

AFM images of PS-*b*-PMMA films with different PS-*b*-PMMA concentrations after solvent annealing (THF, 18h): a) 3.0 mg/ml, b) 5.0 mg/ml, c) 10.0 mg/ml, d) 15.0 mg/ml and e) 20.0 mg/ml.

As seen in Fig. 2.11, the AFM images show the evolution of film surface morphology with different PS-*b*-PMMA concentrations after solvent annealing (THF, 18.0 h). At lower concentra-

tions, a disordered wormlike structure can be observed. As one moves to the concentration of 15.0 mg/ml (Fig. 2.11d), a relatively ordered micro-phase separation structure can be observed. However, a disordered spherical structure appears when the concentration is too high (20.0 mg/ml, Fig. 2.11e). The results show that a suitable PS-b-PMMA concentration is important.

The surface ordering for PS-b-PMMA films was investigated during the solvent annealing process at room temperature. Fig. 2.12 shows AFM images of PS-b-PMMA thin films with various solvent annealing time under THF vapor. The spin-coated film (Fig. 2.12a) displayed a poorly ordered structure, but the time dependent structures (Fig. 2.12b-d) of the PS-b-PMMA films indicated rapid structural development from disordered wormlike structure to relatively ordered micro-phase separation structure. For annealing times from 3.5 h to 5.5 h, the defects slowly eliminated, further enhancing the ordering of spherical micro-phase separation structure. From the surface morphology, we can see that the average domain size is about 80 nm, and the average distance between two domains is about 154 nm. As the solvent annealing times continue to increase, the distance between two domains increases to 185 nm (Fig. 2.12g). However, the PS-b-PMMA films annealed for 31.0 h (Fig. 2.12h) displayed the serious loss in the spherical domains as a result of the ordering failure.

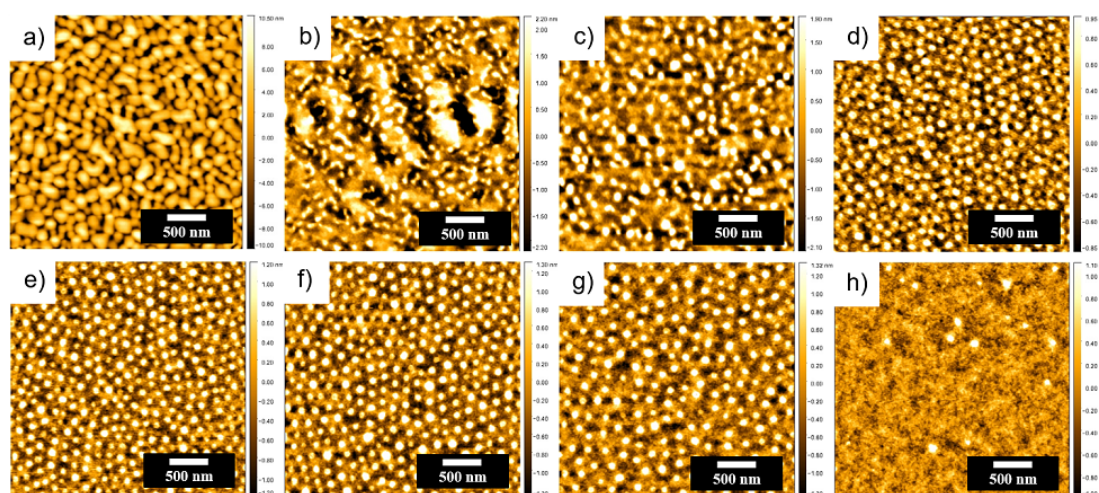


Figure 2.12:

AFM images of PS-b-PMMA films with different solvent annealing time (THF): a) 0 h, b) 0.5 h, c) 1.0 h, d) 2.0 h, e) 3.5 h, f) 5.5 h, g) 18.0 h, and h) 31.0 h.

Thus, a suitable solvent annealing time is necessary for getting highly ordered micro-phase separation structure. The blocks cannot separate completely from each other when the annealing time is not long enough, and there will have serious loss of ordering if the annealing time is too long.

- [1] Y. Mai, A. Eisenberg, *Chem. Soc. Rev.* **41**, 5969-5985 (2012)
- [2] E. Kim, H. Ahn, S. Park, H. Lee, M. Lee, S. Lee, T. Kim, E. A. Kwak, J. H. Lee, X. Lei, J. Huh, J. Bang, B. Lee, D. Y. Ryu, *ACS Nano* **7**, 1952-1960 (2013)
- [3] Y. Yao, E. Metwalli, M. A. Niedermeier, M. Opel, C. Lin, J. Ning, J. Perlich, S. V. Roth, P. Müller-Buschbaum, *ACS Appl. Mater. Inter.* **6**, 5244-5254 (2014)
- [4] J. K. D. Mapas, T. Thomay, A. N. Cartwright, J. Ilavsky, J. Rzyayev, *Macromolecules* **49**, 3733-3738 (2016)

## 2.7 Sputter deposition of gold electrodes on photoactive polymer thin films for organic electronics

F. C. Löhner, V. Körstgens, M. Schwartzkopf<sup>1</sup>, A. Hinz<sup>2</sup>, O. Polonskyi<sup>2</sup>, T. Strunskus<sup>2</sup>, F. Faupel<sup>2</sup>, S. V. Roth<sup>1</sup>, P. Müller-Buschbaum

<sup>1</sup> DESY, Hamburg, Germany

<sup>2</sup> FAU Kiel, Kiel, Germany

Photoactive polymers have received high attention in recent years for a variety of different applications in organic photovoltaics (OPV) or light emitting diodes (OLED). Due to their well-known advantages, OPV or OLED devices could be integrated into a wide range of applications, combining functionality with design in fields as diverse as mobility, architecture or clothing. Although those devices mainly consist of organic materials, their electrodes are in many cases still made from metals. Thus, polymer-metal interfaces are inherently present in most organic electronic devices. Understanding the growth mechanisms of metal contacts on polymer thin films plays a crucial role in identifying potential ways to enhance the performance of organic electronics. Recent research efforts focus on engineering the optical bandgap of photoactive polymers by tuning their side groups, thereby creating families of polymers with the same backbone, but tunable optoelectronic behavior. Amongst those polymer families, especially PTB7 and its derivatives are interesting. Fig.2.13 illustrates the change in the bandgap and therefore the absorption behavior between PTB7 and PTB7-Th. By introducing a thiophene ring into the side-chains, the bandgap of PTB7-Th is significantly decreased, which leads to absorption of less energetic photons and thereby higher solar cell efficiencies.

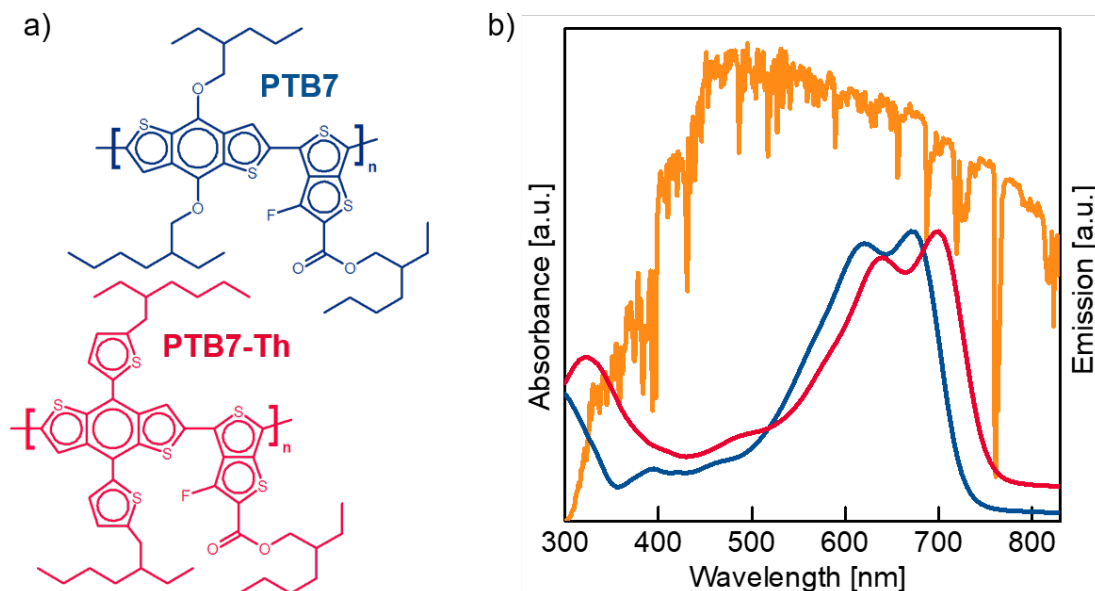


Figure 2.13:

a) Monomer units of PTB7 (blue) and PTB7-Th (red) and b) the corresponding UV/vis absorption spectra in comparison to the solar emission spectrum.

We investigated the morphological changes during the sputter deposition of gold electrodes onto thin films of both polymers via in-situ grazing incidence small angle X-ray scattering (GISAXS). [1] This technique allows for highly time-resolved insights into the deposition behavior of the metal on the organic film, which strongly depends on the film structure.

Making use of the outstanding time resolution at the P03 instrument at DESY in Hamburg, we compared the deposition behavior of sputtered gold particles on both samples. With a mobile sputter chamber, which can be implemented directly into the GISAXS setup, we followed the creation and growth of gold clusters and the subsequent layer formation. The acquired large data sequences were analyzed using the fast data reduction software DPDAK. Hereby, the 2D raw data were cut at specific regions of interest, such as the horizontal line cuts shown in figure 2.14 a, which give information about the lateral film morphology.

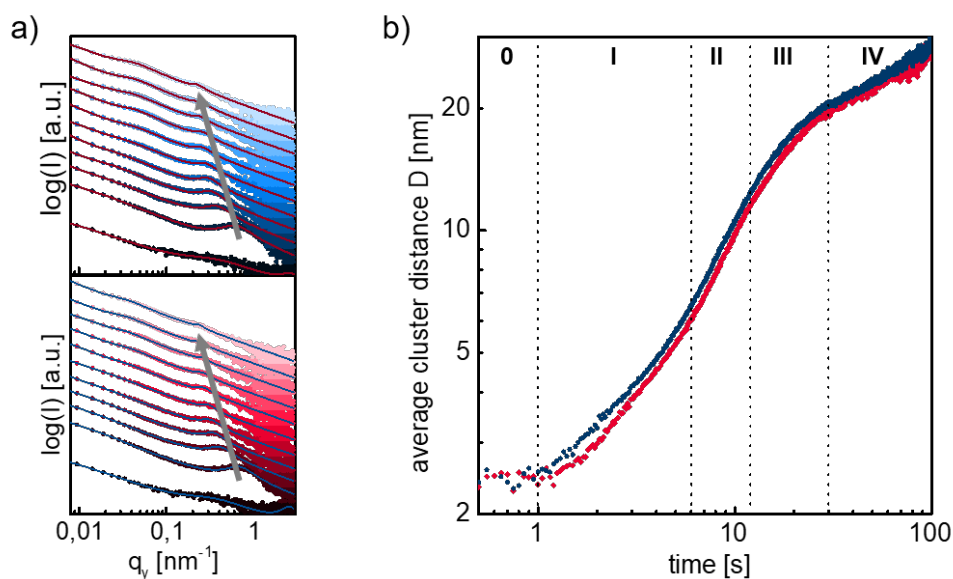


Figure 2.14:

Exemplary direct data analysis with a) horizontal cuts from the raw 2D GISAXS data taken after certain time intervals for PTB7 (top graph) and PTB7-Th (lower graph) and b) the evolution of the corresponding correlation distance during the deposition process for PTB7 (blue) and PTB7-Th (red).

The evolution of the maximum over time can be translated into a real-space value, the average cluster distance  $D$  (see figure 2.14 b), which is a measure for the mean distance of gold clusters on the polymer surface. This direct data analysis gives an impression of the different growth phases during the deposition process. The results are in good accordance with a step-like growth shown in other works. [2, 3, 4] In a first analysis, no significant changes in the growth behavior of gold on both polymer films could be distinguished.

- [1] P. Müller-Buschbaum, *Adv. Mater.* **26**, 7692–7709 (2014)
- [2] G. Kaune, M. A. Ruderer, E. Metwalli, W. Wang, S. Couet, K. Schlage, R. Röhlberger, S. V. Roth, P. Müller-Buschbaum, *ACS Appl. Mater. Interfaces* **1**, 353-360 (2009)
- [3] M. Schwartzkopf, G. Santoro, C. J. Brett, A. Rothkirch, O. Polonskyi, A. Hinz, E. Metwalli, Y. Yao, T. Strunskus, F. Faupel, P. Müller-Buschbaum, S. V. Roth, *ACS Appl. Mater. Interfaces* **7**, 13547-13556 (2015)
- [4] M. Schwartzkopf, A. Hinz, O. Polonskyi, T. Strunskus, F.C. Löhner, V. Körstgens, P. Müller-Buschbaum, F. Faupel, S. V. Roth, *ACS Appl. Mater. Interfaces* **9**, 5629-5637 (2017)

## 2.8 Self-assembly of quantum confined perovskite nanoplatelets in perovskite thin film

R. Wang<sup>1</sup>, E. Kentzinger<sup>2</sup>, H. Frielinghaus<sup>1</sup>, P. Müller-Buschbaum

<sup>1</sup> JCNS at MLZ, Garching, Germany

<sup>2</sup> JCNS, Jülich, Germany

Lead halide perovskite materials have attracted tremendous interest due to their promising applicability in optoelectronic devices. On the basis of its intrinsic dielectric properties, such as large absorption coefficient and long charge carriers diffusion length, perovskite based solar cells (PSCs) have achieved a best record power conversion efficiency (PCE) of 22.7%. [1] However, the moisture sensitivity of PSCs restricts its industrial application. In order to improve the moisture stability of PSCs, one focus is on using mixed dimensional perovskite as the photoactive layer, in which both two-dimensional (2D) perovskite platelets and three-dimensional (3D) perovskite bulk crystals are employed as the photon absorber. In comparison to the neat 3D bulk perovskite, the surface of the layered perovskite crystals is covered by hydrophobic organic spacers and thus good moisture resistance can be added to the resulting films. [2] In addition, the band structure of the 2D layered perovskite is greatly altered due to the dimensional changes and as a consequence energy funnels from 2D to 3D perovskite crystals emerge. The energy transfer efficiency is demonstrated to be closely related to the morphology of perovskite thin film. [3] Therefore, an in-situ understanding about the multidimensional structural formation is necessary towards the further optimization of the device performance.

In the present work, the formation of mixed dimensional perovskite thin films is steadily investigated at different reaction times via grazing incidence small angle X-ray scattering (GISAXS). In order to have good synthetic control at specific reaction state, a two-step vapor evaporation route is selected for sample preparation due to the fast ionic nature of the metathesis reaction of the perovskite formation. To be more specific, lead bromide  $PbBr_2$  perovskite thin films are pre-deposited on substrates via spin-coating, and then exposed to a mixture of organic vapor containing methylammonium bromide (MABr) and octylammonium bromide (OABr) for different reaction times (5 min, 30 min, 60 min and 120 min).

Figure 2.15 a-b) show the spectroscopic results of the resulting samples. As shown in the UV-Vis spectra, an absorption band edge at 520 nm progressively grows upon increasing the reaction time, which is close to the band gap of 3D bulk  $MAPbBr_3$  perovskite crystals (525 nm). For the sample with the longest exposure time, the absorption onset is blue-shifted toward large energy due to the onset of weak quantum confinement. In addition, three more features at 472 nm, 451 nm and 433 nm become more apparent in samples with longer exposure time, indicating the formation of 2D perovskite platelets with perovskite unit cell thicknesses ( $n$ ) of 3, 2 and 1, respectively. Similar results can be seen in the PL-spectra. As evidenced by the changes of the main emission peak position, the quantum confinement effect becomes more apparent in samples with longer reaction times (Figure 2.15 b). The reaction time induces stark differences on the surface morphology. In Figure 2.15 c), the surface morphology varies at different reaction times. The domain sizes increase at longer exposure time. Samples with the reaction time of 60 min and 120 min exhibit micrometer size domains but no platelets-like structures can be seen at this magnification scale. To have a complete understanding about the structural formation in the total film volume, samples are characterized by GISAXS.

Figure 2.16 a-d) exhibit the 2D GIWAXS data of the mixed dimensional perovskite films with four different reaction times. For sample with the shortest exposure time (5 min), a powder-like scattering feature is seen at  $q \approx 2 \text{ nm}^{-1}$ . In combination with the previous spectroscopic results, we speculate the 2D platelets are already formed in the film but exhibit low inter-correlation ordering. At larger  $q$  values, a narrow debye scherrer ring is identifiable at  $q \approx 5.6 \text{ nm}^{-1}$ , arising

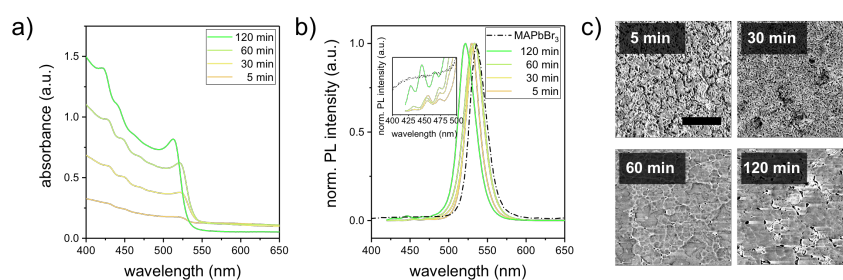


Figure 2.15: a) UV-Vis absorption, b) PL emission and c) scanning electron microscopy (SEM) images (scale bar 1  $\mu\text{m}$ ) of the resulting perovskite films. The reaction times are indicated in images.

from the unconverted precursors. This feature vanishes with increasing the reaction time and therefore evidences that  $\text{PbBr}_2$  is converted in to perovskite crystals. More specifically, a Bragg peak becomes prominent at  $q_z = 1.9 \text{ nm}^{-1}$  in samples 60 min and 120 min, and a shoulder like intensity contribution gained in intensity at  $q_z = 2.3 \text{ nm}^{-1}$  (Figure 2.16e). These two values are in agreement with the previous report and can be ascribed to the 2D perovskite platelets with perovskite unit cell thickness of 3 and 2, respectively.[3] Higher orders of both peaks are only seen in sample 120 min and distribute along the  $q_z$  direction. Therefore, this observed result elucidates that the 2D platelets tend to form superlattices and orient parallel to the substrate. In Figure 2.16 f), horizontal line cuts at the Yoneda peak positions are plotted in Kratky plot to reveal the in-plane domain structures. Firstly, the peak located at larger  $q_y$  values shifted by  $0.4 \text{ nm}^{-1}$  from sample 30 min to sample 120 min, indicating the inter-platelets spacing becomes bigger at longer reaction time. In addition, a shoulder like intensity distribution is seen in sample 120 min at  $q_y \approx 0.2 \text{ nm}^{-1}$ , suggesting the presence of ordered superlattices with inter domain distance of around 29.1 nm. The analysis of the scattering data is undergoing and a manuscript is in preparation.

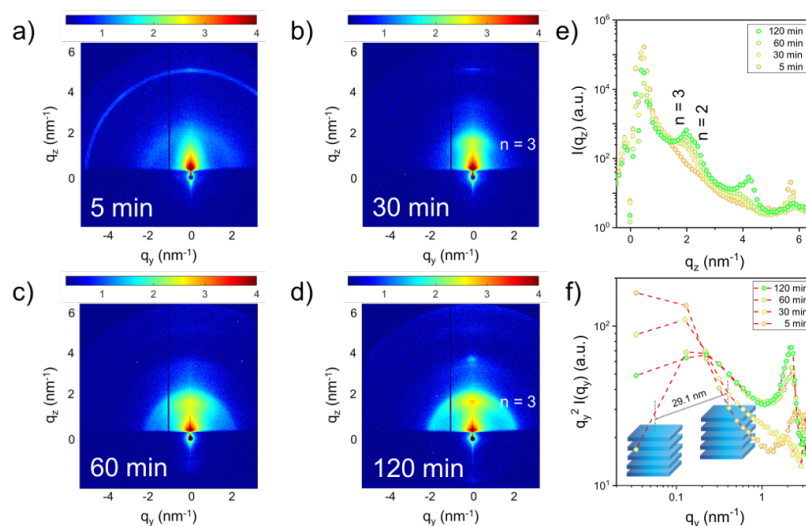


Figure 2.16: a-d) 2D GIWAXS data of the resulting perovskite films with four different reaction times. e) Vertical line cuts of the 2D GIWAXS data. f) Kratky plots of the horizontal line cuts of the 2D GIWAXS data. An representation of the resulted superlattice structures is schematically illustrated.

- [1] NREL, <https://www.nrel.gov/pv/assets/images/efficiency-chart.png> (2018)
- [2] I. Smith, E. Hoke, D. Solis-Ibarra, M. McGehee, H. Karunadasa, *Angew. Chem.* **126**, 11414-11417 (2014)
- [3] R. Wang, Y. Tong, A. Manzi, K. Wang, Z. Fu, E. Kentzinger, J. Feldmann, A. Urban, P. Müller-Buschbaum, H. Frielinghaus, *Adv. Optical Mater.* 1701311 (2018) DOI: 10.1002/adom.201701311

## 2.9 Doping of the n-Type Polymer P(NDI2OD-T2) for improvement of its thermoelectric properties

R. Kluge, N. Saxena, W. Chen, V. Körstgens, M. Schwartzkopf<sup>1</sup>, Q. Zhong<sup>2</sup>, S. V. Roth<sup>1</sup>, P. Müller-Buschbaum

<sup>1</sup> DESY, Hamburg, Germany

<sup>2</sup> Zhejiang Sci-Tech University, Hangzhou, China

Thermoelectric generators are a promising approach in renewable energies, as they are able to convert waste heat into electricity. Possible applications are large scale applications like recovering the waste heat of a car engine as electricity as well as niche applications like using the heat emitted by human skin to drive a watch.

In practice, a thermoelectric generator traditionally consists of a p- and an n-type semiconductor electrically connected. In order to put the device into operation, a temperature gradient is applied along the legs. As a consequence, charge carriers, i.e., holes in the p-type and electrons in the n-type leg, respectively, diffuse from the hot to the cold side. This diffusion current causes a build-up of charge at the cold end that can be extracted by connecting a load. All in all, a thermoelectric generator is able to convert a temperature gradient into electric energy.

In order to build high efficiency thermoelectric devices, suitable thermoelectric materials are needed. Unfortunately, state-of-the-art thermoelectric materials have the drawback of using toxic or less abundant constituents, making it necessary to look for alternatives. One promising approach is to use conjugated polymers. They have the encouraging ability of easy and various types of scalable solvent-based production processes like roll-to-roll printing. Although they are still less efficient than their inorganic counterparts, their potential flexibility and eco-friendliness make them a valuable alternative.

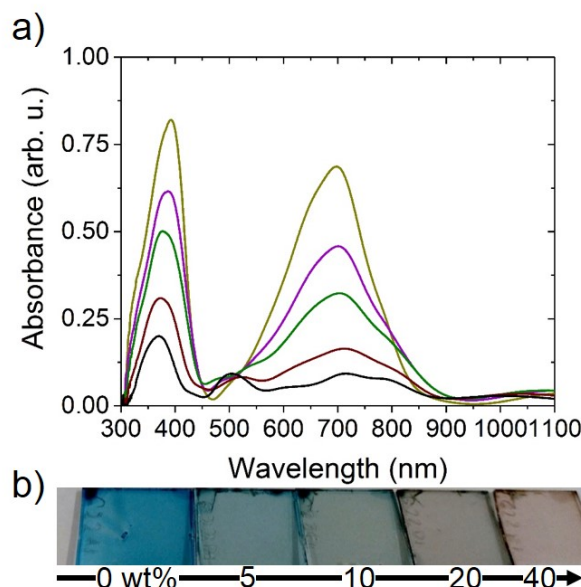


Figure 2.17:

(a) UV-Vis spectra and (b) photographs of P(NDI2OD-T2) films doped with different concentrations of N-DPBI.

Various, especially p-type, conducting polymers have been investigated as thermoelectric materials. A very promising candidate among them is the hole-conducting PEDOT. Unfortunately, n-type polymers have rather been neglected which might stem from their low stability towards

oxygen and moisture. Nonetheless, both types are needed for a thermoelectric device as explained before. Therefore, we also focus on the thermoelectric properties of the n-type polymer P(NDI2OD-T2). Its successful application to transistors and solar cells encourages an auspicious attempt in building an all-polymer thermoelectric generator.

The main focus of this work is to enhance the so-called power factor  $pF = \sigma \cdot S^2$  where  $\sigma$  is the electrical conductivity and  $S$  is the Seebeck coefficient. As already indicated by its name, the larger the power factor the larger the power output and subsequently the efficiency of the device. To this end, we used the organic small molecule N-DPBI successfully to dope P(NDI2OD-T2) which can be seen in the optical response of the films as well as a color change, both of which are depicted in Figure 2.17.

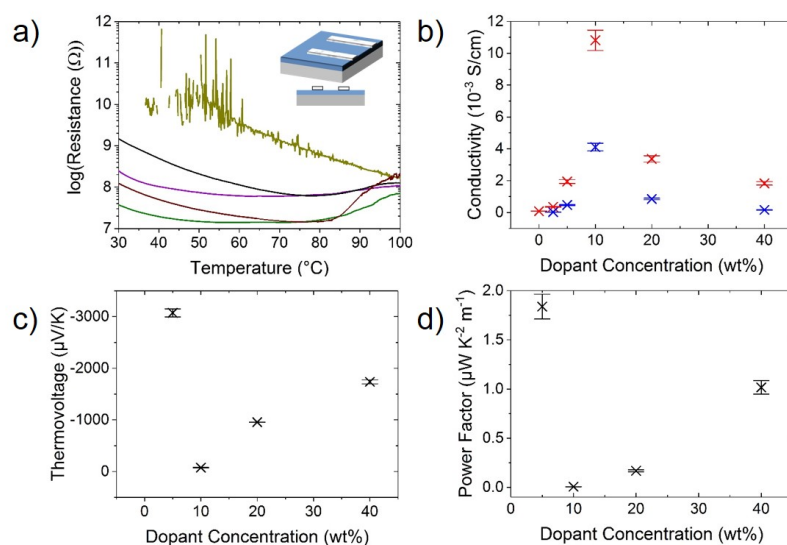


Figure 2.18:

(a) UV-Vis spectra and (b) photographs of P(NDI2OD-T2) films doped with different concentrations of N-DPBI.

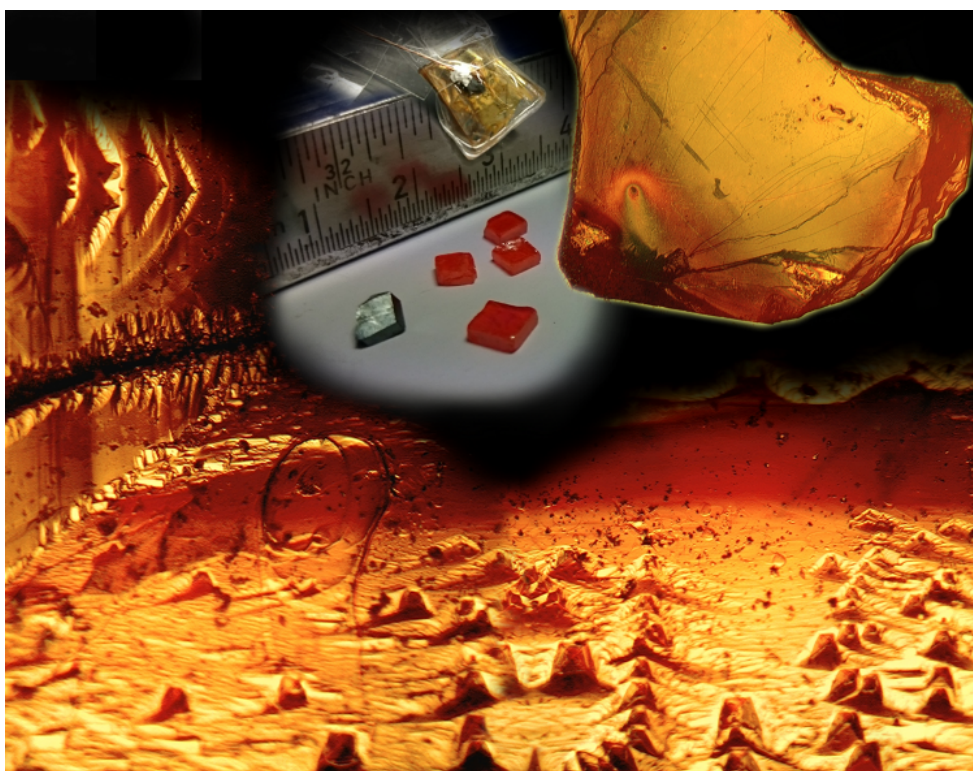
In order to investigate the thermoelectric properties of the P(NDI2OD-T2) films as function of dopant concentration, thin films were prepared on clean glass substrates, upon which two aluminum electrodes were evaporated at a distance of 10 mm. These electrodes are used for contacting the substrates for the temperature-dependent resistance measurements as well as for the measurements of the Seebeck coefficient. The former measurement is performed by placing the substrate on a hot plate, contacting the Al electrodes and ramping up the temperature while continuously measuring the current resulting from a bias voltage. The results are shown in Figure 2.18a, where a decrease of resistance is apparent as function of dopant concentration. From the resistance curves, electrical conductivities are extracted for the different dopant concentrations at 30°C and 70°C, as shown in Figure 2.18b. A maximum value of  $(1.84 \pm 0.13) \cdot 10^{-3}$  S/cm is obtained for low dopant concentrations at 70°C. The Seebeck coefficients shown in Figure 2.18c exhibit an inverse trend to the one of the electrical conductivity, which is expected due to the inverse relationship of these quantities to each other.

The power factor is a quantity which relates to the absolute power output of a thermoelectric device, irrespective of an overall conversion efficiency. It is shown in Figure 2.18d, exhibiting that doping of P(NDI2OD-T2) with N-DPBI results in a maximum power factor of  $(1.84 \pm 0.13) \mu$ W K $^{-2} \cdot$  m $^{-1}$  for low dopant concentrations.

[1] G. J. Snyder, *The Electrochemical Society Interface* (2008)



### 3 Photovoltaics



### 3.1 High efficiency organic solar cells based on low band-gap polymers

C. Bilko, F. C. Löhner, P. Müller-Buschbaum

In the last years, the formerly poor efficiencies of organic photovoltaics have been greatly increased. However, further improvements in the device architecture and stability are needed to reach industrially relevant efficiencies. To enhance the performance of organic solar cells, recent research efforts focus on identifying new highly efficient materials. One way to achieve this is the development of new low band-gap polymers, which absorb light of lower energies and therefore increase the overall absorption.

Our work focuses on a newly developed semiconducting polymer for organic photovoltaics (OPVs) called PffBT4T-C9C13, which shows an efficiency of approximately 12% [1]. These efficiencies are due to a low band-gap, broad absorption spectrum and a high crystallinity of the polymer, providing excellent transport mobilities of the order of  $10^{-3} \text{ cm}^2 \text{ V}^{-1} \text{ s}^{-1}$ , and the ability to use a thick active layer, resulting in improved light absorption.

To achieve this high efficiency, the donor polymer PffBT4T-C9C13 was dissolved in 1,2,4-trimethylbenzene (TMB) with the fullerene derivative acceptor PC70BM in a 1:1.2 ratio (donor:acceptor). Further, the additive 1-phenylnaphthalene (PN) was used to control morphological properties of the blend, since it was reported that fullerene derivatives has high solubility properties in it [2]. PN drives the polymer backbone orientation relative to the substrate from edge-on to face-on, reduces the domain size, and increases the domain purity of the bulk-hetero-junction of the active layer of a OPV.

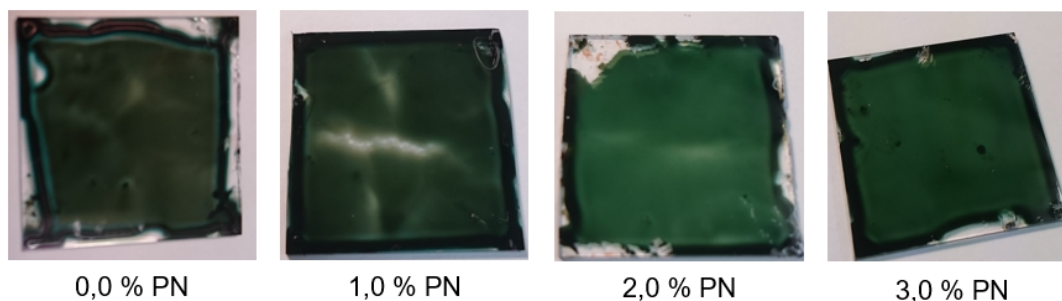


Figure 3.1:  
Coating behavior of the active layer blend PffBT4T-C9C13:PC70BM (ratio 1:1.2) for different PN concentrations

Investigating the influence of PN on the organic blend, a measurement series was created. For the substrates, soda-lime glass was cleaned in an acid bath. A 4 mg/ml solution of PffBT4T-C9C13 in TMB was added to PC70BM with a donor:acceptor ratio of 1:1.2. Different amounts of PN were added and the resulting solution finally spin-coated on the glass substrates, which is shown in Fig. 3.1. For this, the blend and the substrates were preheated at 100 °C before spincoating.

It was observed that the spin-coating behavior and hence the homogeneity improves dramatically with a higher amount of PN, resulting in a better quality of the active layer films, which is due to PN being still liquid in the blend.

Since the PN has no other purpose in the active layer than improving the morphological properties, it is necessary to remove it from the active layer to ensure a high performance. Further it is also shifting the optical absorption of the active layer, shown in Fig. 3.2 a, and making the active layer film soft and wet, resulting in an unstable thinfilm, not suitable for further processing.

With a boiling point of 324 °C for PN, thermal evaporation for extracting the additive out of the active layer would damage the organic compounds. To bypass this problem a vacuum of  $2.5 \cdot 10^{-5}$  mbar was applied with the result, that the PN has been almost completely removed from the active layer, shown in Fig. 3.2 b. Without changing the overall film-morphology this procedure ensures the positive morphological effects of the PN without its absorbing and film-softening behavior.

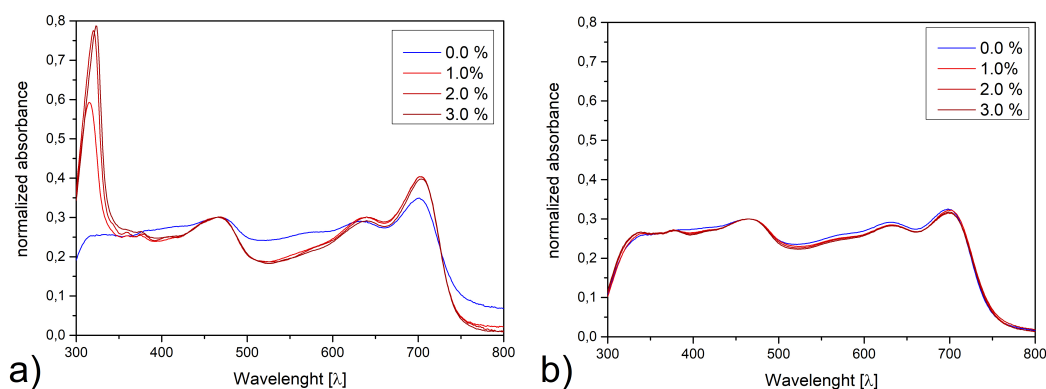


Figure 3.2:  
Normalized absorbance spectra of the active layer blend PffBT4T-C9C13:PC70BM (ratio 1:1.2) a) before and b) after vacuum treatment

PN results in a good additive for our fullerene based PffBT4T-C9C13 blend, due to its morphological impact as well as its enhancing behavior towards the coatability of the blend on substrates. Furthermore, the indulgent vacuum treatment for removing the PN out of the bulk-hetero-junction ensures an undamaged active layer.

- [1] J. Zhao, Y. Li, G. Yang, K. Jiang, H. Lin, H. Ade, W. Ma, H. Yan, *Nature Energy* **1**, 15027 (2016)
- [2] K. N. Semenov, N. A. Charykov, V. A. Keskinov, A. K. Piartman, A. A. Blokhin, A. A. Kopyrin, *J. Chem. Eng. Data* **55** (1), pp 13-36 (2010)

### 3.2 Printed organic thin films for photovoltaic applications

R. Delgado Andrés, S. Grott, P. MüllerBuschbaum

The past decades have seen the development of the photovoltaic technology as a promising candidate to counter the growing energy demand. This has motivated the research on new materials exhibiting enhanced photoelectrical properties and the study of applicability of large industrial-scale fabrication techniques to build photovoltaic devices in larger numbers. In the broad field of materials used for photovoltaic applications, polymer-based materials have received increased attention due to the wide range of processing techniques that can be used to build the final devices. Including solution based printing methods, which offer the opportunity to be adapted to industrial scales. By use of this technique, large areas of organic solar cells can be produced much faster and vastly cheaper than their organic counterparts. In addition, almost any substrate, including light and flexible ones, can be used for organic photovoltaic (OPV) devices. Lastly, the relatively ease with which new polymers can be synthesized compared to inorganic semiconductors makes OPV a competitive technology for energy generation. Among the different OPVs devices, solution-processed bulk heterojunction (BHJ) solar cells have been the most prominent candidate. The basic scheme of an BHJ OPV cell is composed of a donor and an acceptor, which built up the active layer. Fullerene derivatives have been so far the main choice of acceptor materials with polymeric semiconductors as donors. The importance of the active layer is that the photo-physical processes that lead to an external current take place here. It is sandwiched between two electrodes that serve as current collectors (shown in Fig 3.3a)). In this kind of OPV device, the donor and acceptor are mixed and deposited in one step to form the active layer, making the BHJ solar cells good candidates for printing techniques. The good knowledge of the active's layer characteristics and behavior on different fabrication methods is imperative to bring this technique to an industrial scale.

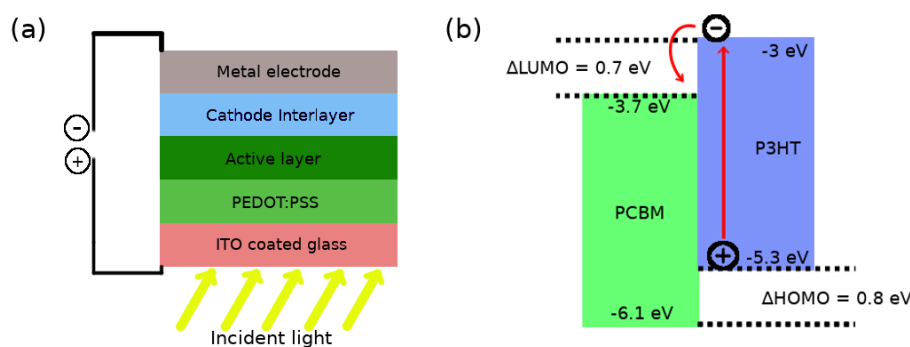


Figure 3.3:

a) Schematic of a organic solar cell stacking, b) Energy band diagram of donor (P3HT) and acceptor (PCBM).

Upon absorption of a photon within the active layer, an electron is excited, giving rise to an exciton which can diffuse to the interface. The dissociation of the exciton at the donor/acceptor interface leads to the formation of a hole (positive charge) at the highest occupied molecular orbital (HOMO) of the donor and an electron (negative charge) at the lowest unoccupied molecular orbital (LUMO) of the acceptor (Fig. 3.3.b)). These free charges can diffuse and be extracted at the corresponding electrodes, thereby generating a current. The most important points of the process are exciton generation and dissociation. The latter is a consequence of the active's layer morphology, while the former which happens within the active layer is material dependent. Since the exciton diffusion length is about 10nm, a high degree of intermixing of the

donor/acceptor is desired to offer a high interfacial area. In an ideal BHJ solar cells, the intermixing is a comb like structure offering a high interfacial area. Then by choosing the adequate constituents, an electric field can be created to overcome the energy barrier to separate the exciton. Nevertheless, the morphology of the active layer is in most cases far from ideal and the efficiency lower than theoretically possible, due to enlarged diffusion lengths which result in higher recombination rate.

The blend poly(3-hexylthiophene):[6,6]-phenyl-C61-butyric acid methyl ester (P3HT:PCBM) is already well known in the fabrication of BHJ OPVs devices and thus offers the chance to study its scalability. To better understand the influence of the active layer morphology evolution in the final efficiency of printed devices, *in situ* measurements have been carried out during printing processes[1]. The work presented consist in the fabrication of a printing setup capable to deposit solvent-based active layers for photovoltaic applications following the procedure introduced by Pröller et al [2] presented in Fig. 3.4. The design of this printer simulates conditions that might be encountered during industrial processing. Thus the printer is capable to print under various atmospheric conditions and offers the possibility to perform *in situ* studies on the active layer's inner morphology using advanced scattering techniques, like grazing incidence small angle X-ray scattering (GISAXS) and grazing incidence wide angle X-ray scattering (GIWAXS) [3]. Due to the fact that the final morphology depends on the film deposition's conditions (deposition speed, drying time, etc.), different coating techniques will lead to different morphologies and to different power conversion efficiencies. Hence, understanding the formation process of the active layer and its morphology in comparison to data obtained using lab-scale deposition techniques is of high interest. This information can be correlated with the usually obtained photoelectrical properties of any solar cell device, giving full characteristics of the printed solar cells.

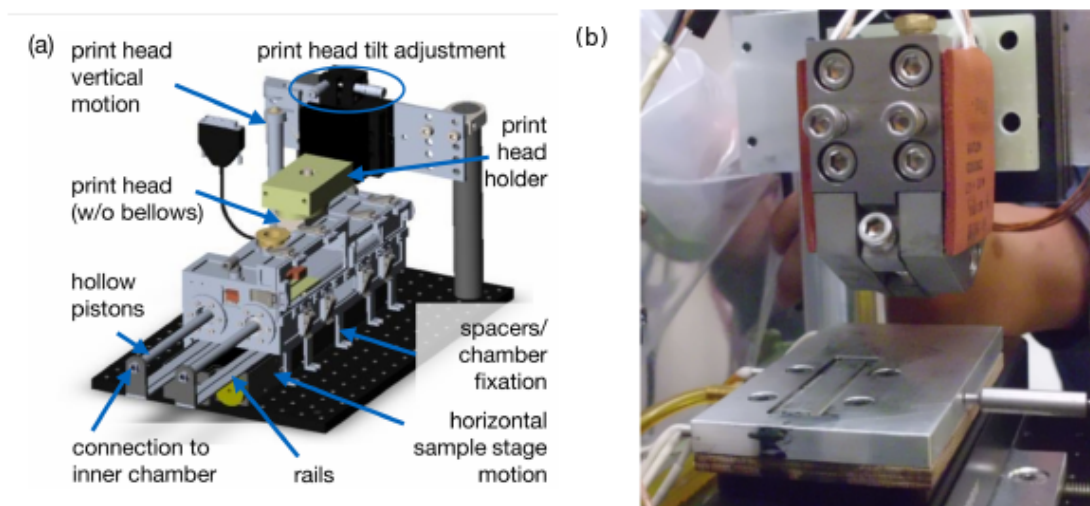


Figure 3.4:

(a) 3D CAD model of the printer with most important parts indicated (b) Photograph of the printhead and the substrate stage made by Pröller et al [2].

- [1] S. Pröller, F. Liu, C. Zhu, C. Wang, T. P. Russell, A. Hexemer, P. Müller-Buschbaum, and E. M. Herzig *Adv. Energy Mater.* **6**, 1501580, (2016)
- [2] S. Pröller, D. M. González, C. Zhu, E. Schaible, C. Wang, P. Müller-Buschbaum, A. Hexemer, and E. M. Herzig *Rev. Sci. Instrum.* **88**, 066101 (2017)
- [3] P. Müller-Buschbaum *Anal. Bioanal. Chem.* **376**, 3-10 (2003)

### 3.3 Active layers for hybrid solar cells based on laser-ablated metal oxide nanoparticles and water-soluble polythiophenes

J. Gui, V. Körstgens, K. Stallhofer<sup>1</sup>, H. Iglev<sup>1</sup>, R. Kienberger<sup>1</sup>, P. Müller-Buschbaum

<sup>1</sup> LS Laser- und Röntgenphysik, TU München, Garching, Germany

Hybrid solar cells combine organic and inorganic materials to utilize the low cost, adjustable molecular structures for energy band alignment, etc. from organic photovoltaics and some other characteristics, such as tunable absorption spectra, high carrier mobility and so on from inorganic part. Regarding the environmental impact hybrid solar cells which can be processed from aqueous solutions are of special interest. Such solar cells are feasible with an active layer consisting of laser-ablated titanium dioxide and a water-soluble polythiophene [1]. Due to its low cost, non-toxicity, high photoelectric conversion efficiency, and high chemical stability, TiO<sub>2</sub> has been widely used in hybrid photovoltaics whereas alternative materials such as zinc oxide can be considered as the inorganic part in the active layer, given its stability in air and good light transmittance.

We fabricated an active layer of TiO<sub>2</sub> with poly[3-(potassium-6-hexanoate) thiophene-2,5-diyl] (P3P6T). The introduction of a carboxyl-group in the series of polymers named P3PmT (m = 4, 5, 6, 7), derived from the well-known polythiophene P3HT, make the molecules water-soluble. P3P6T was reported to have the highest hole mobility in the series of water-soluble polythiophenes [2]. It has been shown that the processing of TiO<sub>2</sub> nanoparticles with laser ablation in water is necessary for decent working hybrid solar cells [1]. The laser-ablated particles are functionalized with the polythiophene and a better intermixing of the components of the active layer is ensured.

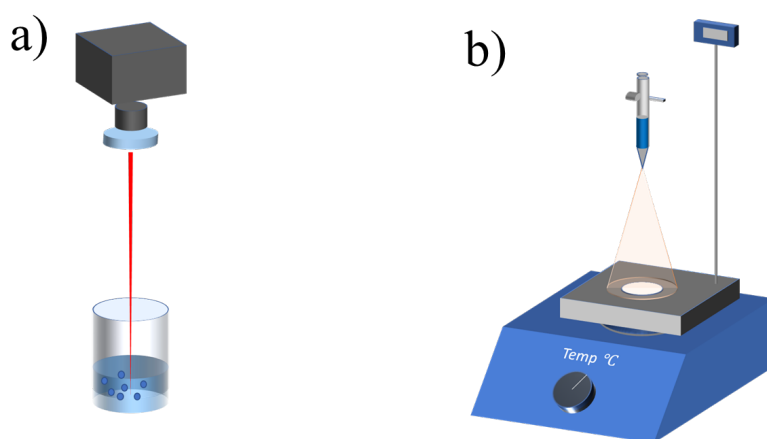


Figure 3.5:

a) Basic set-up for laser ablation in liquid. b) Spray process for the active layer consisting of titanium dioxide and the polythiophene P3P6T.

Laser ablation in liquid works by focusing a pulsed laser beam onto a solid immersed in a liquid. Whereas the source material for the particles can be a metal plate, it is also possible to process a dispersion of nanoparticles. Then the pulsed laser hits a large number of particles as shown in 3.5a. The efficiency of the laser ablation process depends on the intensity, pulse length, and wavelength of the laser, as well as the material itself [3]. The laser radiation is provided by using a home-built titanium:sapphire laser system delivering pulses at a central wavelength of 779 nm with a pulse energy of 900  $\mu$ J and a repetition rate of 100 kHz. The pulse duration  $t_{pulse}$  of 150 fs

was measured by frequency-resolved optical gating. The laser beam was focused on an aqueous dispersion of P25 TiO<sub>2</sub> nanoparticles via a fused silica lens ( $f = 100$  mm) as shown in Fig. 3.5a. Afterwards the ablated TiO<sub>2</sub> nanoparticles were mixed with a solution of P3P6T and the mixture was deposited on calcium fluoride (CaF<sub>2</sub>) windows. Calcium fluoride has a low absorption coefficient and high damage threshold, making these windows good choices for use with free-space lasers and designated pump probe experiments. In order to investigate the influence of the laser ablation process also mixtures of non-ablated TiO<sub>2</sub> particles and P3P6T were deposited on CaF<sub>2</sub> windows. Spray-deposition as a cost-effective method was chosen for the preparation of the samples. Spray deposition allows to obtain a homogeneous film and good measure of film thickness by controlling the amount of sprayed solution. Spray deposition has also been utilized as the technique to produce corresponding hybrid solar cells out of the laser ablated nanoparticles and the water-soluble polythiophene [1]. The spray deposition was performed at a substrate temperature of 80°C on CaF<sub>2</sub> windows as shown in Fig. 3.5b.

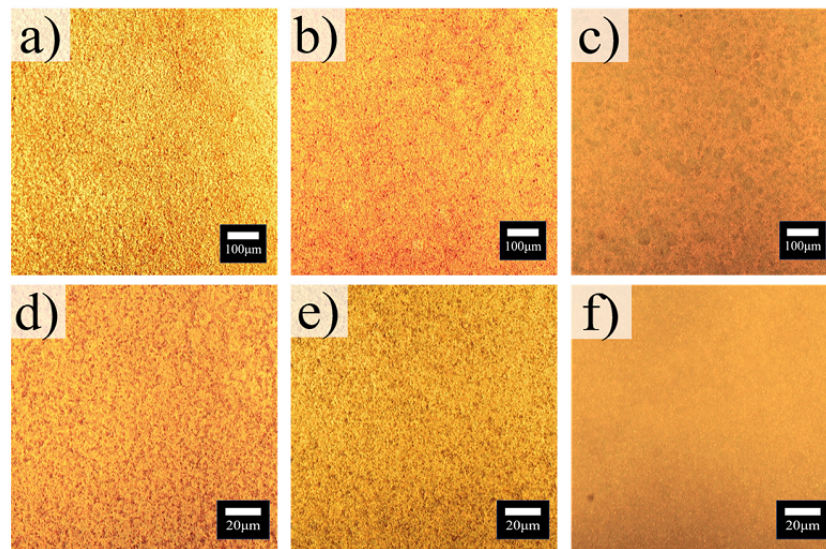


Figure 3.6:

a) Optical microscope images in two different magnifications of a),d) ablated TiO<sub>2</sub>/P3P6T; b), e) non-ablated TiO<sub>2</sub>/P3P6T; c), f) ZnO layer.

Whereas the spectroscopic characterization of the active layers is currently under investigation, the prerequisite of homogeneous sprayed layers is given as shown in in Fig. 3.6. The optical microscope images in Fig. 3.6a) and d) show the active layer composition of polythiophene and laser-ablated TiO<sub>2</sub> in two different magnifications, Fig. 3.6b) and e) show the corresponding layers of polythiophene with non-ablated TiO<sub>2</sub>. Whereas both layers show a homogeneous distribution on the CaF<sub>2</sub> substrate, the film with laser-ablated surface appears to have a slightly smoother surface. The application of ZnO as source material for laser-ablated nanoparticles in the active layer for hybrid solar cells is in preparation. Fig. 3.6c) and f) show a spray-deposited films of ZnO nanoparticles before the ablation process. A breaking-up of the large spherical aggregates already visible in optical microscopy (Fig. 3.6f)) is one of the beneficial consequences expected with the laser ablation process in liquid for these particles.

- [1] V. Körstgens, S. Pröller, T. Buchmann, D. Mosegui González, L. Song, Y. Yao, W. Wang, J. Werhahn, G. Santoro, S. V. Roth, H. Iglev, R. Kienberger, P. Müller-Buschbaum, *Nanoscale* **7**, 2900-2904 (2015)
- [2] G. K. V. V. Thalluri, J. C. Bolsée J C, A. Gadisa, et al., *Solar Energy Materials and Solar Cells* **95(12)**, 3262-3268 (2011)
- [3] D. Zhang, B. Gökce, S. Barcikowski, *Chem. Rev.* **117**, 3990-4103 (2017)

### 3.4 PBDB-T-SF for high efficiency solar cells

K. Wienhold, P. Müller-Buschbaum<sup>1</sup>

<sup>1</sup> MLZ, Garching, Germany

Organic solar cells have attracted growing interest as a renewable energy source as they consist of highly tunable materials. Their properties can be optimized by modification of the chemical structure of the conjugated polymer electron donor as well as the acceptor molecule. Current research focuses on enhancing efficiency and lifetime of organic solar cell devices.

To date, an efficiency of over 13 % can be obtained with a PBDB-T-SF:IT-4F organic solar cell device.[1] The conjugated high efficiency polymer donor PBDB-T-SF and the small molecule acceptor IT-4F are fluorinated. The introduction of fluorine down-shifts the energy levels of the highest occupied molecular orbital (HOMO) and the lowest unoccupied molecular orbital (LUMO) of both the donor and the acceptor molecule. PBDB-T-SF and IT-4F show higher chemical stability, higher absorption coefficients and enhanced noncovalent interactions compared to their nonfluorinated counterparts. Fluorination improves crystallinity and facilitates charge transport. In addition, the Coulomb potential between holes and electrons is reduced and the probability of charge recombination decreased.

In order to further improve efficiency and lifetime of organic solar cells, the donor and acceptor materials have to be analysed in detail to understand the impact of the molecular structure and the active layer on the performance of organic solar cells.[1-3]

The absorption properties of the donor material in the range of ultraviolet and visible light (UV/VIS) is essential for solar cell application as the ability to absorb sun light is indispensable for all solar cells. Therefore, an absorbance spectrum of PBDB-T-SF was measured (Figure 0.1).

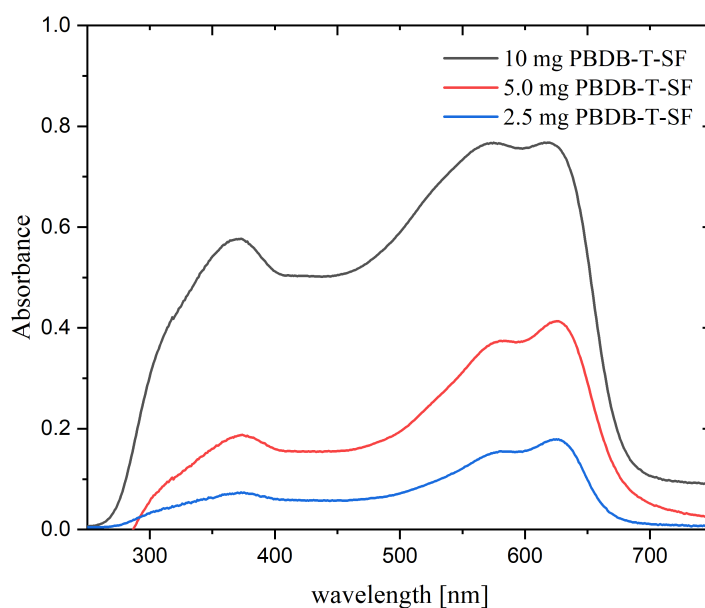


Figure 3.7: Absorbance of PBDB-T-SF on a PEDOT coated glass substrate.

All samples were prepared by spin coating. Therefore, PBDB-T-SF was dissolved in chlorobenzene at 100 °C to produce solutions with concentrations of 10 mg/mL, 5.0 mg/mL and 2.5 mg/mL. The glass substrates were coated with PEDOT (Poly(3,4-ethylenedioxythiophene)). After spin coating (3000 rpm, 60 s) of the polymer solution, the absorbance spectrum of PBDB-T-SF was measured with a Perkin Elmer Lambda 650 S UV/VIS spectrometer.

PBDB-T-SF shows efficient absorbance over a broad wavelength range in the region of UV/VIS light (Figure 0.1). Thus, the donor material is able to absorb sun light which is a fundamental property of all solar cells even though other criteria have to be met too.

In organic solar cells, photons are absorbed by the donor material and excitons are generated.[3] These excitons have to diffuse to the donor-acceptor interface and dissociate by electron transfer to the acceptor molecule. These electron-hole pairs are bound by Coulomb forces. Electrical fields and material disorder enable separation and charge extraction. To generate this photocurrent, the structure of the active layer and its interface are important. In many organic solar cells, the active layer has a bulk heterojunction (BHJ) structure.[2-3] Domains of donor and acceptor molecules overlap at a large interface for efficient charge transport. To have a first look at the structure, PBDB-T-SF was spin coated on a PEDOT coated glass substrate and analysed with an optical microscope with a tenfold (Figure 0.2 a) and fiftyfold (Figure 0.2 b) enlargement. Over the whole sample area, a thin film of the polymer was formed even though inhomogeneities are visible. Due to its ability to spread on the substrate, PBDB-T-SF might be able to form a large interface e.g. a bulk heterojunction structure if mixed with IT-4F.

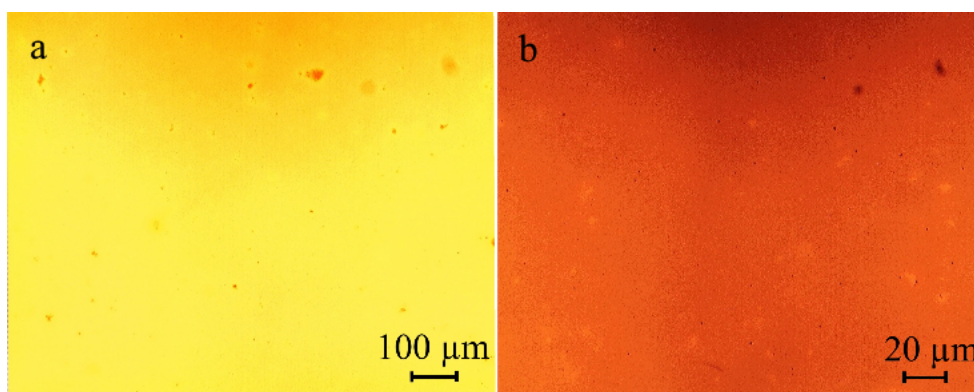


Figure 3.8: Optical microscope picture of PBDB-T-SF with (a) tenfold and (b) fiftyfold enlargement.

The conjugated high efficiency polymer PBDB-T-SF is able to absorb photons in a broad wavelength range in the region of UV/VIS light and to form thin films which is necessary for solar cell production. If mixed with the small molecule acceptor IT-4F, a high organic solar cell efficiency of over 13 % can be reached. The structure of the active layer has to be further investigated in order to understand its impact on the solar cell performance. This knowledge is essential for the processing of marketable organic solar cells with high efficiency and lifetime.

- [1] W. Zhao, S. Li, H. Yao, S. Zhang, Y. Zhang, B. Yang, J. Hou *J. Am. Chem. Soc.* **139**, 7148-7151 (2017)
- [2] Q. Zhang, L. Yan, X. Jiao, Z. Peng, S. Liu, J. J. Rech, E. Klump, A. Ade, F. So, W. You *Chem. Mater.* **29**, 5990-6002 (2017)
- [3] S. H. Park, A. Roy, S. Beaupré, S. Chao, N. Coates, J. S. Moon, D. Moses, M. Leclerc, K. Lee, A. J. Heeger *Nat. Photon.* **3**, 297-302 (2009)

### 3.5 Low temperature fabricated ZnO films for solid-state dye-sensitized solar cells

K. Wang, V. Körstgens, D. Yang, N. Hohn, P. Müller-Buschbaum

Nanostructured inorganic metal oxides with tunable morphologies are of great importance for dye-sensitized solar cells, especially for solid-state dye sensitized solar cells (ss-DSSCs), due to the exciton separation at the interfaces and the inadequate nanopore penetration of hole transport materials in the mesoscopic inorganic semiconductor scaffolds. Among the inorganic metal oxides, zinc oxide (ZnO) has been widely explored due to its outstanding electrical and optical properties and rich variety of morphologies [1]. To date, many different routes towards ZnO nanostructures have been reported [2-3]. However, most of them use high-temperature fabrication routes to prepare ZnO films, which is a drawback for future fabrication of lightweight and flexible solar cells and causes high fabrication costs and long energy payback times as well. In the present work, a sol-gel method templated with a diblock copolymer polystyrene-block-poly(ethylene oxide) (PS-b-PEO) is combined with low temperature annealing to fabricate mesoporous nanostructured ZnO films. Worm-like ZnO films are investigated for different annealing times to see the growth evolution. Moreover, depending on the response of the ZnO/PS-b-PEO films to different annealing temperatures, a vast range of reproducible morphologies can be obtained. Based on the different morphologies of the ZnO films, all ss-DSSCs with transparent active layers are fabricated.

The growth process of the obtained worm-like hybrid films annealed at 120 °C is shown in Fig. 3.9. For the as-cast hybrid film (Fig. 3.9a), an interconnected foam-like 3D structure is observed, which suggests that mesoporous network structures at nanoscale can be generated via the sol-gel method. Along time increasing to 0.5 min (Fig. 3.9b), some large ZnO clusters appear at random positions. This is possibly due to the comprehensive effect of residual solvent inside the film, the softness of the PS and PEO blocks and the presence of ZnO nanoparticles in the films. When annealing the films for 1 min (Fig. 3.9c), more large domains are present, and unevenly dispersed ZnO clusters can be observed. With further annealing to 2 min (Fig. 3.9d), we can clearly observe the presence of a worm-like structure, suggesting that some ZnO clusters already change from foam-like to worm-like structure. However, there are still some large clusters and they become significantly larger than the previously observed ZnO nanoparticles. A further increase of the annealing time to 8 min (Fig. 3.9e-g) induces an ongoing change of the film morphology. The worm-like structure remains unchanged while the large clusters vanish gradually. Fig. 3.9f and g show the large clusters first become thinner and then change to worms constituting to a more homogeneous film. After annealing for 15 min (Fig. 3.9h-j), no large clusters are observed anymore. Instead, a vast homogeneous worm-like structure is seen, implying that the growth of worm-like structure is completed.

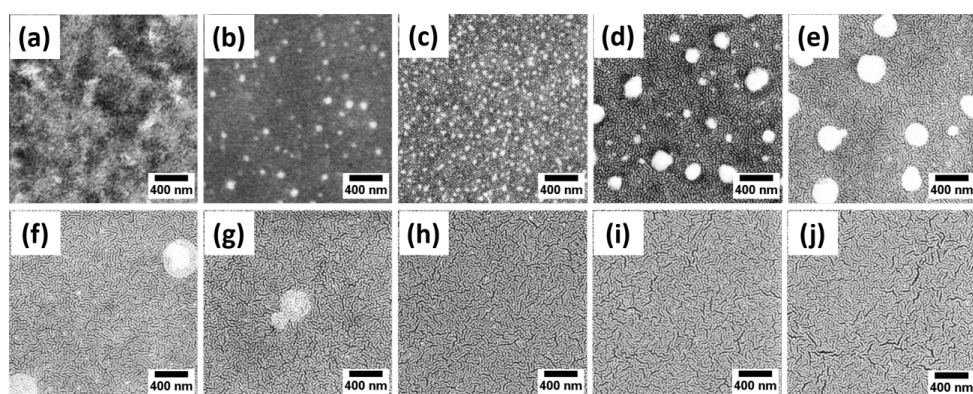


Figure 3.9:

Influence of annealing time: SEM images of the hybrid ZnO films annealed at 120 °C for: (a) 0 min, (b) 0.5 min, (c) 1 min, (d) 2 min, (e) 3 min, (f) 5 min, (g) 8 min, (h) 15 min, (i) 30 min and (j) 60 min.

To tune the morphology of ZnO films, annealing temperature is adjusted depending on the

response of ZnO/PS-b-PEO films to temperature. Fig. 3.10a-d show the morphologies annealed at different temperatures. The ZnO films annealed at 80 °C (Fig. 3.10a) exhibit a high interconnectivity of the foam-like structures. Upon temperature increasing to 120 °C (Fig. 3.10b), the morphology is altered to a worm-like structure, with ZnO nanoparticles connecting with each other. As a consequence, ZnO films can not only leave vast parts of the volume for filling with dye molecules, but will also exhibit good electron transport, which is beneficial for application in ss-DSSCs. With further temperature increasing to 160 °C (Fig. 3.10c) and 200 °C (Fig. 3.10d), almost monodisperse, sphere-like structures are observed on the sample surface.

In order to investigate the photovoltaic performance of complete devices, the ZnO films with different morphologies are prepared as ss-DSSCs. Fig. 3.10e presents the current density-voltage (J-V) curves of the ss-DSSCs and the device parameters ( $J_{sc}$ ,  $V_{oc}$ , FF, and PCE, in Fig. 3.10f and g) are extracted from the J-V curves. It is noticed that the device performance is closely associated with the annealing temperature. The ss-DSSCs based on ZnO films annealed at 120 °C have higher PCE values (about 0.42 %) than the others due to the higher  $J_{sc}$ ,  $V_{oc}$  and FF. With increasing the annealing temperature from 120 °C to 200 °C, the PCE values of the corresponding ss-DSSCs decrease dramatically. As the prepared ss-DSSCs show mostly transparent active layers with a slight color as shown in the inset of Fig. 3.10h, it is promising for applications as windows materials with photovoltaic performance. For a detailed analysis, IPCE normalized by (1-transmittance) is a reasonable technique to characterize the highly transparent active layers. In these normalized IPCE curves, the efficiency is significantly higher in the wavelength range from 450 to 650 nm. The highest efficiency of 98.2 % is obtained at 590 nm for ss-DSSCs fabricated from 120 °C annealed ZnO films. It is higher than those values probed on 80 °C (65.5 %), 160 °C (58.9 %), and 200 °C (46.6 %) annealed ZnO films at 590 nm. These ss-DSSCs performance show great relationship with the morphology of the nanostructured ZnO films.

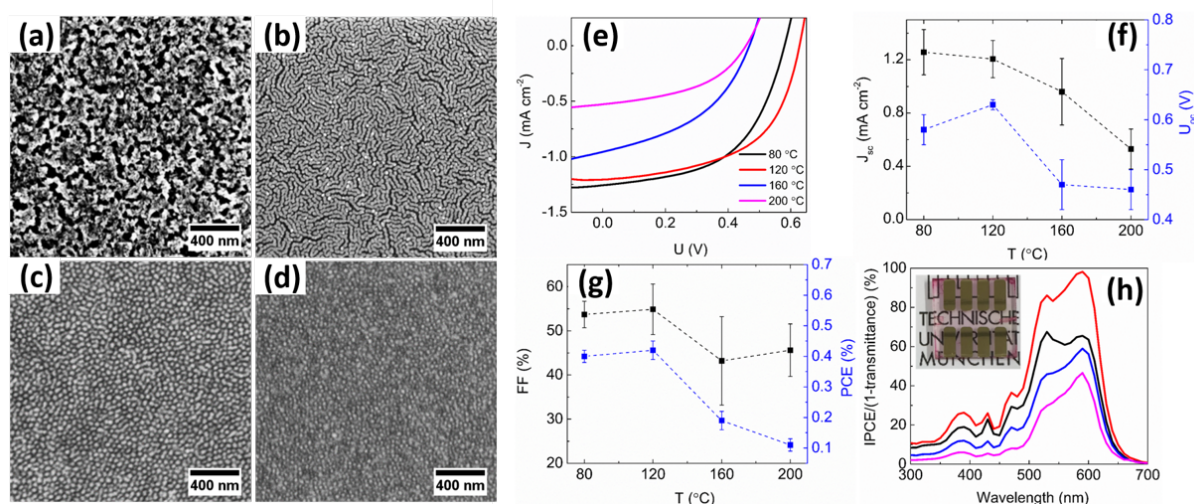


Figure 3.10:

Influence of annealing temperature: SEM images of mesoporous ZnO films annealed at different temperatures after polymer removal: (a) 80 °C, (b) 120 °C, (c) 160 °C, and (d) 200 °C. (e) current density–voltage characteristics (including the extracted device parameters in (f and g)) and (h) IPCE normalized by (1-transmittance) of ss-DSSCs based on ZnO prepared at different annealing temperatures. (inset in h: optical image of a ss-DSSC from 120 °C annealed ZnO film)

- [1] H. Yu, Z. Zhang, M. Han, X. Hao, F. Zhu, *J. Am. Chem. Soc.* **127**, 2378 (2005)
- [2] B. O'Regan, D. T. Schwartz, S. M. Zakeeruddin, M. Grätzel, *Adv. Mater.* **12**, 1263 (2000)
- [3] C. Xu, J. Wu, U. V. Desai, D. Gao, *Nano Lett.* **12**, 2420 (2012)

### 3.6 Sputter deposition of gold contacts for hybrid solar cells

V. Körstgens, A. Haussmann, F. Löhner, H. Iglev<sup>1</sup>, M. Schwartzkopf<sup>2</sup>, A. Rothkirch<sup>2</sup>, A. Hinz<sup>3</sup>, O. Polonskyi<sup>3</sup>, T. Strunskus<sup>3</sup>, F. Faupel<sup>3</sup>, S. V. Roth<sup>2</sup>, R. Kienberger<sup>1</sup>, P. Müller-Buschbaum

<sup>1</sup> LS Laser- und Röntgenphysik, TU München, Garching, Germany

<sup>2</sup> DESY, Hamburg, Germany

<sup>3</sup> Institut für Materialwissenschaften, CAU, Kiel, Germany

One approach in the emerging field of photovoltaics is the concept of water-processed hybrid solar cells. Here the use of harmful or toxic materials is avoided in the production of devices. The fabrication process is also very efficient in terms of energy demand and costs. These solar cells consist, on the one hand, of a water-soluble, polythiophene which acts as a donor in the active layer. On the other hand  $\text{TiO}_2$ -nanoparticles are used, which serves as an electron acceptor in the cell. Thus advantages of both organic and inorganic materials are combined. The organic material provides high absorption and flexibility, while the inorganic part provides good conductivity and stability [1].

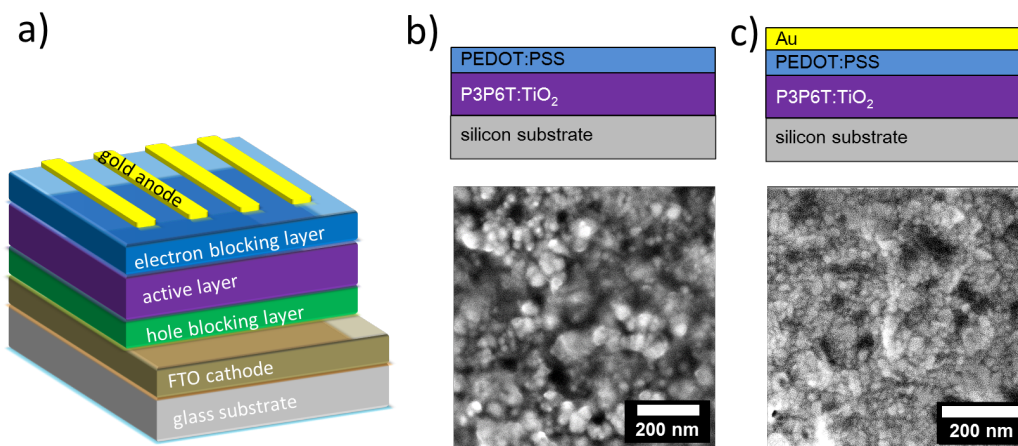


Figure 3.11:

a) Layer stack of a hybrid solar cell b) sketch of the layered structure used for sputter deposition experiment and corresponding top-view SEM image c) sketch of layered structure after gold deposition and corresponding top view SEM image.

The device structure for such a hybrid solar cell is shown in Fig. 3.11a). The used cell geometry is inverted compared to the standard cell geometry of organic solar cells. While the fabrication and functionality of a device based on laser-ablated titania and a water-soluble thiophene already has been shown [1] the focus here is on the investigation of the gold contact of such devices. Regarding the layer stack of the actual devices given in Fig. 3.11a) for the in situ sputter experiment the sample described in Fig. 3.11b) was chosen. The bulk-heterojunction from the polymer poly[3-(potassium-6-hexanoate)thiophene-2,5-diyl] (P3P6T) and the  $\text{TiO}_2$  nanoparticles is a relatively thick layer of several hundred nanometers ( $\approx 350$  nm). The pure PEDOT:PSS layer on top of the active layer is thinner ( $\approx 25$  nm). The gold contact is now sputtered onto this upper polymer layer. Fig. 3.11b) shows the top view SEM image of PEDOT:PSS coated active layer. The  $\text{TiO}_2$ -nanoparticles are very distinctive whereas the polymers show generally only very weak structures in this size range in SEM measurements. These images indicate a rough surface, which has been proven by atomic force microscopy. The surface after gold deposition is shown in Fig. 3.11c). The grain structure, which is typical for sputtered gold layers, stands

out. The growth of these gold cluster is studied in situ by GISAXS and GIWAXS. From these measurements the gold crystal growth can be observed and its crystallinity is observed to rise with larger film thickness. By investigating the vertical structure, the GISAXS data reveal the evolution of the effective layer thickness to increase in a linear way. From the lateral structure the development of the horizontal correlation distance between the occurring gold clusters is achieved. The correlation distance shows an increasing behavior over the deposition process with basically two regimes: A first strong increase and a second significantly slower increase. Based on already performed growth studies of gold on polymers, a similar growth is expected for the hybrid solar cell system since the upper layer is also a polymer, namely PEDOT:PSS.

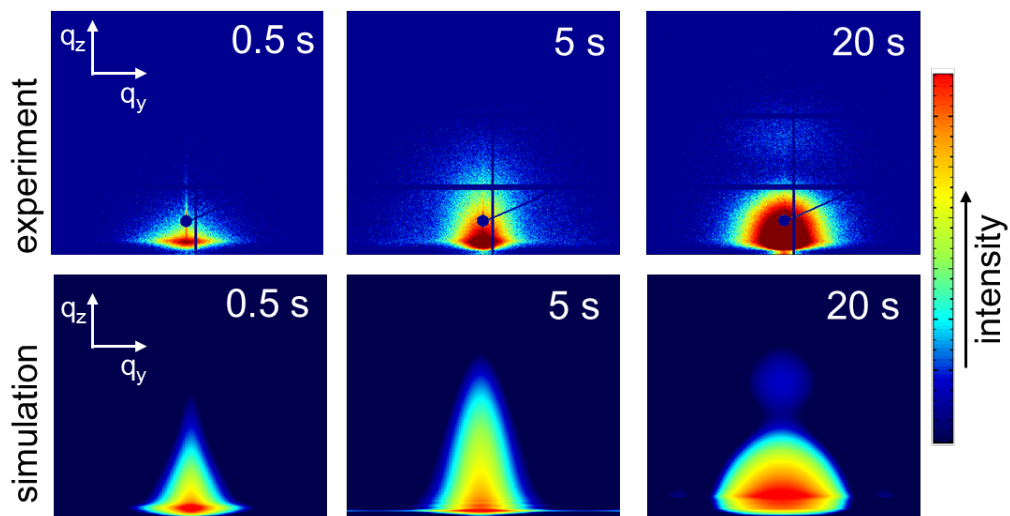


Figure 3.12:

Top row shows the experimental measured GISAXS data after 0.5 s, 5 s and 20 s of sputter deposition. Bottom row shows the corresponding IsGISAXS 2D simulations. The images cover the same reciprocal space region from  $-1.9$  to  $1.9 \text{ nm}^{-1}$  in  $q_y$ -direction and a range from  $0.45$  to  $3.8 \text{ nm}^{-1}$  in  $q_z$ -direction.

In Fig. 3.12, simulations performed with IsGISAXS [2] are accompanied by the experimental data of in situ GISAXS after 0.5 s, 5 s and 20 s of sputter deposition. The simulated scattering patterns based on truncated spheres are in good agreement with experimental 2D data. Therefore the use of the growth model of Schwartzkopf et al. [3] is justified since it is based on spherical shaped particles. However, for the description of the cluster growth on a rough active layer the roughness has to be considered. One possible approach is the modeling of sinusoidal shaped surface of the underlying layer which leads to a larger effective correlation distance by an additional height difference between the gold clusters. Such model modification takes into account a geometrical aspect and saves the models simplicity while explaining the observed behavior well. Applying this modified growth model on the data yields good results and shifts the onset of growth phases, especially the percolation threshold to later deposition times.

- [1] V. Körstgens, S. Pröller, T. Buchmann, D. Mosegui González, L. Song, Y. Yao, W. Wang, J. Werhahn, G. Santoro, S. V. Roth, H. Iglev, R. Kienberger, P. Müller-Buschbaum, *Nanoscale* **7**, 2900-2904 (2015)
- [2] R. Lazzari, *Appl. Cryst.* **35**, 406-421 (2002)
- [3] M. Schwartzkopf, A. Buffet, V. Körstgens, E. Metwalli, K. Schlage, G. Benecke, J. Perlich, M. Rawolle, A. Rothkirch, B. Heidmann, G. Herzog, P. Müller-Buschbaum, R. Röhlberger, R. Gehrke, N. Striebeck, S. V. Roth, *Nanoscale* **5**, 5053-5062 (2013)

### 3.7 Printing ITO-free electrode for low bandgap polymer solar cells

X. Jiang, W. Cao, S. Xia, N. Li, P. Müller-Buschbaum

Bulk heterojunction (BHJ) polymer solar cells have gained significant improvements via novel organic synthesis and easy fabrication methods, especially their potential roll to roll processing and large-area processability on low cost makes conjugated polymer-based organic solar cells very attractive as a cost-effective solution to today's energy-shortage problem. However, some crucial problems still need to be solved before using. For the traditional electrodes for organic solar cells, indium tin oxide (ITO) electrodes have many drawbacks such as the shortage of indium on earth, high mechanical brittleness, expensive deposition techniques, poor adhesion to organic and polymeric materials, release of oxygen and indium into the organic layer, poor transparency in blue region, and the need for high temperature processing[1]. The conductive polymer poly(3,4-ethylene dioxythiophene) (PEDOT) doped with poly(styrene sulfonate) (PSS) is quite promising as a next-generation transparent electrode material, for its high transparency in the visible range, high mechanical flexibility, excellent thermal stability and as it can be fabricated through conventional solution processing. Furthermore, PEDOT:PSS films can be easily nano-structured to enhance the localized light intensity to the active layer and generate more power. Figure 3.13a shows the typical device configurations of ITO-free BHJ solar cells. When the light is absorbed in the active layer, the electrons and holes are created. At the same time, the excitons are dissociated and transferred to the electrodes. Printing technique allows for up-scaling to industrial-oriented scales which is not the case for laboratory techniques like spin coating. Thus, roll-to-roll processing on flexible substrates is the goal of production techniques for organic solar cells. Several methods of printing techniques can be used to reach this goal, such as slot-die coating, screen printing or flexographic printing. Especially slot-die coating, is a very cost-effective production technique that offers the possibility of large scale manufacturing and custom designed pattern coating [2]. Figure 3.13b shows the sketch of the slot-die coating to obtain thin film.

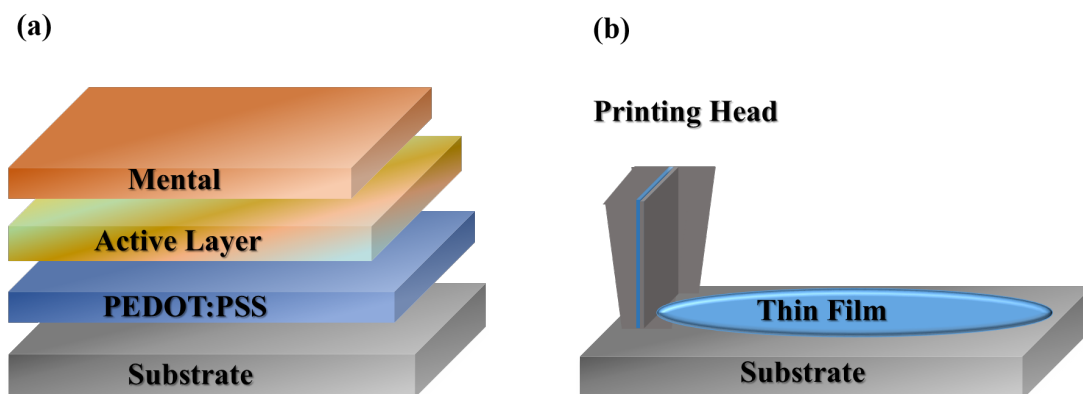


Figure 3.13:  
Device configurations of organic solar cells (a);Sketch of the slot-die coating to obtain thin film (b).

We focus on fabricating an ITO-free BHJ polymer solar cell with slot-die printing technique. In such a BHJ polymer solar cell with printing technique, the morphology plays an important role for device efficiency. Different factors can influence the morphology of active layer. For example, the topology of the underlying layer can influence the nanostructure of the active layer. Therefore the preparation of uniform PEDOT:PSS thin electrode with printing technique is the first step for large scale production for BHJ solar cells. In the present work, we study

printed transparent PEDOT:PSS thin film with respect to morphology and optical properties when different heating-treatment process for substrates. The main experiment details were as following. First, the substrates were cleaned by ethanol, acetone, DI water for 15min, respectively, then put in acid bath at 80°C for 15 min. Second, PEDOT:PSS was coated on substrates by the slot-die printing machine which has a temperature control system for the substrates. Finally, pure PEDOT:PSS solid film was prepared after annealing at 140°C for 10 min in air. The morphology and optical properties of samples were tested by optical microscope and UV-Vis spectroscopy.

The main morphology for the samples without and with substrate heating during the printing process tested by optical microscope are shown in Figure 3.14a and Figure 3.14b. In Figure 3.14a, PEDOT:PSS thin film shows different reflect color, which means the film has different thickness. This is due to the “coffee ring effect” when solvent evaporation [3]. During the drying process, printed PEDOT:PSS thin film edges become pinned to the substrate, and capillary flow outward from the centre of the drop brings PEDOT:PSS to the new edge as evaporation proceeds. After evaporation, PEDOT:PSS were left highly concentrated along the original drop edge. So, the printed PEDOT:PSS film is not uniform. When the substrate was heated, the solvent started evaporating intensively as soon as the solution printed on the substrate, “coffee ring effect” decreased obviously. Therefore, Figure 3.14c performed much more uniform than Figure 3.14b. The influence of the heat treatment for sample’s optical properties was further investigated by UV-Vis spectroscopy, corresponding UV-Vis spectra shown in Figure 3.14c. The spectra show a much higher transmittance when the substrate is heated. The changes in the spectra might be due to the decreased “coffee ring effect” for the sample.

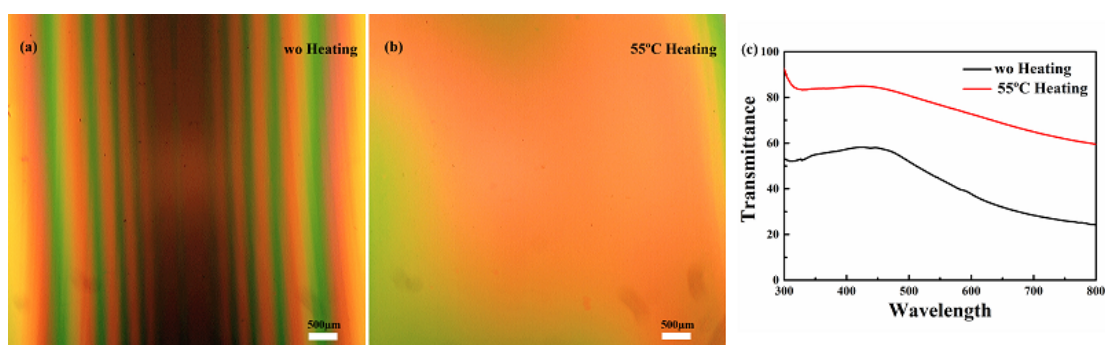


Figure 3.14: Tested morphology of the sample without a) and with b) heating treatment by optical microscope; UV-Vis transmittance spectra for the PEDOT:PSS thin film with different heating treatment c).

For a better understanding of the results gained by the optical microscope and UV-Vis spectra further investigations via scanning electron microscope (SEM) and atomic force microscopy (AFM), X-ray reflectometry and grazing incidence small/wide angle X-ray scattering (GIWAXS/GISAXS) will be tested. Furthermore, the active layer for solar cells will be printed and investigated.

[1] C. Tao, J. Jiang, M. Tao *Sol. Energ. Mat. Sol. C.* **95**, 3176-3180 (2011)

[2] C. M. Palumbiny, F. Liu, T. P. Russel, A. Hexemer, C. Wang, P. Müller-Buschbaum, *Adv. Mater.* **27**, 3391-3397 (2015)

[3] P.J. Yunker, T. Still, M. A. Lohr, A. G. Yodh, *Nature.* **476**, 308-311 (2011)

### 3.8 Spray deposition of polymer thin films for photovoltaic application

D. Chakraborty, S. Grott, P. Müller-Buschbaum

The bulk-heterojunction (BHJ) organic solar cells (OSC) have emerged as a promising alternative for conventional inorganic based solar cells over the past few years reaching power conversion efficiencies exceeding 11% [1]. OSC exhibit the potential to be light-weight, flexible and semi-transparent which makes them ideal candidates for a variety of applications. They can be processed using much simpler and low-cost techniques because the conductive polymers can be deposited out of solutions. The organic solar cell systems consisting of poly(3-hexylthiophene) (P3HT) as electron-donor and [6,6]-p-phenyl-C61 butyric acid methyl ester (PCBM) as electron-acceptor have been studied extensively in recent years [2-3]. Though the most common scientific method for the preparation of OSC in solution processed solar cells is spin coating, the possibility to process this kind of solar cells out of solution offers the chance to apply industrial upscaleable methods like roll to roll printing or spray coating. The advantage of the spray casting method is the usage of small amount of material in a diluted solution and thereby minimizes the amount of material discarded during deposition compared to spin coating. However, there are several drawbacks of this processing technique, like, bare control on the inner morphology. Furthermore, by spray casting, it is not only difficult to control the inner morphology but also difficult to achieve an overall homogeneity which results in a higher surface roughness.

The presented work focuses on achieving a homogeneous layer thickness using spray casting. P3HT:PCBM blend solutions were prepared in mass ratio of 1:1. The deposition conditions of the P3HT:PCBM film was optimized to minimize the surface roughness by controlling various spray parameters like flow rate, nozzle to substrate distance etc. The spray process was carried out with different spray shot with a certain drying time in between. Keeping the flow rate at 135  $\mu\text{L}/\text{sec}$ , using solution volumes between 100  $\mu\text{L}$  to 250  $\mu\text{L}$  of the solution blend already lead to the average layer thicknesses ranging from 200 nm to 500 nm. However, the film layer was not homogeneous. To further enhance the homogeneity, the samples were thermally annealed at 140  $^{\circ}\text{C}$  for 10 minutes. The surface roughness is observed to be decreased by thermal annealing

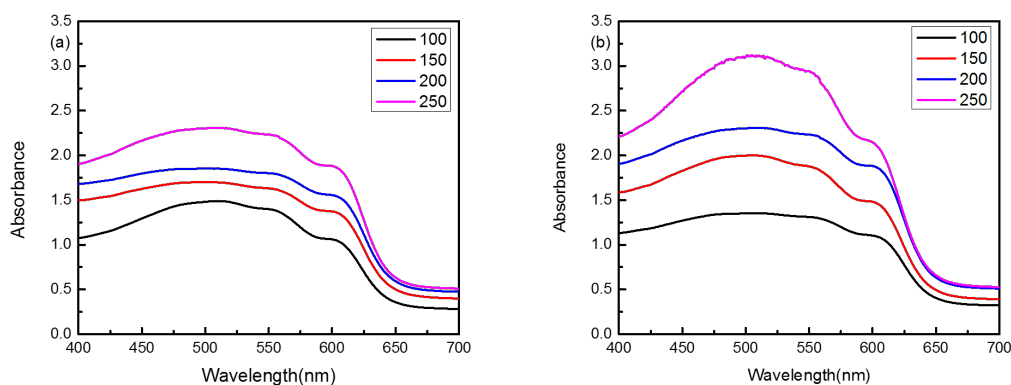


Figure 3.15: Normalized UV-vis absorption spectra for P3HT:PCBM sprayed films (a) before and (b) after thermal annealing at 140  $^{\circ}\text{C}$  for 10 minutes.

of the thin film layers. UV-vis spectroscopy measurements were performed in order to gain information about the absorption behaviour for different film thicknesses. The results are shown in Fig. 3.15. A maximum peak at about 500 nm and two shoulder peaks at about 550 nm and 600 nm are observable. The absorbance is found enhanced with increasing layer thickness for

both non-annealed and annealed samples, which was expected. Furthermore, after thermal annealing the shoulder at about 600 nm is getting more pronounced which indicates an increase in crystallinity of the samples. In addition P3HT:PCBM blends with different mass ratios were prepared and sprayed keeping the spray parameters to be constant. The average film thickness was measured to be around 400 nm. Example for the embedding of a png file

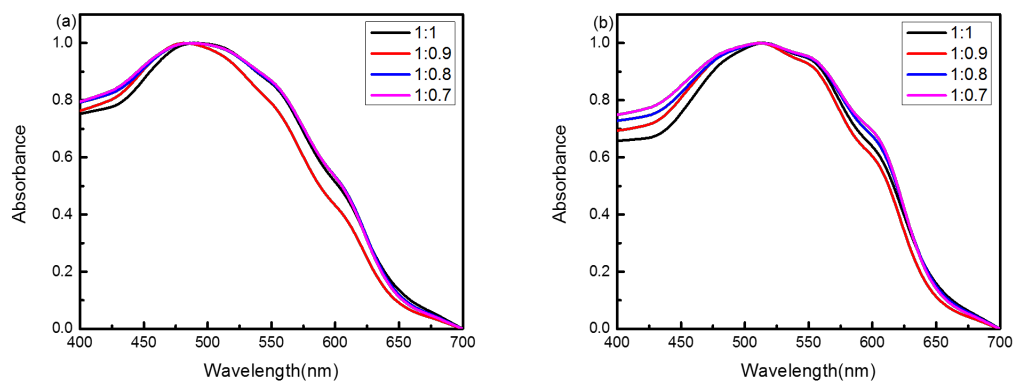


Figure 3.16:

Normalized UV-vis absorption spectra for different P3HT:PCBM mass ratios with total concentration of 10 mg/ml (a) before and (b) after thermal annealing at 140 °C for 10 minutes.

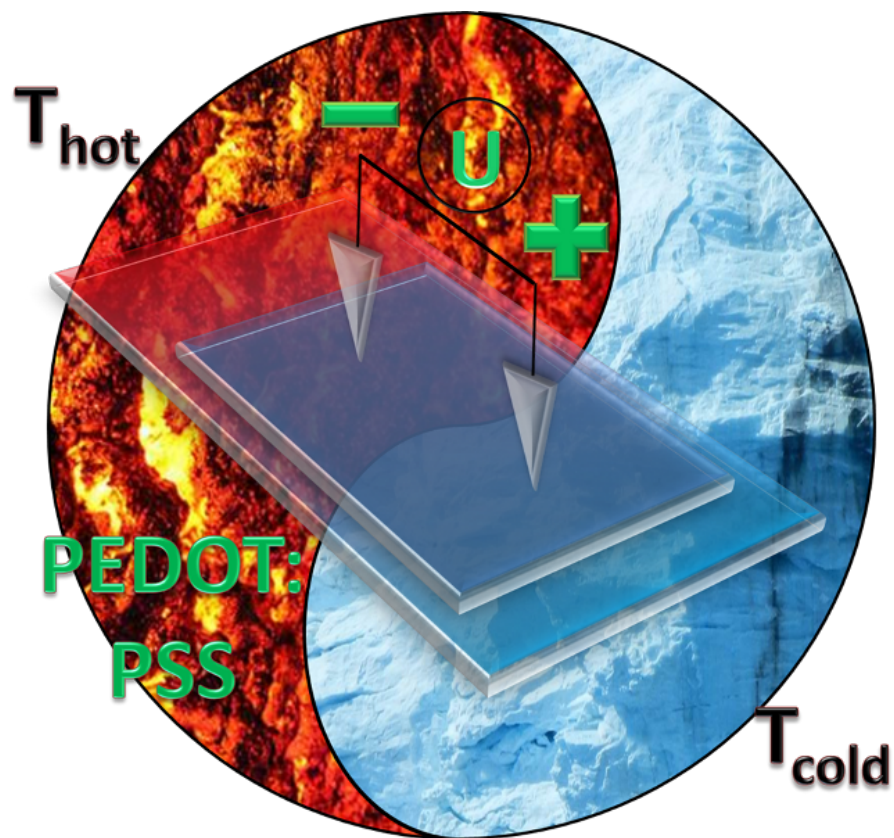
UV-vis measurements performed on films with different the P3HT:PCBM mass ratios are shown in Fig. 3.16. The main absorption peak at about 500 nm as well as two shoulders at about 550 nm and 600 nm are observable. The shoulder peak at about 600 nm is found to be more pronounced and the overall absorbance in the higher wavelength regime increased with higher content of P3HT. Furthermore, after thermal annealing the absorption in the wavelength range between 400 nm to 500 nm is intensified with increasing P3HT content.

In conclusion, the spray parameters were optimized to achieve the desired average layer thicknesses. The work is still in progress. In order to obtain information on the morphology of the thin films, further investigations are required like X-ray diffraction and advanced X-ray scattering techniques like grazing-incidence small/wide angle X-ray scattering (GISAXS/GIWAXS) which are complimentary to each other. Moreover, the photovoltaic performance will be investigated by measuring J-V characteristics in order to determine a correlation between the morphology and photoelectric characteristics of the thin films.

- [1] W. Zhao, D. Qian, M. Hernandez, S. Zhang, S. Li, O. Inganäs, F. Gao, J. Hou, *Adv. Mater.* **28**, 4734-4739 (2016).
- [2] J. Cui, A. Rodriguez-Rodriguez, M. Hernandez, M. C. Garcia-Gutierrez, A. Nogales, M. Castillejo, D. Mosegui Gonzalez, P. Müller-Buschbaum, T. A. Ezquerro, E. Rebollar, *Appl. Mater. Interfaces* **8**, 31894-31901 (2016).
- [3] D. M. González, V. Körstgens, Y. Yao, L. Song, S. V. Roth, P. Müller-Buschbaum, *Adv. Energy Mater.* **5**, 1401770 (2015).



## 4 Polymer-hybrid system



#### 4.1 Mathematical modeling of distribution of droplet size in thermal spray coating process

B. Su, H. A. Caller-Guzman

To scale-up deposition processes, the use of spray deposition is advantageous, because it is easy to be controlled and has no limitation concerning substrate geometry. In the previous study, the controllable pore size of titania film was achieved via wet spray condition. It was demonstrated that the weight fraction of titanium precursor titanium tetraisopropoxide (TTIP) mainly controlled the pore size, and the spray interval waiting time also crucial to obtain the ordered porous structure on nanoscale.[1-2] However, the size distribution of droplets through the whole thermal wet spray process is rarely reported. Fig. 4.1 shows the sketch of the spray set-up, which consists of an air brush, a heating plate and a solution container. The control parameters are the nozzle-to-sample distance, the spray angle, and the temperature of the heating stage.

The simulation model is based on the theory provided by Filipovic and coworkers, which neglects surface tension [3]. Due to the difference of the pressure inside and outside of the spray gun, the spray solution is splitting into small droplets with the carrier gas by the nozzle. Then the droplets emerge from the nozzle orifice with different sizes and velocities, which mainly depend on the nozzle type (nozzle size and geometry), spray angle, pressure of the carrier gas and the constitution of spray solution. The simulation is programmed with the parameters, such as 16 cm of nozzle-to-substrate distance, 50 °C of the heating stage, 1 bar of N<sub>2</sub> carrier gas pressure, and 10° for the spray angle with respect to the vertical direction. The total number of simulated droplet is  $9 \times 10^6$ , which is determined by total volume of sprayed solution. We assume the speed of the droplets inside the nozzle is  $v_{in} = 0$ , and the pressure outside the nozzle is  $p_{out} = 0$ .

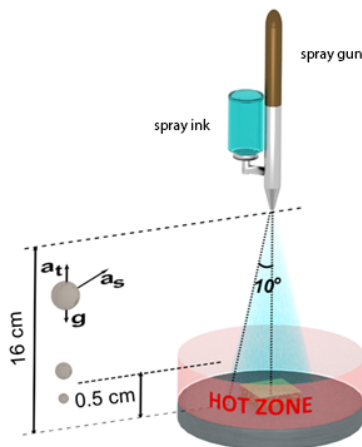


Figure 4.1:  
Schematic drawing of the simulation conditions of the spray coating process.

The initial droplet sizes are set in the range of  $r_{min} = 25 \mu\text{m}$  to  $r_{max} = 28 \mu\text{m}$ , which is typical value for the thermal spray coating. Gravity is the vertical driving force for the droplet transport towards the substrate, which is taken into account in the whole process. The aerodynamic force (Stokes force) is a retard force, which has a lift component and a component parallel to the substrate, which is caused by the friction between the droplet and the air molecules. The thermophoretic force is also taken into account, which results of the thermal gradient created by the heated substrate. We divide the regime from nozzle to sample stage into three zones, where different forces affect the simulation results. The temperature in zone I, starting from 0 cm to 5 cm with respect to the nozzle position, is 25 °C, and gravity and stoke force are inferred in this regime. The temperature changes linearly from 25 °C to 50 °C in zone II, starting from

5 cm to 15.5 cm, and gravity, Stokes force and thermophoretic force are included. Gravity and Stokes force are involved in zone III, starting from 15.5 cm to 16 cm, and the temperature is kept constant at 50 °C.

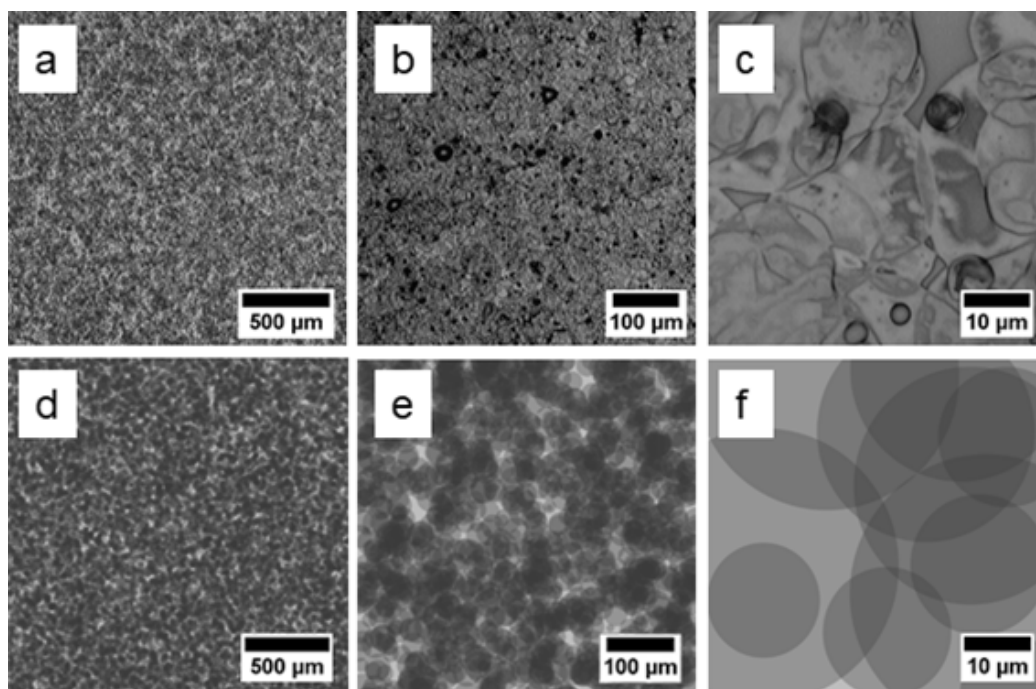


Figure 4.2:

a-c) Optical microscopy images of the films after spray coating taken with different magnifications. d-f) Simulated structures shown of same scale as explained in the text. In the simulated images some degree of transparency is used to better show the droplet overlap.

Fig. 4.2 shows the simulation results compared with optical microscopy images taken for sprayed films. Due to the superposition of individual droplets during the spray coating, a characteristic patchy film surface is observed. In images from the simulation, we set the transparency to a value of 0.3 for each droplet to show droplets overlap. Such overlap cannot be seen in low magnification optical microscopy images of the compact films, which causes deviations in the images obtained from the optical microscopy and simulation. In the simulation, the color intensity indicates the information about the height of the layered film. The darker the color, the more droplets overlap at that position. The size distribution in simulated images well matches with the observations of the optical microscopy images. Overall, the spray coated film is almost uniform over the entire surface. In Fig. 4.2 c) and f), the individual droplets become visible. However, due to neglecting surface tension in the modelling not all features from the optical images are fully covered. For example, the irregular splat shape in Fig. 4.2 c) is not present in the simulation results. It results from the Marangoni effect, which is caused by surface tension gradients.

- [1] B. Su, H. A. Caller-Guzman, V. Körstgens, Y. Rui, Y. Yao, N. Saxena, G. Santoro, S. V. Roth, P. Müller-Buschbaum, *ACS Appl. Mater. Interfaces* **9**, 43724 (2017)
- [2] B. Su, V. Körstgens, Y. Yao, D. Magerl, L. Song, E. Metwalli, S. Bernstorff, P. Müller-Buschbaum, *J. Sol-Gel Sci. Technol.* **81**, 346 (2017)
- [3] L. Filipovic, S. Selberherr, G. C. Mutinati, E. Brunet, S. Steinhauer, A. Köck, J. Teva, J. Kraft, J. Siegart, F. Schrank, *Microelectron. Eng.* **117**, 57 (2014)

## 4.2 Morphology phase diagram of printed titania films derived from block copolymer assisted sol-gel templating

N. Li, L. Song, L. Bießmann, P. Müller-Buschbaum

Nanostructured titania ( $\text{TiO}_2$ ) thin films are promising candidates for a wide range of applications, such as photocatalysis, sensors, and especially in photovoltaics.[1] For example, the crystalline anatase titania with network, as an electron-conducting layer, has attracted considerable attention in hybrid solar cells, because it has a larger surface area, accessibility of the inner surface, and suitable morphology.[2] Until now, several methods for the preparation of titania thin film, such as spin coating, solution casting, doctor blading or dip coating, are extensively used in laboratory scale.[3] While for an industrial scale, printing is a simple and low-cost technique and available in large quantities for producing films. Moreover, it is easy to control the film thickness since simple relationship can be used to describe the wet film thickness, and possible to simultaneously fabricate multilayer films with high speed. In the meanwhile, the sol-gel process combination with amphiphilic block copolymer templates is a promising route to tune the morphology of titania. Therefore, investigation on the morphology phase diagram of printed titania films based on sol-gel templating is significant for large-scale application.

In the present work, titanium tetra isopropoxide (TTIP) is used as precursor and diblock copolymer polystyrene-block-polyethylene oxide (PS-*b*-PEO) as the structure-directing template. The amphiphilic block copolymer PS-*b*-PEO undergoes phase separation and self-assembly due to a good-bad pair solvent, namely 1,4-dioxane and hydrochloric acid (HCl). By adjusting the weight fraction of 1,4-dioxane, HCl and TTIP, while keeping the copolymer concentration at 16.5 mg/mL, the titania films with different morphologies, containing foam-like structure, nanowire aggregates, collapsed vesicles and nanogranules, are obtained after solvent evaporation and calcination at 500 °C. The surface morphology is probed via scanning electron microscopy (SEM) and optical microscopy (OM), and the inner morphology is detected by grazing incidence small-angle X-ray scattering (GISAXS).

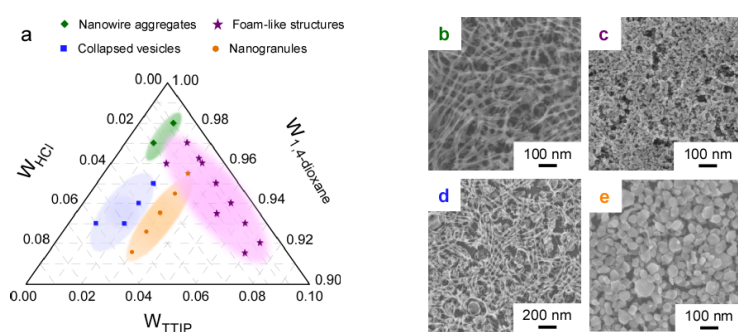


Figure 4.3:

(a) Phase diagram of printed  $\text{TiO}_2$  after calcination with varying weight fraction of 1,4-dioxane, HCl and TTIP ( $W$  represents the weight fraction). SEM images of different  $\text{TiO}_2$  morphologies after calcinating the printed films (b) nanowire aggregates, (c) foam-like structures, (d) collapsed vesicles and (e) nanogranules.

Fig. 4.3a shows the ternary phase diagram of  $\text{TiO}_2$  nanostructure morphologies within the probed composition, which is mainly divided into four regions, nanowire aggregates, foam-like structures, collapsed vesicles and nanogranules, respectively. With a very low weight fraction of TTIP (1 wt%) and HCl, the nanowire aggregates are observed (Fig. 4.3b). We assume that the cylinder micelles are formed in the solution according to the results reported by Eisenberg.[4] Meanwhile, it implies that the copolymer does act as a template to control the morphologies

of final TiO<sub>2</sub> films. When using a moderate amount of HCl (2 wt% and below), a foam-like structure is obtained (Fig. 4.3c) With higher weight fraction of TTIP and comparable amount of HCl, the cylinder micelles change into spherical shape, which implying that besides HCl, the TTIP component in the solution is also of special importance on the morphologies of micelles. Because TTIP incorporated into PEO domains through coordination bonds undergoes the hydrolysis and condensation reaction, which results in forming Ti-O covalent bonds on the surface of adjacent PEO domains. In addition, the hydrolysis and condensation reaction of TTIP will produce 2-propanol, which is also a bad solvent for the PS block, then further makes the solvent system more poor for the hydrophobic PS domains. With further increasing HCl weight fraction, the nanowire structures will gradually transform into vesicles (Fig. 4.3d). As the solvent becomes more and more poor for the PS block with continuously adding the amount of HCl, it leads to a rising surface energy between PS block and the solvent. In order to decrease the surface area, and thus minimize the surface energy, vesicle-like structures are formed. If HCl is roughly more than 2 wt% and the amount of TTIP is increased, thickening the shell of the vesicles, the granular morphology occurs as shown in Fig. 4.3e. Considering the application in hybrid solar cells, a high surface area in titania films combined with network structure is desirable because it can improve the light absorption and inhibit electron-hole recombination. Comparing with other morphologies, the foam-like structure is promising to produce higher photovoltaic performance. Thus, the foam-like area is detailed probed for fine adjusting the weight fraction of the component.

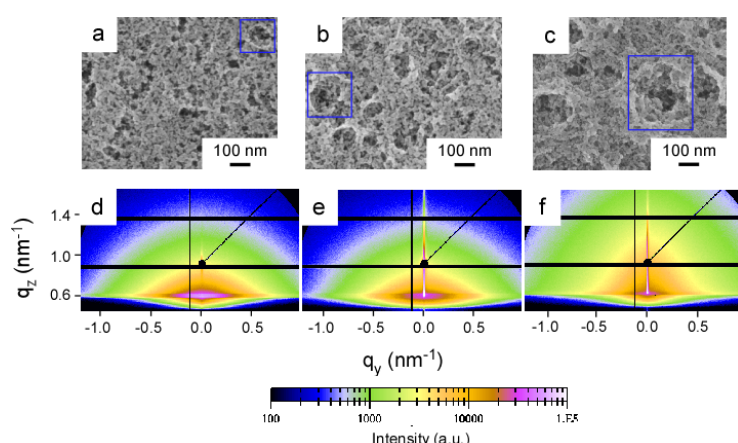


Figure 4.4: SEM images and 2D GISAXS data of printed TiO<sub>2</sub> films with different weight fraction of 1,4-dioxane, HCl and TTIP, (a, d) 0.96: 0.0075: 0.0325, (b, e) 0.94: 0.0075: 0.0525, and (c, f) 0.92: 0.0075: 0.0725.

when the weight fraction of HCl is fixed at 0.75 wt% and TTIP is increased from 3.25 wt% to 7.25 wt%, the foam-like morphologies are obtained as shown in Fig. 4.4a, b and c. when keeping HCl unchanged, with a higher Weight fraction of TTIP, the foam-like structures should show more dense since more TTIP will undergo hydrolysis and condensation. Therefore, GISAXS measurements are performed to further investigate the morphology in the bulk of films, as shown in Fig. 4.4d, e and f. The average pore size and the distance between two neighboring pores can be calculated by the cut of the 2D GISAXS data fitted with corresponding modeling.

- [1] P. Kohn, S. Pathak, M. Stefik, C. Ducati, U. Wiesner, U. Steiner, S. Guldin, *Nanoscale* **5**, 10518 (2013).
- [2] D. Fattakhova-Rohlfing, M. Wark, T. Brezesinski, B. M. Smarsly, J. Rathouský, *Adv. Funct. Mater.* **17**, 123 (2007).
- [3] C. M. Palumbiny, F. Liu, T. P. Russell, A. Hexemer, C. Wang, P. Müller-Buschbaum, *Adv. Mater.* **27**, 3391 (2015).
- [4] Y. Yu, A. Eisenberg, *J. Am. Chem. Soc.* **119**, 8383 (1997).

### 4.3 Morphology-function relationship in thermoelectric nanocomposites from PEDOT:PSS with inorganic silicon nanoparticles

N. Saxena, M. Coric<sup>1</sup>, A. Greppmair<sup>2</sup>, J. Wernecke<sup>3</sup>, M. Pflüger<sup>3</sup>, M. Krumrey<sup>3</sup>, M. S. Brandt<sup>2</sup>, E. M. Herzig<sup>1</sup>, P. Müller-Buschbaum

<sup>1</sup> MSE, Garching, Germany

<sup>2</sup> WSI, Garching, Germany

<sup>3</sup> PTB, Berlin, Germany

Even though ventures into methods for energy generation from renewable sources like hydropower to solar and wind energy are promising, independence from fossil fuels has still not been achieved. Therefore, it is reasonable to think of further ways of harvesting other types of renewable energy sources, one of which is energy in the form of waste heat.

Waste heat occurs in all processes found in daily life, such as in the human body, car engines, power plants, etc. This heat is usually emitted into the environment and is thus rendered useless for all intents and purposes. Since a large amount of energy is lost in this fashion, one can think about methods which allow for making it usable again. A concept this can be based off is thermoelectricity, which allows for the transformation of a temperature gradient along a thermoelectric material into electrical power.

The Seebeck effect describes the flow of charge carriers in a material along a temperature gradient due to diffusion. This leads to an accumulation of charges at the cold end and to a deficiency of charges at the hot end, ultimately resulting in an electrical potential. This potential in turn forces part of the charges in the direction opposite to the temperature gradient due to drift. The resulting effective potential is commonly termed thermovoltage, since its magnitude depends on the magnitude of the temperature gradient. Other quantities that determine the efficiency of a thermoelectric material are on the one hand the electrical conductivity, which describes the ability of charges to travel through the material, and the thermal conductivity which describes the ease of maintaining a temperature gradient. Only if a temperature gradient is present, electrical power can be harvested.

Common thermoelectric materials mostly comprise heavy elements such as bismuth, tellurium, lead, etc. While these compounds often show promising thermoelectric conversion efficiencies, the often found toxicity, rarity, high cost and difficulty in processing of these elements has impeded a large-scale implementation of thermoelectric devices for energy generation in daily life. In an alternative approach, we wish to make use of conducting polymers as promising candidates for thermoelectric materials. Some of the advantages include the environmentally friendly materials, which are mostly carbon-based, and due to the dispersability in solvents, also the possibility for economic and easy large-scale processing through methods such as printing or spray-coating. Among the many different conductive polymers, PEDOT:PSS (poly(ethylene dioxythiophene):poly(styrene sulfonate)) has attracted great attention in the research community to its promising properties regarding optical semi-transparency, environmental aspects, since water can be used as a solvent and potentially high electrical conductivity. Especially the high electrical conductivity, which approaches that of inorganic semiconductors, renders this material interesting for thermoelectric application.

In this work, we use PEDOT:PSS in combination with inorganic single-crystalline silicon nanoparticles, in order to increase the thermoelectric efficiency of the composite film through a nanostructuring approach.[1] Through the introduction of scattering centers for phonons, a change in the thermal conductivity is expected, similarly to how grain boundaries, heteroatoms, etc. reduce thermal conductivity in inorganic thermoelectrics.

The measurement of the thermal conductivity is carried out using steady-state infrared thermography.[2] For this purpose, free-standing composite films adapted from a procedure published by Greco *et al.* were prepared.[3] These were suspended on steel substrates with small

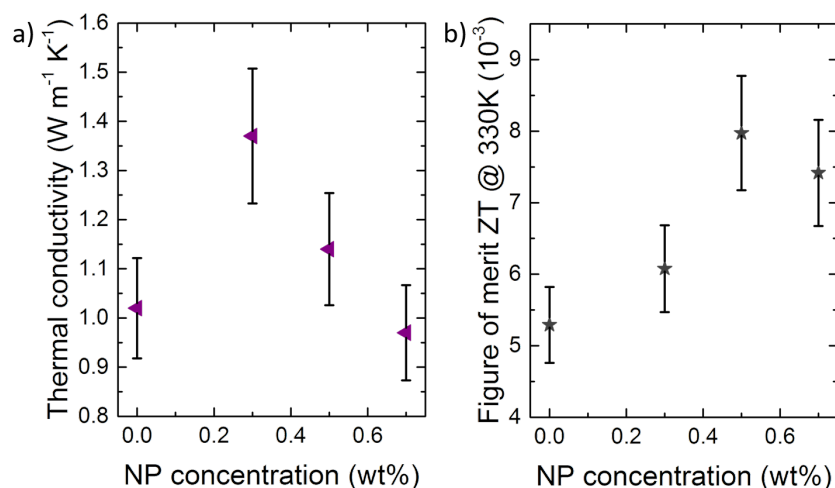


Figure 4.5:

(a) Thermal conductivity and (b) thermoelectric figure of merit ZT as function of silicon nanoparticle concentration in PEDOT:PSS/nanoparticle composite films.

cavities, on top of which the film does not rest on a substrate and is actually free-standing. Thus it can be thermally excited using a visible light LED, while the thermal excitation of the film is probed from the top using an infrared camera. After plugging in the optical properties and thickness of the film, the thermal conductivity can be calculated. Figure 4.5 shows the influence of the introduction of silicon nanoparticles into the polymer film. After an increase in the thermal conductivity is observed for small concentrations, the former drops for higher concentrations of silicon nanoparticles. Combining the thermal conductivity with the thermoelectric power factor, which shows a maximum for nanoparticle concentrations of 0.5 wt%, it is also possible to calculate the figure of merit, which also shows a maximum of 0.008 at concentrations of 0.5 wt%.

The changes in thermal conductivity can be understood through the use of grazing incidence resonant tender x-ray scattering (GIR-TeXS). Since x-ray scattering experiments were carried out in the vicinity of the sulfur K-edge and two of three components in the system, namely PEDOT and PSS contain sulfur, it is possible to determine in which of the other two components the nanoparticles are preferentially embedded. Through careful analysis of the intensity evolution of the different structural contributions to the scattering as function of x-ray energy, the nanoparticles are found to be preferentially embedded inside the hydrophobic PEDOT-rich domains. Due to the single-crystalline nature of the nanoparticles, for low concentrations an increase in the thermal conductivity is found, while for higher concentrations the internal structure of the PEDOT-rich domains increasingly breaks up, ultimately leading to a drop in the thermal conductivity. In conclusion, the thermal conductivity was successfully tuned through the introduction of silicon nanoparticles.

- [1] N. Saxena, M. Coric, A. Greppmair, J. Wernecke, M. Pflüger, M. Krumrey, M. S. Brandt, E. M. Herzig, P. Müller-Buschbaum, *Adv. Electron. Mat.*, 1700181 (2017)
- [2] A. Greppmair, B. Stoib, N. Saxena, C. Gerstberger, P. Müller-Buschbaum, M. Stutzmann, M. S. Brandt, *Rev. Sci. Instr.* **88**, 44903 (2017)
- [3] F. Greco, A. Zucca, S. Taccola, A. Menciassi, T. Fujie, H. Haniuda, S. Takeoka, P. Dario, V. Mattoli *Soft Matter* **7**, 10642 (2011)

#### 4.4 Conductive dry adhesives for detecting biosignals

A. Zheng, V. Körstgens, H.-Y. Chiang<sup>1</sup>, P. Müller-Buschbaum

<sup>1</sup> Rythm, Paris, France

In medical applications wet electrodes are commonly used to obtain biosignals. Biosignals are electric potentials, which result from biological activity such as from the human brain. These signals can be used to monitor the activity of the brain and also to detect diseases. The use of wet electrodes however, has some drawbacks though, as they can cause skin irritation and the signal quality decreases as the gel of the electrode dehydrates. Hence, wet electrodes are not suitable for long-time measurements. These drawbacks are overcome by dry adhesives, as they do not rely on wet components for adhesion, but on a microstructured surface. Additionally to the adhesion to the skin, electrical conductivity has to be ensured in order to obtain biosignals. One way to achieve this is to employ a metal contact like wet electrodes do and embed it within a dry adhesive pad. However, this greatly limits the stretchability of the total device [1]. In an alternative approach conductive fillers are added into the polymer matrix, making it a conductive dry adhesive, which fulfills both purposes, the adhesion, as well as the electrical conductivity.

The polymer polydimethylsiloxane (PDMS), which is made of two components, namely its base and a curing agent, is used as the matrix for the conductive dry adhesive. Due to its nonconductive property, different carbon nanofillers are added into the polymer matrix to provide an electrical percolation path for the signal. Since the base of PDMS is a very viscous liquid, the distribution of filler material into the matrix is difficult. One possibility is using organic solvents to lower the viscosity of the solution. First the carbon nanofiller and the PDMS are suspended in the organic solvent by ultrasonication separately. After mixing both parts the organic solvent is evaporated overnight. In the final step, the curing agent is added and conductive PDMS samples of 2 cm x 2 cm are obtained after curing inside a mold at 80 °C in a furnace. The conductivity of these patches is then measured using a 4-point probe setup. Different carbon based fillers can be utilized, e.g. with multi-walled carbon nanotubes at 9.5 wt%, resistances as low as  $298 \frac{\Omega}{\text{sq}}$  can be achieved. Since PDMS has a very low surface energy, its adhesion towards various other surfaces is limited. To overcome this problem, the concept of contact splitting is applied by adding a microstructure to the surface of PDMS. Basically, the van der Waals forces between two surfaces are higher for several micro-sized pillars than for a flat large contact [2]. This idea of using microstructures for adhesion is bioinspired by many adhesive structures in nature, most prominent geckos, who excel with their ability to climb steep walls. Their ability to exert strong adhesion to different surfaces, while easy to release on demand is a desired feature for dry adhesives in order to adhere on rough surfaces as human skin. To achieve a microstructured surface for PDMS, the liquid PDMS is filled into a prepatterned mold with a regular hole pattern. The density of holes on the pattern vary from  $6.4 \cdot 10^5$  to  $1.4 \cdot 10^6$  holes per  $\text{cm}^2$ , with radii of the pillars of 1.5 - 2.5  $\mu\text{m}$ . The depth of the holes is about 10  $\mu\text{m}$ . After curing the PDMS in a furnace at 80 °C, the PDMS is demoulded and a regular pillar pattern is obtained.



Figure 4.6:

Fabrication process to obtain mushroom tips. a) Inking of PDMS pillars into liquid PDMS film b) Printing PDMS pillars with uncured PDMS drops onto anti-adhesive foil c) Desired mushroom tip structure

In order to further increase the adhesion force, the desired structure for the PDMS surface would be not consisting of simple pillars, but pillars with a mushroom tip with diameters of about  $5\ \mu\text{m}$ . The fabrication process for this is shown in Fig. 4.6. First liquid PDMS is blade coated onto a glass substrate in order to obtain a thin film of liquid PDMS (see also Fig. 4.6a). After that the previously prepared PDMS with pillar structure is inked into the thin film of PDMS, which places a small drop of uncured PDMS on top of the pillars (Fig. 4.6b). After attaching the inked pillars onto an anti-adhesive foil, the PDMS is cured again at  $80\ ^\circ\text{C}$  resulting in the desired pillar structure with mushroom tips, which is shown in Fig. 4.6c [3].

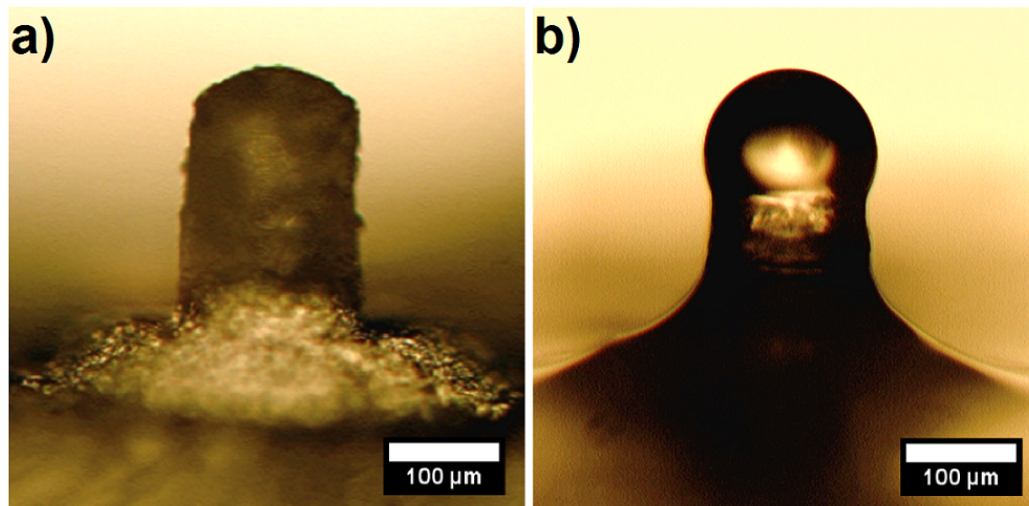


Figure 4.7:  
Optical microscopy images of a single pillar. a) Untreated pillar b) Pillar treated with ink+print method

Fig. 4.7 compares two pillars of a preliminary test with pillar diameters of  $100\ \mu\text{m}$ , one before the inking and printing treatment and one after the process. In Fig. 4.7 with optical microscopy it is focused on one single pillar as part of a large 2D pattern of pillars. It shows that the drop of uncured PDMS was successfully placed on top of the pillar. The example in Fig. 4.7b shows the cured drop-like shape on top of the pillar. In order to obtain flattened mushroom-shaped tips, the process parameters such as force applied during the inking and also during the printing process still have to be refined. Furthermore the homogeneity of the applied force over the backing layer of the PDMS structure is of high importance for achieving a consistent quality of the tips of the pillars over the whole area of 2D pattern.

Overall, both, the electrical conductivity, as well as the microstructure for skin adhesion still have to be tweaked in the future. For the electrical conductivity, other filler materials have been proposed to deliver good results, especially when combining fillers of different dimensions, e.g. graphene sheets or silver nanowires. The adhesion force depends strongly on the aspect ratio of the pillars, which is the length of a pillar divided by its diameter [1]. Further studies have to be carried out to optimize the aspect ratio. The final goal is to combine both features optimized to achieve a conductive dry adhesive with comparable properties to wet electrodes in terms of signal quality and skin adhesion.

[1] T. Kim, J. Park, J. Sohn, D. Cho, S. Jeon, *ACS Nano* **10**, 4770-4778 (2016)

[2] M. Kamperman, E. Kroner, A. d. Campo, R. M. McMeeking, E. Arzt, *Adv. Engin. Mater.* **12**, 335-348 (2010)

[3] L.-F. Wang, J.-Q. Liu, B. Yang, X. Chen, C.-S. Yang, *Microsyst. Technol.* **21**, 1093 (2015)

#### 4.5 Influence of inorganic nanoparticles on the morphology of polymer blends for photovoltaic applications

S. Grott, C. Ott<sup>1</sup>, M. Schwartzkopf<sup>2</sup>, N. Hohn, S. Xia, K. Wang, S. V. Roth<sup>2</sup>, T. Nilges<sup>1</sup>  
P. Müller-Buschbaum

<sup>1</sup> Chemie-Department, TU München, Garching, Germany

<sup>2</sup> DESY, Hamburg, Germany

Bulk heterojunction (BHJ) organic solar cells (OSC) have received high attention in the last years due to their outstanding properties. These polymer based solar cells can be produced out of abundant and low cost materials and exhibit the advantages of being light-weight, semi-transparent and tuneable. So they offer a vast versatility for applications. Furthermore the devices can be processed via spray casting or printing which are scalable and low-cost techniques. This led to an increase in the research activities on OSC and their precursors.

Recently it has been shown, that the incorporation of inorganic magnetite nanoparticles into the active layer of an OSC can improve the overall power conversion efficiency (PCE) up to 11 %.[1] In the presented work, we focus on doping the organic photo-active layer with inorganic nanoparticles. In this case we use SnIP nanocrystals (scanning electron microscopy (SEM) images are shown in Fig. 4.8), synthesized by the group of Prof. Nilges of the Chemistry Department of the TU Munich.[2] These nanoparticles show semi-conducting properties and are promising candidates to improve the PCE of organic photovoltaic devices. Therefore we dope the well studied system of poly(3-hexylthiophen-2,5-diyl) (P3HT) blended with phenyl-C61-butyric acid methyl ester (PCBM) with different concentrations of SnIP nanoparticles. These compounds are dissolved and spin coated on a substrate to produce the active layer as a thin film.

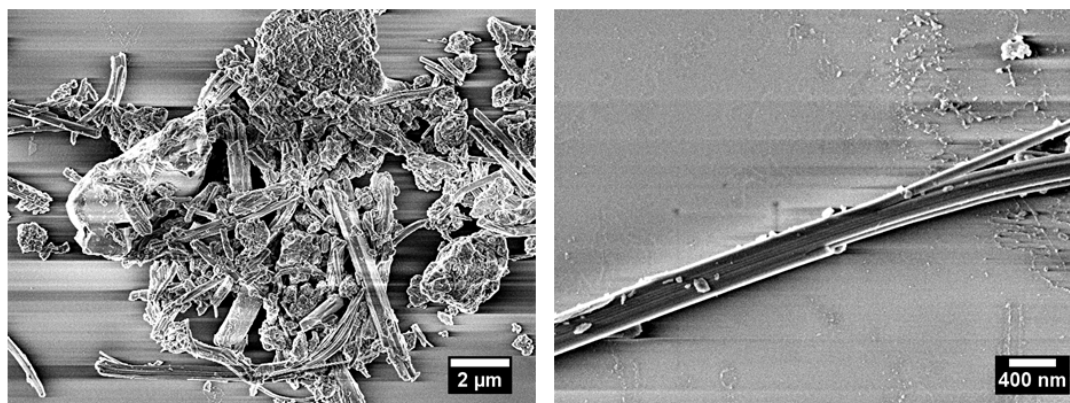


Figure 4.8: SEM images of spin coated pure SnIP nanoparticles.

It is well known, that the inner morphology of the active layer applied in OSC is a key to a high PCE. Since the generated exciton, generated by the absorption of photons, has to reach an interface between the donor and acceptor within the active layer. Hence we are investigating the influence of different inorganic SnIP nanoparticle concentrations on the morphology using the P03 beamline at DESY Hamburg to conduct grazing incidence wide angle X-ray scattering (GIWAXS) experiments and gain insight into the morphology of the prepared P3HT:PCBM:SnIP thin films. The obtained 2D GIWAXS detector images are shown in Fig. 4.9.

From the detector image real space distances for the (100) crystal plane can be calculated. In Fig.

4.9 a) the (100) as well as the higher order reflexes are marked. The obtained lattice values are plotted in Fig. 4.9 c) showing that with increasing nanoparticle concentration the lattice parameter slightly changes. Furthermore the increase in intensity indicates an increase in crystallinity. Also information about the orientation the the P3HT within the active layer can be obtained from the detector image (shwon in Fig. 4.9 b) ). Thereby it is of major interest whether the orientation of the P3HT changes with higher nanocrystal concentrations. The plot of the azimuthal cut shown in Fig 4.9 d), indicates no change in the orientation of P3HT. Since the detailed data analysis of the obtained data is still ongoing

Furthermore the influence of the nanoparticles on further parameters has to be studied and will then be correlated to the photo-electronic properties of the organic solar cell devices. Therefore UV-Vis spectra, I-V characterization and other techniques are applied to gain further knowledge about the influence and the contribution of SnIP semi-conducting nanocrystals on the characteristics of photovoltaic devices.

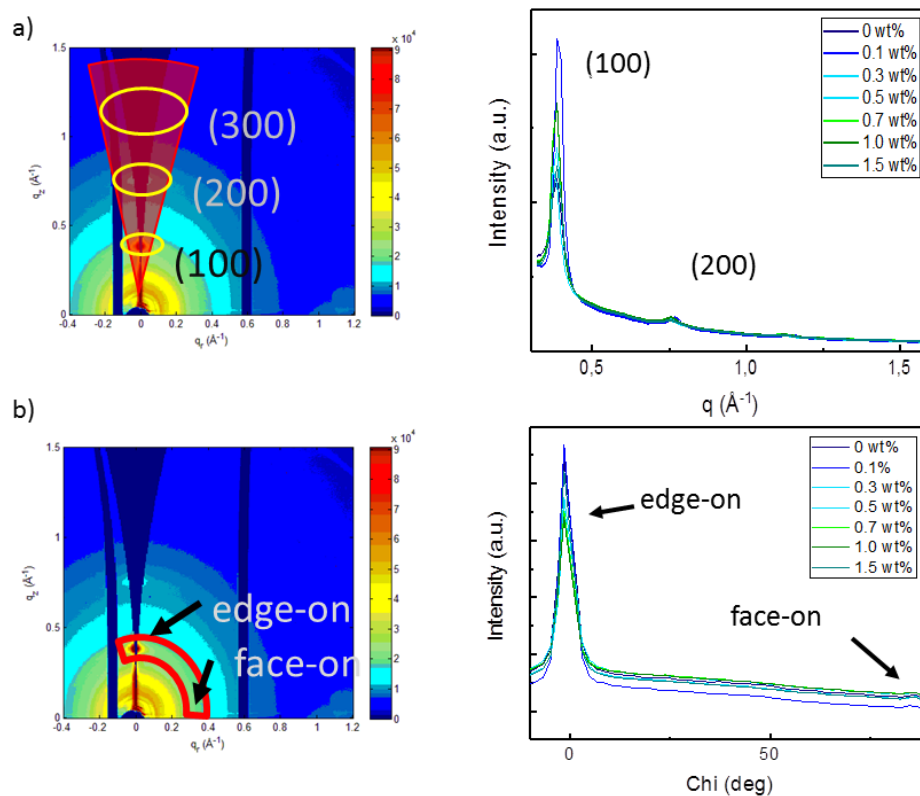


Figure 4.9:

Example of 2D GIWAXS data of P3HT:PCBM organic thin films doped with SnIP nanoparticles. a) detector image with marked sector integration, b) plot of the different c) azimuthal integration.

- [1] D. Moseguí González, V. Körstgens, Y. Yao, L. Song, G. Santoro, S. V. Roth, P. Müller-Buschbaum, *Adv. Energy Mater.* **5**, 1401770 (2015)
- [2] D. Pfister, K. Schäfer, C. Claudia, B. Gerke, R. Pöttgen, O. Janka, M. Baumgartner, A. Efimova, A. Hohmann, P. Schmidt, S. Venkatachalam, L. van Wüllen, U. Schürmann, L. Kienle, V. Duppel, E. Parzinger, B. Miller, J. Becker, A. Holleitner, R. Wehrich, T. Nilges, *Adv. Mater.* **28**, 9783-9791 (2016)

#### 4.6 Printed diblock copolymer films embedded with magnetic nanoparticles

S. Xia, L. Song, V. Körstgens, M. Opel<sup>1</sup>, M. Schwartzkopf<sup>2</sup>, S. V. Roth<sup>2</sup>, P. Müller-Buschbaum

<sup>1</sup> WML, Garching, Germany

<sup>2</sup> DESY, Hamburg, Germany

For magnetic-sensor applications, the alignment of magnetic nanoparticles (NPs) is essentially required. Several approaches have been explored to arrange magnetic NPs via an external magnetic field. [1] Our previous investigation also proved that aligned wires composed of magnetic NPs can be achieved by applying external magnetic field during solution casting. [2] And the results show that the fabricated wire-containing hybrid films have strong magnetic anisotropy. All the studies above provide a set of magnetic NP alignment and orientation in polymer films within external magnetic field, however, they are not suitable for continuous manufacturing process, like roll-to-roll casting and printing, which are beneficial to large scale production. In this regard, the present study provides an easy, straightforward, and reproducible method for fabricating well-ordered NP aggregates orienting perpendicularly in polymer matrix without application of any external field. We employed the asymmetric DBC polystyrene-block-polyN-isopropylacrylamide (PS-*b*-PNIPAM), which can form PS cylinders standing vertically inside PNIPAM matrix. Upon solvent vapor annealing, the cylindrical nanostructures can achieve a very high order. For the application purpose, commercialized magnetic NPs, iron oxide coated with oleic acid organic chains, are employed. After incorporation of NPs into polymer matrix, the NPs can be preferentially located and aggregate inside PS cylinders due to their hydrophobic organic coatings.

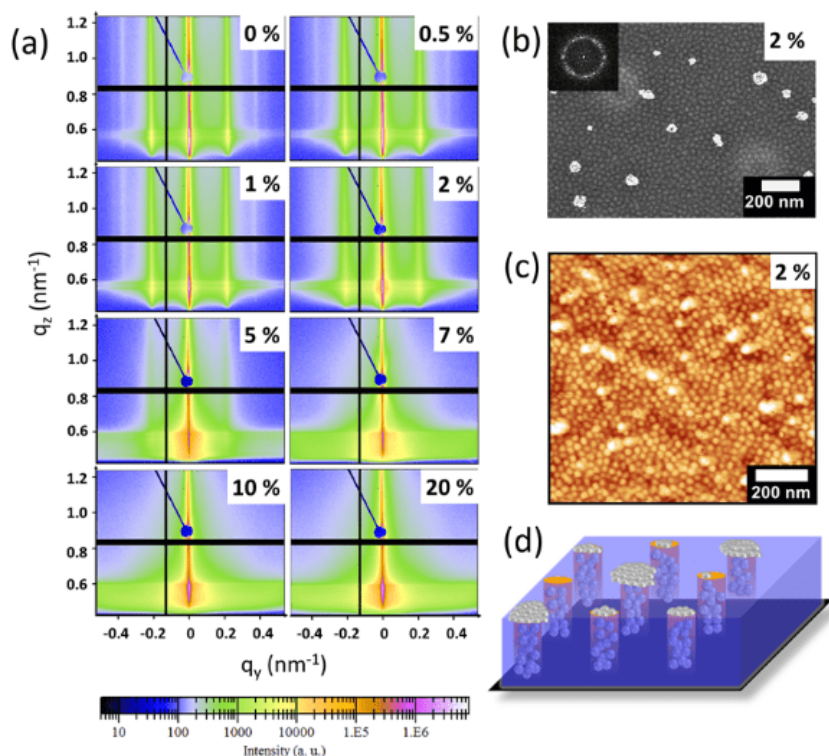


Figure 4.10:

(a) 2D GISAXS patterns of hybrid films with different NP concentrations. (b) SEM image of the sample with 2 wt % of NPs. The Fast Fourier Transform image is shown on the top left. (c) AFM image of the sample with 2 wt % of NPs. (d) A simplified sketch of nanostructured films containing 2 wt % of NPs.

Surface nanostructures were characterized via atomic force microscopy (AFM) and scanning electron microscopy (SEM). Fig. 4.10 (b) and (c) show that vertical cylindrical morphology is obtained for NP-free sample after solvent annealing post-treatment. After doping small amount

of NPs, NPs disperse individually inside PS domains. Further NPs incorporation leads to the formation of NP aggregates with increasing size. At high NP loading, the initial aggregates develop into large net-work structures covering the film surface. In order to probe the internal nanostructure of printed films, grazing incidence small angle X-ray scattering (GISAXS) was employed for characterization. Scattering data (see Fig. 4.10 (a) ) further prove the cylindrical morphology and indicate that adding small amount of NPs has no negative influence on the polymer morphology. The structure can still maintain a very high order even at 2 wt % of NP concentration (Fig. 4.10 (d)). Higher loading of NPs into the system results in a perturbed structure.

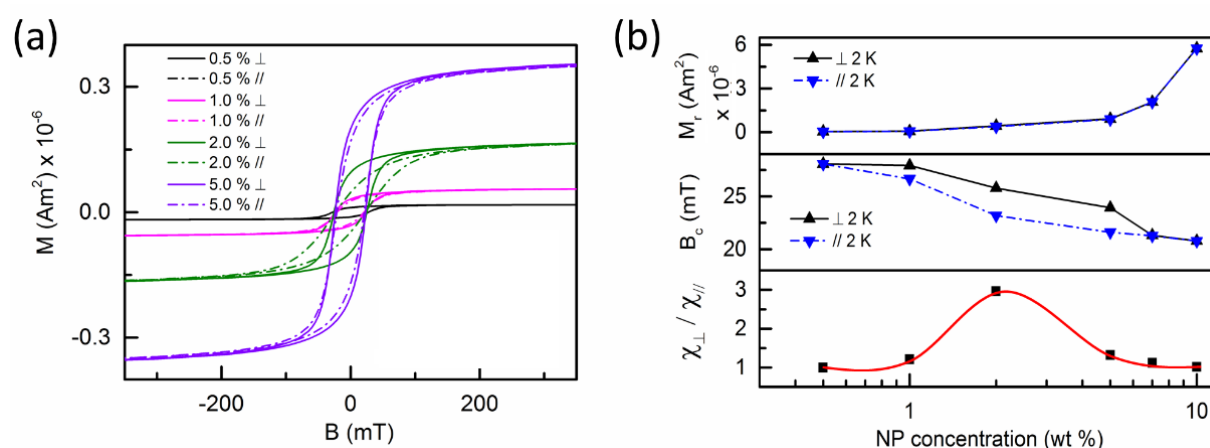


Figure 4.11:

(a) Magnetization curves of selected sample with different NP concentrations measured in two orientations. (b) Comparison of the remanence, coercivity and saturation magnetization as a function of NP concentration measured at 2 K in both orientations. The magnetic susceptibility in both parallel ( $\chi_{\parallel}$ ) and perpendicular ( $\chi_{\perp}$ ) orientation were obtained from a linear fit at zero remanence area. The susceptibility ratio  $\chi_{\parallel} / \chi_{\perp}$  was calculated and plotted as a function of NP concentrations. The red line serves as a guide to the eye.

Magnetic measurements were collected using a superconducting quantum interface device (SQUID). Results prove that all NP-polymer hybrid films follow a superparamagnetic behavior. To further probe the magnetic anisotropy, all hybrid films were measured in two directions with magnetic field parallel and vertical to the films surface. Fig. 4.11 shows that magnetic anisotropy exists only at certain NP concentrations, and the strength of magnetic anisotropy differs at different NP concentrations. Through the comparison of susceptibility, the strongest anisotropy is observed at 2 wt % of NPs. Such behavior can be explained by the nanostructure of polymer. GISAXS data reveal that the perpendicularly standing PS nanocylinders are saturated with NPs at 2 wt %, and still stay in a very high order. Due to the preferential localization of NPs inside PS domains, NP aggregates can follow the orientation of PS cylinders. Accordingly, vertically aligning NP aggregates with high order are achieved at 2 wt %, leading to the strong magnetic anisotropy.

- [1] T. Kimura, H. Ago, M. Tobita, S. Ohshima, M. Kyotani, M. Yumura, B. *Adv. Mater.* **14**,1380-1383 (2002)
- [2] Y. Yao, E. Metwalli, M A. Niedermeier, M. Opel, C. Lin, J. Ning, J. Perlich, S V. Roth, P. Müller-Buschbaum, *ACS Appl.Mater.Interfaces.* **6**, 5244-5254 (2014)

#### 4.7 Nanostructured TiO<sub>2</sub> lithium-Ion battery anode templated by electron conductive amphiphilic block copolymer

S. Yin, L. Song, S. Xia, P. Müller-Buschbaum

Nanostructured TiO<sub>2</sub> thin films have been widely studied as Lithium ion battery anode during the past decades due to its stability on electrochemical performance and flexibility on structural regulation. In addition to the crystallinity, the morphology of the TiO<sub>2</sub> plays a crucial role for its practical application as well. Preparing porous structure was expected to be effective to improve the charge and discharge performance of the TiO<sub>2</sub> during the cycling. Since the existence of the pores can not only buffer the volume expansion of the TiO<sub>2</sub> matrix but also facilitate the penetration of the electrolyte.

TiO<sub>2</sub> thin films were fabricated by spin coating with PS<sub>20500</sub>-b-PEO<sub>8000</sub> as structure directing agent. The preparation of the stock solution for spin coating can be described as follows: Firstly, 35.66mg PS<sub>20500</sub>-b-PEO<sub>8000</sub> was fully dissolved in to 1.72ml 1,4-dioxane under magnetic stirring. 0.012ml Concentrated HCl and 0.018ml TTIP was diluted in to the same volume by 0.5ml 1,4-dioxane, respectively. Secondly, the diluted HCl and TTIP were slowly added in to PS<sub>20500</sub>-b-PEO<sub>8000</sub> solution under constant stirring. Thirdly, as prepared HCl and TTIP was slowly added in to PS<sub>20500</sub>-b-PEO<sub>8000</sub> accompanied by 1h stirring. After that, the stock solution was spin coated on the substrate to obtain TiO<sub>2</sub> thin film. The polymer template in the spin coated thin film can be totally removed during the calcination process in air atmosphere. During the preparation process of stock solution, TTIP was the precursor of TiO<sub>2</sub>, 1,4-dioxane was a good solvent for PS and PEO block, and HCl was the poor solvent for PS and catalyst for hydrolysis process. The density of PS<sub>20500</sub>-b-PEO<sub>8000</sub> in the stock solution is 16.09mg/ml, and the volume ratio of 1,4-dioxane : TTIP : HCl in the stock solution is 0.92 : 0.075 : 0.005, respectively.

The morphology of the calcined TiO<sub>2</sub> Thin film was characterized by scanning electron microscopy (SEM). Figure 4.12 show the SEM images with different magnification. The low magnification SEM image indicates very homogeneous distribution of the TiO<sub>2</sub> at the micron level (Figure 4.12a). With the increase of the magnification, the foam like structure composed of mutually linked nanoparticles can be observed (Figure 4.12b and c). The formation mechanism of the form like structure proposed in YJ Cheng's work can be summarized as follows: Because of the low content of HCl, large amount small microphase-separated structures can be formed in the solution. As the precursor of TiO<sub>2</sub>, TTIP are always confined into the hydrophilic PEO domains through the Ti-O coordination bond, which makes the chemical reactivity of the PEO domains greatly increased. Further hydrolysis and condensation between different PEO domains will occur when they collide together. This process is highly frequent since the presence of large amount of small structures in the solution. As a result, a lot of random structures composed of mutually linked nanoparticles formed, resulting in the formation of foamlike structure after calcination [1]. The formation process of the foam like structure is illustrated in Figure 4.12d.

Compared with YJ Cheng's work, the foam like structure in Figure 4.12b and c exhibit a slightly sintered pattern, which can be assigned to collective effect of the higher calcination temperature and the different thickness of the TiO<sub>2</sub> thin film. Specifically, the structure reorganization of the TiO<sub>2</sub> thin film occurs when the calcination temperature reach at 500°C. In addition, Figure 4.12b and c show obviously stacked structure, and the DektakXT stylus profiler show an average thickness of 83.3nm±7.2nm of the TiO<sub>2</sub> film, which is thicker than the almost single layered structure in YJ Cheng's work. This phenomenon may result from the different molecular weight of the polymer source. For the thicker TiO<sub>2</sub> film, the structures further away from the substrate surface would suffer reorganization due to anisotropic stresses during calcination.

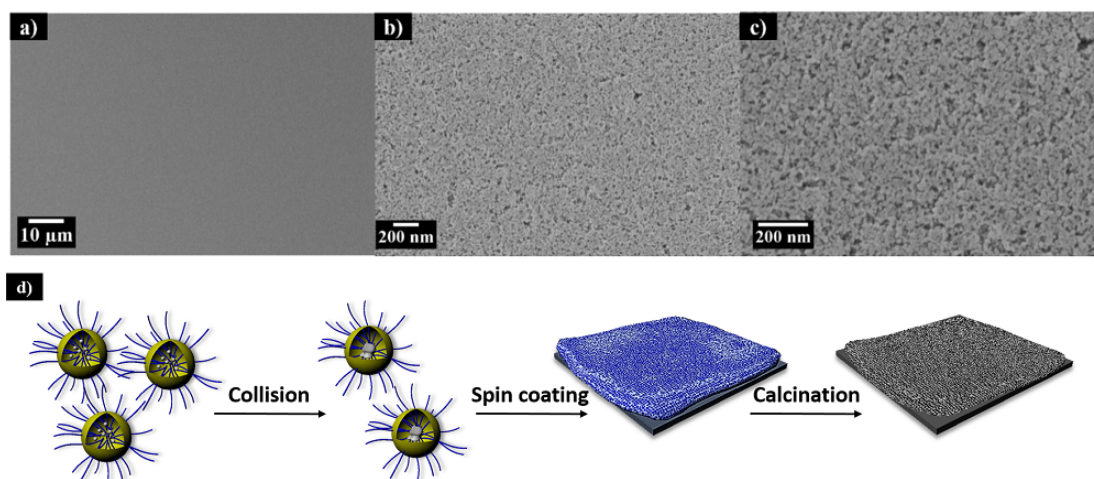


Figure 4.12: SEM images of the calcined  $\text{TiO}_2$  thin film with different magnification. a): 1000, b) 40000, c) 80000. d) The formation process of the foam like structure.

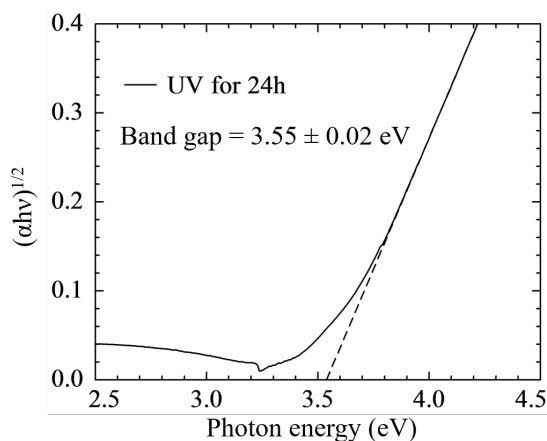


Figure 4.13: Plot of  $(\alpha h\nu)^{1/2}$  as function of the photon energy for calcined  $\text{TiO}_2$  film. Extrapolation (dashed line) is used to analyze the absorption edge for the indirect transition.

Figure 4.13 refers to the UV/Vis curve of the  $\text{TiO}_2$  film. The optical band gap of the calcined  $\text{TiO}_2$  can be obtained by extrapolation of the absorbance versus the photo energy. The linear fit in the absorption edge region shows a band gap of  $3.55 \pm 0.02$  eV (Figure 4.13). The band gaps of the anatase, rutile phases are 3.2, 3.02 respectively [2]. However, the amorphous titania typically has larger band gap energy. Here, the band gap of  $3.55 \pm 0.02$  eV suggest that both amorphous and crystalline  $\text{TiO}_2$  exist in the foamlike thin film. When used as anode material of lithium ion battery, the amorphous  $\text{TiO}_2$  can exhibit more excellent electrochemical performance than that of crystallized one [3]. This can be assigned to the existence of the defects caused from the alkoxide groups in the amorphous structure. However, the poor electroconductivity is likely unfavorable to the charge transfer.

[1] Y. J. Cheng, G. S. Gutmann, *J. AM. CHEM. SOC.* **128**, 4658-4674 (2006)

[2] L. Song, V. Körstgens, D. Magerl, B. Su, T. Fröschl, N. Hüsing, S. Bernstorff, P. Müller-Buschbaum, *MRS Advances* **2**, 2315-2325 (2017)

[3] X. Wang, J. Q. Meng, M. Wang, Y. Xiao, R. Liu, Y. Xia, Y. Yao, E. Metwalli, Q. Zhang, B. Qiu, Z. Liu, J. Pan, L. D. Sun, C. H. Yan, P. Müller-Buschbaum, Y. J. Cheng, *ACS Applied Materials & Interfaces*. **7**, 24247-24255 (2015)

#### 4.8 Inner structure analysis on annealing treated colloidal quantum dots solids

W. Chen, K. Wang, D. Yang, P. Müller-Buschbaum

Colloidal quantum dots solar cells (CQDs-SCs) have many priorities, like earth abundant elements employed (e.g. Pb and S), solution processability for device fabrication, narrow and tunable band gap for active materials make CQDs able to absorb large range solar spectra even covering near infrared (NIR). Moreover, the band gap of CQDs could be easily tuned to the ideal value which is undoubtedly beneficial for improving the power conversion efficiency (PCE) of the device towards to the theoretical value. For the last 7 years, by the state-of-the-art band alignment and surface engineering on CQDs, the PCE of CQDs-SCs has been greatly improved to 13.4% [1], which is pretty close to the new record of 14% for organic photovoltaics recently. Additionally, the small size of CQDs make them compatible with present advanced device fabrication techniques, like roll-to-roll printing, spray coating, dip-coating on hard or flexible substrates. And the chemical stability of CQDs also make the them possible to be applied in air condition at room temperature for device fabrication, thus avoid using glove-box like facilities, which is believed to be beneficial for mass production with low cost.

From principle, CQDs are regularly made of inorganics semiconductor nano-crystal core capped with organic shell by long chain ligands like oleic acid. The long chain organic ligands normally will be substituted by short chain ions during ligands exchange process to reduce the inter-dot spacing and therefore improve the carrier transportation by space distance dependent electronic coupling [2]. However, during the layer-by-layer (LBL) deposition integrated with ions exchange, it is inevitable for CQDs nanoparticles to get inhomogeneously aggregate during the process and result in energy funneling effect, which is believed to slower the charge mobility, decrease the excitons extraction rate and therefore result in consequent low efficiency for the device [1, 3].

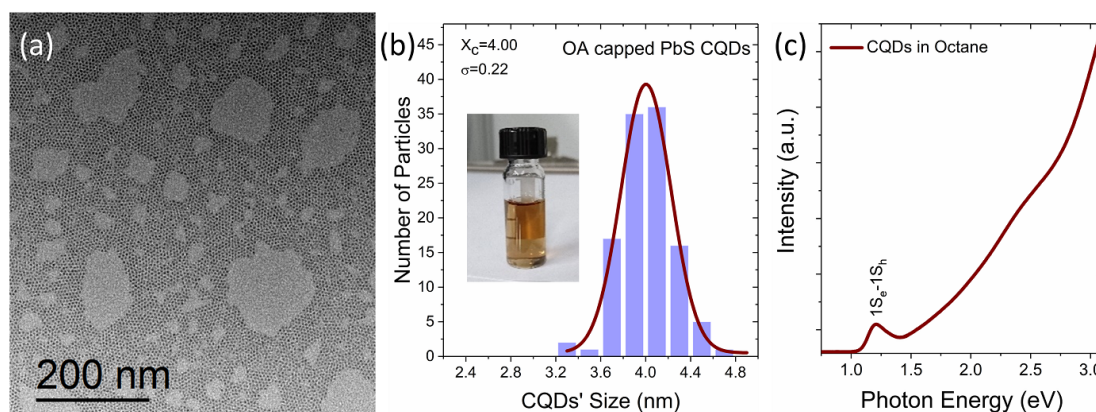


Figure 4.14:

a) TEM image of as employed CQD b) statistical information of CQDs size and the consequent Gaussian distribution c) the absorption spectrum of the CQDs dispersed in Octane.

In this work, in order to better understand the inner structure of CQDs solids and further improve the performance of related devices, we supposed to use the thermal annealing treatment applying on ligand exchanged CQDs' solids to improve the inner structure orderness. We used transmission electron microscope (TEM) to acquire the size distribution information as shown in Fig. 4.14 (a). And the average diameter of as employed CQDs is about 4.00 nm and the full width at half maximum (Fw) is 0.52 (sigma=0.22) from the statistical data and the consequent Gaussian fitting from Fig. 4.14 (b). The absorption peak energy (the first exciton absorption

peak) shown in Fig. 4.14 (c) also confirms the consistency between the particle size and the band-gap energy described by the quantum confinement effect (also known as quantum size effect).

The grazing incidence small angle X-ray scattering (GISAXS) was also employed to investigate the inter-dot spacing of CQDs from the scattering pattern as shown in Fig. 4.15. The scattering patterns of samples are all shown as Fig. 4.15 (b-d). According to the horizontal line cut ( $q_y$ ) concentrated at Yoneda peaks position of the CQDs materials on all 2D GISAXS data [4] as shown in Fig. 4.15 (e), the inter-dot spacing is inferred as Fig. 4.15 (f) which indicates that the inter-dot spacing inside of CQDs' solid varied under different temperature treatment.

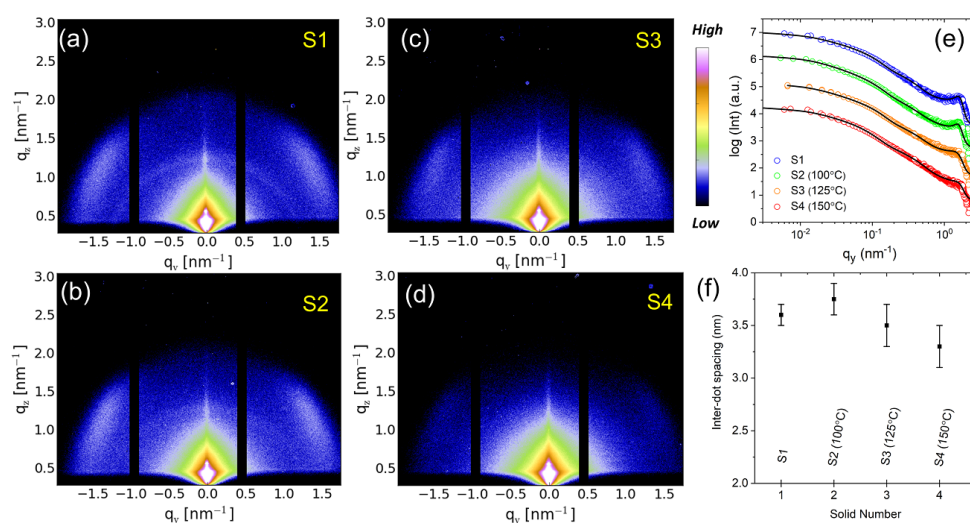


Figure 4.15:

a) two-dimensional scattering patterns for CQDs' sample without thermal treatment b) with 100°C treatment, c) with 125°C treatment d) with 150°C treatment, e) horizontal line cuts ( $q_y$ ) of the 2D GISAXS data, f) inter-dot spacing variation in the function of the different annealing temperature

With the higher temperature (100°C) applying on solids, the slightly increased inter-dot spacing, from 3.6 to 3.75 nm, is supposed to be the contribution of the position adjustment of CQDs array by the thermalization and residual ligands. It is believed this adjustment would improve the structure order as well as the energy state order[3]. When the thermal temperature is getting further higher to 125°C and 150°C, the inter dot spacing is getting decreased. this is supposed to be the fusion effect. In this inter dot spacing range, the electronic wave functions of the CQDs are strongly overlapped and coupled thus the electronic excitations are able to be de-localized and beneficial for the charge transportation. Additionally, the thermal annealing treatment is also believed to be effective for the reduction the intermediate trap states, which is still in our investigation.

- [1] M.Liu, O. Voznyy, R. Sabatini, F. P.Garcia de Arquer, R. Munir, A. H.Balawi, X. Lan, F. Fan, G. Walters, A. R. Kirmani, S. Hoogland, F. Laquai, A. Amassian, E. H. Sargent, *Nat. Mater.* **16**, 258-263 (2017)
- [2] J. J. Choi, J. Luria, B. R. Hyun, A. C. Bartnik, L. Sun, Y. F. Lim, J. A. Marohn, F. W. Wise, T. Hanrath, *Nano Lett.* **10**, 1805-11 (2010)
- [3] R. H. Gilmore, E. M. Lee, M. C. Weidman, A. P. Willard, W. A. Tisdale, *Nano Lett.* **17**, 893-901 (2017)
- [4] S. Xia, E. Metwalli, M. Opel, P. A. Staniec, E. M. Herzig, P. Müller-Buschbaum, *ACS Appl. Mater. Inter.* (2018)

#### 4.9 An insight into atmospheric degradation processes by mapping local nanoheterogeneities within hybrid polycrystalline perovskite films

S. Pratap, J. Schlipf, K. John, V. Körstgens, P. Weiser<sup>1</sup>, A. Holleitner<sup>1</sup>, A. Davydok<sup>2</sup>, C. Krywka<sup>2</sup>, P. Müller-Buschbaum

<sup>1</sup> WSI, Physik Department, Garching

<sup>2</sup> HZG Outstation, DESY, Hamburg

Hybrid perovskites have emerged as an exciting and highly versatile class of materials within the photovoltaic community. Their versatility emerges from their crystallographic structure which allows for functionalization of materials into hybrid species by partial/ complete compositional substitution at various lattice sites. Their manufacturing is economically attractive since perovskite materials have low activation energies for crystallization and they require low temperatures for formation. However, as a result they are known to be sensitive to structural and chemical degradation in ambient atmosphere, especially in the presence of humidity and oxygen. Although it is known that structures undergo degradation, their distribution through the sample is as yet unknown.

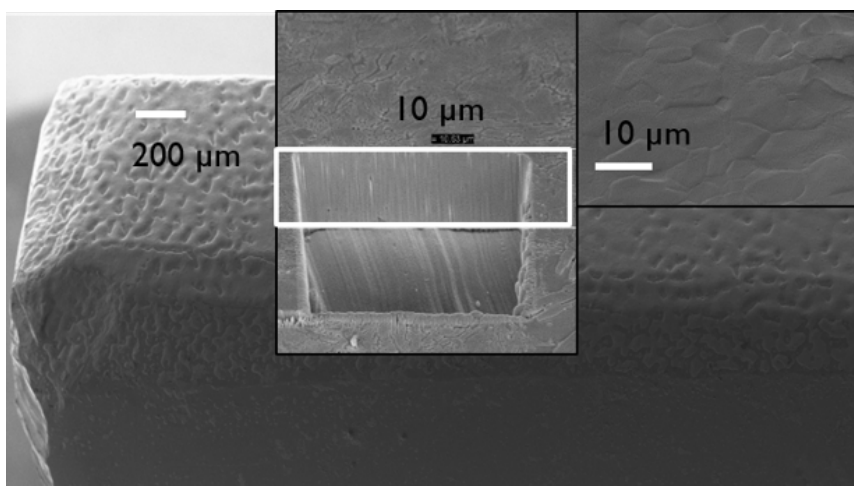


Figure 4.16:

SEM image exhibiting the sprayed perovskite film, the morphology of the film at different lengthscales.

Within this study, we map local crystallographic characteristics of two exemplary perovskite systems: a stoichiometrically pure  $\text{MAPbBr}_3$  and a mixed hybrid perovskite- $(\text{MAPbBr}_3)_{0.50}(\text{FAPbI}_3)_{0.50}$ . Both films were prepared by spray deposition on steel sample supports of special geometry as required by the setup of the experiment. The samples were etched with a focussed ion beam and probed with the aid of a nanofocussed x-ray beam. For the initial characterization, both films were scanned with WAXS in a grid of about  $80 \mu\text{m} \times 10 \mu\text{m}$  using a step-size of 500 nm. Both samples investigated provided strong Bragg reflexes indicative of high crystallinity. Localized heterogeneities within the films, the characteristic crystal sizes and a potential phase transformation within the hybrid perovskite system to lower symmetry perovskites were probed.

Within the two prototypical materials, the stoichiometrically pure  $\text{MAPbBr}_3$  was found to be more resistant to ambient elements and showed no remarkable degradation products within the film. The material purity was found to be fairly consistent within all areas of the film (see Fig. 2, top panel).

Au contraire, the hybrid  $(\text{MAPbBr}_3)_{0.50}(\text{FAPbI}_3)_{0.50}$  perovskite was found to be susceptible to degradation. Vertical gradients of purity were noted within the hybrid perovskite with the same crystalline mass exhibiting degradation and lowering of crystalline symmetry closer to the air interface, as compared to the mass which was closer to the substrate (see Fig 2, bottom panel). This was a first indication of the distribution and propagation of the degradation products within hybrid perovskites. With this information, chemical protection routes for perovskites can be envisaged, especially by protecting and passivating the exposed interface from the known enemies of moisture and oxygen.

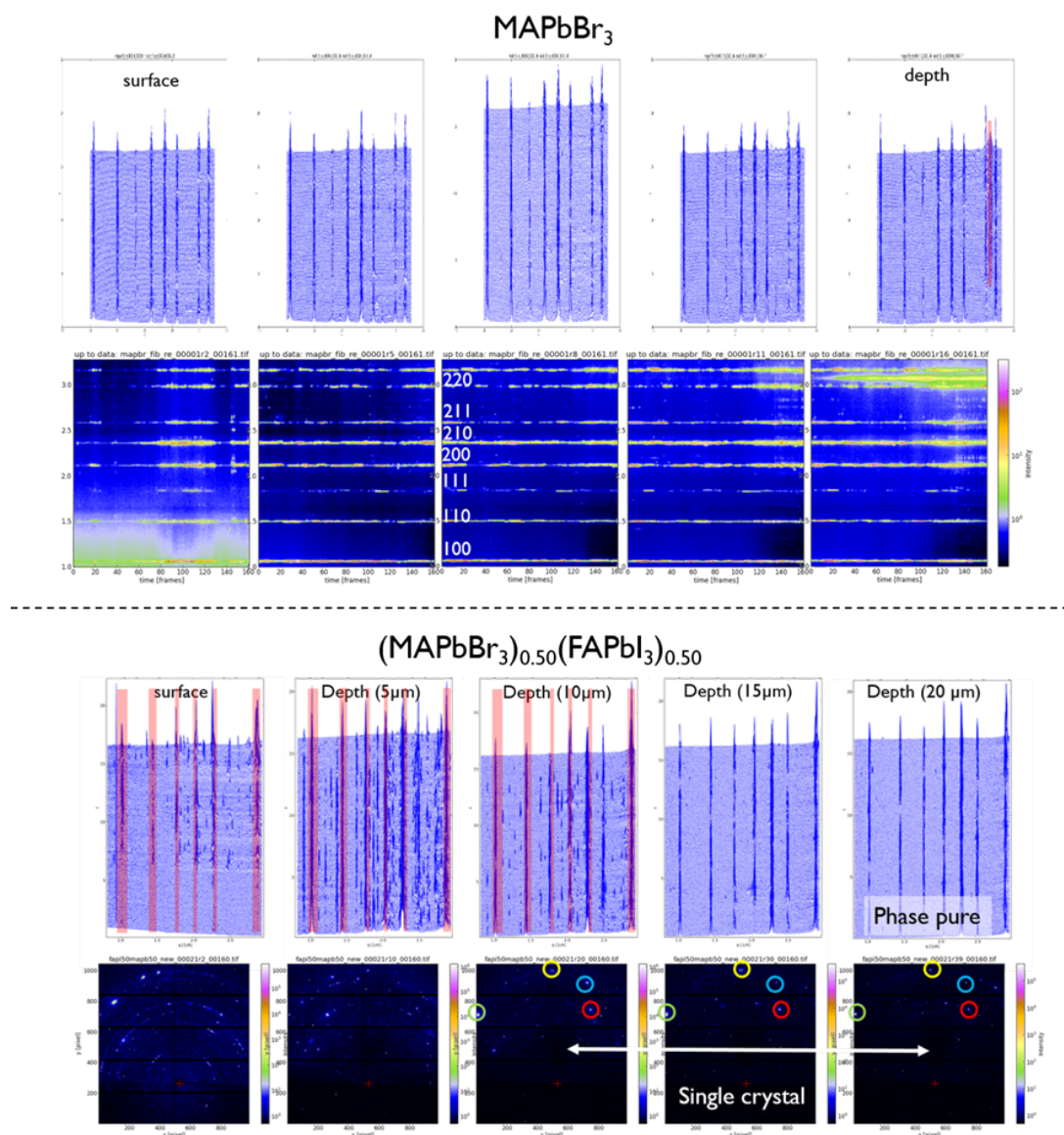


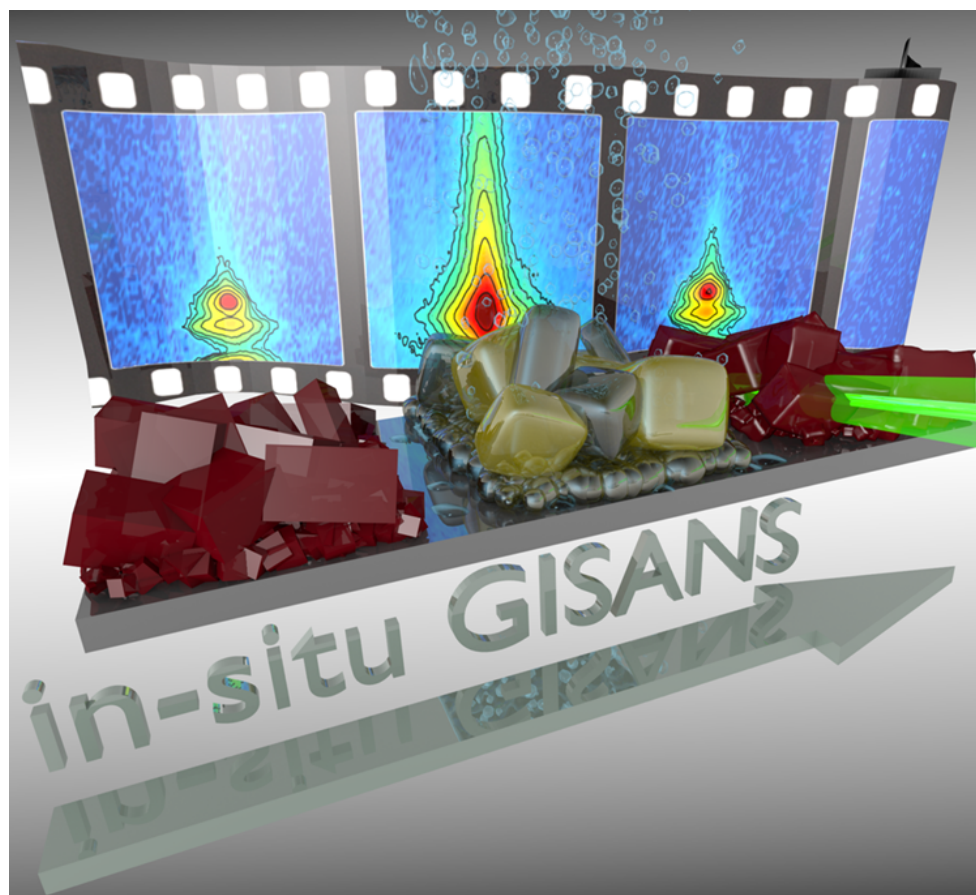
Figure 4.17:

Lateral scans of  $\text{MAPbBr}_3$  (top panel) and  $(\text{FAPbI}_3)_{0.50}$  (bottom panel) at 5 exemplary depths exhibiting the distribution of phase pure perovskite and degradation products through the film depths. The red box exhibits the reflections from the steel substrate.

The current experiment exhibits premier data regarding the local heterogeneities emerging at the nanoscale, making it possible for the first time to map individual crystallites of solution-processed thin films and pinpoint local sites of degradation within hybrid perovskites.



## 5 Real-time characterization



## 5.1 Investigating the degradation of PffBT4T-2OD: PC<sub>70</sub>BM solar cells by in-operando GIWAXS measurements

D. Yang, F. C. Löhner, V. Körstgens, A. Schreiber, S. Bernstorff<sup>1</sup>, J. M. Buriak<sup>2</sup>, P. Müller-Buschbaum

<sup>1</sup> Elettra, Trieste, Italy

<sup>2</sup> University of Alberta, Edmonton, Canada

Polymer bulk heterojunction solar cells are showing great potential as a cost-effective alternative to conventional solar cells in near future due to their easily scalable and solution-based manufacturing. The power conversion efficiencies (PCE) of lab-scale devices have already exceeded 13 %. [1] However, much higher efficiencies are still needed to make them economically viable. Many efforts are being put on optimizing the device morphology which plays the most important role in attaining high efficiencies. Aside from optimizing the initial PCE of solar cells, their long-term stability must be considered as a key role in the organic solar cell (OSCs) development. The degradation of OSCs mainly focuses on the role of oxygen, water and intrinsic degradation of constituent materials. Although encapsulation technology can minimize the decay from oxygen and water, the degradation mechanisms of constituent materials are still needed to improve understanding. To investigate the degradation behaviors of donor material in organic solar cells, in-operando GIWAXS measurements are performed on poly[(5,6-difluoro-2,1,3-benzothiadiazol-4,7-diyl)-alt-(3,3''-di(2-octyldodecyl)-2,2';5',2'';5'',2'''-quaterthiophen-5,5'''-diyl)] (PffBT4T-2OD): [6,6]-Phenyl-C71-butyric acid methyl ester (PC<sub>70</sub>BM) solar cells. It is recorded that the solar cells of PffBT4T-2OD: PC<sub>70</sub>BM show high efficiency, which has a PCE up to 10.5%. [2]

In the operando GIWAXS measurements, on one hand, current-voltage curves are periodically recorded every 26 s via the Keithley 2400 source meter for 120 minutes under vacuum. Then, the normalized photovoltaic characteristics can be extracted from the IV-tracking: open-circuit voltage ( $V_{OC}$ ), short-circuit current density ( $J_{SC}$ ), fill factor (FF), and PCE (see Fig. 5.1 a). It can be directly observed that  $V_{OC}$ , FF, PCE and  $J_{SC}$  all drop with time. The PCE experiences a 20% decrease in 120 min. And the main degradation of PCE are from  $J_{SC}$  and  $V_{OC}$ .

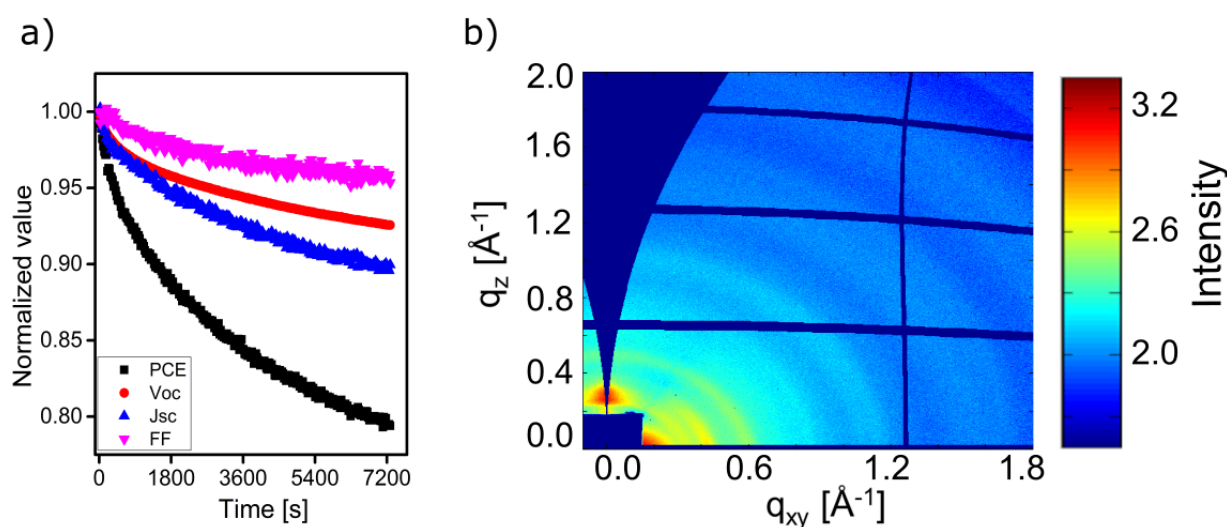


Figure 5.1:

a) Time evolution of the photovoltaic characteristics of the device; b) one of the 2D GISAXS images

On the other hand, the time resolved 2D GIWAXS images (Fig. 5.1 b) can be obtained from the in-operando GIWAXS measurements. To further understanding the crystallinity of the materials, the vertical sector integrals are taken from the 2D GIWAXS images and one of the vertical cuts is shown in Fig. 5.2 a. The PffBT4T-2OD (100), (200), (300) and (010) Bragg peaks are visible in the vertical cut. And the (100) Bragg peak is found with the highest intensity, which means the edge-on orientation being dominant in the film. While the weak (010) peak indicates that the crystallites with face-on orientation are rare in this sample. PC<sub>70</sub>BM crystallites also can be found from the vertical cut. Since PC<sub>70</sub>BM crystallites are without preferred orientation, our analysis focus on the PffBT4T-2OD crystallites. To do a quantitative analysis, the vertical cuts are fitted by Gaussian functions (Fig. 5.2 a).

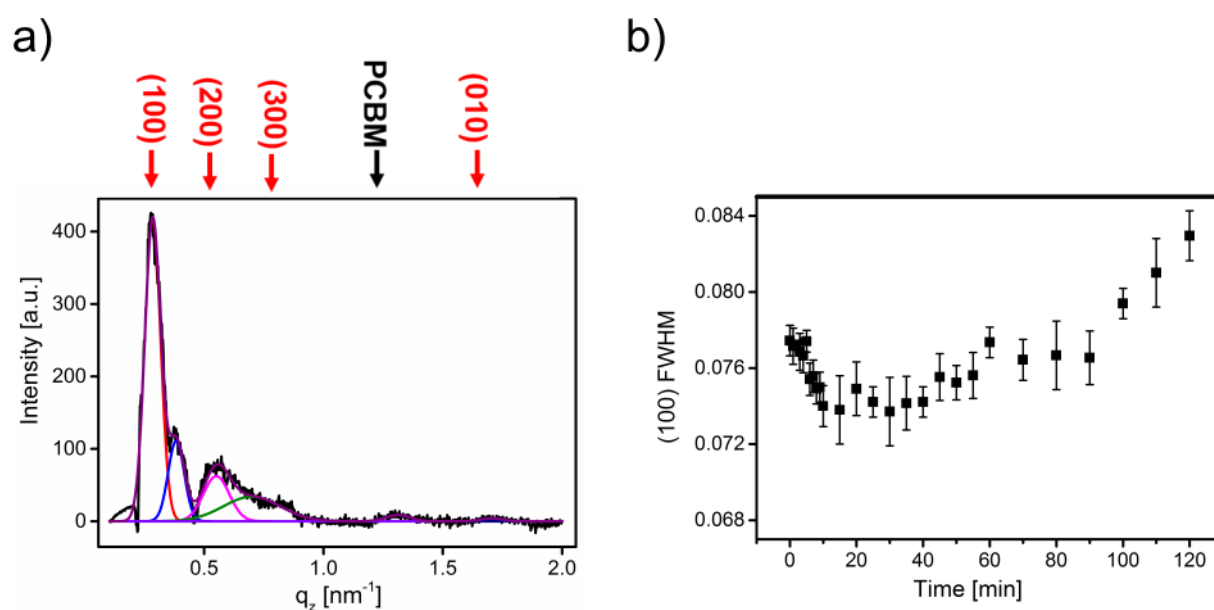


Figure 5.2:

a) vertical cut and fitting curves of one 2D GIWAXS image; b) peak FWHM of (100) Bragg peaks

Then the time evolution of the full-width-half maximum (FWHM) values of the (100) peaks can be concluded from the fitting results (Fig. 5.2 b). In Fig. 5.2 b, the FWHM values undergo a decrease at the initial stage, then the FWHM values start increasing. According to the Debye-Scherrer equation, the crystallite sizes of PffBT4T-2OD firstly increase a little, then the trend reverts and the crystallite sizes show a decrease process.

Combine the crystalline size changes with the J-V performance, we find that the crystalline size has an important effect on the performance of organic solar cells. At first, the changing crystallite sizes can influence exciton and charge carrier transport in the active layer and further cause the  $J_{SC}$  degradation in the J-V performance. What's more, it is published that the decreasing crystalline sizes would lead the degradation of  $V_{OC}$  value either. [3] At last, we conclude that the crystallinity degradation plays a important role on the degradation of OSCs. To further improve the stability of OSCs, this problem needs to be figured out and solved.

[1] W. Zhao, S. Li, H. Yao, S. Zhang, Y. Zhang, B. Yang, J. Hou, *J. Am. Chem. Soc.* **139**, 7148-7151, (2017)

[2] Y. Liu, J. Zhao, Z. Li, C. Mu, W. Ma, H. Hu, K. Jiang, H. Lin, H. Ade, H. Yan, *Nat. Comm.* **5**, 5293, (2014)

[3] D. M. Gonzalez, C. J. Schaffer, S. Pröller, J. Schlipf, L. Song, S. Bernstorff, E. M. Herzig, P. Müller-Buschbaum, *ACS Appl. Mater. Interfaces* **9**, 3282-3287, (2017)

## 5.2 In-situ tracking of composition and morphology of a diblock copolymer film with GISAXS during exchange of solvent vapors at elevated temperatures

F. Jung, A. V. Berezkin, D.-M. Smilgies<sup>1</sup>, D. Posselt<sup>2</sup>, C. M. Papadakis

<sup>1</sup> Cornell University, Ithaca, NY, USA

<sup>2</sup> Roskilde University, IMFUFA, Denmark

Block copolymers (BCP) have attracted a lot of interest due to their ability to self-assemble and form microdomains with length scales of 10-100 nm. This so-called bottom-up approach offers a wide range of interesting applications, e.g. for nanolithography. Imperative for use in these applications is a defect-free, controllable structure.

Solvent vapor annealing (SVA) is a widely used method to obtain highly ordered BCP thin films, that has also been applied to modify the BCP film morphology [1]. In a selective solvent, chemically different nanodomains swell to a different extent, which implies a change in the effective volume fraction of the BCP, thus enabling order-order transitions. This effect is highly controllable by using mixtures of solvents of varying selectivity. Recently, SVA has been combined with thermal annealing (solvo-thermal vapor annealing, STVA), which is expected to significantly improve kinetics of structural rearrangements.

In this work, a thin film from the cylinder-forming diblock copolymer polystyrene-*block*-poly(dimethyl siloxane) (PS-*b*-PDMS), with PDMS as the minority block, is investigated during STVA with solvent mixtures. The solvents used are toluene and *n*-heptane, which are weakly selective for PS and strongly selective for PDMS, respectively. Thus, swelling in toluene mostly swells the glassy PS matrix, while *n*-heptane increases the effective volume fraction of PDMS and enables a transition from the initial cylinder to the lamellar morphology. The experimental setup is shown in Fig. 5.3: The solvent vapor is produced by blowing N<sub>2</sub> gas through bubblers which contain the liquid solvents, and by mixing the such solvent saturated gas streams afterwards. By changing the flow of N<sub>2</sub> gas through the bubblers, different compositions of the solvent vapor can be achieved. Additionally, several parts of the setup are temperature-controlled to enable experiments at higher temperatures. For *in situ* characterization of the film morphology, the sample cell is equipped with a glass window for film thickness measurements using a white light interferometer (WLI) and kapton windows for grazing-incidence small-angle x-ray scattering (GISAXS) measurements. Measurements were performed at beamline D1 at the Cornell High Energy Synchrotron Source (CHESS).

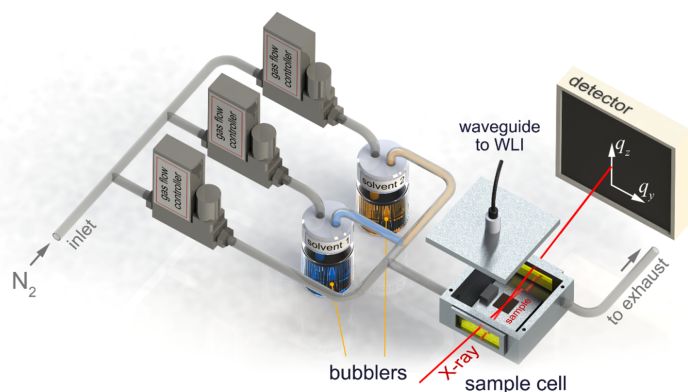


Figure 5.3: Schematics of the experimental setup for *in situ* GISAXS investigations during STVA in mixtures of two solvents. For clarity, the electrical heating and thermal insulation are not shown.

In Fig. 5.4, the results of an experiment are shown. A PS-PDMS film having a thickness of 187 nm was first swollen in pure *n*-heptane for 1 h (Fig. 5.4a). In order to probe different vapor compositions, the *n*-heptane was exchanged by toluene in 10 steps which last 300 s each. Afterwards, the film was dried with pure N<sub>2</sub> gas. The sample was kept at a temperature of 44 °C. Using the time-dependent intensity of a Bragg reflection along with the time-dependent swelling ratio,  $S_R$ , we were able to extract the distribution of the solvents among the PS- and the

PDMS-domains. This allows for a calculation of the effective volume fraction of the PDMS-rich domain,  $f_{\text{eff}}$ , which, together with the polymer volume fraction  $\phi_P = 1/S_R$ , defines a trajectory of the film through its state diagram during STVA (Fig. 5.4b) [2]. The GISAXS map of the initial film is shown in Fig. 5.4c at 0 s. It reveals a cylinder morphology with random orientation. During swelling in *n*-heptane, standing cylinders are observed for a short time at 1200 s, which change back to unoriented cylinders at longer swelling times.  $f_{\text{eff}}$  increases to  $\sim 0.5$  and, according to the theoretical BCP phase diagram, a transition to the lamella morphology is expected. This is not observed, but instead, the randomly oriented cylinder morphology is maintained, which is attributed to the still glassy PS matrix hindering restructuring. Only after initiating the solvent exchange, thus mobilizing the matrix, the transition takes place and results in standing and lying lamellae at 5100 s. By increasing the toluene fraction, thus decreasing  $f_{\text{eff}}$ , first standing and lying cylinders are observed at 5500 s which finally reorder to lying cylinders with very high order, as seen from the second-order Bragg peaks at 6000 s. At the highest swelling ratios, the system crosses an order-disorder transition (not shown). During drying, lying cylinders of two different orientations are observed, indicated by the additional Bragg peaks at 7200 s. This morphology persists in the fully dried film with slightly decreased long range order. In conclusion, we have successfully navigated a PS-*b*-PDMS film through its state diagram by exchange of solvent vapors at elevated temperatures, and simultaneously measured the morphology and solvent composition in the film.

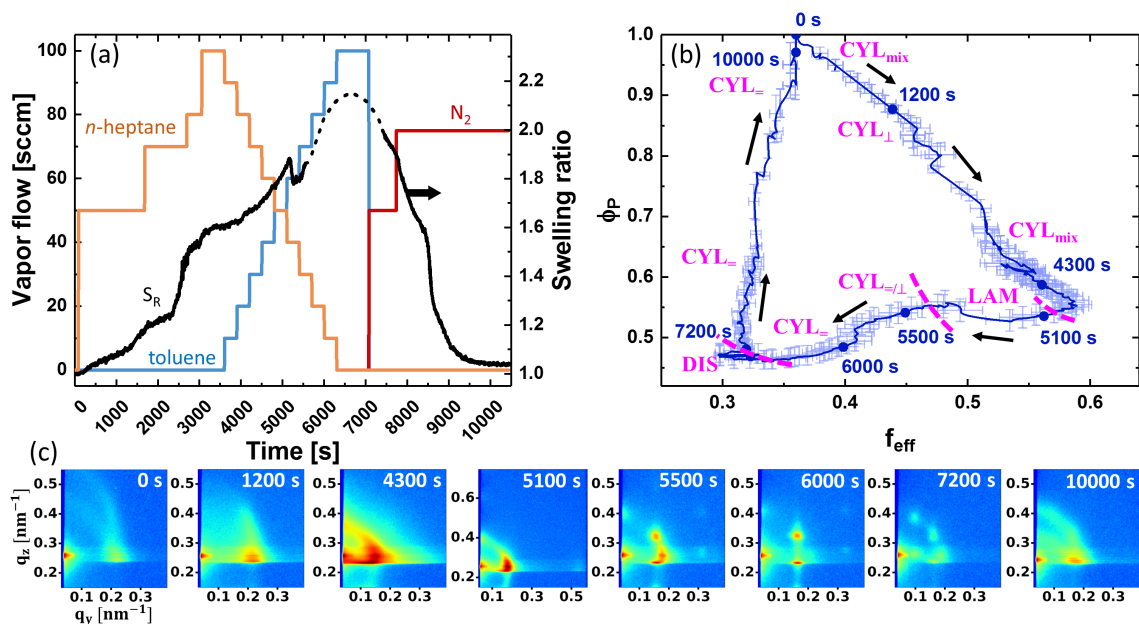


Figure 5.4:

(a) Variation of the vapor flows (all left axis) and the resulting swelling ratio  $S_R$  (right axis). (b) Trajectory of the system during STVA as a function of the effective volume fraction of PDMS,  $f_{\text{eff}}$ , and the polymer volume fraction,  $\phi_P$ . The observed morphologies are indicated. CYL, LAM and DIS stand for cylinders, lamellae and disordered. The subscript "∥" and "⊥" denote lying and standing cylinders, respectively. (c) Measured 2D GISAXS maps at selected times.

The project is funded by DGF (Pa771/10-2) and the Russian Foundation for Basic Research.

[1] D. Posselt, J. Zhang, D.-M. Smilgies, A. V. Berezkin, I. I. Potemkin, C. M. Papadakis, *Prog. Polym. Sci.* **66**, 80-115 (2017)

[2] F. Jung, Master Thesis, Technical University of Munich (2016)

### 5.3 Degradation of plain 3D and 3D\2D heterojunction hybrid perovskite films in high humidity probed with in-situ GISANS

J. Schlipf, Y. Hu<sup>1</sup>, S. Pratap, L. Bießmann, N. Hohn, L. Porcar<sup>2</sup>, T. Bein<sup>1</sup>, P. Docampo<sup>4</sup>, P. Müller-Buschbaum

<sup>1</sup> LMU, Munich, Germany

<sup>2</sup> ILL, Grenoble, France

<sup>3</sup> Newcastle University, Newcastle, United Kingdom

Hybrid lead halide perovskites have revolutionized the field of thin film optoelectronics by combining low-cost and up-scalable fabrication from wet chemistry with high performance when used as active material in photovoltaics. State-of-the-art devices achieve power conversion efficiencies around 22 % with an optimized quaternary cation composition (denoted FAMARC).[1] However, a remaining issue is the fast degradation of hybrid perovskites in ambient moisture.[2] Substitution of the organic cations with longer organic molecules — like phenylethylammonium (PEA) — leads to the formation of a confined perovskite phase a.k.a 2D perovskites that possess higher moisture stability, but this typically provokes cutbacks in device efficiency.[3] A promising approach combines high photovoltaic performance of the 3D perovskites with the good moisture resistance of 2D perovskites by a heterojunction approach that has a thin layer of 2D PEAMAPI perovskite on top of a thick film of 3D MAPI perovskite.[4]

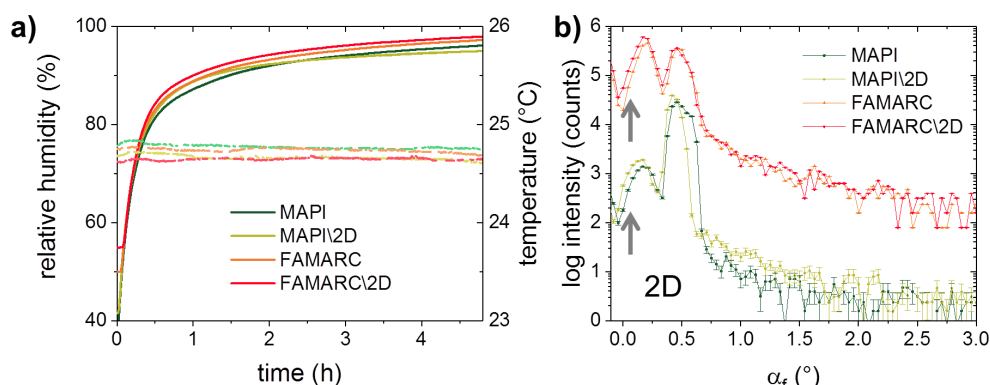


Figure 5.5:

(a) Humidity trends recorded in the experimental chamber during the in-situ GISANS degradation studies of perovskite thin films show that high humidity of over 90 %RH is established within 1 h, while the temperature is kept constant at around 25 °C. (b) Vertical line cuts of 2D GISANS data for all probed samples. The 2D top-layer is embodied in the bulge left of the Yoneda peaks (arrows) as compared to the plain films. Data is shifted for clarity.

Here, the moisture stability of a conventional MAPI film is tested in a plain film and one with a 2D PEAMAPI protection layer (MAPI\2D). With in-situ grazing incidence small angle neutron scattering (GISANS) in combination with deuterated water (D<sub>2</sub>O) it is possible to follow the ingress of moisture into perovskite films due to the high scattering contrast of D<sub>2</sub>O and the resulting shift of the Yoneda peak. A custom aluminum chamber including a basin for the water is used to establish a stable and controlled high relative humidity of > 90 %RH. As the FAMARC composition was shown to be especially sensitive to humidity, we also compare a plain FAMARC film with one where a 2D perovskite was formed in the same manner, i.e. conversion of the upper layer of the 3D film by spin-coating a PEAI:MAI mixture.[4,5] Fig. 5.5 shows the humidity trends and vertical line cuts of the 2D GISANS data for the four studied films. A bulge at lower angles next to the Yoneda peak indicates the presence of the 2D layer on

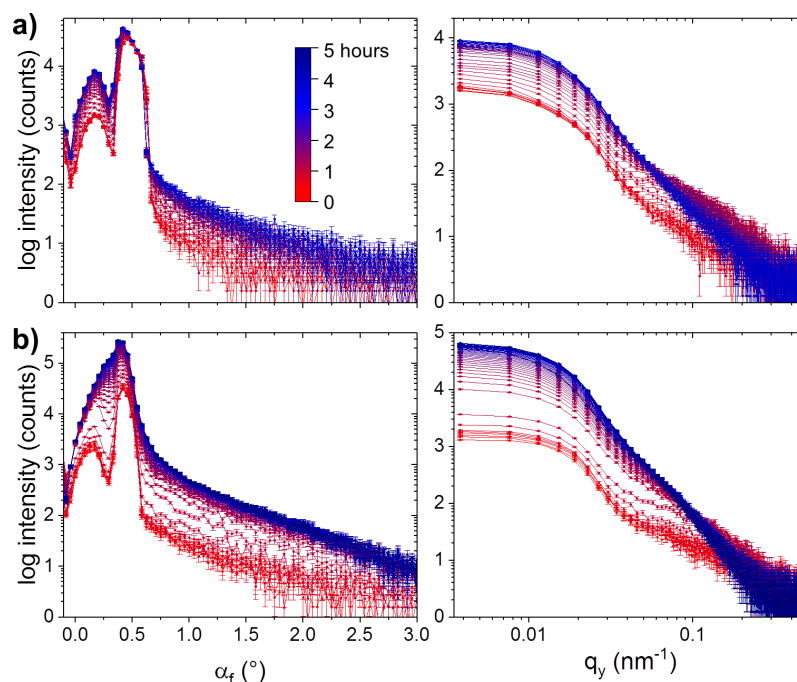


Figure 5.6:

In-situ GISANS data collected for (a) MAPI and (b) MAPI\2D. In the vertical line cuts on the left the position of the Yoneda peak only changes distinctively for the film with protection layer. However, morphological changes are obvious from the horizontal line cuts (right) for both samples.

the film surface in MAPI\2D (green) and FAMARC\2D (red) as opposed to the plain perovskite samples.

Surprisingly, all films showed degradation, the severest (as expected) in the FAMARC compounds. A comparison of the plain MAPI film with the MAPI\2D seems to imply a stronger water uptake in the film with protection layer (cf. Fig. 5.6). However, model fits of the data reveal that only the smallest structures in the MAPI\2D heterojunction deteriorate, and as they are not present in the plain MAPI film, it can be interpreted as the 2D layer being “sacrificed” while the 3D perovskite film underneath is preserved. This important finding helps to understand the protection mechanism of the capping layer. In the case of FAMARC\2D the degradation is also slowed down by the protection layer, although degradation is still observed. This implies that a thicker 2D layer – as achievable with a higher ion concentration in the conversion solution – might be necessary to yield the same level of protection as for the simpler MAPI perovskite composition. Another option might be to reduce the amount of  $\text{Ru}^+$  ions in the 2D layer, as they are blamed for the higher sensitivity to moisture.[5]

- [1] M. Saliba, T. Matsui, K. Domanski, J.-Y. Seo, A. Ummadisingu, S. M. Zakeeruddin, J.-P. Correa-Baena, W. R. Tress, A. Abate, A. Hagfeldt, M. Grätzel, *Science* **354**, 206–209 (2016)
- [2] J. Schlipf, L. Bießmann, L. Oesinghaus, E. Berger, E. Metwalli, J. A. Lercher, L. Porcar, P. Müller-Buschbaum, P. Docampo, *J. Phys. Chem. Lett.* **9**, 2015–2021 (2018)
- [3] Y. Chen, Y. Sun, J. Peng, J. Tang, K. Zheng, Z. Liang, *Adv. Mater.* **30**, 1703487 (2018)
- [4] Y. Hu, J. Schlipf, M. Wussler, M. L. Petrus, W. Jaegermann, T. Bein, P. Müller-Buschbaum, P. Docampo, *ACS Nano* **10**, 5999–6007 (2016)
- [5] Y. Hu, M. F. Aygüler, M. L. Petrus, T. Bein, P. Docampo, *ACS Energy Lett.* **2**, 2212–2218 (2017)

## 5.4 Following the thickness evolution and water uptake of PEDOT:PSS thin films under high humidity conditions by in-situ time-of-flight neutron reflectometry

L. Bießmann, J.-F. Moulin<sup>1</sup>, P. Müller-Buschbaum

<sup>1</sup> MLZ, Garching, Germany

One key parameter in improving device efficiencies of organic electronics is the replacement of commonly used rigid and expensive transparent conducting metal-oxides like indium-doped tin oxide (ITO). The polymer blend poly(3,4-ethylenedioxythiophene):polystyrene sulfonate (PEDOT:PSS) offers good electrical conductivity, transparency and flexibility, which makes it to a promising candidate for polymeric electrodes [1]. It consists of the conducting, hydrophobic PEDOT and the insulating, hydrophilic PSS. The PSS part makes the polymer blend easily water processable and serves as primary doping agent. However, the hydrophilicity of the PSS part provides the PEDOT:PSS electrodes with the risk of degradation by water uptake. It is known that the performance of PEDOT:PSS electrodes drops under ambient conditions, which may be related to water incorporation into the PSS part [2].

Therefore, we investigate different PEDOT:PSS thin films regarding their water uptake and swelling behavior under high humidity conditions with in situ time-of-flight neutron reflectometry (TOF NR) measurements. The measurements were performed at the *REFSANS* instrument at MLZ, Garching. Different PEDOT:PSS thin films treated with Zonyl or ethylene glycol (EG), which are commonly used as hole transport layer or polymeric electrodes, were prepared for investigation. Figure 5.7 shows a detailed overview of the sample preparation.

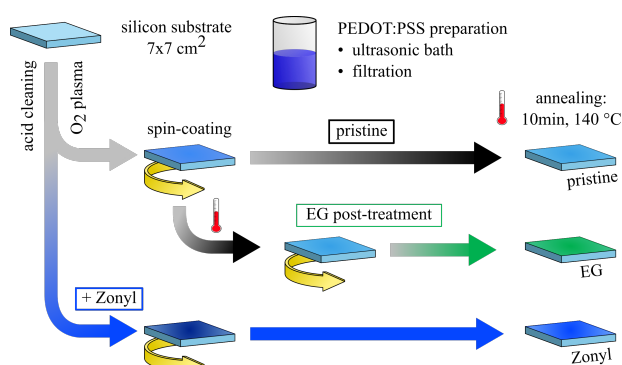


Figure 5.7: Schematic overview of the sample preparation routine for the investigated PEDOT:PSS thin films (pristine, Zonyl additive, EG post-treatment). The silicon substrates were acid cleaned and subsequently spin coated with the prepared PEDOT:PSS solution. After each deposition step a subsequent annealing step at 140 °C was applied.

The PEDOT:PSS thin films of about 20 nm thickness were exposed to high humidity conditions in a special designed measurement chamber. The sample environment was kept at a constant temperature of 26.5 °C. After a static TOF-NR measurement to determine the starting conditions, a specific amount of D<sub>2</sub>O was injected via a syringe into a water reservoir placed below the sample. The high SLD difference between D<sub>2</sub>O ( $6.36 \cdot 10^{-6} \text{ \AA}^{-2}$ ) and the polymer films ( $\approx 1.8 \cdot 10^{-6} \text{ \AA}^{-2}$ ) makes the measurement very sensitive to water incorporation.

The change in relative humidity was tracked with a Sensirion SHT21 temperature and humidity sensor and is depicted in Figure 5.8 d). Simultaneously, a five hours kinetic measurement was started to follow the thickness evolution and the water uptake of the films. The obtained data is binned to 30 s, which provides a very good time resolution in combination with reasonable statistics. The resulting reflectivity data is fitted using the Motofit package for Igor 6.3, using a three layer model. The resulting reflectivity curves including their fits for pristine, Zonyl additive and EG post-treated PEDOT:PSS thin films are shown in Figure 5.8 a)-c). For all curves a significant shift of the critical edge towards larger  $q_z$  values is visible. This corresponds to an increase in the average SLD of the thin films, which is related to a D<sub>2</sub>O incorporation into the PSS domains. While the shift in critical edge seems to be almost identical for the pristine

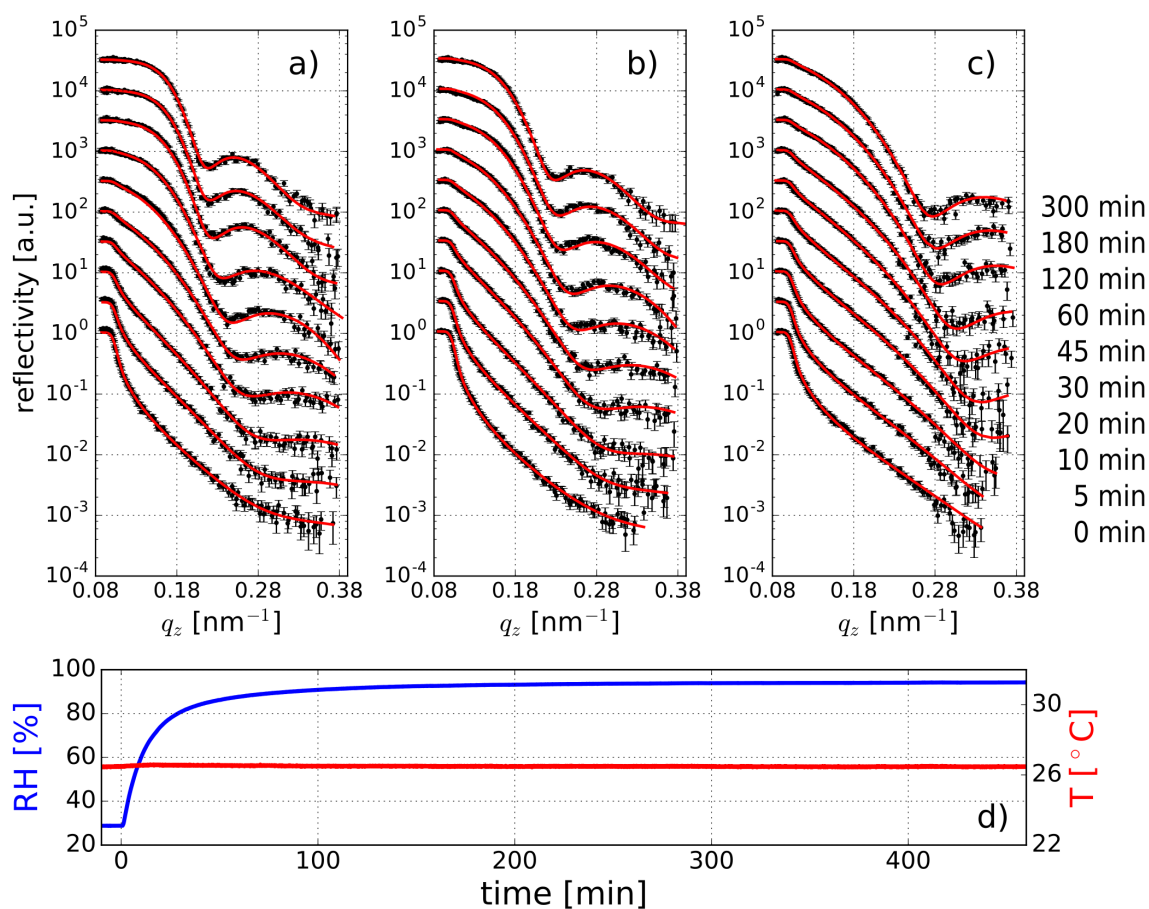


Figure 5.8:

Selected NR data (symbols) and fits (red lines) of PEDOT:PSS thin films exposed to high humidity conditions measured at times as indicated: a) pristine film, b) Zonyl additive, and c) ethylene glycol post-treated film. d) shows the corresponding sample environment regarding relative humidity and temperature. All samples exhibit a thickness increase by shifting reflectivity maxima towards smaller  $q_z$  values, while the increasing average SLD of the film by incorporation of  $\text{D}_2\text{O}$  is represented by a shift of the critical edge to larger  $q_z$  values.

(Figure 5.8 a)) and the Zonyl (Figure 5.8 b)) treated sample, the EG post-treated sample (Figure 5.8 c)) shows a significantly less pronounced shift of the critical edge, which corresponds to less incorporation of  $\text{D}_2\text{O}$ . In addition, reflectivity maxima at higher  $q_z$  are appearing. These reflectivity maxima are shifting towards smaller  $q_z$  values, which corresponds to a thickness increase of the films. Here, the pristine and the Zonyl samples (Figure 5.8 a) and b)) show again an almost identical swelling behavior, while the EG post-treated sample (Figure 5.8 c)) shows a less pronounced thickness increase. In conclusion, the analysis of the kinetic measurement showed the least water incorporation and thickness increase for the EG post-treated film compared to the pristine and the Zonyl treated films. Thus, EG post-treated PEDOT:PSS shows a significantly reduced water sensitivity.

- [1] Y. H. Kim, C. Sachse, M. L. Machala, C. May, L. Müller-Meskamp, K. Leo, *Advanced Functional Materials* **21**, 1079-1081 (2011)
- [2] K. Kawano, R. Pacios, D. Poplavskyy, J. Nelson, D. D. C. Bradley, J. R. Durrant, *Solar Energy Materials and Solar Cells* **90**, 3520-3530 (2006)

## 5.5 Water swelling and exchange kinetics in multi-stimuli responsive polymer thin films followed with in-situ time of flight neutron reflectometry

L. Kreuzer, T. Widmann, N. Hohn, K. Wang, J. F. Moulin<sup>1</sup>, V. Hildebrand<sup>2</sup>,  
A. Laschewsky<sup>2</sup>, C. M. Papadakis, P. Müller-Buschbaum

<sup>1</sup> Institute of Chemistry, University of Potsdam, Germany

<sup>2</sup> MLZ, Garching, Germany

Stimuli responsive polymers can change their properties towards even small variations of an external trigger such as temperature, pressure, pH or light. This behavior makes them attractive for a manifold selection of applications in the fields of nano-sensors, artificial pumps and muscles or optical switches [1]. A promising candidate for the afore mentioned application fields is a newly synthesized block copolymer which consists of a non-ionic poly(N-isopropylacrylamide) (PNIPAM) block and a zwitterionic poly(sulfobetaine) (PSB) block. The chemical structure is shown in Fig. 5.9a. The polymeric components exhibit a lower critical solution temperature (LCST – PNIPAM block) and an upper critical solution temperature (UCST – PSB block) in aqueous solution respectively (Fig. 5.9b) [2]. Therefore, the block copolymer is capable of strong changes in volume only by a small change of temperature or relative humidity. By using the block copolymer in thin film geometry, we generate a smart surface, which in theory is only allowed to swell and shrink in one direction. It is essential to understand and control the occurring sorption/desorption and diffusion processes of low-molecular penetrants in order to establish a reproducible and reversible uptake and release of penetrants [3,4].

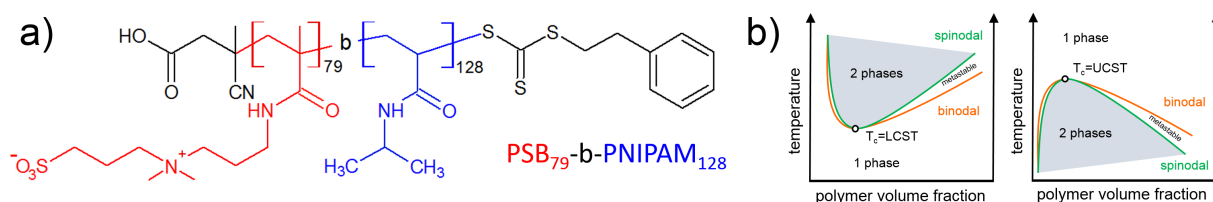


Figure 5.9:

a) chemical structure of PSB<sub>79</sub>-b-PNIPAM<sub>128</sub>. The PSB block is colored red whereas the PNIPAM block is colored blue. b) phase diagram of an LCST-type polymer (left) and a UCST-type polymer

In our recent work, we use time-of-flight neutron reflectometry (TOF-NR) to follow the water and deuterated water swelling and the corresponding exchange processes in a multi-stimuli responsive PSB-b-PNIPAM thin film. TOF-NR measurements were performed at the REFSANS instrument at the FRM 2 neutron source in Garching. This sophisticated measurement technique allows the detection of the dynamic processes with high time resolution. By using a polychromatic incident neutron beam in combination with the TOF wavelength resolution, the REFSANS instrument gives simple access to a large  $q_z$  range. Furthermore, a horizontally smeared out beam of 65 mm width is used in order to maximize intensity. Block copolymer thin films of high homogeneity and tunable thickness are prepared via a combination of spin-coating and solvent annealing on silicon substrates. The samples were placed in a special designed vapor chamber, which allows the control of temperature and relative humidity of a particular atmosphere ( $H_2O$  and  $D_2O$ ). This enables to follow first the  $D_2O$  swelling and then the  $H_2O$  exchange process as well as the vice versa experiment ( $H_2O$  swelling followed by  $D_2O$  exchange). The dynamic swelling and exchange processes were monitored at a fixed incident angle of  $0.76^\circ$ , whereas static measurements at the beginning, between the dynamics and at the end were performed at two different angles,  $0.6^\circ$  and  $2.4^\circ$ , to increase the  $q_z$  range. By applying a fit model to the

obtained reflectivity curves information about thickness, scattering length density (SLD) and roughness are gained. Furthermore, the observed kinetics are modelled to obtain detailed insights about the underlying mechanisms of water uptake and exchange.

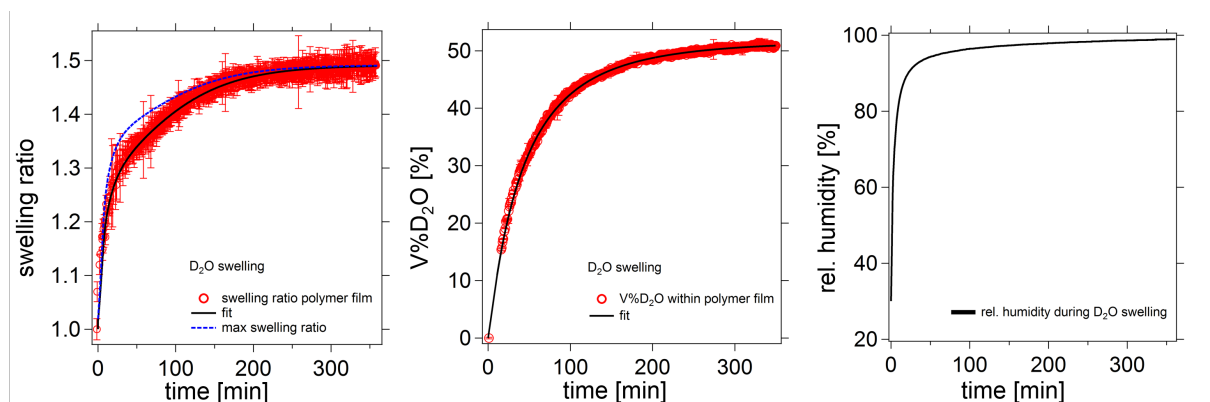


Figure 5.10:

a) swelling ratio of the polymer film upon time. The data is fitted with a theoretical model as is explained in the text (black curve). In addition the maximum swelling ratio is plotted (dotted blue curve). b)  $D_2O$  content versus time. Again the data is fitted with a theoretical model (black curve). c) Ambient relative humidity during the dynamic  $D_2O$  swelling process.

Figure 5.10 shows the high time resolution  $D_2O$  swelling process. The film thickness increases (a) as  $D_2O$  molecules diffuse inside the polymer film (b). A theoretical model is used to fit the dynamic  $D_2O$  swelling process. This model respects not only the diffusion of a low-molecular penetrant inside the polymer film but also the ambient relative humidity during the  $D_2O$  swelling process (Fig. 5.10c). The model gives information about the interactions between the low-molecular penetrants ( $H_2O/D_2O$ ) and the polymer as well as insights on which time scales the dynamic processes are happening. By comparing both swelling processes and both exchange processes with each other, detailed insights into the mechanism of the interaction of low-molecular penetrants and polymer films can be obtained.

Besides TOF-NR, the block copolymer thin film was probed with White Light Interferometry (WLI) and in-situ Fourier Transform Infrared Spectroscopy (FTIR). WLI gives information about the film thickness and the refractive index during the swelling and exchange dynamics. In-situ FTIR is used to gain insights in the molecular interactions between the water molecules and the polymer. Since  $H_2O$  and  $D_2O$  molecules differ in their rotation and vibration energies, FTIR can distinguish between water and deuterated water. This is beneficial especially during the exchange processes, where both solvents are involved.

Alltogether, a complementary characterization of a multi stimuli block copolymer thin film is performed, which results in a more detailed insight into the mechanism of the interaction of low-molecular penetrants and polymer films in order to generate sophisticated materials.

- [1] M. A. Cohen Stuart, W. T. S. Huck, J. Genzer, M. Müller, C. Ober, M. Stamm, G. B. Sukhorukov, I. Szleifer, V. V. Tsukruk, M. Urban, F. Winnik, S. Zauscher, I. Luzinov *Nature Materials* **9**, 101-113 (2010)
- [2] M. Mertoglu, S. Garnier, A. Laschewsky, K. Skrabania, J. Storsberg *Polymer* **46**, 7726-7740 (2005)
- [3] M. Koenig, D. Magerl, M. Philipp, K. J. Eichhorn, M. Müller, P. Müller-Buschbaum, M. Stamm, P. Uhlmann, *RSC Advances* **4**, 17579-17586 (2014)
- [4] M. Philipp, V. Körstegens, D. Magerl, C. Heller, Y. Yao, W. Wang, G. Santoro, S. V. Roth, P. Müller-Buschbaum, *Langmuir* **31**, 9619-9627 (2015)

## 5.6 In-situ GISAXS during sputter deposition of metal nanolayers on functional polymer thin films

S. Schaper, P. Müller-Buschbaum

Understanding the interface between metals, commonly used as contacts and current collectors, and (ion-)conducting polymers used in organic electronics, organic photovoltaics and polymer lithium-ion batteries (LIBs) is crucial to develop highly reproducible, low-cost and reliable devices. To address these issues, sputter deposition is the technique of choice to fabricate scalable, reproducible and controllable nanometer and sub-nanometer metal layers on polymer thin films.[1] The sputter deposition process, being well understood and controlled, offers advantages over chemical methods to tailor metal thin-film morphologies on the nanoscale and offers a superior adhesion of the deposited material.[2] In-situ grazing incidence small angle X-ray scattering (GISAXS) is used to investigate the formation, growth and self-assembled structuring on polymer thin films. To exceed the limits of the polymer LIBs unexploited development the deposition and infiltration of sputtered metals onto the polymer thin film needs to be understood.

The diblock copolymer (DBC) polystyrene-block-poly(ethylene oxide) (PS-*b*-PEO) is one of the most promising materials for solid state polymer LIBs. The rigid PS block provides mechanical stability while the soft and ion-conducting PEO block enables Li-ion's migration between the electrodes. Due to the covalent bond between the hydrophobic PS and the hydrophilic PEO block of the PS-*b*-PEO DBC undergoes a microphase separation creating a self assembled structure in the nanoscale which can prevent the lithium-dendrite's growth leading to a shortcut in LIBs.

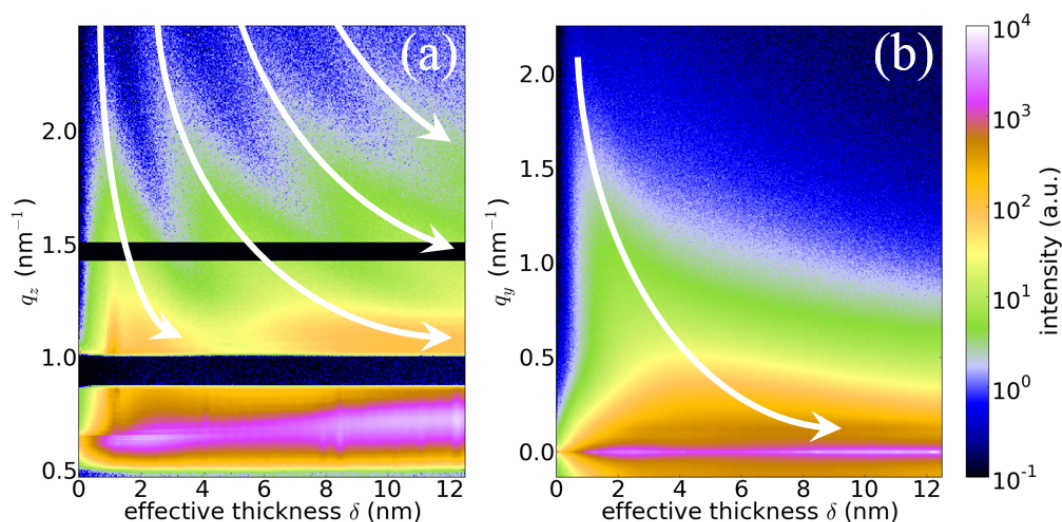


Figure 5.11:

In-situ GISAXS sputter deposition of gold on PS-*b*-PEO DBC thin films: (a) in-plane cuts  $q_z$  and (b) out-of-plane cuts  $q_y$  in the range of the Yoneda peaks versus the effective film thickness  $\delta$ . The white arrows indicate the evolution of the peaks' position to lower  $q$  values leading to larger sizes in real space with increasing film thickness.

The samples under investigation are bare PS-*b*-PEO DBC 90 nm thin films on acid-cleaned silicon substrates prepared from 10 mg  $\text{ml}^{-1}$  solution with  $\text{CHCl}_3$  as solvent via spin coating at 2000 rpm. Subsequently the samples were solvent annealed with  $\text{CHCl}_3$ . The in-situ GISAXS measurements during sputter deposition of gold nanolayers were conducted at the beamline

P03 of DESY in Hamburg using a DC magnetron sputter chamber. In GISAXS measurements the incoming X-rays with an energy of 13 keV impinge on the sample with an incident angle of  $0.4^\circ$ . The reflected and mostly elastically scattered X-rays are detected with a planar Pilatus 300k detector at a sample-detector distance of 2.305 m, while the direct beam ( $q_y = 0 = q_z$ ) and specular beam ( $q_y = 0, q_z = 1$ ) are blocked by beamstops to prevent damage of the detector. The collected scattering pattern is analyzed with in-plane cuts at  $q_y = 0$  and out-of-plane cuts at the position of the Yoneda peak which position is characteristic for the probed material. The plane referred to is defined by the sample's surface normal and the wave vector of the incident X-ray beam. These cut's evolution during the sputter deposition is shown in Fig. 5.11.

The in-plane cuts ( $q_z$  direction) shown in Fig. 5.11 (a) contain information about the sample's structure in the direction of the surface normal and are therefore used to determine the average thickness of the sputter deposited gold nanolayers. The final thickness of the gold layer can be calculated to  $12.5 \pm 1.7$  nm from the distance  $\Delta q_z$  of the  $q_z$ -peaks at higher  $q_z$  values than the specular beam. As the sputter rate is constant the effective thickness  $\delta$  is calculated from the final average gold nanolayer thickness and duration of the sputter process.

The gold nanolayer's morphology perpendicular to the plane on the sample's surface can be seen in the out-of-plane cuts ( $q_y$  direction) shown in Fig. 5.11 (b). Here one peak appears at low  $\delta$  moving from large to small  $q_y$  values with increasing  $\delta$ . This peak can be assigned to gold particles and clusters appearing during the sputter process. Assuming a hemispherical model with local hexagonal order for these gold particles and clusters the particle's distance  $D$  and radius  $R$  can be calculated.[3]

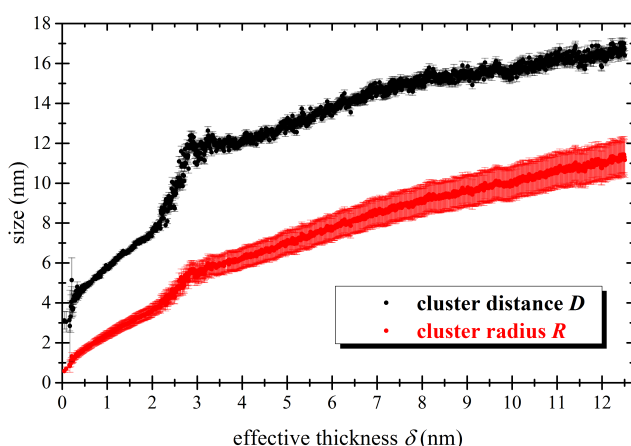


Figure 5.12:  
Evolution of the distance  $D$  and radius  $R$  of the gold nanoparticles on the PS-*b*-PEO DBC thin film during the sputter deposition.

Fig. 5.12 shows the calculated distance  $D$  and radius  $R$  of the gold particles. The growth of these particles on the thin film's surface starts with a nucleation of the first gold atoms in the beginning followed by an almost linear increase in  $D$  and  $R$  indicating the growth of gold nanoparticles. As the ratio between  $D$  and  $R$  reaches a critical value around  $\delta = 2.5$  nm a strong increase in  $D$  and also a faster growth of  $R$  due to enhanced aggregation of small gold clusters to larger ones can be observed. The subsequent plateau in  $D$  upon still increasing  $R$  indicates a growth of immobilized clusters. At effective thicknesses  $\delta > 4$  nm  $D$  and  $R$  again increase almost linearly. Taking the in-plane cuts into account one can conclude that a complete gold layer is formed in this region growing linearly with time.

- [1] F. Faupel, V. Zaporozhchenko, T. Strunskus, M. Elbahri, *Adv. Eng. Mater.* **12**, 1177-1190 (2010)
- [2] M. Schwartzkopf, A. Hinz, O. Polonskyi, T. Strunskus, F. C. Löhner, V. Körstgens, P. Müller-Buschbaum, F. Faupel, S. V. Roth, *ACS Appl. Mater. Interfaces* **9**, 5629-5637 (2017)
- [3] M. Schwartzkopf, A. Buffet, V. Körstgens, E. Metwalli, K. Schlage, G. Benecke, J. Perlich, M. Rawolle, A. Rothkirch, B. Heidmann, G. Herzog, P. Müller-Buschbaum, R. Röhlberger, R. Gehrke, N. Striebeck, S. V. Roth, *Nanoscale* **5**, 5053-5062 (2013)

## 5.7 Spray deposition of conducting composite films of PEDOT:PSS and cellulose studied with in-situ GISAXS

V. Körstgens, F. Martin, C. Brett<sup>1,2</sup>, D. Söderberg<sup>1</sup>, S. V. Roth<sup>1,2</sup>, P. Müller-Buschbaum

<sup>1</sup> KTH, Stockholm, Sweden

<sup>2</sup> DESY, Hamburg, Germany

In the emerging field of printable electronics there is a growing demand for transparent, flexible substrate materials. Cellulose-based substrates are a promising sustainable alternative to fully synthetic polymers [1]. Of special interest are electrical conductive composite materials. We present the fabrication of conducting composite films of cellulose nanofibrils (CNF) obtained from soft wood and poly(3,4-ethylenedioxythiophene) polystyrene sulfonate (PEDOT:PSS). The cellulose nanofibrils are produced in a TEMPO (2,2,6,6-tetramethylpiperidine-1-oxyl radical)-mediated oxidation process leading to a high surface charge of the fibrils [2]. One of the advantages of the polyelectrolyte complex PEDOT:PSS is its processability as an aqueous dispersion. This allows for industrially relevant coating techniques as printing or spray deposition. The complex structure with its non-conductive PSS part although makes it necessary to use additives like glycerol or a post-treatment with ethylene glycole in order to reach high conductivities. The increase in conductivity can be explained by a change of morphology in the meso- and the nanoscale [3]. Different CNF/PEDOT:PSS ratios and the influence of the additive glycerol on the film morphology and conductivity were investigated. The improvement of conductivity with the co-solvent glycerol and alternative post-treatment with ethylene glycole for the composite films follows the same trend as known for pure PEDOT:PSS films. In order to investigate the morphology of the composites the spray deposition was followed in situ with grazing incidence small angle x-ray scattering (GISAXS) experiments. In these experiments dispersions of a blend of PEDOT:PSS and CNF were spray coated on glass slides. A distinct spray protocol with a sequence of 100 short spray pulses of 0.2 s and 2 s waiting in between was applied. In combination with the elevated temperature of the substrate of 85 °C, a complete dry layer was ensured after each individual spray pulse. During spray deposition a continuous alternate motion of the sample avoids beam damage on the sample.

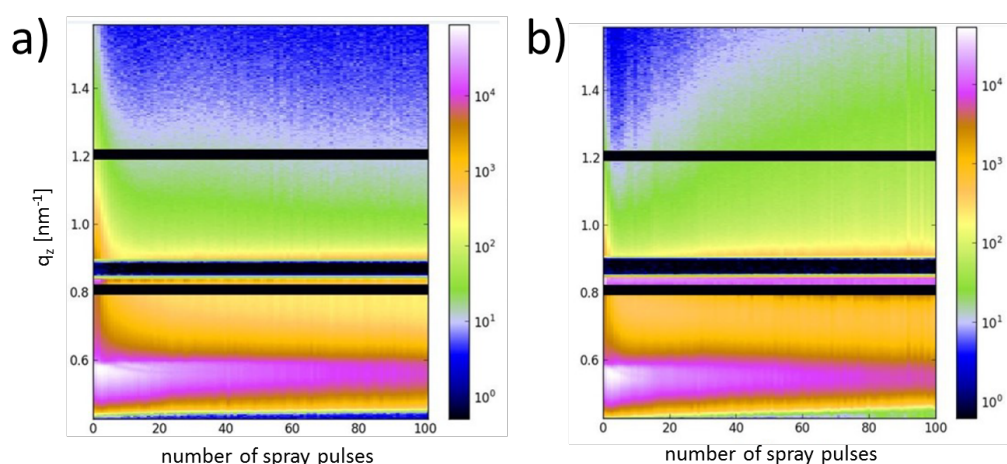


Figure 5.13:

Composite images from vertical cuts from 2D detector patterns around  $q_y = 0$  for 100 spray pulses a) blend of PEDOT:PSS/CNF in 3/1 w/w ratio b) blend of PEDOT:PSS/CNF in 3/1 w/w ratio with addition of the cosolvent glycerol

In Fig. 5.13 the course of spray deposition for a blend of PEDOT:PSS and CNF with a w/w ratio of 3/1 is shown. In the composite images vertical cuts from the 2D detector patterns around  $q_y = 0$  are combined for 100 spray pulses. Whereas in Fig. 5.13a) the pure blend is deposited, Fig. 5.13b) shows the spray deposition of the blend with the addition of cosolvent glycerol. The composite images indicate a smooth layer development with a more pronounced diffuse scattering at higher  $q_z$ -values for the blend including glycerol. In order to get information about lateral structures describing the morphology of the composite films, horizontal line cuts from the 2D data have been performed for the individual number of spray pulses.

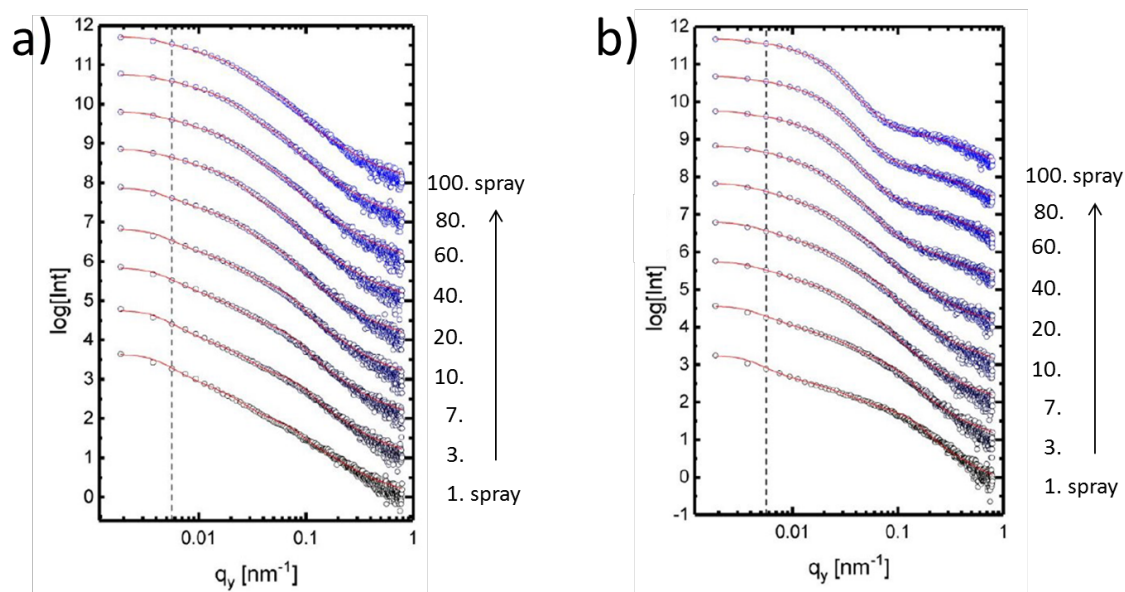


Figure 5.14:

Horizontal line cuts for selected number of spray deposition. a) blend of PEDOT:PSS/CNF in 3/1 w/w ratio b) blend of PEDOT:PSS/CNF in 3/1 w/w ratio with addition of the cosolvent glycerol; red lines are the fits to the data and the dashed line constitutes the resolution limit, the curves are shifted along the intensity axis for clarity

In Fig. 5.14 horizontal line cuts are shown for a selected number of spray pulses together with a fit to the data. With the model applied three spherical structures with a diameter and a corresponding distance are necessary to describe the data. For the composite without cosolvent after about 30 spray pulses the morphology does not change anymore with increasing thickness of the film indicated in 5.14a). In contrast for the composite with the additional cosolvent glycerol there is a continuing growth of medium-sized and larger structures up to the diameter of 140 nm. This behaviour is consistent with the application of glycerol as a plasticizer allowing for morphological changes especially with elevated temperatures as used with the spray deposition process. A more complete description and explanation of the conductivity of the different composites of PEDOT:PSS and cellulose will be achieved by investigating the crystallinity with GIWAXS.

- [1] H. Zhu, W. Luo, P.N. Ciesielski, Z. Fang, J.Y. Zhu, G. Henriksson, M.E. Himmel, L. Hu *Chem. Rev.* **116**, 9305-9374 (2016)
- [2] A. Isogai, T. Saito, H. Fukuzumi, *Nanoscale* **3**, 71-85 (2011)
- [3] C.M. Palumbiny, C. Heller, C.J. Schaffer, V. Körstgens, G. Santoro, S.V. Roth, P. Müller-Buschbaum, *J. Phys. Chem. C* **118**, 13598-13606 (2015)

## 5.8 In-situ study of spray deposited titania nanostructures

L. Song, W. Wang, V. Körstgens, D. Moseguí González, F. C. Löhner, C. J. Schaffer, J. Schlipf, S. V. Roth<sup>1,2</sup>, P. Müller-Buschbaum

<sup>1</sup> DESY, Hamburg, Germany

<sup>2</sup> Department of Fibre and Polymer Technology, KTH Royal Institute of Technology, Stockholm, Sweden

Mesoporous titania films have found a wide variety of applications ranging from photovoltaics to biosensors. The sol-gel synthesis in combination with polymer templates is a facile and common way to prepare titania nanostructures. This so-called polymer-template assisted sol-gel synthesis can tune the morphology of nanostructured titania films efficiently by just regulating the ratio of titania precursors and polymer templates. This solution-based wet chemical synthesis allows for fabrication of titania films with many deposition techniques such as spin coating, solution casting, doctor blading and so on. In particular, spray coating is of high interest as it is cost-efficient and can be adapted to a large-scale manufacturing process. However, spray deposition as a rapid solution-based technology usually involves complicated morphology evolutions. In order to clarify this involved kinetic process, in situ morphological investigations of the spray deposited films are in high demand, but also imply a great challenge.

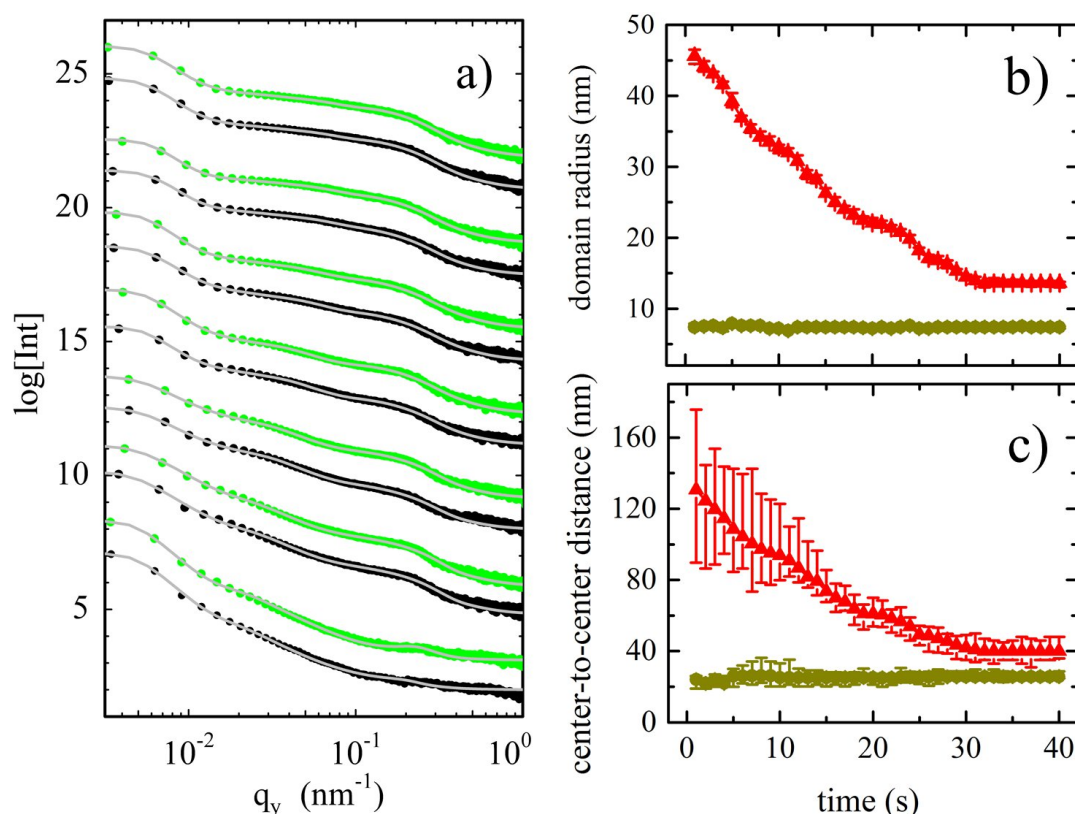


Figure 5.15:

a) Selected horizontal line cuts of the 2D GISAXS data plotted from bottom to top for increasing time. The gray lines represent the fits to the data. Temporal evolution of b) domain radii and c) center-to-center distances of the titania:PEO mixture in the films during spray coating. Yellow circles and red triangles indicate small-sized and large-sized structures, respectively.

The use of conventional real-space mapping techniques is nearly impossible here as they cannot

be compatible with the experimental environment of spray coating and/or cannot provide sufficient time resolution for morphological detection. Grazing-incidence small-angle x-ray scattering (GISAXS) measurement is a powerful tool for in situ characterization of structure and morphology evolutions of spray deposited titania films as this technique can be carried out with a high time resolution and without interrupting the process of spray coating or destroying the deposited films. In the present work, titanium tetraisopropoxide (TTIP) is used as titania precursor and polystyrene-block-polyethylene oxide (PS-b-PEO) is used as polymer template for the sol-gel process. This titania sol-gel solution is applied for in situ GISAXS measurements during spray deposition. Horizontal line cuts are implemented on the obtained 2D GISAXS raw data to give information about inner film morphology (Fig. 5.15a). From data modeling, two domain sizes (form factors) and two center-to-center distances (structure factors) of the titania/PEO mixture are extracted and depicted in Fig. 5.15b and c, respectively. It can be seen that the small-sized structures stay constant in both domain sizes and center-to-center distances during the whole spray deposition, whereas the sizes of large-sized structures and their corresponding center-to-center distances decrease until approximately the 30 second, and subsequently remain unchanged until the end of the spray process. Situated between the small-sized titania:PEO mixture, PS domains are calculated to have an average size of about 10.3 nm over the whole spray coating process, which is independent of the spray time. The PS domains between large-sized titania:PEO mixture decrease in size from about 39.8 nm (first second) to around 12.8 nm (40 s). It is found that the domain sizes of PS areas are similar after spray deposition, although the sizes of small-and large-sized titania:PEO mixture are different.

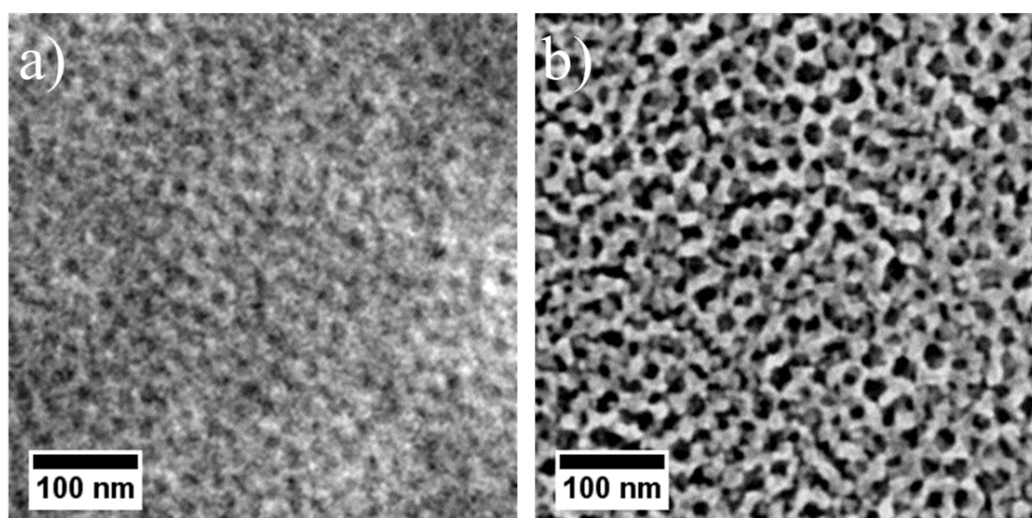


Figure 5.16: Spray deposited titania films a) before and b) after calcination at 500 °C.

After spray deposition, the surface morphology is examined with scanning electron microscopy (SEM) measurements and displayed in Fig. 5.16a. It is noticeable that Most PS domains (darker areas in the SEM image) are isolated by the interconnected titania/PEO mixture. After high-temperature calcination, the polymer template is removed completely and thereby the mesoporous interconnected titania networks is achieved and depicted in Fig. 5.16b. The film features isolated mesopore array, which derives from the isolated PS domains before calcination. The mesopore size in the calcined titania film is calculated to be about 15 nm, which meets the demand for photovoltaic applications quite well.

- [1] L. Song, W. Wang, V. Körstgens, D. Moseguí González, F. C. Löhner, C. J. Schaffer, J. Schlipf, K. Peters, T. Bein, D. Fattakhova-Rohlfing, S. V. Roth, P. Müller-Buschbaum, *Nano Energy* **40**, 317 (2017)

## 5.9 In-situ GISAXS investigation of gold sputter deposition on colloidal polystyrene thin films

M. Gensch<sup>1,2</sup>, P. Müller-Buschbaum<sup>2</sup>, S. V. Roth<sup>1</sup>

<sup>1</sup> DESY, Hamburg, Germany

<sup>2</sup> TUM, Garching, Germany

<sup>3</sup> KTH, Stockholm, Sweden

Understanding the growth of metals on colloidal nanoparticle crystals is crucial for many applications e.g. solar cells [1], antibacterial coatings [2] or biosensors. Thick colloidal crystal films can be used for functional coatings due to their crystal ordering. Common techniques to prepare these nanocomposites of metal/colloidal films are solution casting for thick colloidal films in the micrometer range and sputter deposition for a thin metal film. The sputter process can be controlled precisely to create a thin nanostructured metal film. During the sputtering the samples were investigated by grazing incidence small angle X-ray scattering (GISAXS) to obtain information about the lateral and vertical arrangement of the metal clusters on the colloidal matrix. Atomic force microscopy (AFM) height and phase images were taken after the sputtering of 10 nm Au thickness. The phase images were analysed with the fast-fourier transformation (FFT) to yield information on the size of Au clusters on the colloidal matrix. Polystyrene colloids are used as a basic template for colloidal films as in previous investigations by Herzog et al. [3]. The thickness of the samples are in the micrometer range of the polystyrene colloidal films. The films were deposited by solution casting on acid cleaned silicon substrates. The concentration of the stock solution is 25 mg/mL for the colloidal polystyrene thin film. The *in situ* GISAXS experiments were performed at the beamline P03 in Hamburg DESY [4]. The sputter deposition chamber was used with RF sputter deposition combined with a magnetron to increase the gold deposition rate. The measurements were done at an incident angle of  $\alpha_i = 0.4^\circ$  and beam energy of 0.955 Å. The sample to detector distance was SSD = 2363 mm. The detector was a Pilatus 1M with a pixel size of  $172 \times 172 \mu\text{m}^2$ . The direct and specular beam which is reflected from the sample to the detector are shielded by beamstops to protect the detector from damage. At the Yoneda peak, which is characteristic for every material, out-of-plane cuts were made to analyse the lateral formation of the gold clusters on the PS colloidal crystals. The in-plane cuts describe the vertical growth of gold on the colloidal template.

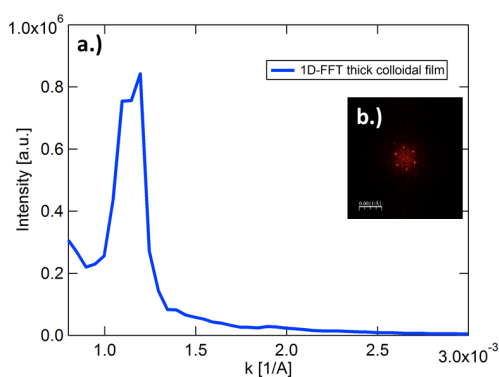


Figure 5.17:  
The FFT results of the phase images show a clear crystal like structure peak for the thicker film. The gold clusters growth on the colloidal and the size of these structures was estimated by the integrated 1D-FFT.

Fig. 5.17 shows the FFT from the phase images of the thick colloidal PS. From the results of the FFT one gain the size of the colloidal template of around  $L = (88 \pm 6)$  nm for the  $\mu\text{m}$  thick layer. While GISAXS yields  $L = 87 \pm 1$  nm, which is seen as lateral strips in the yoneda cut with also higher orders of magnitude in fig. 5.18. The approaching gold cluster peak is clearly visible on the thick colloidal PS film. Due to the ordered colloidal crystal film, a continuous growth on the surface is achieved. These results are gained by the vertical cuts, which indicates

a smooth growth on the colloidal PS films. The results from AFM and GISAXS show that on a thick colloidal film the gold tries to cover the PS colloids. If one compare the growth of gold clusters on the colloids to the growth on a spin coated PS substrate, it is seen that the evolution of the radii is clearly different to thin PS films prepared by spin coating [5]. It seems that the wormy like structure for gold on PS substrate is not formed on the colloidal PS films.

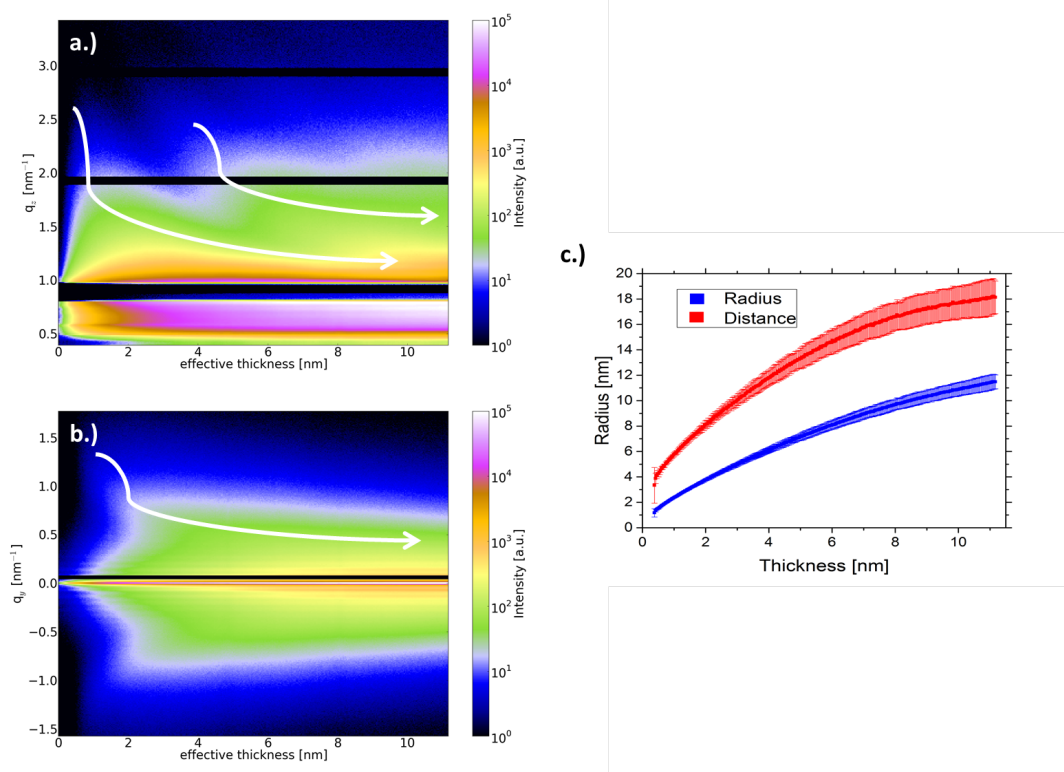


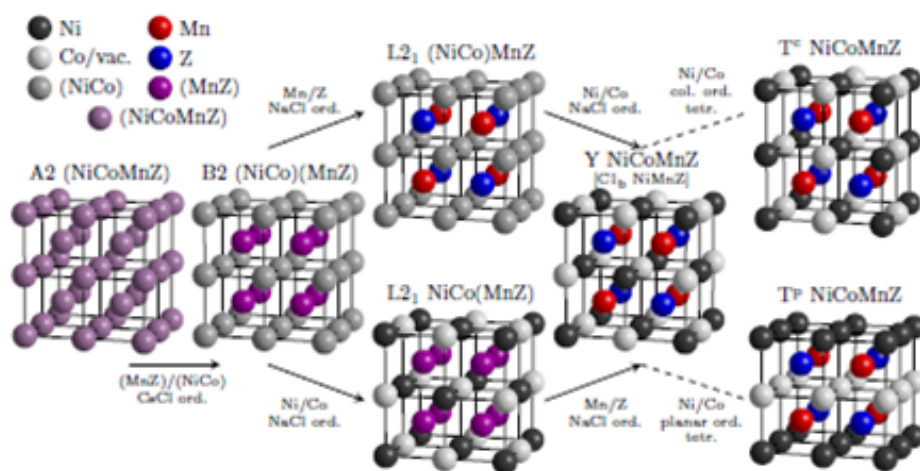
Figure 5.18:

a.) shows the vertical cut of the thick colloidal film, where the approaching height maxima on the thick colloidal film are indicating a smooth growth on the colloidal film. b.) shows the map of the Yoneda cut of the thick colloidal film. The radii and the distances of the gold clusters on the thick colloidal film could be estimated which is seen in fig. 2 c.).

- [1] G. Kaune, M. A. Ruderer, E. Metwalli, W. Wang, S. Couet, K. Schlage, R. Röhlberger, S. V. Roth, P. Müller-Buschbaum, *ACS Appl. Mater. Interfaces* **1**, 353–360 (2009)
- [2] F. Faupel, V. Zaporojtchenko, T. Strunskus, M. Elbahri, M. *Adv. Eng. Mater.* **12**, 1117–1190 (2010)
- [3] G. Herzog, M. M. A. Kashem, G. Benecke, A. Buffet, R. Gehrke, J. Perlich, M. Schwartzkopf, V. Körstgens, R. Meier, M. A. Niedermeier, M. Rawolle, M. A. Ruderer, P. Müller-Buschbaum, W. Wurth, S. V. Roth *Langmuir* **28(21)** 8230–8237 (2012)
- [4] A. Buffet, A. Rothkirch, R. Döhrmann, V. Körstgens, M. M. A. Kashem, J. Perlich, G. Herzog, M. Schwartzkopf, R. Gehrke, P. Müller-Buschbaum, S. V. Roth *Journal of Synchrotron radiation* **19**, 647–653 (2012)
- [5] M. Schwartzkopf, G. Santoro, C. J. Brett, A. Rothkirch, O. Polonskyi, A. Hinz, E. Metwalli, Y. Yao, T. Strunskus, F. Faupel, P. Müller-Buschbaum, S. V. Roth *ACS Appl. Mater. Interfaces* **7(24)**, 13547–13556 (2015)



## 6 Instrumentation and new materials



## 6.1 Monolithic U-Mo plates for the EMPIrE experiment

H. Breitzkreutz, Ch. Steyer, B. Baumeister, C. Reiter, C. Schwarz, J. Shi, T. Chemnitz, W. Petry

The EMPIrE (European Mini-Plate Irradiation Experiment) program is a joint European/US irradiation project designed to gather pivotal information on high-density low-enriched Uranium-Molybdenum research reactor fuels. To this end, EMPIrE will focus on the verification of manufacturing techniques for coating mini-sized ( $19 \times 82.5$  mm) dispersion and monolithic fuel. As part of the monolithic fuel branch, the FRM II fuel conversion group has developed, established and successfully applied a new process for the deposition of a  $20 \mu\text{m}$  zirconium diffusion barrier between the U-Mo core and the aluminum cladding of fuel plates. This process step is located between the bare U-Mo fabrication by BWX Technologies Inc. (USA) and the fuel plate manufacture by AREVA NP (CERCA, France), followed by the irradiation test in the Advanced Test Reactor (ATR) at the Idaho National Laboratory (INL, USA).

### Process Development

One of the main development focuses of the working group “Hochdichte Kernbrennstoffe” has been the application of a dense and homogeneous zirconium coating to bare UMo foils using physical vapor deposition (PVD, Fig. 6.1). The layer properties had to be adapted for proper adhesion to the U-Mo substrate and qualified for the subsequent fuel plate production process at AREVA using the C2TWP process and optimized for PVD-coatings. Therefore, a continuous process of production, examination and parameter optimization has been established between the FRM II and AREVA. Bare UMo foils were delivered by BWXT, coated by TUM with varying parameters and then processed with C2TWP by AREVA. The impact of these variations has been examined by ultrasonic testing, x-ray analysis and optical and electron microscopy.

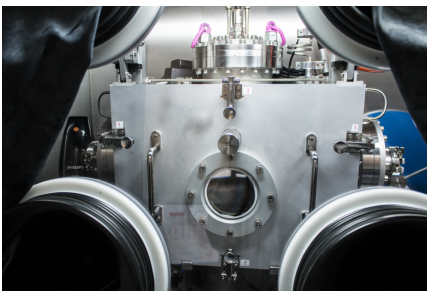


Figure 6.1:  
The PVD device has been designed to explore a large parameter space for the optimisation of coating of U-Mo foils with Zr and other materials.

### Production of the plates

An alkaline wet-chemical cleaning process has been identified as an appropriate first cleaning step. After rinsing and drying, directly before the coating process starts, the foils are treated with a low-pressure argon plasma, where argon ions bombard the uranium foil, removing the remaining impurities and activating the surface for the coating.

After two test sets using stainless steel surrogates and three using depleted uranium, the final coating of the irradiation plates with high-purity reactor-grade zirconium was successfully performed on low enriched uranium (LEU) in mid-2016. Due to the high safety requirements for nuclear fuel, the whole production process was monitored by a comprehensive quality assurance program according to NQA-1. Subsequently, cladding was applied by C2TWP at AREVA

in the fall of 2016, where twice the number of required plates passed the final conformance test, i.e. fulfilled the specification for irradiation in ATR. The fuel plates were transported to the irradiation facility by the end of 2016.

### Plate qualification

In early 2017, additional plate inspections beyond the original performance requirements were carried out at the Idaho National Lab. The measurements revealed the need for further quality assurance in all produced plates, dispersion and monolithic fuel alike. For the monolithic plates, a small gap ( $\approx 200 \mu\text{m}$ ) between the outer edges of the fuel foils and the surrounding aluminum frame had been detected by high resolution ultrasonic. Accordingly, an extensive characterization program has been performed that included all institutions of the original collaboration. Among the measurements that were performed are pulse echo and transmission ultrasound, x-ray, blister- and bend-tests, optical microscopy and SEM, thermography and radiography, neutron diffraction and finite-element simulations as well as an extensive literature study. The role of TUM in this program has mainly been evaluation of heat transport in the plates and a detailed characterization of the monolithic plates. Two members of the working group were recruited in the dedicated expert groups that evaluated the measurements. As a by-product, a new characterization technique which combines thermo- and radiography has been developed (Fig. 6.2). The post-qualification has been concluded with a positive result in 2017 and did not significantly alter the irradiation matrix.

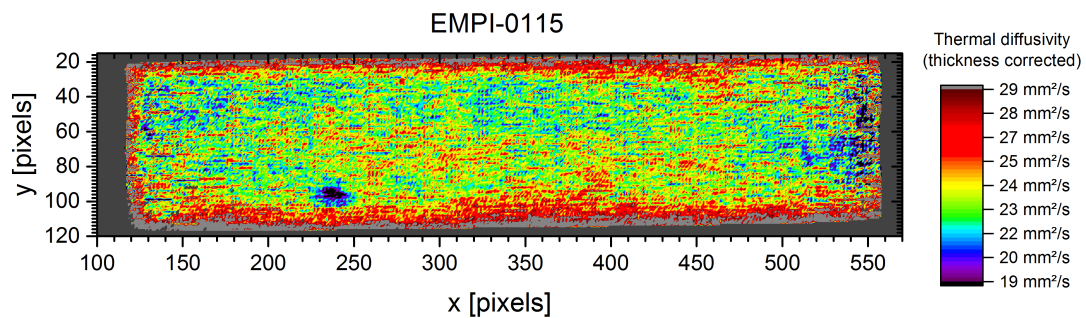


Figure 6.2:  
Radiography-corrected thermography image of the dispersion fuel mini-plate EMPI-0115. The black dot indicates a debond between cladding and fuel core. For that reason, the plate has not been part of the irradiation program.

### Outlook

Plate irradiation in ATR is scheduled to start in March 2018. In total, four monolithic plates will be irradiated, two during the shorter, first cycle, and in case of success, two further plates during the second cycle. Each pair consists of one plate where the foil has been coated at FRM II, and one plate where the zirconium has been co-rolled onto the U-Mo at BWXT. In any case, the final plate has been produced by CERCA. After the irradiation, the plates will be shipped to SCK-CEN in Belgium and CEA in France for the post irradiation examinations. This concludes the prototype phase of the monolithic manufacturing program in Europe. Construction of devices and process development for the subsequent pilot phase has already begun.

## 6.2 A quasi-elastic and inelastic neutron scattering study of the alkaline and alkaline-earth borohydrides $\text{LiBH}_4$ , $\text{Mg}(\text{BH}_4)_2$ and the mixture $\text{LiBH}_4 + \text{Mg}(\text{BH}_4)_2$

L. Silvi<sup>1</sup>, Z. Zhao-Karger<sup>2</sup>, E. Röhm<sup>2</sup>, M. Fichtner<sup>2</sup>, W. Petry<sup>1</sup>, W. Lohstroh<sup>1</sup>

<sup>1</sup> E13 and MLZ, Garching, Germany

<sup>2</sup> Institute of Nanotechnology, Karlsruhe Institute of Technology

Complex tetraborohydrides are a class of materials that have been studied intensely for their high volumetric and gravimetric hydrogen content and their potential use in solid state hydrogen storage applications. However, high thermodynamic stability, sluggish kinetics and poor reversibility make these materials still unsuitable for viable storage systems. Among the complex hydrides, the most investigated compounds are lithium and magnesium which display high hydrogen contents of 18.4 wt.%  $\text{H}_2$  ( $\text{LiBH}_4$ ), and 14.9 wt.%  $\text{H}_2$  in  $\text{Mg}(\text{BH}_4)_2$ . In general, complex hydrides are salt like materials, composed of  $\text{BH}_4^-$  anions where four hydrogen atoms are covalently bound around the central boron atom, and the positively charged alkaline or alkaline-earth cation. Their crystal structures and thermodynamic stability are governed by the structural arrangement of the  $\text{BH}_4$  units, yielding to rich phase diagrams especially for the alkaline-earth compounds.

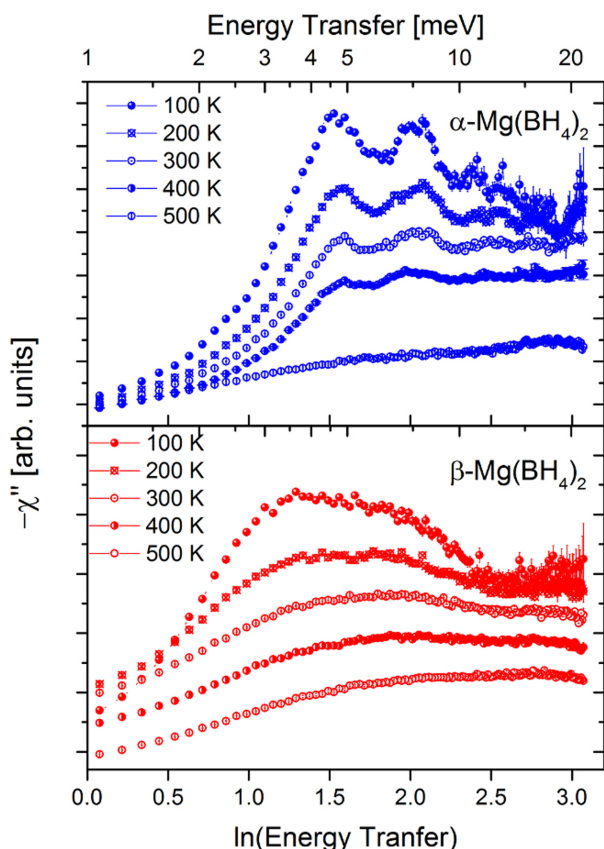


Figure 6.3:  
 $-\chi''$  as function of  $\ln(\text{Energy Transfer})$ .  $\alpha\text{-Mg}(\text{BH}_4)_2$  shows distinct peaks up to high temperatures while  $\beta\text{-Mg}(\text{BH}_4)_2$  has a much broader and slightly softer low energy spectrum. Data are summed for  $Q = 1.5 - 4.25 \text{ \AA}^{-1}$ . The increase towards low energy transfers is due to the quasielastic contributions.

Quasielastic neutron scattering was used to investigate the low energy transfer dynamics of the complex borohydrides  $\text{Mg}(\text{BH}_4)_2$  in the  $\alpha$ - and  $\beta$ -modification,  $\text{LiBH}_4$  in the low and high temperature crystal structure, and the 1:1 molar mixture of  $\text{LiBH}_4 + \alpha\text{-Mg}(\text{BH}_4)_2$ . All investigated compounds show a rich dynamic behavior below energy transfers of  $\Delta E = 10$

meV with the superposition of rotational dynamics of the constituent  $\text{BH}_4$  anions and low lying lattice modes. For  $\text{Mg}(\text{BH}_4)_2$ , the rotational diffusion of the  $\text{BH}_4$  units was found to be much more activated in the metastable  $\beta$ -polymorph compared to the  $\alpha$ -phase [1], and the low lying lattice modes are even softer in the former crystal structure as can be seen in Figure 6.3 which shows the dynamic susceptibility for the two investigated polymorphs of  $\text{Mg}(\text{BH}_4)_2$ .

The complexity and the number of different crystal modifications observed for  $\text{Mg}(\text{BH}_4)_2$  is thought to be the result of the interplay between cation size and interaction between neighboring  $\text{BH}_4$  anions.[2] In ionic crystals, the coordination number around the central cation is given by the ratio of the size of the metal cation in its appropriate oxidation state and the size of the anion. In the borohydrides, additionally, the orientation of the tetrahedral  $\text{BH}_4^-$ -anion, and the mutual repulsion of the hydrogen atoms (each carrying a partial negative charge) comes into play. Energetically, a tridentate orientation of the  $\text{BH}_4^-$  towards the cation is most favorable, most unfavorable is the monodentate orientation which has not been found in any experimental crystal structure so far.[2] For  $\text{Mg}^{2+}$ , the ion radius yields a coordination number on the border between tetragonal and octagonal coordination, and additionally, the tetrahedral  $\text{BH}_4$  can not be packed in a space filling manner. In combination with the various possibilities for the  $\text{BH}_4$  orientation, this yields to a variety of predicted and experimentally observed crystal phases which are almost degenerate in energy. From the above, it follows that the orientation of the  $\text{BH}_4$  units and their dynamics at non-zero temperatures has a significant impact on the stability of the compounds.

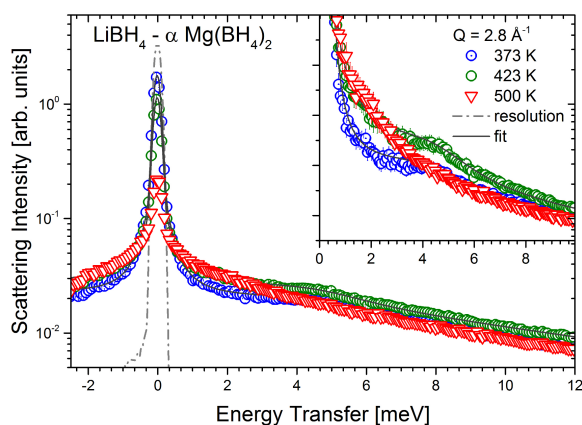


Figure 6.4:

$S(Q, \omega)$  of the 1:1 molar mixture  $\text{LiBH}_4 + \alpha\text{-Mg}(\text{BH}_4)_2$  at 373 K, 423 K and 500 K at  $Q = 2.8 \text{ \AA}^{-1}$ . The dashed line represents the resolution function of the instrument. The inset zooms into the energy transfer region around 4 meV. Solid black lines are fits to the data.

In  $\text{Mg}(\text{BH}_4)_2$ , the structural phase transition is mainly governed by the lattice dynamics, while alkaline  $\text{LiBH}_4$  exhibits a transition of the  $\text{BH}_4$  rotations around the phase transition temperature. These characteristics remain unchanged in the physical mixture of  $\alpha\text{-Mg}(\text{BH}_4)_2 + \text{LiBH}_4$ . Figure 6.4 shows the quasielastic neutron scattering results at temperatures below and above the structural phase transitions of  $\alpha\text{-Mg}(\text{BH}_4)_2$  and  $\text{LiBH}_4$ , together with the fit results of the analysis. A superposition of the dynamic features found for the pure components is sufficient to describe the data for temperature below 500 K. Above that temperature, the physical mixture melts and hydrogen release started. Further studies are needed to characterize dynamics in the molten state

[1] L. Silvi, E. Röhm, M. Fichtner, W. Petry, W. Lohstroh *Phys. Chem. Chem. Phys.* **18**, 14323–14332 (2016)

[2] Z. Łodziana, M.J. van Setten, *Phys. Rev. B* **81** 024117 (2010)

### 6.3 Ordering in quaternary Heusler derivatives

M. Leitner, P. Neibecker, W. Petry

Heusler alloys are a class of intermetallic compounds of large interest both to fundamental and applied physics, as on the one hand their ternary nature coupled with comparatively low ordering energies allows for different states of order to be realized, and on the other hand they host a variety of functional properties. One of these is ferromagnetic half-metallicity, where for a ferromagnetic system the Fermi energy falls into a band gap in one spin channel but not the other, so that any current will involve electrons of only one spin state. This behaviour makes them potentially very attractive for spintronics.

A number of quaternary Mn-based systems of composition  $XX'MnZ$ , where  $X$  and  $X'$  are transition metals and  $Z$  is a main group element, have been predicted by density-functional theory calculations to display a ferromagnetic half-metallic state [1]. In these calculations a specific atomic order is invariably assumed, with each of the four interpenetrating fcc sublattices that make up the Heusler structure being occupied by a distinct element, giving  $Fm\bar{3}m$  symmetry.

$NiCoMnGa$  [2] and  $NiCoMnAl$  [3] are examples of theoretically predicted ferromagnetic half-metals. While for the first system the agreement of the computed and measured saturation magnetization has been taken as evidence for the experimental realization of half-metallicity [2], neutron diffraction on  $NiCoMnAl$  in an unspecified state of thermal treatment has shown the system to be in the B2 state, that is, with perfect disorder both between Ni and Co and between Mn and Al [3].

To determine the ordering thermodynamics in these two systems as well as the associated kinetics, we performed temperature-dependent neutron diffraction measurements at the SPODI

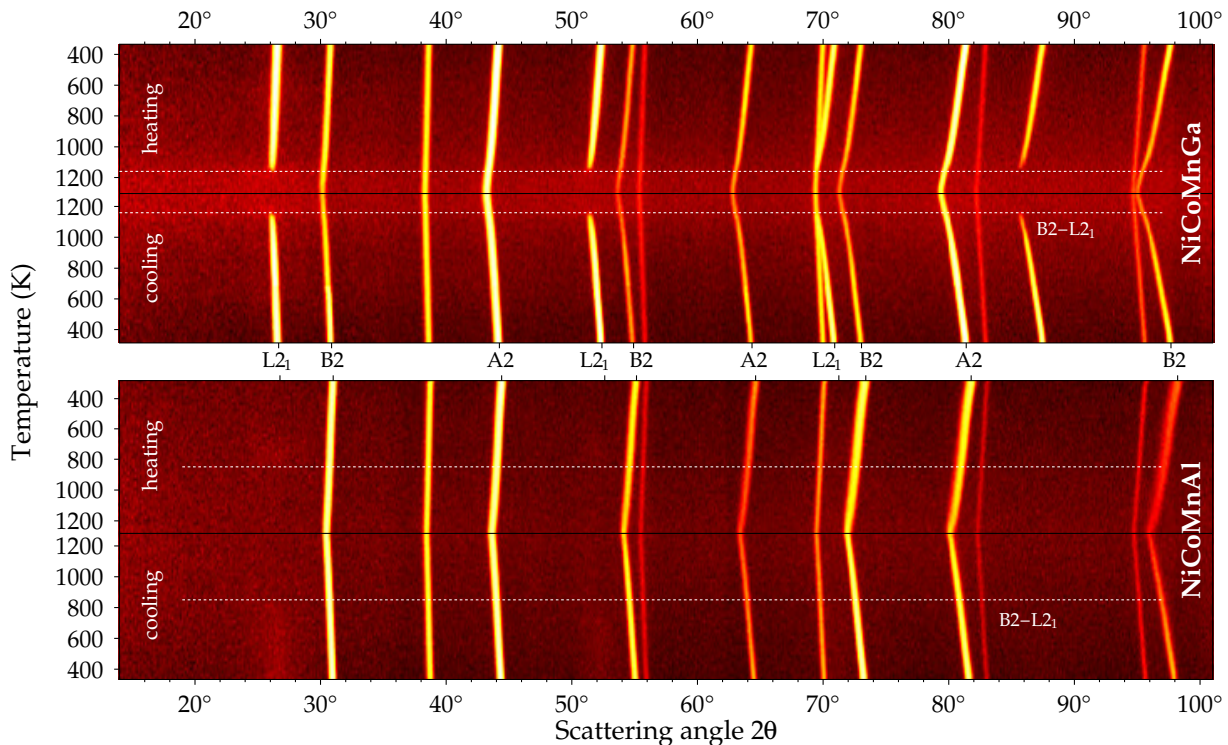


Figure 6.5:

Temperature-dependent neutron diffraction on  $NiCoMnGa$  and  $NiCoMnAl$ . Peak families are indicated, with the unlabelled peaks being due to the Nb sample can (which can additionally be discerned by the different thermal expansion coefficients).

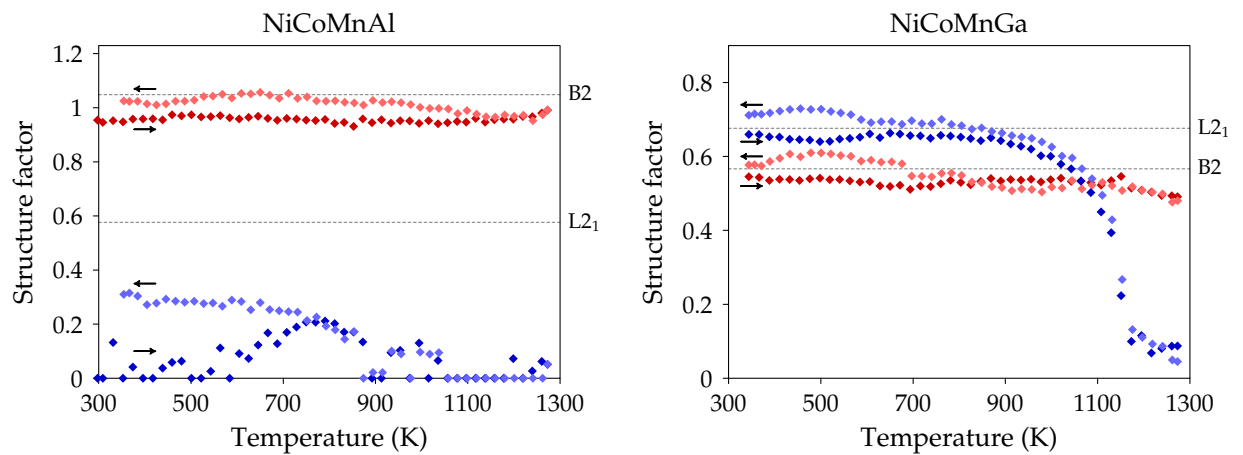


Figure 6.6:

Temperature-dependent structure factors for B2 and  $L2_1$  peaks, with the values for the perfectly ordered states indicated by dotted lines.

diffractometer at the FRM II. The as-cast polycrystalline samples had been subjected to a solution-annealing treatment at 1273 K, followed by quenching in room-temperature water. Starting from this state, the samples were measured continuously both on heating up to 1273 K and cooling at rates of approximately 2 K/min. The resulting temperature-dependent diffractograms are given as waterfall plots in Fig. 6.5.

For NiCoMnGa, a qualitative inspection of the data shows a vanishing of the  $L2_1$  peaks around 1160 K with perfect symmetry between heating and cooling. Thus, we interpret this as the equilibrium phase transition temperature to the B2 state, with kinetics at this elevated temperature being practically instantaneous. On the other hand, in NiCoMnAl the  $L2_1$  peaks are missing in the initial quenched state. During heating, around 600 K a very diffuse peak at the first two  $L2_1$  positions appears and vanishes again around 850 K, reappearing at the same temperature on cooling. This shows that  $L2_1$  order in NiCoMnAl is stable only below 850 K, where the associated ordering kinetics are much slower, thus leading to perfectly B2-ordered states at room temperature by quenching, and secondly restricting the experimentally achievable  $L2_1$  coherence lengths to quite small scales, indicated by the broad peaks.

A quantitative interpretation by the relative structure factors, that is, essentially the ratio of superstructure to fundamental peaks taking into account multiplicity, Lorentz and Debye-Waller factors, is given in Fig. 6.6. This shows that the degree of B2 order, that is, the separation of Ni and Co on the one hand and Mn and Al/Ga on the other hand, is nearly perfect and only weakly dependent on temperature. As discussed above, the  $L2_1$  peaks vanish at the phase transition, but specifically for NiCoMnAl, also below this temperature the structure factor stays significantly below the value expected for a perfect distinction between Mn and Al sublattices. A point to note is that in both cases the theoretically assumed Y-ordering can be ruled out, as the additional distinction between Ni and Co would lead to still higher structure factors. According to our pertaining density-functional theory calculations, both systems are thus not expected to be half-metals in their thermodynamically stable states of order.

- [1] K. Özdoğan, E. Şaşıoğlu, I. Galanakis, *J. Appl. Phys.* **113**, 193903 (2013)
- [2] V. Alijani, J. Winterlik, G. H. Fecher, S. S. Naghavi, C. Felser, *Phys. Rev. B* **83**, 184428 (2011).
- [3] M. Halder, M. D. Mukadam, K. G. Suresh, S. M. Yusuf, *J. Magn. Magn. Mater.* **377**, 220 (2015).
- [4] P. Neibecker, M. E. Gruner, X. Xu, R. Kainuma, W. Petry, R. Pentcheva, M. Leitner, *Phys. Rev. B* **96**, 165131 (2017).



## 7 Teaching and outreach

### 7.1 Lectures, seminars and lab courses

#### Spring Term 2017

Prof. Dr. Peter Müller-Buschbaum, *Experimentalphysik 2 für MSE*

Prof. Dr. Christine Papadakis, *Angewandte Physik: Polymerphysik 2*

Prof. Dr. Peter Müller-Buschbaum, Dr. Volker Körstgens,

*Nanostructured Soft Materials 2*

Prof. Dr. Peter Müller-Buschbaum, Prof. Dr. Christine M. Papadakis,

*Seminar über Struktur und Dynamik kondensierter Materie*

Prof. Dr. Peter Müller-Buschbaum, Prof. Dr. Christine M. Papadakis,

*Seminar: Polymere*

Prof. Dr. Peter Müller-Buschbaum, Prof. Dr. Christine M. Papadakis,

*Studentenseminar: Grundlegende Phänomene der Physik der weichen Materie*

Prof. Dr. Peter Müller-Buschbaum, *Seminar: Aktuelle Probleme der organische Photovoltaik*

Prof. Dr. Peter Müller-Buschbaum, Prof. Dr. Christine M. Papadakis,

*Bachelor-Seminar: Funktionelle weiche Materialien*

Prof. Dr. Peter Böni, Prof. Dr. Winfried Petry, Dr. Christoph Morkel, Dr. Sebastian Mühlbauer,

Dr. Tobias Schrader, *Seminar über Neutronen in Forschung und Industrie*

Prof. Dr. Winfried Petry, *Erasmus Mundus MaMaSELF Summerschool*

Montpellier, France, 4 – 15 Sep 2017

Prof. Dr. Winfried Petry, *Advanced hands-on training no. 61 „Astrophysics and Cosmology“*

Gymnasium Zwiesel, 28 – 30 Apr 2017

Prof. Dr. Winfried Petry, *Ferienakademie Sarntal, Session 8 „Energy Materials“*

Sarntal, Italy, 17 – 29 Sep 2017

#### Autumn Term 2017/2018

Prof. Dr. Peter Müller-Buschbaum, *Experimentalphysik 1 für MSE*

Prof. Dr. Peter Müller-Buschbaum, Dr. Volker Körstgens, *Nanostructured Soft Materials 1*

Prof. Dr. Peter Müller-Buschbaum, Prof. Dr. Christine M. Papadakis,

*Seminar über Struktur und Dynamik kondensierter Materie*

Prof. Dr. Peter Müller-Buschbaum, Prof. Dr. Christine M. Papadakis, *Seminar: Polymere*

Prof. Dr. Peter Müller-Buschbaum, Prof. Dr. Christine M. Papadakis,

*Studentenseminar: Grundlegende Phänomene der Physik der weichen Materie*

Prof. Dr. Peter Müller-Buschbaum, *Seminar: Aktuelle Probleme der organische Photovoltaik*

Prof. Dr. Peter Böni, Prof. Dr. Winfried Petry, Dr. Markos Skoulatos, Dr. Alexandros

Koutsoumpas, *Seminar Neutrons for research and Industry*

Dr. Michael Leitner *Materialphysik auf atomarer Skala 1*

Prof. Dr. Winfried Petry, *Physics with Neutrons 1*

Prof. Dr. Winfried Petry, Dr. Robert Georgii, *Advanced hands-on training no. 61 - Neutron scattering at FRM II*

Prof. Petry, Dr. Markus Kellermeier, *Mastercourse "Radiation Biology"*

**Lab Courses 2017**

*JCNS Laboratory Course - Neutron Scattering* (Forschungspraktikum)

*Neutron scattering at FRM II* (Fortgeschrittenenpraktikum)

*Theoretische und praktische Einführung in AFM* (Fortgeschrittenenpraktikum)

*Thermische Analyse* (Fortgeschrittenenpraktikum)

## 7.2 Conferences and public outreach

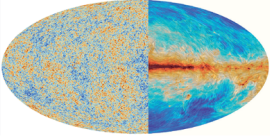
W. Petry

*Erster Spatenstich Neue Zentralgebäude JCNS/HGF - FRM II/TU*

Garching, 20 Feb 2017



P. Müller-Buschbaum  
 Lehrerfortbildung "Astrophysik und Kosmologie"  
 41. Edgar-Lüscher-Seminar  
 Zwiesel, 28 – 30 Apr 2017

Programm	Organisation	41. Edgar-Lüscher-Seminar
<p><b>Freitag, 28. April 2017</b></p> <p>13.00 - 14.30 Studienberatung der TUM                      15.00 - 15.30 Begrüßung                      15.30 - 16.45 Urknall, Hintergrundstrahlung, Expansion  <i>Prof. Dr. Jochen Weller, LMU München</i>                      16.45 - 17.30 Diskussion und Kaffeepause                      17.30 - 18.45 Röntgenastronomie  <i>Prof. Dr. Stern Wilms, Sternwarte Bamberg</i>                      18.45 - 19.00 Diskussion</p> <p><b>Samstag, 29. April 2017</b></p> <p>09.00 - 10.15 Beobachtung von Gravitationswellen mittels Laserinterferometrie  <i>Prof. Dr. Benno Willke, Max-Planck-Institut für Gravitationsphysik Hannover</i>                      10.15 - 11.00 Diskussion und Kaffeepause                      11.00 - 12.15 Allgemeine Relativitätstheorie und Gravitationswellen  <i>Prof. Dr. Ewald Mueller, Max-Planck-Institut für Astrophysik Garching</i>                      12.15 - 12.30 Diskussion                      14.30 - 15.45 Dunkle Materie und Gravitationslinsen  <i>Dr. Jörg Dietrich, Universitäts-Sternwarte München</i>                      15.45 - 16.30 Diskussion und Kaffeepause                      16.30 - 17.45 Vom Anfang der Zeit - unser Kosmos im Mikrowellenlicht  <i>PD Dr. Torsten Enßlin, Max-Planck-Institut für Astrophysik Garching</i>                      17.45 - 18.00 Diskussion</p> <p><b>Sonntag, 30. April 2017</b></p> <p>09.00 - 10.15 Supernovae und Kosmologie  <i>Dr. Benno Leibundgut, ESO Garching</i>                      10.15 - 11.00 Diskussion und Kaffeepause                      11.00 - 12.15 Schwarze Löcher  <i>Dr. Andreas Müller, Exzellenzcluster Universe TU München</i>                      12.15 - 13.00 Diskussion, Themenfindung für das 42. Edgar-Lüscher-Seminar</p>	<div style="display: flex; justify-content: space-between;"> <div style="width: 45%;">  <p><b>Prof. Dr. Peter Müller-Buschbaum</b> TUM</p> <p>Prof. Müller-Buschbaum ist Sprecher für das Netzwerk „Regenerative Energien (NRG)“ in der Munich School of Engineering (MSE) der TU München, Leiter des Keylabs „TUM solar“ im Forschungsnetzwerk „Solar Technologies Go Hybrid“, Deutscher Vertreter bei der European Polymer Federation (EPF) für den Bereich Polymerphysik und Associate Editor der Zeitschrift „ACS Applied Materials &amp; Interfaces“ der „American Chemical Society“ (ACS). Er befasst sich in seiner Forschungsarbeit mit der Entwicklung polymerbasierter Materialien mit neuartigen Struktur-Eigenschaftsbeziehungen.</p> </div> <div style="width: 45%;">  <p><b>Prof. Dr. Winfried Petry</b> TUM</p> <p>Prof. Petry ist Ordinarius am Lehrstuhl für Funktionelle Materialien (E3) des Physik Departments der TU München, Betreuungsdirektor für die Bayerische Eliteakademie und Wissenschaftlicher Direktor der Forschungsneutronenquelle Heinz Maier-Leibnitz (FRM II). Er forscht auf dem Gebiet der Materialwissenschaften mit Neutronen.</p> </div> </div> <p><b>Organisatorische Hinweise</b></p> <p>Organisation vor Ort:                      OSD Heribert Strunz, Gymnasium Zwiesel                      OSR Christian Stoiber, Gymnasium Zwiesel                      SR Claus Starke, Gymnasium Zwiesel                      SR Josef Müller, Gymnasium Zwiesel                      SR Thomas Kufner, Gymnasium Zwiesel</p> <p>E-Mail: luescherseminar@gymnasium-zwiesel.de</p> <p>Hinweise:</p> <ul style="list-style-type: none"> <li>• Alle Vorträge finden in der Aula des Gymnasiums Zwiesel statt.</li> <li>• Für 5,- € erhalten die Teilnehmer am Ende des Seminars eine CD mit sämtlichen freigegebenen Vorträgen und den bisherigen Festschriften.</li> <li>• In den ausgewiesenen Kaffeepausen wird in der Mensa des Gymnasiums Kaffee und Kuchen gegen eine freiwillige Spende angeboten.</li> <li>• Am Rande der Aula findet eine Ausstellung verschiedener Lehrmittelausstattungen und Verlage statt.</li> </ul>	<p style="text-align: center;"><b>Astrophysik und Kosmologie</b></p>  <p style="text-align: center;">am Gymnasium Zwiesel                      Freitag, 28. April 2017 bis Sonntag, 30. April 2017</p> <p><b>Schirmherr:</b>                      Prof. Dr. h.c. mult. Wolfgang A. Herrmann,                      Präsident der TUM</p> <p><b>Veranstalter:</b>                      Ltd. OSD Anselm Råde,                      Ministerialbeauftragter für die Gymnasien in Niederbayern</p> <p><b>Wissenschaftliche Leitung:</b>                      Prof. Dr. Peter Müller-Buschbaum, TUM                      Prof. Dr. Winfried Petry, TUM</p> <div style="display: flex; justify-content: space-around; align-items: center;">    </div> <p style="font-size: small; text-align: center;">Titelbild: PD Dr. Torsten Enßlin ©</p>

W. Petry, P. Müller-Buschbaum  
 3rd internal biennial science meeting of the MLZ  
 Grainau 19 – 22 Jun 2017

**3<sup>rd</sup> internal biennial science meeting of the MLZ – 19.6-22.6.17 in Grainau**  
*All overview talks are 30 min + 15 min discussion, all contributed talks 10 min + 5 min discussion*

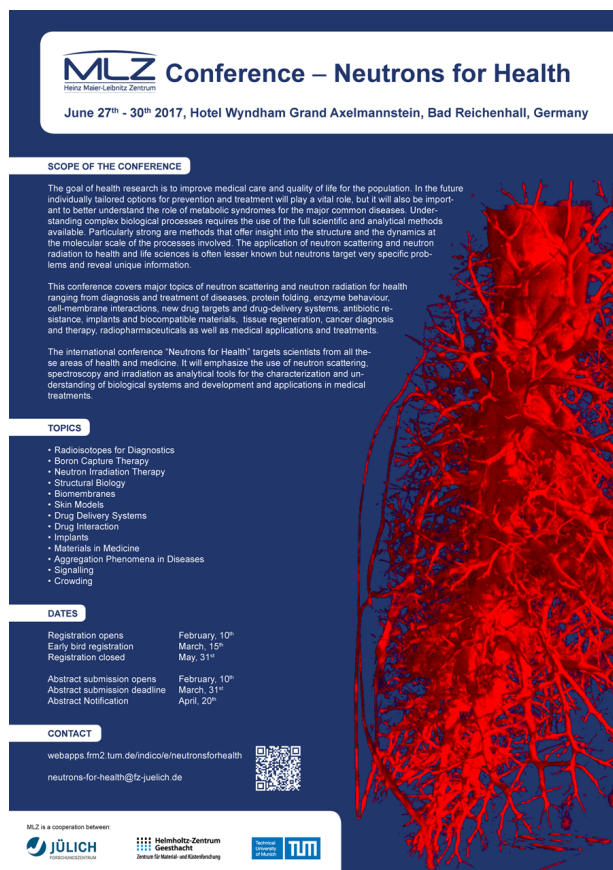
	Monday 19.6.17	Tuesday 20.6.17	Wednesday 21.6.17	Thursday 22.6.17
8:00		Breakfast	Breakfast	Breakfast
9:00–10:30	9:00 Departure (We meet at the Pforte FRM-II)	Plenary session  Overview ESS (A. Schreyer) Overview Talk Quantum Phenomena ()	Plenary session  Discussion: Sample Environment / Poster E13  Overview Talk Soft Matter (S. Wellert)	Parallel sessions  • Structure II • QM II • Soft matter III
10:30–11:00		Coffee	Parallel session	Plenary session
11:00–12:30		Parallel sessions  • Quantum Phenomena Workshop on future needs for Magnets • Material Science I • Soft matter I	• Material Science II • Soft matter II • Structure I • QM I	Newly arrived personnel  The Nobel price 2016 (S. Mühlbauer) Overview Talk Structure (N. Walte)
13:00–14:30	Lunch	Lunch	12:00 Lunch	Lunch
14:30–16:00	Plenary session 14:15 Welcome (T. Brückel)  Overview Material Science (Z. Revay) MLZ Sample Environment (J. Peters, A. Weber)	Plenary sessions  Overview talk Fundamental Physics () Discussion: Integration of HZB instruments and future of MLZ after 2020 / Poster E13	12:45 Excursion  Schneeferner Haus / Wetterstation Zugspitze	14:30 Departure
16:00–16:30	Coffee	Coffee		
16:30–18:30	Parallel sessions  • 4 Scientific groups: Collecting input for plenary sessions on MLZ future and sample environment • Internal meeting E13	Poster presentation  17:30 Walk to the Neuneralm		17:00 Return (to the Pforte FRM-II)
18:30	Dinner	Brotzeit: Neuneralm	Dinner	
20:00		Departure 23:00	Dust from „recent“ supernovae, just around the corner (T. Faestermann, E12, TUM)	



W. Petry

*MLZ-Conference: Neutrons for Health*

Bad Reichenhall, 27 – 30 Jun 2017



**MLZ** Conference – Neutrons for Health  
Heinz Maier-Leibnitz Zentrum

June 27<sup>th</sup> - 30<sup>th</sup> 2017, Hotel Wyndham Grand Axelmannstein, Bad Reichenhall, Germany

**SCOPE OF THE CONFERENCE**

The goal of health research is to improve medical care and quality of life for the population. In the future individually tailored options for prevention and treatment will play a vital role, but it will also be important to better understand the role of metabolic syndromes for the major common diseases. Understanding complex biological processes requires the use of the full scientific and analytical methods available. Particularly strong are methods that offer insight into the structure and the dynamics at the molecular scale of the processes involved. The application of neutron scattering and neutron radiation to health and life sciences is often lesser known but neutrons target very specific problems and reveal unique information.

This conference covers major topics of neutron scattering and neutron radiation for health ranging from diagnosis and treatment of diseases, protein folding, enzyme behaviour, cell-membrane interactions, new drug targets and drug-delivery systems, antibiotic resistance, implants and biocompatible materials, tissue regeneration, cancer diagnosis and therapy, radiopharmaceuticals as well as medical applications and treatments.

The international conference "Neutrons for Health" targets scientists from all these areas of health and medicine. It will emphasize the use of neutron scattering, spectroscopy and irradiation as analytical tools for the characterization and understanding of biological systems and development and applications in medical treatments.

**TOPICS**

- Radiosopes for Diagnostics
- Boron Capture Therapy
- Neutron Irradiation Therapy
- Structural Biology
- Biomembranes
- Skin Models
- Drug Delivery Systems
- Drug Interaction
- Implants
- Materials in Medicine
- Aggregation Phenomena in Diseases
- Signalling
- Crowding

**DATES**

Registration opens	February, 10 <sup>th</sup>
Early bird registration	March, 15 <sup>th</sup>
Registration closed	May, 31 <sup>st</sup>
Abstract submission opens	February, 10 <sup>th</sup>
Abstract submission deadline	March, 31 <sup>st</sup>
Abstract Modification	April, 20 <sup>th</sup>

**CONTACT**

webapps.frm2.tum.de/indico/en/neutronsforhealth  
 neutrons-for-health@fz-juelich.de

MLZ is a cooperation between:

**JÜLICH** Helmholtz-Zentrum für Materialforschung und -entwicklung  
**TUM** Technical University of Munich



W.A. Hermann, T. Hamacher, M. Becherer, G. Friedl, P. Müller-Buschbaum, H. Spliethoff  
 7th MSE Colloquium "Highlights in Energy Research"  
 Garching, 13 Jul 2017

Munich School of Engineering  
 Technische Universität München



7<sup>th</sup> Energy Colloquium of the Munich School of Engineering

## Highlights in Energy Research

July 13, 2017 – 8:30 a.m. to 8:00 p.m.  
 TUM – Center for Energy and Information (ZEI), Garching

**8:30 – 9:00 a.m.**  
 Registration

**9:00 – 9:15 a.m.**  
 Opening  
 Prof. Thomas Hamacher, Director Munich School of Engineering

**9:15 – 9:45 a.m.**  
 Keynote: "The Energiewende, a show case for technical and policy innovation and what other countries can learn from Germany"  
 Dr. Fabian Joas, Agora Energiewende

**9:45 – 11:00 a.m.**  
 Session  
 Session Chair: Dr. Markus Becherer

**Second Generation CO<sub>2</sub> Methanation Catalysts**  
 Thomas Burger, Chair of Chemical Technology I

**Modeling Occupational Disorder in Li<sub>4</sub>Ti<sub>5</sub>O<sub>12</sub> Battery Materials: Intrinsic Complexity and its Effect on Ion Mobility**  
 Hendrik Heenen, Chair of Theoretical Chemistry

**Perovskite: The New Crystalline Sheriff in the Photovoltaic County**  
 Shambhavi Pratap, Functional Materials

**11:00 – 11:45 a.m.**  
 Poster Presentation, Coffee Break

**11:45 – 1:00 p.m.**  
 Session  
 Session Chair: Prof. Hartmut Spliethoff

**Simulation and Optimization of Open Algae Ponds**  
 Andreas Rarrek, Chair of Plant and Process Technology

**The Hybrid Transmission Grid Architecture: A Topology-Preserving Capacity Expansion Strategy**  
 Matthias Hotz, Associate Professorship of Signal Processing

**High Pressure Evaporation Rig for the Investigation of Stationary and Transient Heat Transfer Phenomena**  
 Tobias Gschnaidtner, Energy Valley Bavaria

**1:00 – 2:30 p.m.**  
 Poster Presentation, Lunch Break

**2:30 – 4:10 p.m.**  
 Session  
 Session Chair: Prof. Gunther Friedl

**Synergistic Value of Hybrid Energy Systems: Renewable Power and Hydrogen Production**  
 Gunther Glenk, Chair of Management Accounting

**Mine or Ours? Willingness to Pay for Innovative Battery Storage Concepts**  
 Bernhard Kalkbrenner,  
 Chair of Marketing and Consumer Research

**With Innovative Highlights Towards a Sustainable TUM Campus**  
 Benedikt Schweiger, Chair of Energy Systems

**Nearly Zero Energy Laboratory Buildings?**  
 Michael Keltsch, Institute of Energy Efficient and Sustainable Design and Building

**4:10 – 4:40 p.m.**  
 Poster Presentation, Coffee Break

**4:40 – 5:10 p.m.**  
 MSE-Research  
 Geothermie-Allianz Bayern – Scientists United for Geothermal Energy  
 Dr. Katharina Aubele, Munich School of Engineering

**5:10 – 5:40 p.m.**  
 Keynote: "TUM Startup Li.plus - Battery diagnostics - fast. precise. simple."  
 Christian Huber, Li.plus

**5:40 – 5:55 p.m.**  
 Summary, Closing

**5:55 – 8:00 p.m.**  
 Poster and Presentation Award, Colloquium Dinner

**Registration:**  
<http://www.mse.tum.de>

P. Müller-Buschbaum, W. Petry  
*Lehrerfortbildung "Moderne Materialien"*  
Edgar-Lüscher Lectures  
Dillingen, 27 – 29 Sep 2017

EDGAR-LÜSCHER-LECTURES DILLINGEN/DONAU 2017  
Thema: Moderne Materialien  
Datum: Mittwoch, 27. September bis Freitag, 29. September 2017  
Tagungsort: Akademie für Lehrerfortbildung Dillingen  
Veranstalter: Akademie für Lehrerfortbildung Dillingen und TU München  
wissenschaftliche Leitung: Prof. Dr. Peter Müller-Buschbaum,  
Technische Universität München.

Programm

**Mittwoch, 27. 09. 2017**

15:00 – 15:30 Begrüßung

StD Werner Ettinger / Prof. Dr. Peter Müller-Buschbaum (Physik-Department TUM)

15:30 – 17:00 Prof. Helmut Karl (Universität Augsburg, Institut für Physik)  
Thermoelektrische Materialien

18:30 – 20:00 Prof. Dr. Thomas Hellweg (Bielefeld University, Faculty of Chemistry)  
Hyrogele

**Donnerstag, 28. 09. 2017**

8:30 – 10:00 Prof. Dr. Volker Presser (Leibniz-Institut für Neue Materialien,  
Saarbrücken)  
Kohlenstoff Nanomaterialien

10:00 – 10.30 Kaffeepause

10:30 – 12:00 Dr. Ursula Wurstbauer (TUM, Walter Schottky Institut)  
Zwei-dimensionale Schichtmaterialien

15:30 – 17:00 Prof. Dr. Thomas Weitz (LMU, Fakultät für Physik)  
Organische Elektronik

18:30 – 20:00 Prof. Dr. Ulrich Herr (Universität Ulm, Institut für Mikro- und  
Nanomaterialien)  
Nanokristalline Leuchtstoffe

**Freitag, 29. 09. 2017**

8:30 – 10:00 Dr. Wolfgang Kreuzpaintner (TUM, Physik-Department)  
Dünne magnetische Schichten

10:00 – 10.30 Kaffeepause

10:30 – 12:00 Dr. Friedemann Reinhard (TUM, Walter Schottky Institut)  
Quantensensoren

Ab 12:00 Lehrgangsabschluss  
Prof. Dr. Peter Müller-Buschbaum / StD Werner Ettinger

C.M. Papadakis, P. Müller-Buschbaum

*Kolloid-Tagung Multiresponsive Systems, 48. Hauptversammlung der Kolloid-Gesellschaft  
Garching, 9 – 11 Oct 2017*

### Invited talks

R. Lipowsky (Max-Planck-Institute of Colloids and Interfaces, Potsdam)

*Giant vesicles as multiresponsive microcompartments*

C. Tsitsilianis (University of Patras, Greece)

*Multiresponsive star-shaped polymer-based nanocarriers*

R. H. Müller (Free University of Berlin, Germany)

*Solid lipid nanoparticles - from the academic idea to the market*

S. V. Roth (DESY, Hamburg; KTH, Stockholm, Sweden)

*Nanostructured and colloidal layer formation via spray coating*

M. Shibayama (The University of Tokyo, Japan)

*Precision polymer network science with tetra-PEG gels*

J. G. C. Veinot (The University of Alberta, Edmonton, Canada)

*Highly emissive silicon nanocrystals prepared via simultaneous etching and surface functionalization*

R. von Klitzing (Technische Universität Darmstadt; Technische Universität Berlin)

*Swelling behaviour and mechanical properties of multiresponsive microgels at interfaces*

I. K. Voets (University of Technology Eindhoven, The Netherlands)

*Illuminating interfaces in soft matter by single-molecule localization microscopy*

F. Winnik (Université de Montréal, Canada)

*Responsive and thermo-lockable hydrogels and nanogels*

P. Štěpánek (Institute of Macromolecular Chemistry, Prague, Czech Republic)

*Multiresponsive polymers: cross-talk between pH and temperature responsivity*



C.M. Papadakis, D. Wöll

*3rd Workshop "Fluorescence Correlation Spectroscopy in Soft Matter Science"*

Garching, 11 – 12 Oct 2017

### Invited talks

P. Schuille (Max-Planck-Institute of Biochemistry, Martinsried)

*Wide-Field TIR FCS: Uncovering the secrets of transient membrane binding*

C. G. Palivan (University of Basel)

*How FCS and FCCS give details about artificial organelles as novel solution for protein therapy?*

B. Schuler (University of Zurich, Switzerland)

*Single-molecule spectroscopy and FCS of intrinsically disordered proteins*



### 7.3 Service to the community

**Prof. Dr. Peter Müller-Buschbaum:**

- Since 7/2017 member of the Aptitude Committee of master course Materials Science and Engineering (MS&E) at TUM
- Since 9/2016 spokesman and board member of the Graduate School of "Munich School of Engineering" (MSE) at TUM
- Since 6/2016 member of the doctoral committee of "Munich School of Engineering" (MSE) at TUM
- Since 3/2015 member of "Advanced Light Source (ALS) Review Panel"
- Since 9/2014 member of "Heinz Maier-Leibnitz Zentrum (MLZ) Review Panel"
- Since 6/2014 member of Stanford Synchrotron Radiation Lightsource (SSRL) Review Panel
- Since 9/2012 Associate Editor of journal "ACS Applied Materials & Interfaces" of the American Chemical Society
- Since 3/2012 head of KeyLab "TUM.Solar" at TU Munich
- Since 1/2012 member of the Scientific Selection Panel of the Helmholtz-Zentrum Berlin für Materialien und Energie (HZB)
- Since 2011 member of European Spallation Source (ESS) Scientific Advisory Panel (Reflectivity)
- Since 2011 German representative at the European Polymer Federation (EPF) for polymer physics
- Since 2010 spokesman of the regenerative energies section (NRG) at the Munich School of Engineering (MSE) of TU Munich
- Since 2010 member of TUM Energie at TU Munich
- Since 2010 German representative at the European Synchrotron User Organization (ESUO)
- Since 2008 chairman of "DESY Photon Science User Committee" at the synchrotron radiation laboratory DESY in Hamburg

**Prof. Dr. Christine M. Papadakis:**

- Since 4/2015 Editor-in-Chief for Colloid & Polymer Science, Springer-Verlag
- Vice women's representative of the Physics Department at TU München

**Prof. Dr. Winfried Petry:**

- Since 2016 member of the Evaluation Panel for Neutron Research of the Swedish Research Council
- Since 2015 member of the Neutron Scientific Advisory Committee of the National Research Center Kurchatov Institute "Petersburg Nuclear Physics Institute" (PNPI, Gatchina)
- Since 2012 member of the Scientific Advisory Board of NaWi Graz
- Since 2007 member of the Steering Committee of the Laue Langevin Institute and chairman of the instrumentation review panel of the CEA Leon Brillouin Laboratory
- Since 1999 liaison professor of Bayerische Eliteakademie (Bavarian Leadership Academy) and since May 2011 member of the Board of Trustees

## 8 Publications, talks and funding

### 8.1 Publications

- A. V. Berezkin, F. Jung, D. Posselt, D.-M. Smilgies, C. M. Papadakis  
*Vertical vs lateral macrophase separation in thin films of block copolymer mixtures: computer simulations and GISAXS experiments*  
ACS Appl. Mater. Interfaces **9**, 31291-31301 (2017)
- H. Breitzkreutz, J. Hingerl, J. Shi, W. Petry  
*Ion-irradiation induced inter diffusion layer growth in UMo/Al fuels*  
AccApp'17 (13th International Topical Meeting on the Nuclear Applications of Accelerators), Québec, Kanada (2017)
- H. Breitzkreutz, R. Jungwirth, T. Zweifel, H.-Y. Chiang, J. Shi, W. Petry  
*Heavy ions irradiation as a tool to minimize the number of in-pile tests in UMo fuel development*  
Annual Meeting of Nuclear Technology 2017, Berlin (2017)
- P. Brocca, V. Rondelli, F. Mallamace, M.T. Di Bari, A. Deriu, W. Lohstroh, E. Del Faveroa, M. Cortia, L. Cantu  
*Water response to ganglioside gm1 surface remodelling* Biochimica et Biophysica Acta (BBA)-General Subjects **1861 B**, 3573 – 3580 (2017)
- T.W. Crothers, R.L. Milot, J.B. Patel, E.S. Parrott, J. Schlipf, P. Müller-Buschbaum, M.B. Johnston, L.M. Herz  
*Photon reabsorption masks intrinsic bimolecular charge-carrier recombination in CH<sub>3</sub>NH<sub>3</sub>PbI<sub>3</sub> perovskite*  
Nano Lett. **17**, 5782-5789 (2017)
- M. A. Dyakonova, G. Gotzamanis, B.-J. Niebuur, N. S. Vishnevetskaya, K. N. Raftopoulos, Z. Di, S.K. Filippov, C. Tsitsilianis, C.M. Papadakis  
*pH responsiveness of hydrogels formed by telechelic polyampholytes*  
Soft Matter **13**, 3568-3579 (2017)
- S. K. Filippov, N. S. Vishnevetskaya, B.-J. Niebuur, E. Koziolová, E. A. Lomkova, P. Chytil, T. Etrych, C. M. Papadakis  
*Influence of molar mass, dispersity, and type and location of hydrophobic side chain moieties on the critical micellar concentration and stability of amphiphilic HPMA-based polymer drug carriers*  
Colloid Polym. Sci. **295**, 1313-1325 (2017)
- F. Fuchs, S. Schmitt, C. Walter, B. Engels, E.M. Herzig, P. Müller-Buschbaum, V. Dyakonov, C. Deibel  
*Vibrational spectroscopy of a low band gap donor-acceptor copolymer and blends*  
J.Phys.Chem. C **121**, 19543-19547 (2017)
- A. Glensk, B. Grabowski, T. Hickel, J. Neugebauer, M. Leitner, J. Neuhaus, W. Petry  
*Ab initio determination of phonon lifetimes up to the melting point*  
EMRS Spring 2017, May 2017
- A. Greppmair, B. Stoib, N. Saxena, C. Gerstberger, P. Müller-Buschbaum, M. Stutzmann, M.S. Brandt  
*Measurement of the in-plane thermal conductivity by steady-state infrared thermography*  
Rev. Sci. Instr. **88**, 044903 (2017)

- S. Guo, W. Wang, E.M. Herzig, A. Naumann, G. Tainter, J. Perlich, P. Müller-Buschbaum  
*Solvent-morphology-property relationship of PTB7:PC71BM polymer solar cells*  
ACS Appl. Mater. Interfaces **9**, 3740-3748 (2017)
- V. Hildebrand, M. Heydenreich, A. Laschewsky, H.M. Möller, P. Müller-Buschbaum, C.M. Papadakis, D. Schanzenbach, E. Wischerhoff  
*"Schizophrenic" Self-assembly of dual thermoresponsive block copolymers bearing a zwitterionic and a non-ionic hydrophilic block*  
Polymer **122**, 347-357 (2017)
- V. Hildebrand, A. Laschewsky, M. Päch, P. Müller-Buschbaum, C.M. Papadakis  
*Effect of the zwitterion structure on the thermo-responsive behaviour of poly(sulfobetaine methacrylate)s*  
Polym. Chem. **8**, 310-322 (2017)
- R. Hildner, A. Köhler, P. Müller-Buschbaum, F. Panzer, M. Thelakkat  
*Pi-conjugated donor polymers: Structure formation and morphology in solution, bulk and photovoltaic blends*  
Adv. Energy Mater. **7**, 1700314 (2017)
- L. Karge, R. Gilles, D. Mukherji, P. Strunz, P. Beran, M. Hofmann, J. Gavilano, et al  
*The influence of C/Ta ratio on TaC precipitates in Co-Re base alloys investigated by small-angle neutron scattering*  
Acta Materialia **132**, 354 - 366 (2017)
- S. Koutsoumpis, K. N. Raftopoulos, O. Oguz, C. M. Papadakis, Y. Z. Menceloglu, P. Pissis  
*Dynamic glass transition of the rigid amorphous fraction in polyurethane-urea/SiO<sub>2</sub> nanocomposites*  
Soft Matter **13**, 4580-4590 (2017)
- L. Lautner, K. Pluhackova, N. Barth, T. Seydel, W. Lohstroh, R. Böckmann, T. Unruh  
*Dynamic processes in biological membrane mimics revealed by quasielastic neutron scattering*  
Chemistry and Physics of Lipids **206**, 28 – 42 (2017)
- T. Linderl, T. Zechel, M. Brendel, D. Moseguí González, P. Müller-Buschbaum, J. Pflaum, W. Brütting  
*Energy losses in small-molecule organic photovoltaics*  
Adv. Energy Mater. **7**, 1700237 (2017)
- D. Moseguí González, K. N. Raftopoulos, G. He, C. M. Papadakis, A. Brown, E. Rivard, P. Müller-Buschbaum  
*Bandgap-tuning in triple-chalcogenophene polymer films by thermal annealing*  
Macromol. Rapid Commun. **38**, 1700065 (2017)
- D. Moseguí González, C. J. Schaffer, S. Pröller, J. Schlipf, L. Song, S. Bernstorff, E. M. Herzig, P. Müller-Buschbaum  
*Co-dependence between crystalline and photovoltage evolutions in P3HT:PCBM solar cells probed with in-operando GIWAXS*  
ACS Appl. Mater. Interfaces **9**, 3282-3287 (2017)
- P. Müller-Buschbaum, M. Thelakkat, T.F. Fässler, M. Stutzmann  
*Hybrid photovoltaics - from fundamentals towards application*  
Adv. Energy Mater. **7**, 1700248 (2017)

- P. Neibecker, M. E. Gruner, X. Xu, R. Kainuma W. Petry, R. Pentcheva, et al.  
*Ordering tendencies and electronic properties in quaternary Heusler derivatives*  
Phys. Rev. B **96**, 165131 (2017)
- P. Neibecker, M. Leitner, M. Kushaim, T. Boll, D. Anjum, T. Al-Kassab, F. Haider  
*L1<sub>2</sub> ordering and  $\delta'$  precipitation in Al-Cu-Li*  
Sci. Rep. **7**, 3254 (2017)
- B. J. Niebuur, K.-L. Claude, S. Pinzek, C. Cariker, K. N. Raftopoulos, V. Pipich, M. -S. Appavou, A. Schulte, C. M. Papadakis  
*Pressure-dependence of poly(N-isopropylacrylamide) mesoglobule formation in aqueous solution*  
ACS Macro Lett. **6**, 1180-1185 (2017)
- C. M. Papadakis, C. Tsitsilianis  
*Responsive hydrogels from associative block copolymers: Physical gelling through polyion complexation*  
Gels **3**, 3 (2017)
- M. L. Petrus, J. Schlipf, C. Li, T. P. Gujar, N. Giesbrecht, P. Müller-Buschbaum, M. Thelakkat, T. Bein, S. Hüttner, P. Docampo  
*Capturing the sun: A review of the challenges and perspectives of perovskite solar cells*  
Adv. Energy Mater. **7**, 170026 (2017)
- W. Petry, B. Frick, V. Garcia Sakai  
*Workshop on '50 Years of Neutron Backscattering Spectroscopy'*  
Neutron News **28 (1)**, 6-7 (2017)
- D. Posselt, J. Zhang, D.-M. Smilgies, A. Berezkin, I. I. Potemkin, C.M. Papadakis  
*Restructuring in block copolymer thin films: In-situ GISAXS investigations during solvent vapor annealing*  
Progr. Polym. Sci. **66**, 80-115 (2017)
- S. Pröllner, D. Moseguí González, C. Zhu, E. Schaible, C. Wang, P. Müller-Buschbaum, A. Hexemer, E.M. Herzig  
*Note: Setup for chemical atmospheric control during in situ grazing incidence x-ray scattering of printed thin films*  
Rev. Sci. Instr. **88**, 066101 (2017)
- C. Reiter, H. Breitzkreutz, A. Röhrmoser, A. Seubert, W. Petry  
*High precision neutronic calculations for transient simulations for FRM II*  
RRFM 2017, Rotterdam, Netherlands (2017)
- Y. Rui, H. Xiong, B. Su, H. Wang, Q. Zhang, J. Xu, P. Müller-Buschbaum  
*Liquid-liquid interface assisted synthesis of SnO<sub>2</sub> nanorods with tunable length for enhanced performance in dye-sensitized solar cells*  
Electrochem. Acta **227**, 49-60 (2017)
- N. Saxena, M. Coriç A. Greppmair, J. Wernecke, M. Pflüger, M. Krumrey, M. S. Brandt, E.M. Herzig, P. Müller-Buschbaum  
*Morphology-function relationship of thermoelectric nanocomposite films from PEDOT:PSS with silicon nanoparticles*  
Adv. Electronic Mater. **3**, 1700181 (2017)

- J. Schlipf, P. Müller-Buschbaum  
*Structure of organometal halide perovskite films as determined with grazing-incidence x-ray scattering methods*  
Adv. Energy Mater. **7**, 1700131 (2017)
- C. Schwarz  
*Construction and Commissioning of a Pulsed-DC Sputtering System and Characterization of Sputtered ZrN Layers*  
Masterarbeit, Technische Universität München, (2017)
- M. Schwartzkopf, A. Hinz, O. Polonskyi, T. Strunskus, F.C. Löhner, V. Körstgens, P. Müller-Buschbaum, F. Faupel, S.V. Roth  
*Role of sputter deposition rate in tailoring nanogranular gold structures on polymer surfaces*  
ACS Appl. Mater. Interfaces **9**, 5629-5637 (2017)
- L. Song, V. Körstgens, D. Magerl, B.Su, T. Fröschl, N. Hüsing, S. Bernstorff, P. Müller-Buschbaum  
*Low-temperature fabrication of mesoporous titania thin films*  
MRS Advances **2**, 2315-2325 (2017)
- L. Song, W. Wang, V. Körstgens, D. Moseguí González, F. C. Löhner, C. J. Schaffer, J. Schlipf, K. Peters, T. Bein, D. Fattakhova-Rohlfing, S. V. Roth, P. Müller-Buschbaum  
*In situ study of spray deposited titania photoanodes for scalable fabrication of solid-state dye-sensitized solar cells*  
Nano Energy **40**, 317-326 (2017)
- L. Song, W. Wang, S. Pröller, D. Moseguí González,, J. Schlipf, C. J. Schaffer, K. Peters, E.M. Herzig, S. Bernstorff, T. Bein, D. Fattakhova-Rohlfing, P. Müller-Buschbaum  
*In situ study of degradation in P3HT-titania based solid-state dye-sensitized solar cells*  
ACS Energy Lett. **2**, 991-997 (2017)
- C. Steyer, B. Baumeister, H. Breitreutz, W. Petry, B. Stepnik, M. Grasse, C. Moyroud  
*Characterization of monolithic UMo foils and Zr coatings for the EMPIRE irradiation experiment*  
RRFM 2017, Rotterdam, Netherlands (2017)
- B. Su, H. A. Caller-Guzman, V. Körstgens, Y. Rui, Y. Yao, N. Saxena, G. Santoro, S. V. Roth, P. Müller-Buschbaum  
*Macroscale and nanoscale morphology evolution during in situ spray coating of titania films for perovskite solar cells*  
ACS Appl. Mater. Interfaces **9**, 43724 (2017)
- B. Su, V. Körstgens, Y. Yao, D. Magerl, L. Song, E. Metwalli, S. Bernstorff, P. Müller-Buschbaum  
*Pore size control of block copolymer templated sol-gel synthesized titania films deposited via spray coating*  
J. Sol-Gel. Sci. Technol. **81**, 346-351 (2017)
- M. Tena-Solsona, B. Reiß, R. K. Grötsch, F.C. Löhner, C. Wanzke, B. Käs Dorf, A.R. Bausch, P. Müller-Buschbaum, O. Lieleg, J. Boekhoven  
*Non-equilibrium dissipative supramolecular materials with a tunable lifetime*  
Nat. Commun. **8**, 15895 (2017)

- Y. Tong, B.J. Bohn, E. Bladt, K. Wang, P. Müller-Buschbaum, S. Bals, A. S. Urban, L. Polavarapu, J. Feldmann  
*From precursor powders to CsPbX<sub>3</sub> perovskite nanowires: One-pot synthesis, growth mechanism and oriented self-assembly*  
Angew. Chem. **128**, 14075-14080 (2017)
- N. S. Vishnevetskaya, V. Hildebrand, B.-J. Niebuur, I. Grillo, S.K. Filippov, A. Laschewsky, P. Müller-Buschbaum, C. M. Papadakis  
*“Schizophrenic” micelles from doubly thermoresponsive polysulfobetaine-b-poly(N-isopropylmethacrylamide) diblock copolymers*  
Macromolecules **50**, 3985-3999 (2017)
- J. Wang, Y. Chen, J. An, K. Xu, T. Chen, P. Müller-Buschbaum Q. Zhong  
*Intelligent textiles with comfort regulation and inhibition of bacterial adhesion realized by cross-linking poly(n-isopropyl acrylamide-co-ethylene glycol methacrylate) to cotton fabrics*  
ACS Appl. Mater. Interfaces **9**, 13647-13656 (2017)
- R. Wang, Z.-Y. Di, P. Müller-Buschbaum, H. Frielinghaus  
*Effect of PCBM additive on morphology and optoelectronic properties of P3HT-b-PS films*  
Polymer **121**, 173-182 (2017)
- J. A. Weber, D. Benea, W. H. Appelt, H. Ceeh, W. Kreuzpaintner, M. Leitner, D. Vollhardt, Ch. Huginschmidt, L. Chioncel  
*Electronic correlations in vanadium revealed by electron-positron annihilation measurements*  
Phys. Rev. B **95**, 075119 (2017)
- Q. Zhong, E. Metwalli, M. Rawolle, G. Kaune, A. M. Bivigou-Koumba, A. Laschewsky, C. M. Papadakis, R. Cubitt, J. Wang, P. Müller-Buschbaum  
*Vacuum induced dehydration of swollen poly(methoxy diethylene glycol acrylate) and polystyrene-block-poly(methoxy diethylene glycol acrylate)-block-polystyrene films probed by in-situ neutron reflectivity*  
Polymer **124**, 263-273 (2017)
- Q. Zhong, J. Wang, P. Müller-Buschbaum  
*Smart control of cotton fabric comfort by cross-linking thermo-responsive poly(2-(2-methoxyethoxy) ethoxyethyl methacrylate-co-ethylene glycol methacrylate)*  
Textile Research Journal **87**, 1620-1630 (2017)
- X. Zuo, J. Zhu, P. Müller-Buschbaum. Y.-J. Cheng  
*Silicon based lithium-ion battery anodes: a chronicle perspective review*  
Nano Energy **31**, 113-143 (2017)

## 8.2 Talks

- L. Bießmann, M. Trunk, B. Su, H. Xu, S. Bernstorff, P. Müller-Buschbaum  
*Structural in-operando investigations on PEDOT:PSS electrodes under high humidity conditions*  
DPG-Frühjahrstagung, Dresden, 19 – 24 Mar 2017
- L. Bießmann, L. P. Kreuzer, T. Widmann, N. Hohn, J.-F. Moulin, P. Müller-Buschbaum  
*Monitoring the swelling behavior of PEDOT:PSS thin films under high humidity conditions*  
3rd Internal Biennial Science Meeting of the MLZ, Grainau, 19 – 27 Jun 2017
- L. Bießmann, L. P. Kreuzer, T. Widmann, N. Hohn, J.-F. Moulin, P. Müller-Buschbaum  
*Monitoring the thickness evolution and water uptake of PEDOT:PSS thin films under high humidity conditions by in-situ neutron reflectometry*  
International Conference on Neutron Scattering, Daejeon, South Korea, 9 – 13 Jul 2017
- H. Breitzkreutz, J. Hingerl, J. Shi, W. Petry  
*Ion-irradiation induced inter diffusion layer growth in UMo/Al fuels*  
AccApp'17 (13th International Topical Meeting on the Nuclear Applications of Accelerators), Québec, Kanada, 31 Jul – 04 Aug 2017
- H. Breitzkreutz, Ch. Steyer, B. Baumeister, W. Petry  
*European developments for monolithic UMo fuel: A status report*  
RERTR 2017, Chicago, USA, 12 – 15 Nov 2017
- T. Chemnitz, W. Petry, F. Kraus  
*Development of a dry-chemical process for extraction of Mo99 from irradiated LEU targets*  
Hirscheegg-Seminar Festkörperchemie, Hirscheegg Österreich, 15 – 18 Jun 2017
- W. Chen  
*Introducing colloidal quantum dots in solar cells*  
3rd Internal Biennial Science Meeting of the MLZ, Grainau, 19 – 27 Jun 2017
- K.-L. Claude, B.-J. Niebuur, D. Aravopoulou, V. Hildebrand, A. Laschewsky, A. Kyritsis, P. Müller-Buschbaum, A. Schulte, C. M. Papadakis  
*Phase behaviour of PNIPMAM in dependence on temperature and pressure*  
DPG-Frühjahrstagung, Dresden, 19 – 24 Mar 2017
- M. A. Dyakonova, A. V. Berezkin, N. Stavrouli, M. T. Popescu, C. Tsitsilianis, C. M. Papadakis  
*Physical hydrogels via polyion complexation of a triblock polyampholyte in dependence on charge asymmetry and ionic strength*  
11th International Gel Symposium, Chiba, Japan, 7 – 9 Mar 2017
- M. A. Dyakonova, A. V. Berezkin, N. Stavrouli, M. T. Popescu, C. Tsitsilianis, C. M. Papadakis  
*Responsive polymer hydrogels: physical gelling through polyion complexation*  
DPG-Frühjahrstagung, Dresden, 19 – 24 Mar 2017
- M. A. Dyakonova, A. V. Berezkin, N. Stavrouli, M. T. Popescu, C. Tsitsilianis, C. M. Papadakis  
*Physical hydrogels via polyion complexation of a triblock polyampholyte in dependence on charge asymmetry and ionic strength*

- 9th International Symposium on Molecular Mobility and Order in Polymer Systems, St. Petersburg, Russia, 19 – 23 Jun 2017
- N. Hohn, M. Boone, E. Rivard, P. Müller-Buschbaum  
*Investigation of novel material systems for hybrid photovoltaics - alternatives for the paradigm*  
DPG-Frühjahrstagung, Dresden, 19 – 24 Mar 2017
  - N. Hohn, S. Schlosser, L. Biessmann, S. Xia, P. Müller-Buschbaum  
*Readily accessible structuring routines for hybrid materials*  
3rd Internal Biennial Science Meeting of the MLZ, Grainau, 19 – 27 Jun 2017
  - N. Hohn, P. Müller-Buschbaum  
*Amphiphilic diblock copolymer templating for mesoporous thin film structuring investigated via GISAXS*  
Annual meeting of Alberta/Technical University of Munich International Graduate School, Jasper, Canada, 13 – 17 Nov 2017
  - N. Hohn  
*From physics to chemistry – Investigation of nanostructured materials and introduction to synthesis of pi-extended Te-based molecules*  
Seminar talk in Rivard Group, Edmonton, Canada, 8 Dec 2017
  - F. Jung, A. V. Berezkin, D. Posselt, D.-M. Smilgies, C. M. Papadakis  
*Annealing of diblock copolymer thin films using solvent vapor mixtures*  
3rd Internal Biennial Science Meeting of the MLZ, Grainau, 19 – 27 Jun 2017
  - F. Jung  
*Examples of SAXS/GISAXS research at synchrotrons*  
TUM lecture: "Advanced Materials Analysis with Synchrotron Radiation: Techniques and Applications", Garching, 28 Jun 2017
  - V. Körstgens, F. Buschek, A. Haussmann, H. Iglev, W. Ohm, S. V. Roth, R. Kienberger, P. Müller-Buschbaum  
*Water-processable hybrid solar cells - in situ studies of particular fabrication steps*  
SAXS/WAXS workshop at DESY Photon Science Users' Meeting 2017, Hamburg, 26 – 27 Jan 2017
  - V. Körstgens, F. Buschek, M. Wörle, H. Iglev, W. Ohm, S. V. Roth, R. Kienberger, P. Müller-Buschbaum  
*Water-processed hybrid solar cells: deposition of the active layer with vertical composition gradient*  
DPG-Frühjahrstagung, Dresden, 19 – 24 Mar 2017
  - V. Körstgens  
*Water-processed hybrid solar cells – Looking into steps of device fabrication*  
Zhejiang Sci-Tech University, Hangzhou, China, 11 Sep 2017
  - V. Körstgens, F. Buschek, M. Wörle, H. Iglev, W. Ohm, S. V. Roth, R. Kienberger, P. Müller-Buschbaum  
*Spray deposition of water-processed active layers of hybrid solar cells investigated with in situ X-ray scattering methods*  
AVS 64th International Symposium, Tampa, Florida, USA, 29 Oct – 03 Nov 2017

- L. Kreuzer, T. Widmann, P. Müller-Buschbaum  
*FlexiProb sample environment for neutron scattering experiments on polymer thin films*  
FlexiProb Cooperation Meeting, Lund, 29 May 2017
- L. Kreuzer, T. Widmann, N. Hohn, K. Wang, J. F. Moulin, A. Laschewsky, C. M. Papadakis, P. Müller-Buschbaum  
*In-situ neutron reflectivity investigations of D<sub>2</sub>O-H<sub>2</sub>O exchange kinetics in thermoresponsive PNIPAM based block copolymers*  
3rd Internal Biennial Science Meeting of the MLZ, Grainau, 19 – 27 Jun 2017
- L. Kreuzer, T. Widmann, N. Hohn, K. Wang, J. F. Moulin, A. Laschewsky, C. M. Papadakis, P. Müller-Buschbaum  
*In-situ TOF NR study of the swelling and exchange kinetics of multi-stimuli responsive PNIPAM based block copolymers*  
JCNS Workshop 2017, Tutzing, 10 – 13 Oct 2017
- M. Leitner  
*Experimental determination of vibrational dynamics in the solid state*  
Max-Planck-Institut für Eisenforschung, Düsseldorf, 4 Apr 2017
- W. Lohstroh, Z. Evenson  
*The cold chopper spectrometer TOFTOF and its application to Biology*  
MLZ conference Neutrons for Health, Bad Reichenhall, 26 – 30 June 2017
- F. C. Löhner, V. Körstgens, M. Schwartzkopf, A. Hinz, O. Polonskyi, T. Strunskus, F. Faupel, S. V. Roth, P. Müller-Buschbaum  
*Following the formation of metal electrodes for organic photovoltaics*  
DPG-Frühjahrstagung, Dresden, 19 – 24 Mar 2017
- F. C. Löhner, V. Körstgens, M. Schwartzkopf, A. Hinz, O. Polonskyi, T. Strunskus, F. Faupel, S. V. Roth, P. Müller-Buschbaum  
*Following the formation of metal electrodes for organic photovoltaics*  
3rd Internal Biennial Science Meeting of the MLZ, Grainau, 19 – 27 Jun 2017
- F. C. Löhner, V. Körstgens, M. Schwartzkopf, A. Hinz, O. Polonskyi, T. Strunskus, F. Faupel, S. V. Roth, P. Müller-Buschbaum  
*In-situ investigation of the sputter deposition of gold electrodes for organic electronics*  
8th International Workshop on Polymer Metal Nanocomposites, Prague, Czech, 12 – 15 Sep 2017
- F. C. Löhner, V. Körstgens, M. Schwartzkopf, A. Hinz, O. Polonskyi, T. Strunskus, F. Faupel, S. V. Roth, P. Müller-Buschbaum  
*Highly time-resolved insights into the sputter deposition of metal electrodes on polymer thin films for organic electronics*  
AVS 64th International Symposium and Exhibition, Tampa, USA, 19 – 27 Jun 2017
- P. Müller-Buschbaum  
*Watching aging in organic solar cells - an in-operando study*  
DESY Users' Meeting Hamburg, 26/27 Jan 2017
- P. Müller-Buschbaum  
*Report of the Users Committee (DPS-UC) - report 2016*  
DESY Users' Meeting Hamburg, 26/27 Jan 2017

- P. Müller-Buschbaum, D. Moseguí González, C.J. Schaffer, S. Pröller, J. Schlipf, L. Song, S. Bernstorff, E.M. Herzig  
*In-operando study of changes in the crystalline parts of P3HT:PCBM solar cells*  
DPG-Frühjahrstagung, Dresden, 19 – 24 Mar 2017
- P. Müller-Buschbaum  
*Tailoring Titania Nanostructures for Solar Cell Applications*  
MRS Spring Meeting 2017, Phoenix, USA, 17 – 21 Apr 2017
- P. Müller-Buschbaum  
Polymer and hybrid nanostructures for applications in organic solar cells investigated with advanced scattering techniques  
INM – Leibniz Institut für Neue Materialien Seminar, INM Saarbrücken, 8/9 May 2017
- P. Müller-Buschbaum  
*Polymer and hybrid nanostructures for applications in organic solar cells investigated with advanced scattering techniques*  
Resource Chemistry Workshop, Shanghai, China, 15 – 18 May 2017
- P. Müller-Buschbaum, C.J. Schaffer, C.M. Palumbiny, M.A. Niedermeier, C. Burger, G. Santoro, S.V. Roth  
*Watching aging in organic solar cells - an in-operando study*  
European Polymer Congress EPF 2017, Lyon, France, 3 – 7 Jul 2017
- P. Müller-Buschbaum  
*GISANS – basics, challenges and possibilities*  
Int. Conference on Neutron Scattering 2017, Deajeon, South Korea, 13 – 19 Jul 2017
- P. Müller-Buschbaum  
*In-operando studies probing morphology degradation in organic solar cells*  
Nanostructured Functional Materials for Sustainable Energy Provision (NMEP 2017) Munich, 26 – 28 Jul 2017
- P. Müller-Buschbaum, L. Song, B. Su, K. Wang, S.V. Roth  
*Spray deposition of titania films for application in photovoltaics*  
254th American Chemical Society National Meeting, Washington, USA, 20 – 24 Aug 2017
- P. Müller-Buschbaum  
*Nanostructured polymer films for energy harvesting applications*  
Zhejiang Sci-Tech University in Hangzhou, China, 11– 15 Sep 2017
- P. Müller-Buschbaum  
*Probing nanostructures generated by block copolymer self-assembly using advanced scattering techniques*  
Zhejiang University in Hangzhou, China, 11 – 15 Sep 2017
- P. Müller-Buschbaum  
*Große Instrumente für große Fragestellungen*  
Fachleiter Tagung Physik in Ergolding, 21 Sep 2017
- P. Müller-Buschbaum  
*Polymer and hybrid nanostructures for applications in organic solar cells investigated with advanced scattering techniques*

*ced scattering techniques*

6th SolTech Conference in München, 4 – 5 Oct 2017

- P. Müller-Buschbaum  
*Probing thin film nanostructures generated by block copolymer self-assembly using advanced scattering techniques*  
JCNS Workshop 2017 in Tutzing, 11 – 13 Oct 2017
- P. Müller-Buschbaum  
*Thin film thermoelectrics based on conducting polymers*  
Thermoelectrics Workshop an Universität Augsburg, 10 Oct 2017
- P. Müller-Buschbaum  
*Understanding solar cells structure and functioning via GISAXS and GIWAXS*  
AVS 64th International Symposium & Exhibition in Tampa, USA, 29 Oct – 3 Nov 2017
- B.-J. Niebuur, K.-L. Claude, S. Pinzek, C. Cariker, K. N. Raftopoulos, V. Pipich, M.-S. Ap-pavou, A. Schulte, C.M. Papadakis  
*Influence of pressure on the aggregation behavior of poly(N-isopropylacrylamide)*  
9th International Symposium on Molecular Mobility and Order in Polymer Systems, St. Petersburg, 19 – 23 Jun 2017
- C. M. Papadakis, K. Kyriakos, A. Laschewsky, P. Müller-Buschbaum  
*The impact of a cosolvent on the kinetics of mesoglobule formation in solutions of PNIPAM-based micelles*  
CECAM Workshop "Soft smart responsive materials: Fundamentals and applications", Mainz, 11 – 12 May 2017
- W. Petry  
*Zum Ursprung der Dinge: 60 Jahre Forschung mit Neutronen*  
"Deutsches Museum" Munich, 2 Feb 2017
- W. Petry  
*To the origins of things: 60 years of research with neutrons from Garching*  
Institute for Plasmaphysics, Max Planck Institute, Garching, 17 Mar 2017
- W. Petry  
*To the origins of things: 60 years of research with neutrons from Garching*  
Swedish Foundation for Strategic Research, Stockholm, visiting FRM II, 29 Mar 2017
- W. Petry  
*European perspectives on neutron science facilities*  
APS workshop - NIST Center for Neuron Research, Gaithersburg, USA, 3 Apr 2017
- W. Petry  
*60 years of research with neutrons from Garching – what's new?*  
NIST Center for Neuron Research, Gaithersburg, USA, 4 Apr 2017
- W. Petry  
*Neutronen für Wissenschaft, Industrie und Medizin*  
Ringvorlesung held at the Physics Department, TUM Garching, 10 May 2017
- W. Petry  
*Neutronen wozu?*

Assembly of the “Nationales Begleitgremium” held at TUM headquarters, Munich, 15 May 2017

- W. Petry  
*19. Juli 2017 – 10 Jahre itg*  
Festvortrag, Institute of Advanced Study, TUM Garching, 19 Jul 2017
- W. Petry  
*10 Jahre Forschung mit Neutronen in Garching*  
Festvortrag upon invitation of the City of Garching, Werner-Heisenberg-Gymnasium Garching, 27 Jul 2017
- W. Petry  
*In operando stress analysis with neutrons*  
Invited talk, Raciri summerschool, Ronneby, Sweden, 22 Aug 2017
- W. Petry, H. Breitzkreutz  
*FROM CP TO FOREvER Towards the Conversion of High Performance Research Reactors in Europe*  
Kick-off meeting, EU-Project FOREvER, CEA Cadarache, France, 11 Oct 2017
- S. Pratap, J. Schlipf, P. Müller-Buschbaum  
*On the chemical origins of crystalline preferred orientations in hybrid perovskite thin films*  
DPG-Frühjahrstagung, Dresden, 19 – 24 Mar 2017
- S. Pratap, J. Schlipf, P. Müller-Buschbaum  
*Microstructural evolution during thin film growth*  
3rd Internal Biennial Science Meeting of the MLZ, Grainau, 19 – 27 Jun 2017
- S. Pratap, J. Schlipf, P. Müller-Buschbaum  
*Perovskite: The new crystalline sheriff in the photovoltaic county*  
7th Colloquium of the Munich School of Engineering, Garching, 13 Jul 2017
- S. Pratap, J. Schlipf, P. Müller-Buschbaum  
*On the chemical origins of crystalline preferred orientations in hybrid perovskite thin films*  
NIM Summer Retreat, Schloss Hirschberg, Beilngries, 31 Jul – 2 Aug 2017
- C. Reiter, H. Breitzkreutz, A. Röhrmoser, A. Seubert, W. Petry  
*High precision neutronic calculations for transient simulations for FRM II*  
RRFM 2017, Rotterdam, Niederlande, 14 – 18 May 2017
- N. Saxena, M. Coric, A. Greppmair, J. Wernecke, M. Plüger, M. Krumrey, M. S. Brandt, E. M. Herzig, P. Müller-Buschbaum  
*Thermoelectric thin films based on a polymer/nanoparticle nanocomposite*  
DPG-Frühjahrstagung, Dresden, 19 – 24 Mar 2017
- N. Saxena, M. Coric, A. Greppmair, J. Wernecke, M. Plüger, M. Krumrey, M. S. Brandt, E. M. Herzig, P. Müller-Buschbaum  
*Thermoelectric thin films based on a polymer/nanoparticle nanocomposite*  
3rd Internal Biennial Science Meeting of the MLZ, Grainau, 19 – 27 Jun 2017
- N. Saxena, M. Coric, A. Greppmair, J. Wernecke, M. Plüger, M. Krumrey, M. S. Brandt, E. M. Herzig, P. Müller-Buschbaum

*Thermoelectric thin films based on a polymer/nanoparticle nanocomposite*

European Polymer Federation Congress, Lyon, 2 – 7 Jul 2017

- N. Saxena, M. Coric, A. Greppmair, J. Wernecke, M. Plüger, M. Krumrey, M. S. Brandt, E. M. Herzig, P. Müller-Buschbaum  
*Thermoelectric thin films based on a polymer/nanoparticle nanocomposite*  
Zhejiang Sci-Tech University, Hangzhou, China, 8 – 17 Sep 2017
- C.J. Schaffer, C.M. Palumbiny, M.A. Niedermeier, C. Burger, G. Santoro, S.V. Roth, P. Müller-Buschbaum  
*Morphological degradation in low band gap polymer solar cells – an in operando study*  
16th SAXS/WAXS satellite workshop of DESY Users' Meeting Hamburg, 26/27 Jan 2017
- J. Schlipf, L. Oesinghaus, Y. Hu, N. Giesbrecht, S. Bernstorff, T. Bein, P. Docampo, P. Müller-Buschbaum  
*Strong impact of processing parameters on morphology and crystal orientation of hybrid perovskite thin films for photovoltaic application*  
DPG-Frühjahrstagung, Dresden, 19 – 24 Mar 2017
- J. Schlipf, P. Müller-Buschbaum  
*Mikrostrukturen und Kristallorientierung in polykristallinen Perowskit-Dünnschichten*  
2. EFDS-Seminar "Verbindungshalbleiter für die Photovoltaik", Dresden, 16 May 2017
- J. Schlipf, L. Oesinghaus, L. Bießmann, E. Metwalli, L. Porcar, P. Müller-Buschbaum  
*Impact of moisture on the morphology of hybrid organometal halide perovskite thin films for photovoltaic application*  
International Conference on Neutron Scattering, Daejeon, Korea, 9 – 13 Jul 2017
- C. Steyer, B. Baumeister, H. Breitzkreutz, W. Petry, B. Stepnik, M. Grasse, C. Moyroud  
*Characterization of monolithic UMo foils and Zr coatings for the EMPIrE irradiation experiment*  
RRFM 2017, Rotterdam, Niederlande, 14 – 18 May 2017
- C. Steyer, B. Baumeister, H. Breitzkreutz, W. Petry, B. Stepnik, M. Grasse, C. Moyroud, R. Johnson, R. Mayfield, G. Argon  
*Production results of monolithic UMo plates for the EMPIrE irradiation experiment*  
RRFM 2017, Rotterdam, Niederlande, 14 – 18 May 2017
- B. Stepnik, M. Grasse, C. Rontard, D. Geslin, Y. Guinard, S. Van den Berghe, A. Leenaers, H. Breitzkreutz, W. Petry, H. Palancher, E. Hervieu, Y. Calzavara, H. Guyon  
*Manufacturing of the SEMPER FIDELIS UMo irradiation experiment*  
RERTR 2017, Chicago, USA, 12 – 16 Nov 2017
- B. Su  
*Spray deposition study for titania films*  
3rd Internal Biennial Science Meeting of the MLZ, Grainau, 19 – 27 Jun 2017
- W. Van Renterghem, A. Leenaers, S. van den Berghe, B.D. Miller, J. Gan, J.W. Madden, D.D. Keiser, H. Palancher, G.K. Hofman, H. Breitzkreutz  
*Irradiation effects in Si and ZrN coated UMo particles studied with transmission electron microscopy*  
RRFM 2017, Rotterdam, Niederlande, 14 – 18 May 2017

- K. Wang, Y. Tong, L. Bießmann, S. V. Roth, P. Müller-Buschbaum  
*Morphology improvement of ZnO/P3HT-b-PEO bulk heterojunction films using a low temperature route*  
3rd International Biennial Science Meeting of the MLZ, Grainau, 19 – 27 Jun 2017
- S. Xia, E. Metwalli, M. Opel, P. A. Staniec, E. M. Herzig, P. Müller-Buschbaum  
*Printed block copolymer films with embedded magnetic nanoparticles*  
DPG-Frühjahrstagung, Dresden, 19 – 24 Mar 2017
- S. Xia, V. Körstgens, M. Opel, M. Schwartzkopf, S. V. Roth, P. Müller-Buschbaum  
*Investigation on printed diblock copolymer film embedded with magnetic nanoparticles*  
8th international workshop on polymer metal nanocomposites, Prague, Czech Republic, 12 – 15 September 2017
- X. Zhang, B.-J. Niebuur, P. Chytil, T. Etrych, S. K. Filippov, A. Kikhney, F. Wieland, D. I. Svergun, C. M. Papadakis  
*HPMA-Based drug delivery system -Behavior in protein environment*  
DPG-Frühjahrstagung, Dresden, 19 – 24 Mar 2017
- X. Zhang, B.-J. Niebuur, P. Chytil, T. Etrych, D. I. Svergun, S. K. Filippov, C. M. Papadakis  
*HPMA-Based drug delivery system -Investigated in protein environment using fluorescence methods*  
3rd Workshop "Fluorescence correlation spectroscopy in soft matter science", Garching, 11 – 12 Oct 2017

### 8.3 Posters

- B. Baumeister, Ch. Steyer, M. Hoelzel, H. Breitzkreutz, W. Petry  
*Development options for the TUM PVD Zr application process for monolithic U-Mo fuel*  
RERTR 2017, Chicago, USA, 12 – 16 Nov 2017
- W. Chen, D. Yang, K. Wang, P. Müller-Buschbaum  
*Polymer and nanocrystals hybrid solar cells*  
DPG-Frühjahrstagung, Dresden, 19 – 24 Mar 2017
- W. Chen, P. Müller-Buschbaum  
*Colloidal quantum dots with narrow band gap in solar cells*  
6th SolTech Conference: Solar Technologies go Hybrid, Munich, 4 – 5 Oct 2017
- S. Grott, N. Hohn, P. Müller-Buschbaum  
*Tuning organic solar cells via doping with inorganic nanoparticles*  
DPG-Frühjahrstagung, Dresden, 19 – 24 Mar 2017
- S. Grott, N. Hohn, C. Ott, T. Nilges, P. Müller-Buschbaum  
*Effect of incorporated inorganic nanocrystals on the performance of organic solar cells*  
3rd Internal Biennial Science Meeting of the MLZ, Grainau, 19 – 27 Jun 2017
- S. Grott, N. Hohn, C. Ott, T. Nilges, P. Müller-Buschbaum  
*Effect of inorganic nanocrystals on the performance of organic solar cells*  
7th Colloquium of the Munich School of Engineering, Garching, 13 Jul 2017
- S. Grott, N. Hohn, C. Ott, T. Nilges, P. Müller-Buschbaum  
*Influence of inorganic SnIP nanocrystals on the morphology of P3HT:PCBM blend films for photovoltaic applications*  
6th SolTech Conference: Solar Technologies go Hybrid, Munich, 4 – 5 Oct 2017
- N. Hohn  
*Renewable energies*  
TUM Kick-off Seminar, 8 – 1 May 2017
- N. Hohn, M. A. Giebel, T. F. Fässler, P. Müller-Buschbaum  
*Silylated Ge<sub>9</sub>Si-Zintl clusters as wet chemical precursors for mesoporous films in hybrid solar cells*  
TUM International Graduate School of Science and Engineering Forum, 29 – 31 May 2017
- N. Hohn, F. Guelle, M. A. Giebel, M. Schwartzkopf, S. V. Roth, T. F. Fässler, P. Müller-Buschbaum  
*Controlling the nano-morphology of inorganic thin films for efficient solar energy conversion*  
7th Colloquium of the Munich School of Engineering, Garching, 13 Jul 2017
- F. Jung, A. V. Berezkin, D. Posselt, D.-M. Smilgies, C. M. Papadakis  
*Annealing of diblock copolymer thin films using solvent vapor mixtures – An in situ GISAXS study*  
DPG-Frühjahrstagung, Dresden, 19 – 24 Mar 2017
- F. Jung, C. Ko, S. Gkempoura, M. Rikkou-Kalourkoti, R. Schweins, C. S. Patrickios, C. Tsitsilianis, C. M. Papadakis  
*Structural investigations on multi-responsive physical hydrogels*  
Kolloid-Tagung "Multiresponsive systems", Garching, 9 – 11 Oct 2017

- C. Ko, M. A. Dyakonova, K. Raftopoulos<sup>1</sup>, S. Gkermpoura, M. M. Soledad Lencina, M. Rikkou-Kalourkoti, C. S. Patrickios, C. Tsitsilianis, C. M. Papadakis  
*Multiresponsive hydrogels from telechelic polyelectrolytes*  
Kolloid-Tagung "Multiresponsive systems", Garching, 9 – 11 Oct 2017
- L. Kreuzer, T. Widmann, N. Hohn, K. Wang, J. F. Moulin, V. Hildebrand, A. Laschewsky, C. M. Papadakis, P. Müller-Buschbaum  
*H<sub>2</sub>O-D<sub>2</sub>O exchange kinetics in PNIPAM based block copolymer films followed with in-situ neutron reflectivity*  
DPG-Frühjahrstagung, Dresden, 19 – 24 Mar 2017
- L. Kreuzer  
*Scattering on multi-stimuli responsive block copolymers*  
TUM Graduate School Kick-Off Meeting, Raitenhaslach, 8 – 10 May 2017
- L. Kreuzer, T. Widmann, N. Hohn, K. Wang, J. F. Moulin, V. Hildebrand, A. Laschewsky, C. M. Papadakis, P. Müller-Buschbaum  
*Potential use of thermo-responsive polymers as smart windows*  
7th Colloquium of the Munich School of Engineering, Garching, 13 Jul 2017
- L. Kreuzer, T. Widmann, N. Hohn, K. Wang, J. F. Moulin, V. Hildebrand, A. Laschewsky, C. M. Papadakis, P. Müller-Buschbaum  
*In-situ analysis of swelling and exchange kinetics in multi-stimuli responsive PNIPAM based block copolymers*  
Kolloid-Tagung "Multiresponsive systems", Garching, 9 – 11 Oct 2017
- N. Li, B. Su, L. Song, P. Müller-Buschbaum  
*Hybrid solar cells based on TiO<sub>2</sub>/PTB7-Th*  
7th Colloquium of the Munich School of Engineering, Garching, 13 Jul 2017
- N. Li, B. Su, S. Xia, P. Müller-Buschbaum  
*Fabrication of titania films via combining block copolymer assisted sol-gel templating with printing*  
Kolloid-Tagung "Multiresponsive systems", Garching, 9 – 11 Oct 2017
- F. C. Löhner, V. Körstgens, M. Schwartzkopf, A. Hinz, O. Polonskyi, T. Strunskus, F. Faupel, S. V. Roth, P. Müller-Buschbaum  
*Witnessing the formation of metal contacts on organic solar cells*  
7th Colloquium of the Munich School of Engineering, Garching, 13 Jul 2017
- F. C. Löhner, V. Körstgens, M. Schwartzkopf, A. Hinz, O. Polonskyi, T. Strunskus, F. Faupel, S. V. Roth, P. Müller-Buschbaum  
*Investigating the formation of gold electrodes for organic solar cells*  
NIM Conference "Nanostructured functional Materials for sustainable Energy Provision", München, 26 – 28 Jul 2017
- F. C. Löhner, V. Körstgens, M. Schwartzkopf, A. Hinz, O. Polonskyi, T. Strunskus, F. Faupel, S. V. Roth, P. Müller-Buschbaum  
*Following the formation of metal electrodes on photoactive polymer thin films*  
6th SolTech Conference: Solar Technologies go Hybrid, Munich, 4 – 5 Oct 2017
- W. Mohamed, H. S. Roh, H. Ozaltun, J. Smith, J. Nielsen, I. Glagolenko, G. Hofman, B. Stepnik, H. Breitzkreutz, A.M. Yacout

*Evaluation of effect of post-fabrication voids on the performance of C2TWP mini-plates*  
RERTR 2017, Chicago, USA, 12 – 16 Nov 2017

- B.-J. Niebuur, K.-L. Claude, S. Pinzek, C. Cariker, K.N. Raftopoulos, V. Pipich, M.-S. Appavou, A. Schulte, C.M. Papadakis  
*Influence of pressure on the aggregation behavior of aqueous PNIPAM solutions*  
DPG-Frühjahrstagung, Dresden, 19 – 24 Mar 2017
- B.-J. Niebuur, K.-L. Claude, S. Pinzek, C. Cariker, K.N. Raftopoulos, V. Pipich, M.-S. Appavou, A. Schulte, C.M. Papadakis  
*Influence of oressure on the aggregation behavior of aqueous PNIPAM solutions*  
Kolloid-Tagung "Multiresponsive systems", Garching, 9 – 11 Oct 2017
- B.-J. Niebuur, N.S. Vishnevetskaya, E. Koziolová, E.A. Lomkova, P. Chytil, T. Etrych, S.K. Filippov, C.M. Papadakis  
*Influence of molecular characteristics on the critical micelle concentration of amphiphilic HPMA-based polymer drug carriers*  
3rd Workshop "Fluorescence correlation spectroscopy in soft matter science", 11 – 12 Oct 2017
- S. Pratap, J. Schlipf, P. Müller-Buschbaum  
*On the chemical origins of crystalline preferred orientations in hybrid organometallic lead halide perovskite thin films*  
Nanostructured Functional Materials for Sustainable Energy Provision, Literaruehaus, Munich, 26 – 28 Jul 2017
- S. Pratap, J. Schlipf, P. Müller-Buschbaum  
*On the chemical origins of crystalline preferred orientations in hybrid organometallic lead halide perovskite thin films*  
6th SolTech Conference: Solar Technologies go Hybrid, Munich, 4 – 5 Oct 2017
- S. Pratap, J. Schlipf, P. Müller-Buschbaum  
*On the colloidal behavior of hybrid inorganic-organic lead halide perovskite precursor solutions and its impact on thin film microstructure*  
Kolloid-Tagung "Multiresponsive systems", Garching, 9 – 11 Oct 2017
- N. Saxena, M. Coric, A. Greppmair, J. Wernecke, M. Plüger, M. Krumrey, M. S. Brandt, E. M. Herzig, P. Müller-Buschbaum  
*Thermoelectric thin films based on a polymer/nanoparticle nanocomposite*  
NIM Young Ideas in Nanoscience, Munich, 2 May 2017
- N. Saxena, M. Coric, A. Greppmair, J. Wernecke, M. Plüger, M. Krumrey, M. S. Brandt, E. M. Herzig, P. Müller-Buschbaum  
*Thermoelectric thin films based on a polymer/nanoparticle nanocomposite*  
7th Colloquium of the Munich School of Engineering, Garching, 13 Jul 2017
- N. Saxena, M. Coric, A. Greppmair, J. Wernecke, M. Plüger, M. Krumrey, M. S. Brandt, E. M. Herzig, P. Müller-Buschbaum  
*Thermoelectric thin films based on a polymer/nanoparticle nanocomposite*  
NIM Nanostructured Functional Materials for Sustainable Energy Provision, Munich, 26 – 28 Jul 2017

- J. Schlipf, L. Oesinghaus, L. Bießmann, E. Metwalli, L. Porcar, P. Müller-Buschbaum  
*Impact of moisture on the morphology of hybrid organo-metal halide perovskite thin films for photovoltaic application*  
3rd Internal Biennial Science Meeting of the MLZ, Grainau, 19 – 27 Jun 2017
- J. Schlipf, L. Oesinghaus, N. Giesbrecht, C. J. Schaffer, L. Song, Y. Hu, S. Bernstorff, T. Bein, P. Docampo, P. Müller-Buschbaum  
*Morphology and crystal orientation of hybrid perovskite thin films for application in high efficiency solar cells*  
Nanosystems Initiative Munich Summer Retreat, Schloss Hirschberg, 31 Jul – 2 Aug 2017
- J. Schlipf, L. Bießmann, L. Oesinghaus, E. Metwalli, L. Porcar, P. Müller-Buschbaum  
*Ingression of moisture into hybrid perovskite thin films probed with in-situ GISANS*  
6th SolTech Conference: Solar Technologies go Hybrid, Munich, 4 – 5 Oct 2017
- L. Song, W. Wang, S. Pröllner, D. Moseguí González, J. Schlipf, C. J. Schaffer, K. Peters, E. M. Herzig, S. Bernstorff, T. Bein, D. Fattakhova-Rohlfing, P. Müller-Buschbaum  
*In Situ Study of degradation in P3HT-titania based solid-state dye-sensitized solar cells*  
6th SolTech Conference: Solar Technologies go Hybrid, Munich, 4 – 5 Oct 2017
- B. Su, H. A. Caller-Guzman, V. Körstgens, Y. Rui, Y. Yao, S. V. Roth, P. Müller-Buschbaum  
*morphology evolution of titania films during in situ spray coating for perovskite solar cells*  
DPG-Frühjahrstagung, Dresden, 19 – 24 Mar 2017
- K. Wang, T. Tong, L. Bießmann, S. V. Stephan, P. Müller-Buschbaum  
*Morphology control of low temperature synthesized ZnO/P3HT-b-PEO films via spray deposition*  
DPG-Frühjahrstagung, Dresden, 19 – 24 Mar 2017
- K. Wang, T. Tong, L. Bießmann, S. V. Stephan, P. Müller-Buschbaum  
*Morphology control of low temperature synthesized ZnO/P3HT-b-PEO films via spray deposition*  
7th Colloquium of the Munich School of Engineering, Garching, 13 Jul 2017
- K. Wang, L. Bießmann, M. Schwartzkopf, S. V. Stephan, P. Müller-Buschbaum  
*Morphology control of low temperature synthesized ZnO/P3HT-b-PEO films via spray deposition*  
6th SolTech Conference: Solar Technologies go Hybrid, Munich, 4 – 5 Oct 2017
- K. Wang, L. Bießmann, M. Schwartzkopf, S. V. Stephan, P. Müller-Buschbaum  
*Morphology control of low temperature synthesized ZnO/P3HT-b-PEO films via spray deposition*  
Kolloid-Tagung "Multiresponsive systems", Garching, 9 – 11 Oct 2017
- X. Zhang, B.-J. Niebuur, P. Chytil, T. Etrych, S. K. Filippov, A. Kikhney, F. Wieland, D. I. Svergun, C. M. Papadakis  
*Macromolecular HPMA-based drug delivery system– Behavior in protein environment*  
13th Zsigmondy Colloquium, Saarbrücken, 5 – 7 Apr 2017
- X. Zhang, B.-J. Niebuur, P. Chytil, To. Etrych, S. K. Filippov, A. Kikhney, F. Wieland, D. I. Svergun, C. M. Papadakis  
*Macromolecular HPMA-based drug delivery system– Behavior in protein environment*  
9th International Symposium "Molecular Mobility and Order in Polymer Systems", Saint Petersburg, Russia, 19 – 23 Jun 2017
- X. Zhang, B.-J. Niebuur, P. Chytil, T. Etrych, S. K. Filippov, A. Kikhney, F. Wieland, D. I. Svergun, C. M. Papadakis

*Macromolecular HPMA-Based drug delivery system– Behavior in protein environment*  
Kolloid-Tagung "Multiresponsive systems", Garching, 9 – 11 Oct 2017

#### 8.4 Invited talks at LS Funktionelle Materialien

- Prof. Jiping Wang, Zhejiang Sci-Tech University, Hangzhou, Zhejiang, P.R China  
*Green textile manufacturing: Looking for breakthrough technology systems*  
18 Jan 2017
- Prof. Dr. Natalie Germann, TUM Weihenstephan  
*Experimental and computational investigation of shear banding polymeric solutions*  
24 Jan 2017
- Dr. Manfred Kriechbaum, Graz University of Technology, Austria  
*Phase transitions of membrane lipids investigated by time-resolved small-angle X-ray scattering (SAXS)*  
1 Feb 2017
- Prof. Dr. Thomas Weitz, Physics of Nanosystems, LMU Munich  
*Surface-mediated crystallization of organic semiconductors for field-effect transistors with high electron mobilities*  
25 Apr 2017
- Dr. Wiebke Lohstroh, TUM MLZ Garching  
*The time-of-flight spectrometer TOF-TOF and its possibilities for soft matter*  
23 May 2017
- Prof. Dr. Alfons Schulte, University of Central Florida, USA  
*Spectroscopic approaches to stimuli-responsive polymers at variable pressure and temperature*  
27 Jun 2017
- Prof. Dr. Hans Robert Kalbitzer, University of Regensburg  
*Detection of rare conformational states by high pressure NMR spectroscopy*  
4 Jul 2017
- Prof. Dr. Mirjana Minceva, Biothermodynamics, TUM School of Life Sciences  
*Selection of deep eutectic solvents using predictive thermodynamic model*  
11 Jul 2017
- Dr. Tayebbeh Ameri, Friedrich-Alexander University Erlangen-Nürnberg (FAU)  
*Ternary Sensitization of Organic Solar Cells; A Multifunctional Concept to Boost Power Conversion Efficiency*  
26 Sep 2017
- Dr. Geonho Song, University of Potsdam  
*Elucidating structure-function relationship of tunicate biopolymer*  
8 Nov 2017
- Dr.-Ing. Markus Gallei, Technical University of Darmstadt  
*Porous stimuli-responsive polymer architectures as optical sensing materials and smart membranes*  
22 Nov 2017
- Prof. Dr. Rio Kita, Tokai University, Japan  
*Characterizations of PNIPAM solution in equilibrium and nonequilibrium state*  
6 Dec 2017

## 8.5 Funding

### Deutsche Forschungsgemeinschaft:

- *Zweifach und orthogonal schaltbare Blockcopolymere aus zwitterionischen und thermoresponsiven Blöcken: Synthese und Strukturen in Lösung und im dünnen Film*  
Grant Number: MU 1487/17-1 Project Leader: Prof. Dr. Peter Müller-Buschbaum
- *In-situ Untersuchungen zu Kondensation, Nukleation und Wachstum von Metallfilmen und Nanostrukturen auf organischen Oberflächen während Sputterbeschichtung*  
Grant Number: MU 1487/18-1,2  
Project Leader: Prof. Dr. Peter Müller-Buschbaum
- *Transport und Morphologie, Einfluss auf nichtgeminale Rekombination in Organischen Solarzellen*  
Grant Number: MU 1487/22-1  
Project Leader: Prof. Dr. Peter Müller-Buschbaum
- *Aufbau internationaler Kooperationen zum Thema 'Intelligente Textilien basierend auf thermoresponsiven Copolymerbeschichtungen'*  
Grant Number: MU 1487/23-1  
Project Leader: Prof. Dr. Peter Müller-Buschbaum
- *Cononsolvency-induzierte Selbstorganisation thermoresponsiver Blockcopolymere in Lösung und im dünnen Film*  
Grant Number: MU 1487/29-1, Project Leader: Prof. Dr. Peter Müller-Buschbaum  
Grant Number: PA 771/20-1, Project Leader: Prof. Dr. Christine Papadakis
- Teilprojekt *Inorganic-organic hybrid photovoltaic solar cells using novel hybrid materials* im GRK 2022: University of Alberta / Technische Universität München Internationale Graduiertenschule für Funktionelle Hybridmaterialien (ATUMS) der DFG IRTG-2022  
Project Leader: Prof. Dr. Peter Müller-Buschbaum
- Within DFG Collaborative Research Centre SFB TRR 80/2:  
*Elektronische Struktur und martensitische Phasenumwandlungen*  
Teilprojekt: G04  
Project Leader: Prof. Dr. Winfried Petry
- Im Rahmen des Memorandums of Understanding on Cooperation between DFG and RFBR:  
*Mischungen aus Lösungsmitteln und Mischungen aus Blockcopolymeren für die kontrollierte Präparation strukturierter dünner Blockcopolymerfilme*  
Grant Number: PA 771/10-2  
Project Leader: Prof. Dr. Christine Papadakis
- *Zweifach und orthogonal schaltbare Blockcopolymere aus zwitterionischen und thermoresponsiven Blöcken: Synthese und Strukturen in Lösung und im dünnen Film*  
Grant Number: PA 771/14-1  
Project Leader: Prof. Dr. Christine Papadakis
- *Dünne Filme aus pH und thermoresponsiven Triblockcopolymeren: von der Netzwerkdynamik zum defektfreien Film*

Grant Number: PA 771/19-1

Project Leader: Prof. Dr. Christine Papadakis

- Im Rahmen des Memorandums of Understanding on Scientific Cooperation between DFG and GACR:

*Kugelförmiges Pferd im Vakuum oder anwendbare Mizellen? Verhalten und Form von Nanopartikeln als Wirkstoffträger für Krebsmedikamente in reeller Blutumgebung*

Grant Number: PA 771/17-1

Project Leader: Prof. Dr. Christine Papadakis

#### **Bundesministerium für Bildung und Forschung:**

- *FlexiProb: Flexible Probenumgebungen für die Untersuchung weicher Materie zur Implementierung an der ESS*

Teilprojekt: 3

Project Leader: Prof. Dr. Peter Müller-Buschbaum

- *Optische In-situ Methoden für das Flugzeitspektrometer TOFTOF*

Project Leader: Prof. Dr. Peter Müller-Buschbaum

#### **Bayerisches Staatsministerium für Bildung und Kultus, Wissenschaft und Kunst:**

- Im Rahmen der Munich School of Engineering (MSE):

*Solar Technologies Go Hybrid (SolTech) - Forschungsnetzwerk TUM.solar*

Project Leader: Prof. Dr. Peter Müller-Buschbaum

- Im Rahmen der Munich School of Engineering (MSE): Netzwerk Regenerative Energien  
*Aufbau eines interdisziplinären Netzwerks aus Lehrstühlen der Technischen Universität München und anderen Forschungseinrichtungen zur Förderung der Forschungsaktivitäten im Bereich der regenerativen Energien*

Project Leader: Prof. Dr. Peter Müller-Buschbaum

#### **Technische Universität München:**

- Im Rahmen der International Graduate School of Science and Engineering (IGSSE)

*Interface Science for Photovoltaics - a EuroTech GreenTech Initiative*

Project Leader: Prof. Dr. Peter Müller-Buschbaum

#### **Others:**

- Im Rahmen des Exzellenzclusters Nanosystems Initiative Munich (NIM)

*Nanosystems for Energy Conversion*

Principal Investigator: Prof. Dr. Peter Müller-Buschbaum

- Im Rahmen der Leonhard-Lorenz-Stiftung

*Selbstdiffusion in Aluminium-Germanium Legierungsschmelzen untersucht mit quasi-elastischer Neutronenstreuung*

Project Leader: Prof. Dr. Winfried Petry

## 9 The chair



### 9.1 Staff

**Chair:** Prof. Dr. Winfried Petry

**Head:** Prof. Dr. Peter Müller-Buschbaum

#### Professors

Prof. Dr. Christine M. Papadakis

#### Fellows

Dr. Anatoly V. Berezkin  
Dr. Harald Breitzkreutz  
Dr. Eva Maria Herzig  
Dr. Volker Körstgens  
Dr. Michael Leitner

Dr. Wiebke Lohstroh  
Dr. Ezzeldin Metwalli Ali  
Dr. Jürgen Neuhaus  
Dr. Neelima Paul

**PhD students**

Bruno Baumeister	Stephan Pröller
Lorenz Bießmann	Christian Reiter
Wei Cao	Nitin Saxena
Tobias Chemnitz	Simon Schaper
Wei Chen	Robert Schenk
Mihael Corić	Johannes Schlipf
Stefan Döge	Christian Schwarz
Oliver Filonik	Jingyi Shi
Sebastian Grott	Luca Silvi
Alexander Erwin Heldmann	Lin Song
Nuri Hohn	Riane Elizabeth Stene
Tanja Huber	Christian Steyer
Florian Jung	Bo Su
Jia-Jhen Kang	Sandro Szabò
Lukas Karge	Natalya S. Vishnevetskaya
Chia-Hsin Ko	Kun Wang
Jenny Lebert	Rui Wang
Nian Li	Sebastian Weiß
Xiaohu Li	Tobias Widmann
Franziska Löhner	Kerstin Wienhold
Daniel Moseguí González	Stephan Wlokka
Lucas Kreuzer	Senlin Xia
Pascal Neibecker	Dan Yang
Bart-Jan Niebuur	Shanshan Yin
Shambhavi Pratap	Xiaohan Zhang

**Master students**

Julian Becker	Regina Kluge
Christoph Bilko	Eva Kratzer
Kalyan Biswas	Gilles Möhl
Florian Buschek	Victor Oliveros Colón
Debamitra Chakraborty	Mubashar Rafiq
Pin-Yi Chiu	Steffen Schlosser
Kora-Lee Claude	Armin Schreiber
Rodrigo Delgado Andres	Dominik Schullerer
Fabien Guelle	Christian Schwarz
Jiabin Gui	Kaltrina Shehu
Peter Haslauer	Bernhard Springer
Adrian Hausmann	Margret Thordardottir
Christian Herold	Markus Trunk
Andreas Hetzenecker	Christian Weindl
Kiran M. John	Kejie Zhang
Bernhard Kalis	Andreas Zheng

**Bachelor students**

Johannes Costa  
Felix Fischer  
Benedikt Grünewald  
Simon Helmer  
Nicole Höfer  
Linus Huber  
Irina Ilichewa  
Mike J. Jost  
Josef Keilhofer  
Lucas Krempel  
Alejandro Lòpez

Wolfgang Männer  
Felix Martin  
Robert Neagu  
Leander Peis  
Benjamin Pretzl  
Jonas Puchmayr  
Stephan Rinner  
Maximilian Schart  
Peter Schneider  
Felix Sievers  
Simon Schwärzler

**Students assistants**

Catriona Bruce  
Josef Huber  
Fatemeh Jalaei  
Yifeng Liu

Florian Pantle  
Jonas Puchmair  
Thomas Retzer  
Yinong Zhang

**Internships:**

Alida Severin

**Technical/administrative staff**

Sebastian Fink  
Reinhold Funer  
Josef Kaplonski  
Carola Kappauf

Matthias Maier  
Dieter Müller  
Marion Waletzki

## 9.2 Graduations

- **Accomplished PhD theses**

Daniel Moseguí González

*Magnetic tuning of organic solar cell performance*

Robert Schenk

*REP atomizer engineering & UMo fuel-powder fabrication*

Luca Silvi

*Hydrogen dynamics in complex borohydrides*

Lin Song

*Tailoring titania photoanodes for application in solid-state dye-sensitized solar cells and hybrid solar cells*

Natalya S. Vishnevetskaya

*Orthogonally switchable block copolymers*

- **Accomplished Master theses**

Julian Becker

*Thermal-hydraulic influence of manufacturing tolerances of involute shaped fuel plates*

Florian Buschek

*Water based hybrid solar cells*

Pin-Yi Chiu

*Correlation of magnetic domains and the L21 anti-phase domains in NiMn-based Heusler alloys*

Kora-Lee Claude

*Phase behavior of the thermoresponsive polymer poly(N-isopropylmethacrylamide)*

Adrian Haussmann

*Gold cluster growth kinetics at the metal-polymer interface of water-processed hybrid solar cells studied by in situ GISAXS sputter deposition*

Christian Herold

*Multi-stimuli-responsive polymer thin films*

Andreas Hetzenecker

*Hybrid photovoltaics based on diblock copolymer structured, mesoporous germanium thin films*

Kiran M. John

*Influence of processing parameters in conventional perovskite deposition and its application towards water-processed films*

Bernhard Kalis

*Vacuum chamber for in-operando grazing-incidence x-ray scattering experiments on novel thin-film solar cells*

Regina Kluge

*Investigation of an n-type polymer for thermoelectric applications*

Gilles Möhl

*In operando SAXS/SANS study of polymer electrolytes for lithium-ion batteries*

Victor Oliveros Colón

*Structural investigation of pH-responsive block copolymers using synchrotron SAXS and DLS*

Frank Oriold

*Characterization of defects in ZnO-based diodes grown by PA-MBE by means of electrical and optical techniques*

Mubashar Rafiq

*In-situ polymerized PEDOT:Tos thin films for thermoelectric applications*

Steffen Schlosser

*Investigation and characterization of diblock copolymer controlled titania morphologies*

Dominik Schullerer

*Fabrication and investigation of enhanced organic light emitting diode devices (OLEDs)*

Christian Schwarz

*Construction and commissioning of a pulsed-DC sputtering system & characterization of sputtered ZrN layers*

Bernhard Springer

*Structural and conductivity studies of block copolymer electrolytes for lithium-ion batteries*

Matthias Steinmassl

*Development of capacitive chemical gas sensors for carbon dioxide and humidity*

Margret Eva Thordardottir

*Investigating the humidity impact on mesoscopic perovskite morphology formation*

Markus Trunk

*Hybrid solar cells using plasmonic structure*

Kejie Zhang

*Nanoporous titania/silica hybrid electrodes for lithium-ion batteries*

Yinong Zhang

*PS-b-PEO based ionic liquid containing block copolymer electrolytes for lithium rechargeable batteries*

• **Accomplished Bachelor theses**

Johannes Costa

*Conductive paper*

Felix Fischer

*X-ray scattering and analysis on hybrid organometallic lead halide perovskites*

Benedikt Grünwald

*The influence of the protein HSA on the release of doxorubicin from HPMA copolymer carriers*

Simon Helmer

*Non-equilibrium assembly processes in supramolecular materials*

Nicole Höfer

*Dynamics of responsive polymers under high pressure*

Linus Huber

*Novel free-standing single crystal perovskite solar cells*

**Irina Ilichewa**

*Investigations on ZnO scattering layers for OLED applications*

**Mike J. Jost**

*Introducing Ag<sub>10</sub>Te<sub>4</sub>Br<sub>3</sub>-nanoparticles into a hybrid thermoelectric material based on a polymer-nanoparticle composite*

**Josef Keilhofer**

*Enhancement of thermoelectric properties of PEDOT:PSS by redox doping and acid-base doping*

**Lucas Krempel**

*Device development for organic solar cell characterization on near space missions*

**Felix Martin**

*Conductive paper*

**Robert Neagu**

*Correction for true coincidence summing for a Germanium detector*

**Leander Peis**

*Role of molecular interactions for stimuli-responsive polymers of potential Use in soft robotics*

**Benjamin Pretzl**

*Effect of a ionic liquid post-treatment on thermoelectric properties of PEDOT:PSS thin films*

**Jonas Puchmayr**

*Influence of salt and molar mass on the dynamic behaviour of polyzwitterions in aqueous solutions*

**Stephan Rinner**

*Role of molecular interactions for stimuli-responsive polymers of potential use in soft robotics*

**Maximilian Schart**

*Thin films from multiresponsive polymers*

**Peter Schneider**

*Transporting layers in single crystal perovskite solar cells*

**Simon Schwärzler**

*Experimental determination of a total stress-tensor in welds of austenitic steel*

**Felix Sievers**

*Fabrication and investigation of enhanced organic light emitting diode devices OLEDs*

### 9.3 Guests

- Prof. Dr. Jiping Wang, Prof. Dr. Qi Zhong, Zhejiang Sci-Tech University, PR China  
*15 – 22 Jan 2017*
- Prof. Dr. Natalie Germann, TUM Weihenstephan  
*24 Jan 2017*
- Dr. Manfred Kriechbaum, Graz University of Technology, Austria  
*1 – 2 Feb 2017*
- Prof. Dr. Thomas Weitz, Physics of Nanosystems, LMU Munich  
*25 Apr 2017*
- Prof. Alfons Schulte, University of Central Florida, USA  
*12 May – 25 Jul 2017*
- Prof. André Laschewsky, Fraunhofer Institut für Angewandte Polymerwissenschaften, Potsdam-Golm  
*24 Jun 2017*
- Eric Bergendal, Royal Institute of Technology, Sweden  
*26 – 30 Jun 2017*
- Prof. Dr. Dr. Hans Robert Kalbitzer, University of Regensburg  
*4 Jul 2017*
- Christina Braun, University of Alberta, Canada  
*1 Aug – 5 Oct 2017*
- Dr. Tabeyeh Ameri, Friedrich-Alexander-Universität Erlangen-Nürnberg  
*26 Sep 2017*
- Dr. Gaetano Mangiapia, Forschungszentrum Jülich Garching  
*25 Oct 2017*
- Dr.-Ing. Markus Gallei, Michael Appold, Technische Universität Darmstadt  
*22 Nov 2017*
- Clemens Sachse, Technische Universität Dresden  
*29 Nov - 1 Dec 2017*
- Prof. Dr. Rio Kita, Tokai University, Kanagawa, Japan  
*6 Dec 2017*
- Prof. Dr. Wolfgang Brütting, Universität Augsburg  
*18 Dec 2017*
- Liulai Zhou, Dongfeng Chen, CIAE, China  
*21 Dec 2017*